

**Investigating the viability of using relative humidity—based moisture sorption isotherms to
generate moisture profiles of concrete highway bridge decks**

A Thesis

**Presented to
the faculty of the School of Engineering and Applied Science
University of Virginia**

**in partial fulfillment
of the requirements for the degree**

Master of Science

by

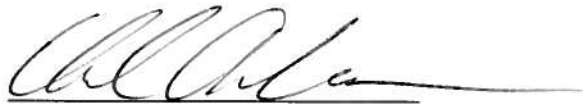
Chad Michael Anderson

December

2013

APPROVAL SHEET

The thesis
is submitted in partial fulfillment of the requirements
for the degree of
Master of Science


AUTHOR

The thesis has been read and approved by the examining committee:

Dr. Michael C. Brown

Advisor

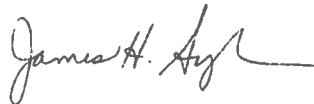
Dr. Steven B. Chase

Dr. Thomas T. Baber

Dr. Devin K. Harris

Dr. Zachary C. Grasley

Accepted for the School of Engineering and Applied Science:



Dean, School of Engineering and Applied Science

December
2013

**Investigating the viability of using relative humidity—based
moisture sorption isotherms to generate moisture profiles of
concrete highway bridge decks**

Table of Contents

1. INTRODUCTION	4
2. LITERATURE REVIEW	6
2.1 THE DIFFERENCE BETWEEN GAS AND VAPOR.....	6
2.2 PSYCHROMETRY METRICS: PERCENTAGE OF SATURATION AND RELATIVE HUMIDITY	7
2.2.1 <i>Brief Overview of Necessary Psychrometry Metrics</i>	7
2.2.2 <i>Vapor and Saturation Vapor Pressures of a Gaseous Mixture</i>	7
2.2.3 <i>Equilibrium Vapor Pressure of a Liquid</i>	9
2.2.3.1 Relationship between the equilibrium vapor pressure of a pure liquid solvent and the saturation vapor pressure of a gaseous mixture	9
2.2.3.2 Effect of temperature on the equilibrium vapor pressure of a solvent	11
2.2.3.3 Effect of nonvolatile solutes on the equilibrium vapor pressure of a solvent.....	13
2.2.3.4 Effect of curvature on the equilibrium vapor pressure of a liquid solvent/solution	19
2.2.4 <i>Percentage of Saturation and Relative Humidity Defined</i>	45
2.2.4.1 Percentage of saturation.....	45
2.2.4.2 Relative humidity	46
2.3 MOISTURE CONTENT AND RELATIVE HUMIDITY IN CONCRETE	48
2.3.1 <i>Porosity of Concrete</i>	48
2.3.1.1 Brief overview of the total porosity volume	48
2.3.1.2 Gel pores	49
2.3.1.3 Capillary pores.....	50
2.3.1.4 Entrained and entrapped air voids.....	52
2.3.2 <i>Moisture Content and Transport Processes in Concrete</i>	52
2.3.2.1 Interlayer moisture	52
2.3.2.2 Capillary moisture	53
2.3.3 <i>Relative Humidity in Concrete</i>	58
2.3.3.1 Capillary adsorbed moisture: BET equation	58
2.3.3.2 Capillary condensed moisture: Kelvin equation	63
2.3.3.3 Sorption isotherms: relative humidity – based	68
2.4 METHODS OF RELATIVE HUMIDITY CALIBRATION AND MEASUREMENT	70
2.4.1 <i>General</i>	70
2.4.2 <i>Methods of Relative Humidity Calibration</i>	71
2.4.2.1 Overview of calibration classifications and types.....	71
2.4.2.2 Primary standards	71
2.4.2.3 Transfer standards	72
2.4.2.4 Secondary devices	73
2.4.3 <i>Methods of Relative Humidity Measurement</i>	73
2.5 ISSUES AND CONCERNS	76
3. BACKGROUND	78
4. PURPOSE	79
4.1 OBJECTIVE	79
4.2 HYPOTHESES	80
4.2.1 <i>Hypothesis I: Non-Trivial, Undetectable Moisture Content</i>	80
4.2.2 <i>Hypothesis II: System Compatibility Assumption</i>	80
5. SCOPE	82
6. METHODOLOGY	82
6.1 METHODOLOGY – TESTING SYSTEM COMPATIBILITY ASSUMPTION.....	82
6.2 METHODOLOGY – NON-TRIVIAL, UNDETECTABLE MOISTURE CONTENT.....	85
7. MATERIALS AND METHODS	85

7.1 MULTI-SENSOR DATA ACQUISITION SYSTEM	85
7.1.1 Overview	85
7.1.2 Sensors Selected	86
7.1.3 Multiplexer and Data-Logger Selections	87
7.1.4 DAQ Programming	89
7.1.5 Sensor Probes	90
7.2 SENSOR CALIBRATION	92
7.2.1 Relative Humidity Sensor Calibration Method	92
7.2.2 Temperature Sensor Calibration Method	95
7.2.3 Relative Humidity Sensor Calibration Method – Apparatus Design	96
7.2.4 Example RH Calibration Function Calculation	98
7.2.4.1 Overview	98
7.2.4.2 Step 1 – Data collection from RH calibration apparatus	99
7.2.4.3 Step 2 – Calculation of theoretical RH residual values	101
7.2.4.3 Step 3 – Calculation of the RH residual and calibration models	110
7.2.4.4 Step 4 – Implementation of the RH calibration model	117
7.3 REPRESENTATIVE SPECIMEN AND SENSOR PLACEMENTS	118
7.3.1 Representative Specimen	118
7.3.2 Sensor placement and data collection	119
7.4 MOISTURE SORPTION ISOTHERM CREATION	122
7.4.1 DAQ and Environmental Apparatus Design	122
7.4.2 Disc Specimen Design	126
7.4.3 Calculations	130
7.4.3.1 Introduction	130
7.4.3.2 Desorption data	131
7.4.3.3 Saturated and dry mass determination	138
7.4.3.4 Moisture sorption (desorption) isotherm	143
8. RESULTS	151
8.1 COLLECTED DATA FROM REPRESENTATIVE BRIDGE DECK SPECIMEN	151
8.2 MOISTURE CONTENT AND PERCENT OF SATURATION PROFILES	166
9. FINDINGS	170
10. DISCUSSION	178
11. CONCLUSIONS	179
12. RECOMMENDATIONS	180
13. ACRONYMS & VARIABLES	182
14. ACKNOWLEDGEMENTS	188
15. BIBLIOGRAPHY	189
16. APPENDICES	195
16.1 APPENDIX – A: SENSOR PROBE DESIGN AND FABRICATION TECHNIQUES	195
16.1.1 Probe 1	195
16.1.2 Probe 2	203
16.2 APPENDIX – B: RH & T SENSOR CALIBRATIONS	204
16.3 APPENDIX – C: PREPARATION OF CONCRETE DISC SPECIMENS	208

1. INTRODUCTION

Moisture is a critical factor, fundamental to driving many of the deterioration mechanisms, reactions and processes of reinforced concrete structures, especially when the structures are exposed to natural weathering. In at least three general ways moisture can lead to structural deterioration, which includes: physical mechanisms, chemical reactions (including electrochemical and physico-chemical reactions) and transport-related processes. An example of a physical moisture deterioration process would be freeze-thaw deterioration. Freeze-thaw deterioration is deterioration which occurs as a direct result of moisture inside the concrete pore system expanding when frozen (by approximately 9% in volume), potentially generating relatively large expansive pressures. Over time, these expansive pressures may lead to significant structural damage. The degree to which the expansive pressures generated will degrade a structure with time is dependent upon several factors, including the degree of pore saturation (Neville 2011; Lamond and Pielert 2006). An example of a physico-chemical reaction is alkali-silica reaction (ASR). As a result of chemical reactions between the pore water, alkalis from cement and poor quality siliceous materials (found in some aggregates) an alkali-silica gel is formed. Once formed, this gel will take in available moisture and swell; consequently, this leads to hydraulic pressure build-up and cracking (Neville 2011).

One could compile a rather lengthy list of moisture-driven chemical reaction-based attacks, which either attack hydration products directly or react to produce destructive internal pressures. Additionally, there are several ways in which embedded reinforcement may come under attack, leading to additional sources of destructive internal pressures and reinforcement section loss. While it is true that some of the materials responsible for many such attacks could be initially present in the concrete mix, a variety of attacks may be caused or exacerbated when certain materials from external sources diffuse into the concrete through the pore solution. Corrosion is an example of a process that relies heavily on the transport of certain materials through pore solution (i.e., diffusion) from external sources prior to the initiation of the actual deterioration mechanism. Though the amount is debatable within the corrosion community, there exists a chloride ion concentration threshold within concrete below which corrosion does not initiate (unless induced by an alternate mechanism, such as low pH.) Much of the harmful chloride ion content is transported into the concrete from external sources by diffusion through the pore solution. When the threshold is reached, corrosion may initiate, leading to reinforcement section loss, but more importantly high expansive internal pressures that rupture the concrete (Neville 2011).

Based on these very few examples, it seems advantageous to be able to determine and track the levels of moisture inside in-service concrete structures, especially if this can be accomplished in a non-destructive way. Being able to determine the “real-time” moisture levels in concrete structures would lead to better moisture-related deterioration correlations, and facilitate the determination of certain material properties, like diffusion

coefficients. Additionally, other applications of obtained moisture information would include determining the effectiveness of moisture barrier products. A particular application is to use moisture information to determine the water-tightness of overlay systems applied to concrete bridge decks.

One possible method for determining the internal moisture levels of concrete structures, in a relatively non-destructive way, is through the use of relative humidity sensors. The idea is that there is an almost intuitive relationship between the level of moisture in a concrete material and the measurable internal relative humidity. This constitutive relationship is encapsulated by the relative humidity—based moisture sorption isotherm. That is to say, there exists a constitutive relationship between relative humidity and the moisture contained in a hygroscopic material (i.e., concrete) at a given temperature, termed the **relative humidity—based moisture sorption isotherm**. Where “isotherm” indicates that this experimentally correlated relationship [function] is created at a single temperature. The focus of this paper is to investigate whether or not this approach to determining moisture levels inside concrete bridge structures (i.e., specifically the concrete bridge decks), is viable. If there are limitations to this approach, this investigation is expected to uncover and define them.

It should be explained, that while the objective of this investigation is to investigate the viability of a method for determining moisture, in many applications it may not be necessary to determine the actual moisture contained in a concrete structure. As was stated, there is a constitutive relationship between relative humidity and moisture content. That being said, in general, a rise in relative humidity would in many cases indicate an increase in moisture. Consequently, applications may be found written in terms of the relative humidity parameter. For example, currently there is an ASTM standard which provides guidance for assessing the maturity of concrete floor slabs written in terms of internal relative humidity (ASTM Standard F2170 2011). Additionally, work has been done to correlate relative humidity levels to drying stresses in young concrete (Grasley, Lange, and D'Ambrosia 2006). Also, governing equations will be developed in this investigation relating relative humidity to certain physico-chemical properties of pore solution. It is possible that such properties are more useful for a particular application than knowing the absolute level of moisture. The author shall not offer an opinion as to which parameter may be superior. Rather, the author understands that the decision to use one parameter over another is application dependent, and should be left up to the reader's judgment.

This investigation is divided into two main parts: a thorough review of current literature and the experimental study. The literature review is an integral piece of this investigation, as it not only serves as the theoretical basis for all of the author's hypotheses and assumptions, but it also offers a scientific foundation necessary to understand the experimental results being observed and the conclusions. The experimental section is where the author shall test the hypotheses and assumptions made. Based on the experimental results and findings, the author shall be able to comment on the viability of using relative humidity—based moisture sorption isotherms to generate moisture [content] profiles of concrete highway bridge decks.

2. LITERATURE REVIEW

2.1 THE DIFFERENCE BETWEEN GAS AND VAPOR

Throughout this paper the terms gases (or gas mixtures) and vapor will be used. They are not interchangeable terms. There is a definite distinction between a gas and a vapor, which will be defined in this section of the paper. Figure 1 below is a generic **phase diagram**, which defines physical phases (or states) of matter as a function of temperature and pressure (Masterton and Hurley 2004; Atkins 1990). Each substance in general has its own phase diagram.

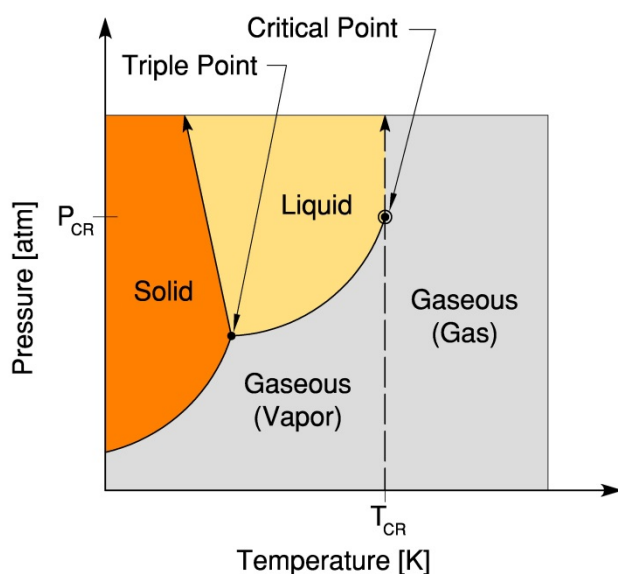


Figure 1: Phase Diagram (Generic)

The phases shown in the figure above are solid, liquid, and gaseous (vapor and gas) states. They are separated by solid lines representing phase equilibrium. In general, substances can change phase from gaseous to liquid or solid through reduction of temperature, increase in pressure, or some combinations thereof. The point at which all three phases are in phase equilibrium is called the **triple point**. At some point along the horizontal axis the temperature reaches a **critical temperature** (T_{CR}) value, above which increased pressure alone is not sufficient to alter the gaseous state. This critical temperature and the corresponding **critical pressure** (P_{CR}) together make up the **critical point**. A substance in a gaseous state is called a vapor when it exists below and to the left of the critical point. In this range it is possible to alter the substance's physical state by only changing the pressure. A substance in a gaseous state is called a gas (or is also called a supercritical fluid or a permanent gas) when it exists above the critical temperature, as delineated above in Figure 1 by the dashed line (Atkins and De Paula 2006; Masterton and Hurley 2004). A gas will not change state by just changing the pressure. For a gas to change state, a cooling in temperature must also be applied. The

critical point for water is defined by the critical temperature and critical pressure, 374 [°C] (or 647 [K]) and 218 [atm] respectively. Since the temperatures we are likely to deal with in this study are well below the critical temperature for water, we presume that any water in gaseous form is a vapor (Wyer 1906; Masterton and Hurley 2004; Zumdahl and Zumdahl 2003).

2.2 PSYCHROMETRY METRICS: PERCENTAGE OF SATURATION AND RELATIVE HUMIDITY

2.2.1 Brief Overview of Necessary Psychrometry Metrics

Earth's atmosphere near sea level is composed of Nitrogen (N_2), Oxygen (O_2) and lesser concentrations of other important gases; also present is water vapor (H_2O) (Zumdahl and Zumdahl 2003). Water vapor contained in the atmosphere results primarily from the vaporization (or evaporation) of the earth's liquid water (lakes, rivers and oceans). Vaporization is an endothermic process. Energy absorbed from the sun facilitates the release of water molecules into the atmosphere when the level of kinetic energy necessary to overcome the intermolecular hydrogen bonding forces binding them together in a liquid state is achieved. The energy level necessary to achieve vaporization is called the **Heat of Vaporization** (ΔH_v), and is defined as the “*energy required to vaporize 1 mole of a liquid at 1 atm*”. The heat of vaporization for water is 40.7 kJ/mol (Zumdahl and Zumdahl 2003).

The field of scientific study directly concerned with the properties of gaseous (gas-vapor) mixtures like our atmosphere is called **psychrometry** (Perry and Green 2008). A general term used in psychrometry to define water existing as a vapor in a carrier gas or gas mixture is **humidity** (Wyer 1906; Wiederhold 1997). When humidity is present in a gas, the gas is described as being “wet”. Conversely, a gas containing no humidity is described as being “dry”. Two mathematical metrics that are most widely used to quantify the degree of humidity content in a gaseous mixture are the percentage of saturation (S) (or percentage of absolute humidity) and relative humidity (RH). During this review, the percentage of saturation and relative humidity metrics shall be defined, along with the relationship between them. First it will be necessary to define vapor pressure (p_v) and saturation vapor pressure (p_{sat}) of gaseous mixtures, which are key parameters common to both S and RH .

2.2.2 Vapor and Saturation Vapor Pressures of a Gaseous Mixture

Dalton's Law of partial pressures states that “*The total pressure of a gas mixture is the sum of the partial pressures of the components of the mixture*” (Masterton and Hurley 2004). Thus, the pressure that the atmosphere exerts is the sum of the individual pressures, or partial pressures, of the gases and vapor within it, as shown in equation 2.1 below. The partial pressure attributed to vapor molecules, which we shall assume to be pure water, is called the **vapor pressure** (p_v) of the gaseous mixture.

$$P_{atm} = p_{N_2} + p_{O_2} + p_{other} + p_v \quad \text{Equation 2.1}$$

In general, Dalton's Law would follow the form shown in equation 2.2

$$P_{total} = \sum_{i=1}^N p_i \Rightarrow p_1 + p_2 + \dots + p_N \quad \text{Equation 2.2}$$

where

- P_{total} : Total pressure of the gaseous (gas-vapor) mixture [*Force/Area*²]
- p_1 : Partial pressure of gas or vapor No. 1 in the gaseous mixture
- p_2 : Partial pressure of gas or vapor No. 2 in the gaseous mixture
- p_N : Partial pressure of the Nth gas or vapor in the gaseous mixture

When the ideal gas law (*i. e.* $PV = nR_uT$) is substituted into to Dalton's Law, the general form then looks like:

$$P_{total} = \frac{R_uT}{V} \sum_{i=1}^N n_i \Rightarrow \frac{R_uT}{V} (n_1 + n_2 + \dots + n_N) \quad \text{Equation 2.3}$$

where

- R_u : Universal Gas Constant ~ 8.31451 [*J/(K × mol)*]
- T : Temperature [*K*]
- V : Volume of the gaseous (gas-vapor) mixture [*Length*³]
- n_1 : Number of moles of gas or vapor No. 1 in the gaseous mixture [*mol*]
- n_2 : Number of moles of gas or vapor No. 2 in the gaseous mixture [*mol*]
- n_N : Number of moles of the Nth gas or vapor in the gaseous mixture [*mol*]

It shall be assumed that both gases and vapors obey the ideal gas law (Masterton and Hurley 2004). By letting n_N equal the number of vapor moles (n_v) and collecting the remaining molar gas terms ($n_g = n_1 + n_2 + \dots + n_{N-1}$), equation 2.3 can be rewritten in the following way:

$$P_{total} = \frac{R_uT}{V} (n_g + n_v) \quad \text{Equation 2.4}$$

Then after some basic algebraic manipulation/substitution we arrive at a useful mathematical expression for the vapor pressure of a gaseous mixture, shown in equation 2.5 below (Perry and Green 2008).

$$p_v = \left(\frac{n_v}{n_g + n_v} \right) P_{total} \Rightarrow X_v P_{total} \quad \text{Equation 2.5}$$

where

- X_v : Mole fraction of vapor molecules present in the total mixture [*mol/mol*]

The **saturation vapor pressure**(p_{sat}) is a special case of a gaseous mixture's vapor pressure, where an equilibrium condition exists between the *pure* solvent and its vapor phase, in a closed system at a given temperature. That is to say the same molar quantities of water molecules are entering the gaseous phase as are leaving it. With the exception of extreme cases (i.e., super-saturation), the pressure exerted by this vaporized molar quantity, existing at a given temperature, is the largest (or saturation) pressure which may be exerted by the *pure* solvent. Later, the author shall discuss how this equilibrium is affected by solute(s) and meniscus curvature, resulting in a new peak exerted vapor pressure that is generally reduced to values below the saturation pressure (Wyer 1906; Zumdahl and Zumdahl 2003). For the purposes of this paper the author shall assume the solvent to be pure water in a liquid phase unless expressed to be otherwise.

The vapor pressure formulated above in equation 2.5 is for a gaseous (gas-vapor) mixture. As we proceed forward to discuss saturation vapor pressure, the term equilibrium vapor pressure(P_{eq}) will be introduced. Equilibrium vapor pressure is often used interchangeably with the term vapor pressure of a liquid (Zumdahl and Zumdahl 2003). However, in the latter context we are referring to a liquid state property, not a gaseous state property. It is important at this juncture to understand that there is a distinction to be made with this terminology since the vapor pressure of a gaseous mixture is not the same as the vapor pressure of a liquid. To avoid confusing the reader, the author will explicitly indicate the physical state when using this terminology.

2.2.3 Equilibrium Vapor Pressure of a Liquid

2.2.3.1 Relationship between the equilibrium vapor pressure of a pure liquid solvent and the saturation vapor pressure of a gaseous mixture

As mention previously, the saturation vapor pressure (p_{sat}) is a special case of a gaseous mixture's vapor pressure that can be determined experimentally in a few different ways. Three classical ways include the sealed chamber, barometric, and chilled mirror hygrometer methods (Zumdahl and Zumdahl 2003; Wiederhold 1997). The sealed chamber method shall be discussed here in detail, as the principles are fundamental and directly applicable to understanding the techniques used by the author to calibrate and measure with relative humidity sensors in a system assumed to be closed.

A liquid solvent, assumed to contain no dissolved gases, is sealed in a container with an attached pressure gauge, as shown in figure 2. The goal is to measure the change in pressure as the gaseous atmosphere sealed inside the container takes on solvent vapor, thereby effectively measuring only the partial pressure attributable to the vapor. To this end the atmosphere inside the container above the gaseous-liquid interface needs to be initially dry. So, one can either add the solvent, sealing the container very quickly afterward, or seal the container first and then add the solvent, similar to the schematic shown in Grasley's paper "*Relative Humidity in Concrete: What does it mean?*" (Grasley et al. 2006, 51-57).

In the beginning, the liquid's molecules will evaporate into the volume above it, defined by the container; almost simultaneously the molecules in the vapor phase will start to condense, returning to liquid phase. Initially, the rate of evaporation will exceed the rate of condensation, resulting in a net loss of liquid. Consequently, this causes a net gain of vaporized solvent molecules and an increase in the observed pressure, as shown in figure 2(B). In time though, as shown in figure 2(C) the rate at which the liquid evaporates will equal the rate it condenses.

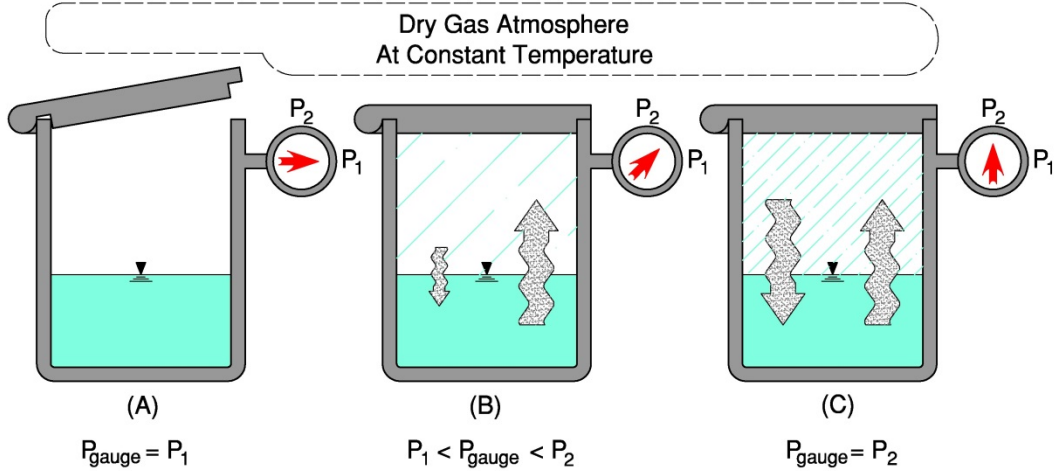


Figure 2: Container with solvent at a constant temperature, (A) open to the “dry” atmosphere, (B) sealed with evaporation rate exceeding condensation rate, (C) sealed with evaporation rate equal to the condensation rate.

When the gaseous-liquid system reaches an evaporation/condensation equilibrium condition, at a fixed temperature, the system is said to have reached **dynamic equilibrium**. The change in pressure observed when this system has reached dynamic equilibrium is called the **equilibrium vapor pressure** (P_{eq}) or vapor pressure of the liquid, at that temperature ($p_v = \Delta P = P_2 - P_1 = P_{eq}$). At dynamic equilibrium, the gaseous mixture will no longer accept additional humidity (i.e. vaporized liquid), indicating that the vapor has saturated the gaseous mixture. So then, the vapor pressure of the liquid solvent is equal to the saturation vapor pressure of the gaseous mixture in the closed system, shown in figure 3 and equation 2.6 (Zumdahl and Zumdahl 2003; Wyer 1906; Atkins and De Paula 2006).

$$P_{eq} = p_{sat} \quad \text{Equation 2.6}$$

where

P_{eq} : Equilibrium vapor pressure of a liquid solvent [$Force/Area^2$]

p_{sat} : Saturation vapor pressure of a gaseous mixture [$Force/Area^2$]

Since the equilibrium vapor pressure of a liquid solvent at a temperature is in general a uniquely fixed property of the solvent, and the individual partial pressures of the gaseous mixture are independent of each other, dynamic equilibrium is between the solvent's vapor and the solvent alone. The composition of the dry gas mixture does nothing to

change the partial vapor pressure of the solvent with which the gaseous mixture is in equilibrium (Zumdahl and Zumdahl 2003; Masterton and Hurley 2004; Atkins and De Paula 2006). It should also be pointed out that the volumes of the liquid solvent and container were not critically defined here. This is because the vapor pressure of a solvent is also, in most cases, an intensive property of the solvent; that is the volume has no effect on its properties. While it is possible for high pressure, applied to the solvent, to alter the vapor pressure of the solvent, there is no chance that such high pressure systems will be used in this study. As an example, Atkins and De Paula calculate that for liquid water (at 25°C) a change in the applied pressure of 10 bar (≈ 7500 mmHg), applied mechanically or by an inert gas, will increase the vapor pressure of the solvent by less than one percent (Atkins and De Paula 2006; Poling, Prausnitz, and O'Connell 2001). The only requirements are an air-tight container and a gaseous atmosphere that is initially dry. Again, the reason for an initially dry atmosphere is to ensure the partial vapor pressure of the gaseous mixture is zero at the beginning of the experiment, thereby allowing the change of pressure measured to be attributed entirely to the liquid's vapor.

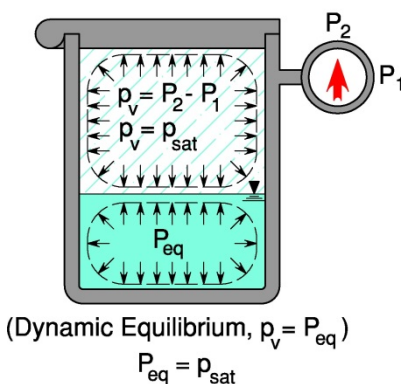


Figure 3: Container with solvent at dynamic equilibrium at constant temperature

Had we started with a wet atmosphere, the change in observed pressure measured at dynamic equilibrium would have been less, since the gaseous mixture would have started with an initial partial vapor pressure greater than zero. Regardless, the same saturation vapor pressure would have been achieved by the gaseous mixture, though not completely measured, and the system would still have achieved dynamic equilibrium. If some of the liquid solvent were removed from the container, decreasing its liquid volume, the solvent would resume the process of trying to achieve dynamic equilibrium until it was reestablished. When reestablished there would be no change to the magnitude of the equilibrium vapor pressure. This is provided that we have left ourselves with enough liquid solvent to reach dynamic equilibrium prior to its total evaporation, and we have maintained a constant temperature (Masterton and Hurley 2004).

2.2.3.2 Effect of temperature on the equilibrium vapor pressure of a solvent

As stated, temperature directly affects the equilibrium vapor pressure of a liquid solvent. In fact, the equilibrium vapor pressure of a solvent is a non-linear function of temperature, and cannot be completely defined without it. By increasing the solvent's temperature, the chemical potential energy of the solvent is reduced, which allows more

molecules to obtain the kinetic energy required to break free from the intermolecular forces binding them in liquid phase. This, in turn, increases the equilibrium vapor pressure of the liquid solvent. Conversely, a decrease in temperature removes energy from the system, which results in fewer molecules obtaining the kinetic energy required to break free, and a decrease in the equilibrium vapor pressure of the liquid solvent. Based on the relationship between the equilibrium vapor pressure of a liquid solvent and the saturation vapor pressure of the gaseous mixture above it, established previously, the saturation vapor pressure is also defined by the same non-linear function of temperature.

Although non-linear, the relationship between the equilibrium vapor pressure and temperature can be linearized (of the form $y = m \times x + b$) by the following empirical equation (Masterton and Hurley 2004; Zumdahl and Zumdahl 2003):

$$\ln(P_{eq}) = -\frac{\Delta H_v}{R_u} \left(\frac{1}{T} \right) + c \quad \text{Equation 2.7}$$

where

- ΔH_v : Heat of vaporization [*Energy/mol*]
- R_u : Universal Gas Constant ~ 8.31451 [*J/(K \times mol)*]
- T : Temperature [*K*]
- c : Constant – Does not depend on temperature

The equilibrium vapor pressure of pure solvents, like water, can often be found tabulated in handbooks (for various temperature ranges) (Perry and Green 2008). However, if the value for an arbitrary temperature is desired, one can substitute a known set of values, tabulated or experimentally obtained, into equation 2.7 and solve for the constant (c). Once the constant has been determined for that solvent, it can then be substituted into the same equation and used in the calculation of subsequent equilibrium vapor pressures existing at arbitrary temperatures. However, if one must use a known set of values to determine an unknown value in a second set, the classical **Clausius-Clapeyron equation** should be considered. The Clausius-Clapeyron equation is formulated by first solving equation 2.7 for the constant as shown in Equation 2.8 below:

$$\ln(P_{eq}) + \frac{\Delta H_v}{R_u} \left(\frac{1}{T} \right) = c \quad \text{Equation 2.8}$$

Next, two equations, based on equation 2.8, can be expressed to form equations 2.9 and 2.10; it is implied that both equations are referencing the same solvent at two different temperatures.

$$\ln(P_{eq_A}) + \frac{\Delta H_v}{R_u} \left(\frac{1}{T_A} \right) = c \quad \text{Equation 2.9}$$

$$\ln(P_{eq_B}) + \frac{\Delta H_v}{R_u} \left(\frac{1}{T_B} \right) = c \quad \text{Equation 2.10}$$

Since the constant term (c) is the same for each expression, we set equations 2.9 and 2.10 equal to each other and collect terms. This has the added benefit of eliminating the need to solve for the constant term. The resultant Clausius-Clapeyron equation is shown in equation 2.11.

$$\ln \left(\frac{P_{eq_A}}{P_{eq_B}} \right) = \frac{\Delta H_v}{R_u} \left(\frac{1}{T_B} - \frac{1}{T_A} \right) \quad \text{Equation 2.11}$$

where

- P_{eq_A} : Equilibrium vapor pressure for a solvent at temperature A [$Force/Area^2$]
- P_{eq_B} : Equilibrium vapor pressure for a solvent at temperature B [$Force/Area^2$]
- T_A : Temperature A [K]
- T_B : Temperature B [K]

It should be noted that while equation 2.11 is generally accepted as a “close enough” approximation in most cases, it is still based on an empirical fit to experimentally obtained values; and is known to induce error near the critical values (i.e. the triple and critical points). Other rigorous methods that are generally more accurate and attempt to overcome the limitations of the Clausius-Clapeyron equation do exist. However, they shall not be covered in this review, as the scope of this study does not include conditions in the vicinity of the critical values; nor will it become necessary to actually calculate the equilibrium vapor pressure of a liquid solvent. The objective here is to understand conceptually what equilibrium vapor pressure is, how it is defined, and its relationship to saturation vapor pressure (Poling, Prausnitz, and O'Connell 2001; Perry and Green 2008).

2.2.3.3 Effect of nonvolatile solutes on the equilibrium vapor pressure of a solvent

When exposed to moderate ambient conditions, liquid solvents like pure water have certain fixed intensive properties that allow for the predictable calculation of equilibrium vapor pressure as a function of temperature. However, when in solution with nonvolatile solutes, certain properties of the solvent are affected. These affected properties are termed **colligative properties** and vary with the concentration of the solute in the solution. Colligative properties include the boiling point, osmotic pressure, the freezing point and the equilibrium vapor pressure of a liquid solvent. In this section the author shall briefly concentrate focus on the single colligative property assumed to critically affect the outcome of this study, the equilibrium vapor pressure of a liquid solvent. More specifically, the focus shall be on the equilibrium vapor pressure of a liquid solvent in solution with inorganic, nonvolatile solutes (Masterton and Hurley 2004; Atkins and De Paula 2006).

Nonvolatile solutes, as the name might suggest, do not vaporize out of solution and so do not contribute to the vapor pressure of a gaseous mixture over a liquid solution in a sealed environment. Instead, when a nonvolatile solute is combined with a liquid solvent, like water, the dissolved molecules of solute act to block some of the pathways a solvent molecule might have used to escape from the liquid phase, thus slowing down the evaporation rate, while not interfering with condensation rate; the net effect is to lower the equilibrium vapor pressure of the solvent. Subsequently, this causes the vapor pressure of the gaseous mixture above the solution to equilibrate at a pressure below the saturation vapor pressure of the [pure] solvent. Therefore, the gas does not become saturated, though dynamic equilibrium has been achieved, as shown in equations 2.12, 2.13 and figure 4 (Atkins and De Paula 2006; Zumdahl and Zumdahl 2003).

So, when the sealed gaseous-liquid/solution system has reached dynamic equilibrium at a constant temperature:

$$p_v = P_{eq(soln)} \quad \text{Equation 2.12}$$

And

$$P_{eq(soln)} < p_{sat} \quad \text{Equation 2.13}$$

where

p_{sat} : Saturation vapor pressure of a gaseous mixture, above a pure solvent in a sealed container at dynamic equilibrium and constant temperature. [$Force/Area^2$]

$P_{eq(soln)}$: Equilibrium vapor pressure of a liquid solution at a constant temperature. [$Force/Area^2$]

p_v : Vapor pressure of a gaseous mixture, in a sealed container at dynamic equilibrium and constant temperature. [$Force/Area^2$]

If the nonvolatile solute forms a nonelectrolyte solution, then knowing the molar quantity of solute being dissolved into the solvent alone is generally sufficient for the determination of the solution's reduced equilibrium vapor pressure by comparison to that of the pure solvent. If however, the nonvolatile solute forms an electrolyte solution, then more information about the solvent will need to be known.

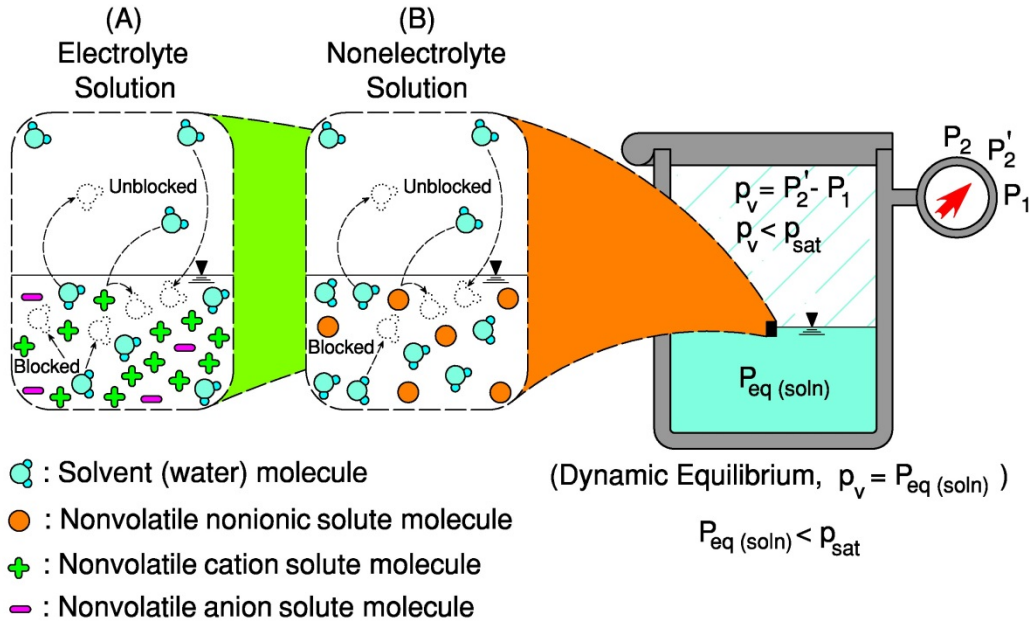


Figure 4: Container with solution containing a nonvolatile solute at dynamic equilibrium and constant temperature; where the solution is, (A) an electrolyte, (B) a nonelectrolyte.

If initially it is assumed that the solution formed is a nonelectrolyte, then according to equation 2.14 below, **Raoult's law**, the equilibrium vapor pressure of the solution is proportional to the amount of nonvolatile solute that is dissolved into it (Zumdahl and Zumdahl 2003; Masterton and Hurley 2004; Atkins and De Paula 2006).

$$P_{eq (soln)} = \left(\frac{n_{solv}}{n_{solv} + n_{sol}} \right) P_{eq} \Rightarrow X_s P_{eq} \quad \text{Equation 2.14}$$

where

- X_s : Mole fraction of solvent molecules in the solution [*mol/mol*].
- n_{sol} : Number of solute moles dissolved in the solution mixture [*mol*]
- n_{solv} : Number of solvent moles in the solution mixture [*mol*]

And after substituting equations 2.5 and 2.12 into equation 2.14, Raoult's law can be expressed (as shown in equation 2.15 or 2.16) in terms of the solvent saturation vapor pressure, at constant temperature:

$$p_v = X_s p_{sat} \quad \text{Equation 2.15}$$

or

$$X_s = \frac{p_v}{p_{sat}} \quad \text{Equation 2.16}$$

However, the scope of this study will deal exclusively with electrolyte solutions, as the pore solution in concrete is generally alkaline (Newman and Choo 2003). As stated earlier, more effort is necessary to estimate the effects of electrolyte solutes on the equilibrium vapor pressure of a solvent due to at least two primary differences between the solute molecules of electrolytes and nonelectrolytes.

When nonelectrolyte solutes are dissolved by the solvent, the configuration of the individual molecules is preserved. This means the total number of moles of nonvolatile, nonelectrolyte solute molecules in solution is equal to the number of moles of the same solute out of solution. This is not so when dealing with electrolyte solutes. This is because an electrolyte molecule is made up of ions, positively charged cations and negatively charged anions, which become separated when dissolved in solution. This in turn increases the number of moles present in the solution to an amount greater than contained in the solute's un-dissolved form. In a text by Masterson and Hurley, the nonvolatile electrolyte molecule sodium chloride (NaCl) is used to illustrate this concept. One mole of NaCl out of solution becomes two total moles of solute in solution, since 1 mole of NaCl is the product of 1 mole of Na^+ cations and 1 mole of Cl^- anions (Masterton and Hurley 2004). If the dissolved molar quantities were the only difference between a nonvolatile electrolyte and a nonelectrolyte solution, then Raoult's law could still be used directly once the **Van't Hoff factor** (i) is obtained and the molar quantities in solution were calculated. The Van't Hoff factor is simply the ratio of the number of moles in the solution to the number of solute moles prior to being dissolved into solution, as represented by equation 2.17 (Masterton and Hurley 2004; Zumdahl and Zumdahl 2003).

$$i = \frac{\text{Moles of Solute in Solution}}{\text{Moles of Solute}} \quad \text{Equation 2.17}$$

where

i : Van't Hoff factor [*mol/mol*].

However, the linear proportionality of Raoult's law implies that the dissolved solute molecules are uniformly distributed throughout the solution. An assumption of uniform distribution simply cannot be made in the case of electrolyte solutions. This is because although the electrolyte molecules have been dissolved into their ionic components they are still attracted to each other. This attraction, as explained by the **Debye-Hückel theory** of electrolyte solutions, results in the clustering of oppositely charged ion particles, as shown in both figures 4 and 5, and is also known as ion pairing (Atkins and De Paula 2006; Masterton and Hurley 2004; Zumdahl and Zumdahl 2003). Consequently, the resulting clustered distribution is less effective at blocking escape pathways, and in turn, the resulting equilibrium vapor pressure of the solution is somewhat higher than would be predicted by Raoult's law (Masterton and Hurley 2004; Atkins and De Paula 2006).

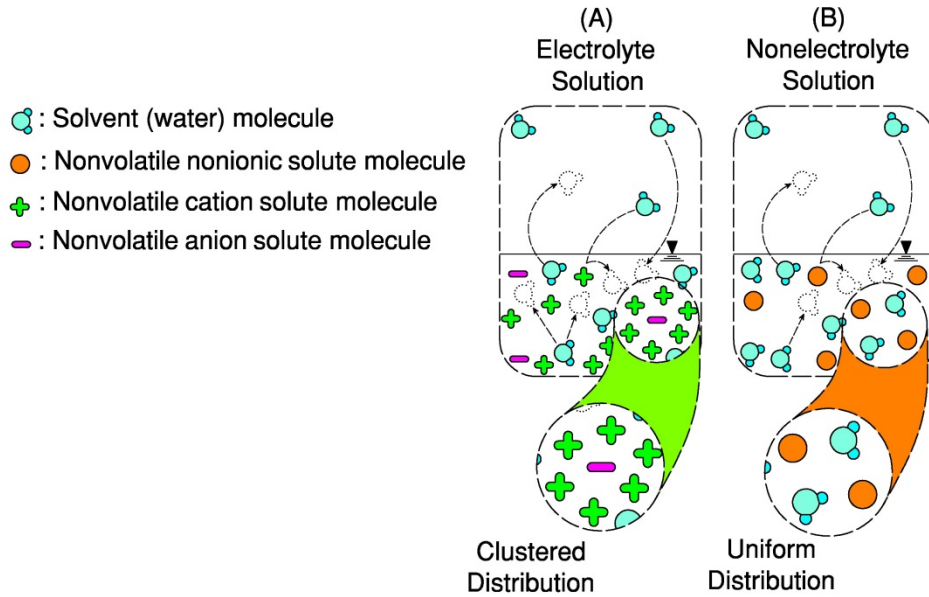


Figure 5: Distribution of dissolved solute molecules of a nonvolatile (A) electrolyte solution, (B) nonelectrolyte solution.

In this case, one would no longer simply use the mole fraction (X_s), but apply the more general, “effective mole fraction” or **activity** (a_s) of the solvent in solution, shown by equation 2.18. The activity (a_s) is actually the product of the mole fraction (X_s) and a multiplier termed the **activity coefficient** (ψ_s), which is dependent upon the solute(s) species, the solute(s) concentration, temperature and pressure (Atkins 1990; Atkins and De Paula 2006; Horvath 1985).

$$a_s = \psi_s X_s = \frac{p_v}{p_{sat}} \quad \text{Equation 2.18}$$

where

a_s : Activity of solvent in a solution [*mol/mol*].

ψ_s : Activity coefficient of solvent in a solution [*Unitless*]

In the context of equation 2.18, if one were looking at a solute that did conform to the linearly proportional scheme of Raoult’s law (i.e. a non-electrolyte), then the activity coefficient would be set equal to a constant value of one. So in general, any deviation of the vapor pressure (p_v) at equilibrium with respect to the saturation vapor pressure (p_{sat}) can be expressed by the activity term(a_s).

It should be noted that throughout literature the Greek letter gamma(γ) is widely used to denote activity coefficients. However, gamma is also widely used to denote surface tension, a concept explored later. Therefore, to avoid confusion the author has decided to use the Greek letter psi(ψ) to denote the activity coefficient.

While an actual determination of activity coefficients is beyond the scope of this investigation, the author feels that some further explanation is warranted. It should be noted at this time that as the author proceeds various models will be introduced; however, their mathematical expressions shall not be expressed here. If the reader is interested in learning more they are encouraged to review the cited literature. Ultimately, activity coefficients are determined empirically (Pitzer 1991). However, they may be obtained in one of a few ways. There exist records of empirically derived activity coefficients in published literature, which may encompass the complete parameter range required by the user. As a starting point, Horvath, in his book entitled “*Handbook of Aqueous Electrolyte Solutions: Physical properties, estimation and correlation methods*”, presents a large compilation of such references (Horvath 1985). Additionally, Pitzer published a second edition to a book entitled “*Activity Coefficients in Electrolyte Solutions*”; the first edition was published by Pytkowicz (referenced in Horvath’s book) (Pitzer 1991). Inevitably though, there will not be a table of activity coefficients available for every conceivable solution and range of parameters; therefore, values may need to be estimated or correlated.

Though having definite limitations, satisfactory estimations may be made by various empirically derived models. Estimations are most useful in the absence of actual empirical data. Two of the earliest estimation models were developed in 1923 by Peter Debye and Erich Hückel; they were called the **Debye-Hückel Limiting Law** and the **Extended Debye-Hückel Limiting Law** and are still useful today. However, their usefulness is limited in scope to solutions that range from extremely to moderately dilute, depending on whether one is employing the Debye-Hückel Limiting Law or the Extended Debye-Hückel Limiting Law, respectively. Over the years since the development of the Debye-Hückel limiting laws, improvements to these laws along with the development of newer models have come along and have reduced the limitations of the older models to now include, among other things, the ability to account for solutions containing multiple solute species. This is especially necessary in systems of increasing ionic solute concentration, generally quantified in terms of **ionic strength** (Atkins and De Paula 2006; Horvath 1985). It should be mentioned that if the ionic solution is sufficiently dilute, Raoult’s law may actually still yield satisfactory estimations. For more information on these or other estimation models, the reader is referred to Horvath and Pitzer in addition to physical chemistry texts.

However, when empirical data is available, so too are correlation models. The reader is again referred to Horvath and Pitzer for an introduction to such models. A comprehensive review of current correlation models is beyond the scope of this investigation; however, as a benefit to the reader, the author will bring attention to a specific correlation model, called the **Pitzer Equations** (Horvath 1985; Pitzer 1991). The original Pitzer Equations were developed in 1973 to handle the correlation of binary aqueous salt solutions; they were later modified in 1974 to handle the aqueous solutions containing mixed salts having molality concentrations of up to 6 [mol/kg]. Subsequently, other models were developed to extend the concentration limitations of the Pitzer Equations. The Pitzer Equations are considered a correlation model since they require parameters that can only be correctly determined by empirical data. Though the methods used in practice for

obtaining the empirical data necessary shall not be covered here, the reader is again directed to Pitzer (Pitzer 1991). For an example of how the Pitzer Equations may be used to calculate the activities of cementitious systems similar to that of this investigation, the reader is referred to a paper by Grasley, entitled “*Desiccation shrinkage of cementitious materials as an aging, poroviscoelastic response*” (Grasley and Leung 2011). In his paper, Grasley makes a comparison of the Pitzer Equations to Raoult’s Law as the concentration of dissolved salts increases in a cementitious system due to an increasing loss of moisture. It should be mentioned that though Grasley makes use of the Pitzer Equations, he is forced to omit some of the empirical parameters due to a lack of certain empirical data. Regardless, an interesting observation can be made by Grasley’s comparison. His findings seem to imply that for many practical situations, Raoult’s law may be used with very little introduced error.

In conclusion, for the purposes of this paper, the author has chosen to ignore certain factors which in theory may have some bearing on the equilibrium vapor pressure of a liquid solvent/solution. The author has considered these omissions acceptable as the effects are assumed to be either negligible or would presume conditions to exist which are outside the scope of this study. However, it should be acknowledged that such factors do exist and include such conditions as elevated pressure acting either on the liquid directly or on the gas above the liquid. When high pressure is applied directly to the liquid solution/solvent surface by a semi-permeable membrane, this generally will cause a rise in the liquid’s vapor pressure, as molecules are squeezed out of liquid phase. When pressure is applied to the gaseous mixture, the non-vapor ideal gases, according to **Henry’s law**, will become increasingly soluble, thereby increasing, perhaps significantly, the amount of gaseous mixture to become dissolved into the solvent/solution. As stated earlier though, pressure alone will not cause a gas to change physical phase; any dissolved gas would still remain gaseous, with an example of this being a carbonated beverage. These and other factors may be investigated more fully by the reader in many physical and general chemistry texts (Atkins and De Paula 2006; Zumdahl and Zumdahl 2003; Masterton and Hurley 2004).

2.2.3.4 Effect of curvature on the equilibrium vapor pressure of a liquid solvent/solution

A single water molecule, our assumed solvent, is comprised of two hydrogen atoms and an oxygen atom, bonded together covalently. A **covalent bond** is a type of chemical bond that results from the sharing of valence electron pairs between two atoms. However, since the electrons are not shared evenly between the hydrogen and oxygen atoms this gives rise to an unequal polar charge distribution, resulting in a **dipole moment**: two opposing charges separated by some distance, or moment arm. In some cases when three (or more) atoms bond in this way, they geometrically arrange themselves, as predicted by the Valence-Shell Electron-Pair Repulsion (VSEPR) model, to form a molecule having a net zero dipole moment. In order for a water molecule to be non-polar (i.e. having a net zero dipole moment) the required arrangement would have the hydrogen atoms align linearly, separated by an angle of 180 degrees, with the oxygen atom positioned equidistance between them; however, this is not the case. The water molecule actually has a bent geometry as shown in figure 6, with a separation angle of

approximately 105 degrees, per the VSEPR model, and is consequently a polar molecule. It has a net negative charge near the oxygen atom and a net positive charge near the hydrogen atoms (Zumdahl and Zumdahl 2003; Masterton and Hurley 2004).

A body of water forms when water molecules, having sufficiently low levels of kinetic energy, coalesce and condense out of the atmosphere (Atkins and De Paula 2006). The forces at work between molecules, attracting and binding them together, are collectively termed **intermolecular forces** and are far weaker than the **intramolecular forces** at work within the molecule to bind its atoms. In the case of water, the intermolecular force of interest is a **dipole-dipole force**, one of three van der Waals forces, arising from the electrostatic interaction between polar (or dipole) molecules. As also shown in figure 6, depending on the orientation of the molecules, they will either attract or repulse each other. Attraction occurs when the negatively charged end of one dipole interacts electrostatically with the positively charged end of another dipole. Conversely, repulsion occurs when similarly charged ends of dipoles electrostatically interact with each other.

Hydrogen bonding is the name given to the special subset of dipole-dipole bonds involving hydrogen interactions. While far weaker than the forces that bind atoms together, hydrogen bonds are stronger than typical dipole-dipole bonds and are how molecules of water are bound together (Zumdahl and Zumdahl 2003; Masterton and Hurley 2004; Meyers 1991).

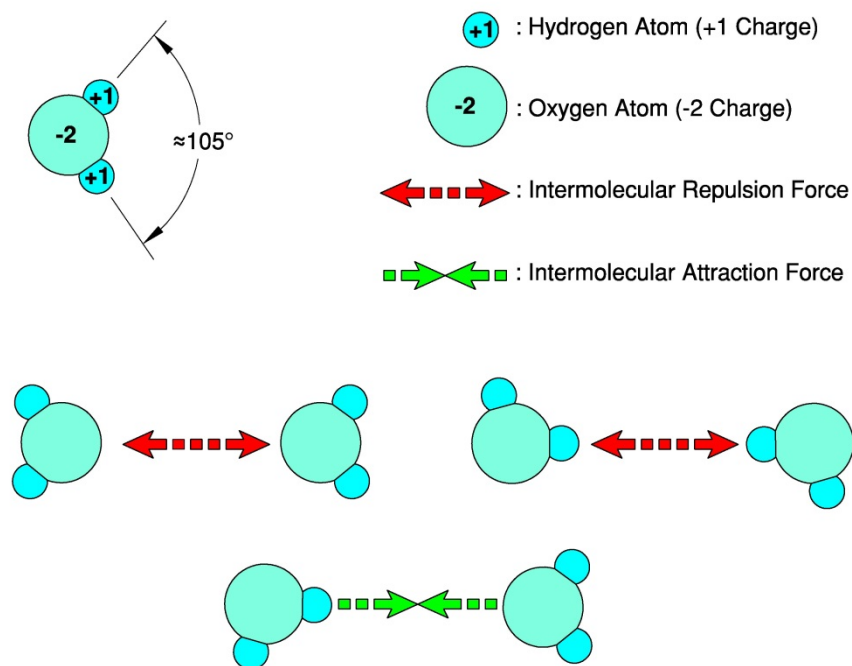


Figure 6: Molecular geometry and intermolecular forces for/between water molecules

At this point there is a need to distinguish between adhesive and cohesive forces, generic terminology that divides intermolecular forces into two groups. While purely contextual, this distinction is necessary to avoid confusion and advance the concepts to come.

Adhesion is a rather nebulous term, lacking a single definition that completely satisfies

the needs of both the theoretical and practical. However, for the purposes of this study, the author finds it best to simply define Adhesion as the bonding of materials that differ in composition and/or physical states at a common interface. **Cohesion**, like adhesion, is the bonding of two materials at a common interface, but the two materials in this case are of similar composition and physical state. More directly, adhesion occurs at the solvent-container interface, while cohesion occurs at the interfaces between solvent (or solution) molecules (i.e. hydrogen bonding).

Adhesion can be broken down into at least three categorical groups: Thermodynamic (non-chemical) adhesion, Chemical adhesion and Mechanical adhesion (Meyers 1991; Zumdahl and Zumdahl 2003). While a determination of a solvent's (or solution's) composition may be made, leading to an accurate understanding of the cohesive forces at work within it, determining adhesive forces is not so straight forward. To determine the actual adhesive forces existing between two materials requires knowledge of precisely the physical and chemical composition of each (Meyers 1991). Due to the uncertain (and perhaps unknowable) characteristics of concrete pore geometry, interfacial conditions and chemistry, it becomes a virtual impossibility to formally declare the actual adhesive forces at work. However, since the scope of this study shall not require such a formal declaration, the author shall use generic terminology. Also for this reason, it will be necessary to employ simplifying assumptions (i.e. geometry of pores, interfacial interactions, etc.) as needed.

When in the condensed state, molecules located beneath the gaseous-liquid interface or surface layer (often referred to as the **meniscus**) and not in direct contact with the container are said to be in the bulk volume. The cohesive forces (attraction/repulsion) act on them from all directions, as shown in part A of figure 7. The net result is that, while the molecules tend to find a rotational equilibrium that optimizes the attraction and repulsion forces with neighboring molecules, the molecules have no real preference as to their translational location within the bulk volume. Conversely, the molecules at the surface layer do not have cohesive forces acting on them in all directions; they lack these forces above the gaseous-liquid interface. Consequently, the force imbalance causes the molecules at the surface to favor a position inside the bulk volume. For obvious reasons, not all the molecules can be inside the bulk simultaneously and so in the absence of external forces, like gravity, it is the tendency of liquids to seek minimum energy by forming a sphere, as shown in part B of figure 7. This volumetric shape (the sphere) maximizes the amount of liquid that is located beneath the surface, in the bulk volume, while minimizing the surface area. However, in the presence of earth's gravitational forces, the liquid has no choice but to conform to its container with a level surface across most of the gaseous-liquid interface (Gentle and Barnes 2005; Zumdahl and Zumdahl 2003; Atkins and De Paula 2006).

The meniscus is often simplistically described to be a surface layer with a quasi-constitutive property termed surface tension, which acts to resist surface area deformation caused by externally applied loads. While simplistic, this interpretation can lead to a fundamental misunderstanding of what surface tension is. The tendency of the novice is to envision the meniscus as an independent stratum, capable of stretching elastically, like

a rubber membrane, to resist deformation independent of the bulk volume, when in truth, solvent molecules in the bulk volume work with the molecules in the meniscus to resist deformation and changes to the surface area of the meniscus. For this reason it is encouraged that the surface tension (γ) be thought of as the change in work (dw) or equivalently the change in (Gibbs) free surface energy (dG) required to pull molecules from the bulk volume to the surface, thereby changing the surface area by some amount (dA), as shown in the following two equations (equation 2.19 and 2.20):

$$\frac{dw}{dA} = \gamma \quad \text{Equation 2.19}$$

$$\frac{dG}{dA} = \gamma \quad \text{Equation 2.20}$$

It should be noted that the thermodynamic definition (equation 2.20) is valid under the condition that we are only considering changes to the meniscus surface. However, it is by the thermodynamic definition that an argument can be made to show temperature has an effect on the solvent's surface tension. In general, by the definition of Gibbs free energy (not shown here), when the constant temperature of a system is increased, Gibbs free energy is reduced. Consequently, the surface tension is also reduced. So then, the surface tension of a solvent is temperature dependent, generally being reduced as the temperature increases (Meyers 1991; Gentle and Barnes 2005; Atkins and De Paula 2006).

In addition to temperature, the surface tension of a solution is also affected by the concentration and composition of the solutes within. Whether the net effect is to increase or decrease the surface tension of a solution with respect to the surface tension of the pure solvent requires specific knowledge about the solution. In cases where the solution contains electrolytes, an increase in the surface tension is plausible. It has been suggested, that a first approximation could involve a linear averaging of the individual surface tensions according to their molar fraction contribution (Meyers 1991). However, since calculating the actual surface tension of a pore solution is beyond the scope of this investigation, the reader need not be overly concerned with more rigorous methods of calculation.

Neglected in most illustrative figures, and often quickly dismissed as a trivial detail, is the general tendency of the meniscus to curve in the vicinity of the perimeter defined by the convergence of the gaseous atmosphere, liquid solvent/solution and the container, or triple interface (Gentle and Barnes 2005). However, the scope of this study shall require the author's consideration of meniscus curvature. It will be shown that the effect of curvature on the liquid's equilibrium vapor pressure in small pores is non-trivial.

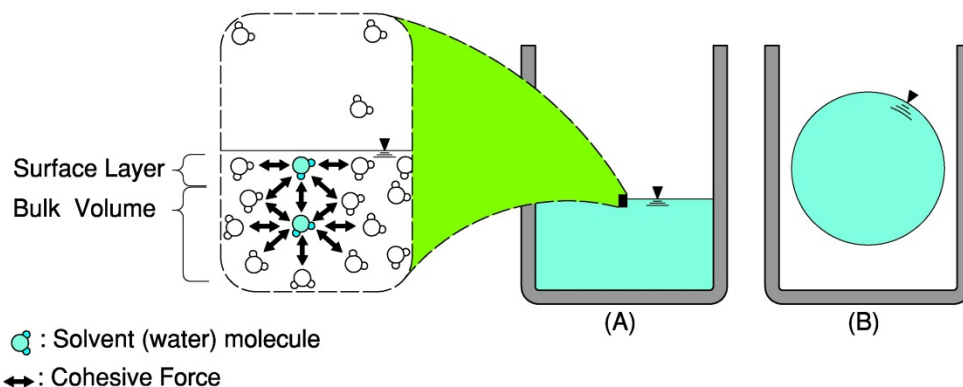


Figure 7: Cohesive forces acting between water molecules to minimize surface area (A) in the presence of gravity (B) in the absence of gravity.

If one considers a relatively large container, like a coffee cup, filled with the liquid solvent, meniscus curving can generally be observed along the triple interfacial perimeter of the liquids surface, as previously described. The curving starts at the perimeter and continues for some small distance inward, away from the perimeter until the liquids surface levels out. Next, shifting the attention to a container of moderately small diameter, like a graduated cylinder or pipet, meniscus curvature can again be observed. This time the curvature does not appear to level off. While the curvature is not of constant value (i.e. non-spherical), it has some amount of curvature at all points along the meniscus (Zumdahl and Zumdahl 2003). Finally, further reducing the size of the container to a tube of very small diameter, like that of a **capillary tube**, it is at this point that one can really begin to observe and appreciate the effects of curvature. Taking a capillary tube (e.g., glass) that is open at each end and dipping it into a large container or reservoir of solvent (e.g. water), immediately the solvent begins to rise in the tube, stopping at some height (Gentle and Barnes 2005). At this point the meniscus appears to be spherical; all menisci of water-based solutions in very small tubes will be assumed spherical for further discussion. This assumption allows one to mathematically relate the small tubes' radii to the curvature of the meniscus (Meyers 1991). The steps of this capillary rise phenomenon can be broken down into three distinct phases, as outlined in figure 8.

The first phase is the adhesion of solvent molecules to the walls of the container, a process called **wetting**, and is driven by the strength of the adhesive forces with respect to the cohesive forces. When the adhesive forces between the solvent and the container are stronger than the cohesive forces within the solvent, energy is minimized when the solvent molecules along the interface adhere to and move upward along the surface of the container.

The second phase actually occurs in unison with the first phase and is the product of surface tension. As adhesive forces pull the solvent molecules toward and up the walls of the container, they are also being pulled away from neighboring solvent molecules in the surface layer. This happens because the adhesive forces are stronger than the cohesive

forces. Simultaneously, molecules in the bulk volume are being pulled by cohesive forces into the surface layer to fill spots being vacated. This results in an increase in the meniscus surface area and formation of concave curvature. In the case where the cohesive forces are dominant, as is in the case of liquid mercury in a glass tube, the molecules will tend to not favor adhesion, but to minimize energy by continuing to favor a position inside the bulk volume. This tendency to not wet leads to downward or convex meniscus curvature (Meyers 1991; Zumdahl and Zumdahl 2003). However, since our assumed solvent (water) has the tendency to adhere to the container, the figures have been illustrated to show upward or concave meniscus curvature.

The third phase is the rise of the solvent in the capillary tube. The capillary rise is in response to a pressure difference across the meniscus layer caused by its curvature. The height to which the column of solvent will rise above the elevation of the leveled solvent in the reservoir to the bottom of the meniscus curvature is proportional to the pressure difference necessary to satisfying hydrostatic pressure equilibrium. Similarly, in the case where convex meniscus curvature is formed, the pressure difference is reversed; causing the solvent inside the tube to plunge below the elevation of solvent in the reservoir, to some proportional depth (Meyers 1991).

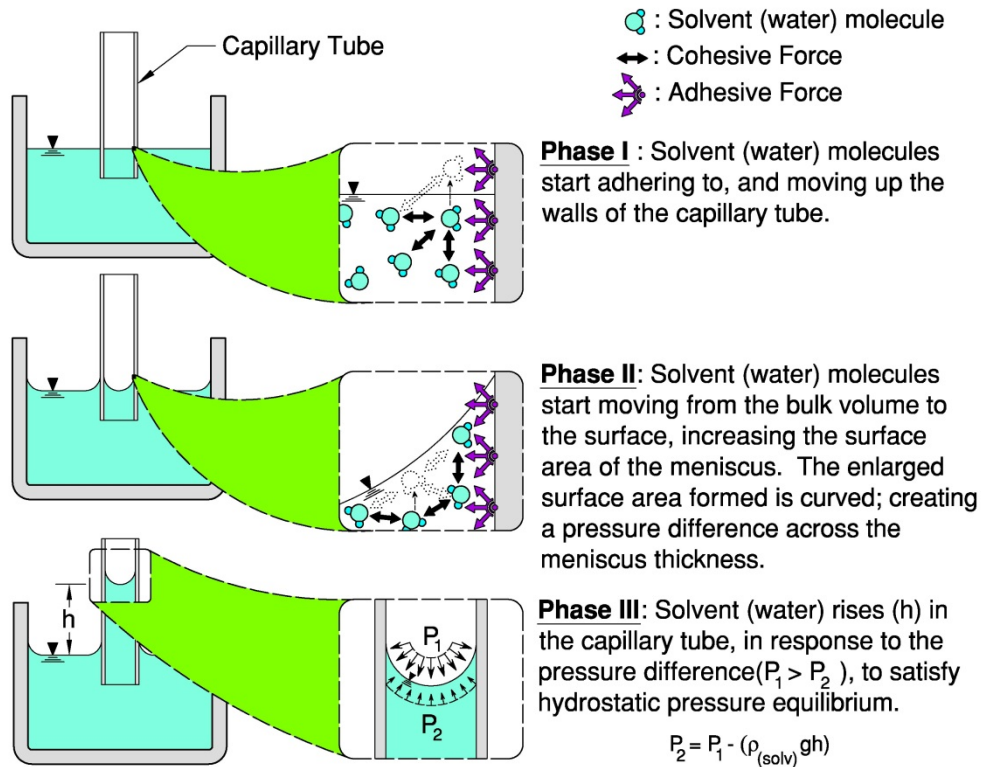


Figure 8: Three phases of capillary rise, shown with assumed concave meniscus.

The significance of capillary rise to this study is not that the solvent rises in a capillary tube, but rather why it rises. There is a pressure difference created when curvature occurs at the gaseous-liquid interface. As illustrated in figures 8 and 9, the pressure on the convex side of the meniscus (P_2) is lower than the pressure on the concave side (P_1)

(Atkins and De Paula 2006). While theoretically there is a pressure profile through the finite thickness of the interfacial layer, the distribution of the actual profile is a matter of some speculation within the scientific/engineering community. For the purposes of simplifying the interface model, the general practice is to assume that the interface is infinitely thin and the pressure transition profile (from P_1 to P_2) is treated as a step function (Defay 1966; Gentle and Barnes 2005).

A classical relationship intended to relate meniscus curvature to the change in pressure across the interfacial layer (from P_1 to P_2) is the **Laplace equation**, as shown in equation 2.21.

$$P_2 - P_1 = \frac{2\gamma}{R} \quad \text{Equation 2.21}$$

where

- P_1 : Hydrostatic pressure acting on the concave side of meniscus [*Force/Area*²].
- P_2 : Hydrostatic pressure acting on the convex side of meniscus [*Force/Area*²].
- R : Mean radius of the meniscus curvature [*Length*].
- γ : Surface tension [*Force/Length*].

Recalling that curvature has a reciprocal relationship to its radius, the mean curvature (k) is then:

$$k = \frac{1}{R} \quad \text{Equation 2.22}$$

Substituting this back into equation 2.21 allows one to express the Laplace equation in a way that explicitly relates pressure change to mean curvature:

$$P_2 - P_1 = 2\gamma k \quad \text{Equation 2.23}$$

However, a more useful form of the Laplace equation is an expanded version which facilitates the calculation of the mean curvature from orthogonal principle curvatures. This form is better suited for calculations where the meniscus is non-spherical. To envision such a curvature distribution, consider a capillary of oval, rather than circular, cross-section, and picture the curvatures of a meniscus spanning the long versus short axes of the oval. The benefit to using this form will become obvious later during the review of capillary/pore adsorption and desorption processes.

$$P_2 - P_1 = \gamma (k_1 + k_2) \Rightarrow \gamma \left(\frac{1}{R_1} + \frac{1}{R_2} \right) \quad \text{Equation 2.24}$$

where

- k_1 : Principle (max or min) meniscus curvature, orthogonal to k_2 [*Length*].
- k_2 : Principle (min or max) meniscus curvature, orthogonal to k_1 [*Length*].
- R_1 : Principle (max or min) meniscus radius of curvature, orthogonal to R_2 [*Length*].

R_2 : Principle (min or max) meniscus radius of curvature, orthogonal to R_1 [*Length*].

Interestingly, in the equation above (equation 2.24) the principle meniscus curvatures or radii of the curvatures may be substituted by any two meniscus curvatures or radii of curvature values provided that the planar intersections they are defined along are orthogonal with respect to each other and share the same common points of intersection as the orthogonal principle values. This result is a consequence of a theorem by Euler, which will be seen later in an abbreviated derivation of the Laplace equation (Gentle and Barnes 2005; Defay 1966; Rowlinson and Widom 2002). In the case of figures 8 and 9, the common point of intersection on the meniscus is located at the minima extrema of the surface interface.

The Laplace equation in either form above (equations 2.21 and 2.24) is only valid under an assumption that the meniscus radii of curvature (R_1 and R_2) are constant along the planar sections on which they are defined, resulting in circular section views, as shown in figure 9. By definition the orthogonal principle curvatures are likewise constant. The existence of constant curvature is assumed to be a reasonable assumption for very small capillaries or pores where gravitational effects may be assumed negligible (Rowlinson and Widom 2002). If both of the orthogonal radii of curvature are constant and equal, as in the case of a circular capillary tube (or pore), then the meniscus is assumed spherical. Based on the constant curvature assumption, one can now relate the mean radius of the meniscus curvature inside the capillary tube (R) to the mean radius of the capillary tube (r) using basic trigonometric relationships, as shown below in equation 2.25.

$$P_2 - P_1 = \frac{2\gamma \cos \theta_c}{r} \quad \text{Equation 2.25}$$

Of course, this form is most easily applied to a tube (or pore) of circular cross-section where the mean radius of the cross-section can simply be taken as the tube (or pores) radius. Similar to equation 2.24, equation 2.26 is an expanded form of equation 2.25 for use in cases where the meniscus is not spherical.

$$P_2 - P_1 = \gamma \left(\frac{\cos \theta_{c1}}{r_1} + \frac{\cos \theta_{c2}}{r_2} \right) \quad \text{Equation 2.26}$$

where

θ_{c1} : Principle (max or min) Contact angle, orthogonal to θ_{c2} [*RAD.*].

θ_{c2} : Principle (min or max) Contact angle, orthogonal to θ_{c1} [*RAD.*].

r_1 : Principle (max or min) tube (or pore) radius, orthogonal to r_2 [*Length*].

r_2 : Principle (min or max) tube (or pore) radius, orthogonal to r_1 [*Length*].

Again, similar to equation 2.24 any two orthogonal radii may be used provided they share the same point of intersection as the orthogonal principle values.

The angle of contact (or contact angle, θ_c), is shown in figure 9 using the positive sign convention, and is related to the degree that the liquid covers, or wets, the solid container interface. As highlighted earlier, wetting is driven by the strength of the adhesive forces (solution-container) with respect to the cohesive forces (solution-solution). The contact angle is the result of force equilibrium between the forces along each of the interfaces (liquid-gaseous, liquid-solid and gaseous-solid) at the triple interface; in fact, the $\cos \theta_c$ term is called the **wetting coefficient**. The larger the adhesive force is between the liquid and the solid container with respect to the other forces at the triple interface, the smaller the angle tends to be (Atkins and De Paula 2006; Rowlinson and Widom 2002). While this relationship may seem straight forward, an actual determination of the contact angle may not be practical or even possible for many applications. This complication often leads to educated assumptions about the degree of wetting. In the case of concrete pores, it is not uncommon to assume near perfect wetting, leading to a near zero contact angle. The convenience of this assumption shall become obvious later during the review of capillary/pore adsorption and desorption processes (Ruthven 1984; Grasley et al. 2006, 51-57).

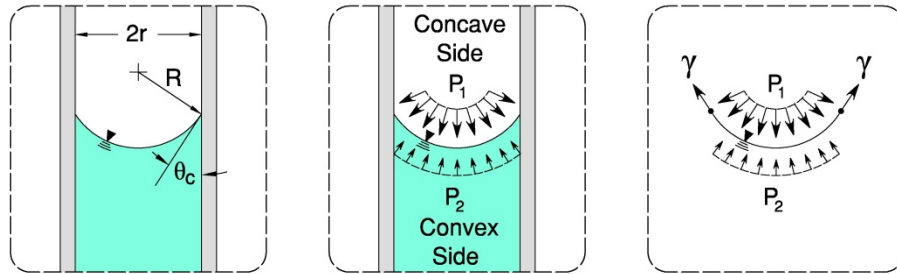


Figure 9: Details of a meniscus in a capillary tube.

The Laplace equation relates meniscus curvature to pressure change; the useful forms of the equation have been presented above (equations 2.21 thru 2.26). Since so much of this review relies on this particular relationship, it is fitting that a derivation be carried out. Fortunately, this relationship can be derived from the principles of mechanical equilibrium on the interface element, which shall now be considered in an abbreviated way (Defay 1966; Gentle and Barnes 2005; éCernây and Rovnanâikovâa 2002). It should be noted that more detailed/rigorous derivations, using either the force balance approach (used here) or the concept of virtual work, are available (Skjaeveland 1993; Adamson and Gast 1997).

This derivation is based on the equilibration of two forces. The first of these is the force resulting from a pressure imbalance $F_{(\Delta p)}$. On either side of the meniscus, a hydrostatic pressure is being exerted; the pressure is from the bulk liquid on one side of the meniscus and from the gaseous atmosphere on the other. If either pressure is greater than the other, there is a net pressure imbalance that must be resisted if equilibrium is to exist. The second force results from surface tension $F_{(\gamma)}$, which acts to resist the pressure imbalance.

In differential geometry, when the surface in the very near vicinity about a point of interest is an ellipsoid, the common or origin point through which orthogonal principle values pass is called the **elliptic point** of the Dupin Indicatrix for that very small, local area of the surface. In the special case where the orthogonal principle values are equal, yielding a spherical surface, the same point may also be termed the **umbilic** (or navel) point (Kreyszig 1991; Rowlinson and Widom 2002).

The forces that are actually the focus of this derivation are the vertical force components of the forces described above. The coordinate system being used has been assigned to a generalized non-spherical (ellipsoid) surface with very small cap-like area in vicinity of an elliptic point, as shown in figure 10. The vertical axis assigned, which passes through the elliptic point, is also normal to the surface at the point of intersection (point E) (Kreyszig 1991; Defay 1966). It is by observation that we determine, due to symmetry, the horizontal components of the forces are recognized to resolve themselves, and are not necessary to this derivation. Therefore, the vertical force equilibrium expressed below by equation 2.27 is the starting point for this derivation.

$$F_{v(\gamma)} = F_{v(\Delta p)} \quad \text{Equation 2.27}$$

where

- $F_{v(\gamma)}$: Total surface tension force acting in the vertical direction [*Force*]
- $F_{v(\Delta p)}$: Total pressure imbalance force acting in the vertical direction [*Force*]

The reader is cautioned not to presume that figure 10 is a generalized isometric view of figure 9. Figure 9 details in cross-section a total meniscus, while figure 10 does not. The very small area of figure 10 is assumed to exist on the surface of an ellipsoid, about an elliptic point of origin (point E in the figure). Both the arc lengths (ε) and the coordinate system were chosen for their convenience when making the calculations to follow. The goal is to relate a pressure difference to curvature; just because the geometry of the area on the surface and the orientation of the coordinate system were chosen to facilitate a cleaner derivation does not invalidate the results.

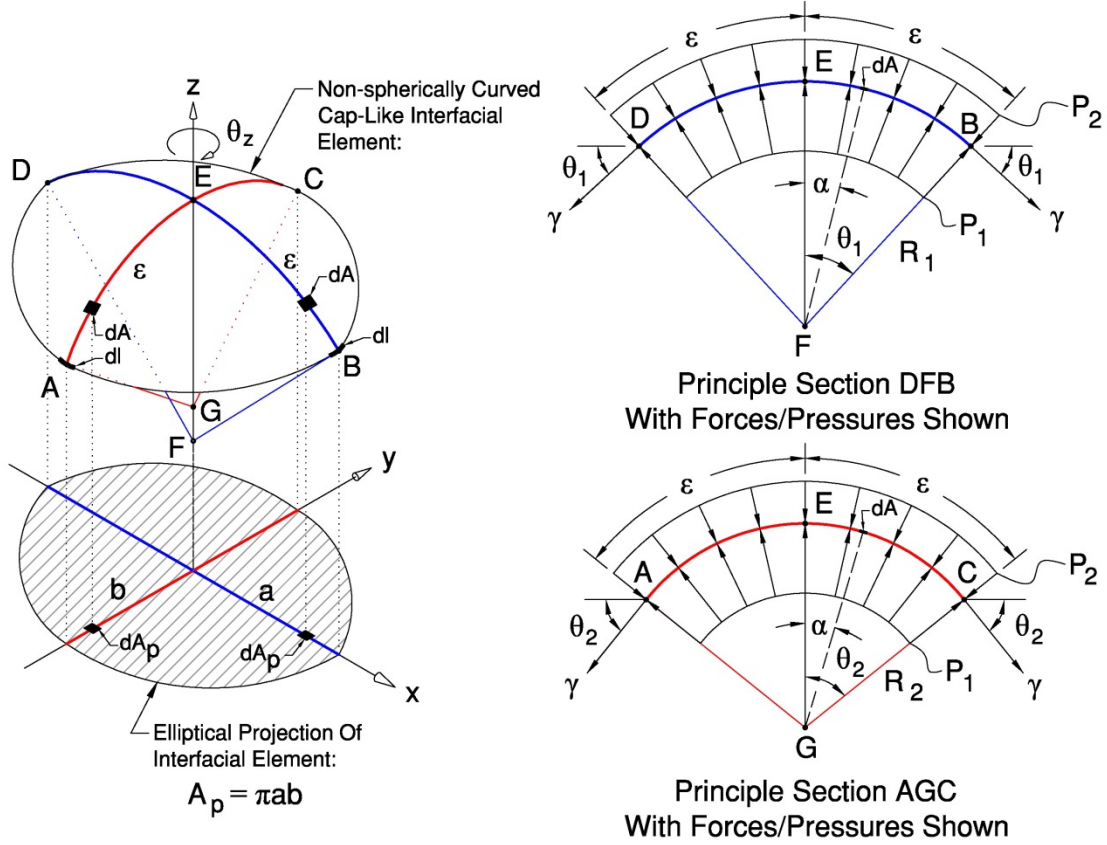


Figure 10: Cap-like ellipsoid element with views of principle sections and loadings

With the left hand side of equation 2.27 in mind, we sum the two vertical force components of section DFB, resulting from surface tension, as show in equation 2.28 below.

$$dF_{v(\gamma)_1} = 2\gamma \sin(\theta_1) dl \quad \text{Equation 2.28}$$

where

- $dF_{v(\gamma)_1}$: Infinitesimal surface tension force acting in the vertical direction on the principle section DFB [*Force*]
- γ : Surface tension constant [*Force/Length*]
- θ_1 : Small angle of a circular sector of a radius (R_1) and an arclength (ϵ) on the principle section DFB [*Rad.*]
- dl : Infinitesimal length of the elements perimeter [*Length*]

Since the angle θ_1 is assumed to be very small ($\theta_1 \ll 1$):

$$\sin(\theta_1) \cong \frac{\varepsilon}{R_1} \quad \text{Equation 2.29}$$

where

- R_1 : Principle meniscus radius of curvature, of section DFB, orthogonal to R_2 [Length]
- ε : The constant arc length defined by the intersection of any planar section normal to the defined vertical axis, and the elements surface (from the point E along the surface to the perimeter) [Force/Length]

Substituting equation 2.29 into equation 2.28 we get:

$$dF_{v(\gamma)_1} = 2\gamma \left(\frac{\varepsilon}{R_1} \right) dl \quad \text{Equation 2.30}$$

A similar argument can be made for the forces located on the planar section defined points AGC, resulting in equation 2.31.

$$dF_{v(\gamma)_2} = 2\gamma \left(\frac{\varepsilon}{R_2} \right) dl \quad \text{Equation 2.31}$$

where

- $dF_{v(\gamma)_2}$: Infinitesimal surface tension force acting in the vertical direction on the principle section AGC [Force]
- R_2 : Principle meniscus radius of curvature, of section AGC, orthogonal to R_1 [Length]
- θ_2 : Small angle of a circular sector of a radius (R_2) and an arclength (ε) on the principle section AGC – (not shown explicitly)[Rad.]

Summing equations 2.30 and 2.31 we arrive at a vertical surface tension force $dF_{v(\gamma)}$, composed of all 4 vertical surface tension components acting over the infinitesimal lengths dl located at the quarter points (points A, B, C and D) of the element perimeter.

$$dF_{v(\gamma)} = dF_{v(\gamma)_1} + dF_{v(\gamma)_2} \Rightarrow 2\gamma\varepsilon \left(\frac{1}{R_1} + \frac{1}{R_2} \right) dl \quad \text{Equation 2.32}$$

At this point it becomes necessary to expand upon a concept seen earlier in a commentary concerning equation 2.24.

An equation (or theorem) of Euler, found in differential geometry texts, shall now be introduced. In the context of a very small area on a surface in the vicinity about an elliptic point, this theorem relates the curvature (K) along any arbitrary planar section, normal to the elliptic point (or the vertical axis as defined in figure 10), to the principle curvatures (k_1 and k_2) defined along the orthogonal principle normal sections (DFB and AGC of figure 10, respectively) by the following relationship (Kreyszig 1991).

$$K = k_1 \cos^2 \beta + k_2 \sin^2 \beta \quad \text{Equation 2.33}$$

where

- K : Curvature of an arbitrary normal section [$1/Length$]
- k_1 : Principle (max or min) meniscus curvature along a normal section, assumed to be along the x-axis and orthogonal to k_2 [$1/Length$]
- k_2 : Principle (min or max) meniscus curvature along a normal section, assumed to be along the y-axis and orthogonal to k_1 [$1/Length$]
- β : Angle between the principle normal section along which the curvature k_1 is defined and the arbitrary normal section along which the arbitrary curvature k is defined [$Radians$]

It should be noted that the principle curvature terms have been modified here to include an assumed direction.

Using this theorem, one can describe the curvature of another normal section orthogonal to K , denoted by K_{\perp} , in the following two equations (Equations 2.34 and 2.35):

$$K_{\perp} = k_1 \cos^2 \left(\beta + \frac{\pi}{2} \right) + k_2 \sin^2 \left(\beta + \frac{\pi}{2} \right) \quad \text{Equation 2.34}$$

or

$$K_{\perp} = k_1 \sin^2 \beta + k_2 \cos^2 \beta \quad \text{Equation 2.35}$$

The useful consequence of the theorem of Euler can be seen when the two arbitrary, but orthogonal, normal section curvatures are summed (Equation 2.36), the principle curvature terms k_1 and k_2 are collected (Equation 2.37) and trigonometric identities are substituted (Equation 2.38).

$$K + K_{\perp} = [k_1 \cos^2 \beta + k_2 \sin^2 \beta] + [k_1 \sin^2 \beta + k_2 \cos^2 \beta] \quad \text{Equation 2.36}$$

$$K + K_{\perp} = k_1 (\sin^2 \beta + \cos^2 \beta) + k_2 (\sin^2 \beta + \cos^2 \beta) \quad \text{Equation 2.37}$$

$$K + K_{\perp} = k_1 + k_2 \quad \text{Equation 2.38}$$

The sum of the curvatures along any two orthogonal normal sections, are equal to the sum of the principle curvatures. Hence, the sum is independent of angle (β or θ_z), and is therefore a constant value. This then implies that the mean radius of curvature (k) is also constant, which is useful later during steps requiring integration.

The application of this consequence is straightforward. The sum of the curvatures defined by the radii of normal sections DFB and AGC are equal to the sum of the curvatures defined by the radii of any pair of normal orthogonal sections. The radii of these arbitrary normal orthogonal sections are denoted by the use of a star (*) superscript in equation 2.39.

$$\left(\frac{1}{R_1} + \frac{1}{R_2} \right) = \left(\frac{1}{R_1^*} + \frac{1}{R_2^*} \right) \quad \text{Equation 2.39}$$

where

R_1^* : Arbitrary meniscus radius of curvature, orthogonal to R_2^* [Length].

R_2^* : Arbitrary meniscus radius of curvature, orthogonal to R_1^* [Length].

Back substituting equation 2.39 into equation 2.32, we obtain the more general equation 2.40.

$$dF_{v(\gamma)} = 2\gamma\varepsilon \left(\frac{1}{R_1^*} + \frac{1}{R_2^*} \right) dl \quad \text{Equation 2.40}$$

Since according to equation 2.39 the summed values are equivalent, it was not really necessary to make this substitution. However, it was done in the interest of reinforcing the concept. Next we apply the same small angle assumption made previously in the formulation of equations 2.30 and 2.31, to formulate equation 2.41.

$$dl \cong \varepsilon d\theta_z \quad \text{Equation 2.41}$$

where

$d\theta_z$: Infinitesimal angle of rotation about the vertical z-axis of the element [Rad.]

Equation 2.41 can be substituted into equation 2.40 to form equation 2.42.

$$dF_{v(\gamma)} = 2\gamma\varepsilon^2 \left(\frac{1}{R_1^*} + \frac{1}{R_2^*} \right) \theta_z \quad \text{Equation 2.42}$$

At this point a vertical force $dF_{v(\gamma)}$, which is really the sum four vertical point force components located at the quarter points along the perimeter, has been defined. All that is left to do is calculate and sum all the remaining vertical forces along the perimeter. Since the Theorem of Euler has shown that the sum of the curvatures is constant, one can simply carry out an integration of all four vertical force components simultaneously, each

through one quarter revolution, to obtain the total vertical force component $F_{v(\gamma)}$ as shown in equation 2.43.

$$F_{v(\gamma)} = \int_0^{\frac{\pi}{2}} 2\gamma\epsilon^2 \left(\frac{1}{R_1^*} + \frac{1}{R_2^*} \right) d\theta_z \Rightarrow \gamma\pi\epsilon^2 \left(\frac{1}{R_1^*} + \frac{1}{R_2^*} \right) \quad \text{Equation 2.43}$$

Setting this result aside until later, the next part of this derivation shall require the calculation of the vertical force component created by any pressure imbalance $F_{v(\Delta p)}$. Looking at either section (DFB or AGC) of figure 10, one can quickly define an infinitesimal pressure imbalance force ($dF_{(\Delta p)}$) normal to the surface to be:

$$dF_{(\Delta p)} = (P_2 - P_1)dA \quad \text{Equation 2.44}$$

where

dA : Infinitesimal area on the surface of the interfacial element [*Length*²]
 $dF_{(\Delta p)}$: Infinitesimal force resulting from a pressure imbalance [*Force*]

from which the vertical component (equation 2.45) can be calculated.

$$dF_{v(\Delta p)} = dF_{(\Delta p)} \cos \alpha \Rightarrow (P_2 - P_1)dA \cos \alpha \quad \text{Equation 2.45}$$

where

α : Arbitrary angle between the vertical axis and small angle of a circular sector, θ_1 or θ_2 as shown in figure 10 [*Rad.*]
 $dF_{v(\Delta p)}$: Infinitesimal vertical force component resulting from a pressure imbalance [*Force*]

To arrive at the total pressure imbalance force acting in the vertical direction ($F_{v(\Delta p)}$), we need to integrate the force obtained in equation 2.45 over the entire surface area of the element.

$$F_{v(\Delta p)} = (P_2 - P_1) \iint_{Area} dA \cos \alpha \quad \text{Equation 2.46}$$

where

$F_{v(\Delta p)}$: Total pressure imbalance force acting in the vertical direction [*Force*]

At this point it is recognized that the term inside the integrand is equal to the projected area of the infinitesimal upon which the pressure imbalance is acting, onto the x-y plane of figure 10, giving equation 2.47.

$$F_{v(\Delta p)} = (P_2 - P_1) \iint_{Area} dA_p dA \quad \text{Equation 2.47}$$

where

dA_p : Projection of the infinitesimal surface area (dA) onto the x-y plane of figure 10 [*Force*]

At this point it is clear that the entire integrand is equivalent to the area being projected by the total surface element onto the x-y plane of figure 10, thus reducing equation 2.47 down further.

$$F_{v(\Delta p)} = (P_2 - P_1)A_p \quad \text{Equation 2.48}$$

where

A_p : Projection of the total surface area of the interfacial element onto the x-y plane of figure 10 [*Force*]

Since we happen to know that the projected area (A_p) is an ellipse defined by equation 2.49, we shall use this (Washington 1999; Larson, Hostetler, and Edwards 2002).

$$A_p = \pi ab \quad \text{Equation 2.49}$$

where

a : Semi-major axis of an ellipse, as projected onto the x-y plane in figure 10 [*Length*]

b : Semi-minor axis of an ellipse, as projected onto the x-y plane in figure 10 [*Length*]

The semi-major/minor values (a) and (b) respectively can be calculated by the following two equations.

$$a = R_1 \sin \theta_1 \quad \text{Equation 2.50}$$

$$b = R_2 \sin \theta_2 \quad \text{Equation 2.51}$$

Again, because we are making a small angle assumption, equations 2.50 and 2.51 can be simplified, as shown in the next two equations.

$$a \approx R_1 \left(\frac{\varepsilon}{R_1} \right) \Rightarrow \varepsilon \quad \text{Equation 2.52}$$

$$b \approx R_2 \left(\frac{\varepsilon}{R_2} \right) \Rightarrow \varepsilon \quad \text{Equation 2.53}$$

Substituting these equations back into equation 2.49 and then 2.48, gives us equation 2.54, the total vertical force due to any pressure imbalance ($F_{v(\Delta p)}$).

$$F_{v(\Delta p)} = (P_2 - P_1) \pi \varepsilon^2 \quad \text{Equation 2.54}$$

Finally, all that is left to do is plug equations 2.43 and 2.54 into equation 2.27 as shown in equation 2.55, then solve for the change in pressure (equation 2.56).

$$\gamma \pi \varepsilon^2 \left(\frac{1}{R_1^*} + \frac{1}{R_2^*} \right) = (P_2 - P_1) \pi \varepsilon^2 \quad \text{Equation 2.55}$$

$$(P_2 - P_1) = \gamma \left(\frac{1}{R_1^*} + \frac{1}{R_2^*} \right) \quad \text{Equation 2.56}$$

Or equivalently, by equation 2.39 we get back an equation that is identical to the Laplace equation of the form found in equation 2.24.

$$(P_2 - P_1) = \gamma \left(\frac{1}{R_1} + \frac{1}{R_2} \right) \quad \text{Equation 2.57}$$

Interestingly, the $(\pi \varepsilon^2)$ terms on either side of equation 2.55 were the direct result of small angle approximations and they cancelled each other out.

The difference in pressure that is calculated by the Laplace equation is a total pressure difference. Recalling that the goal is to determine the effect of curvature on the equilibrium vapor pressure, the change to the partial pressure attributed to the solvent (or water) vapor is the fractional piece of the total pressure change actually needed. However, since the Laplace equation alone does not parse out total pressure change into the individual partial pressure changes, something additional is needed. The **Kelvin** equation has historically been used instead of the Laplace equation to bridge this gap. Since the Kelvin equation extends the Laplace equation's usefulness by incorporating thermodynamic considerations, it looks more complex than it really is, the author has chosen to first develop the Kelvin equation prior to presenting it in its final form.

Physical laws (or physics) underpin the science of chemistry. Physical chemistry is the broad branch of chemical science that includes (but is not entirely limited to) the study of these laws as they pertain to explaining the behavior of chemical substances, along with the physical and chemical properties revealed. **Physicochemical** is a term often used to identify a property or principle rooted in, or pertaining to, the teachings of physical chemistry. The Laplace equation alone views the capillary tube system as a mechanical

one upon which force equilibrium can be imposed. However, the system is also one of chemical substances coexisting in multiple phases. Therefore, an equilibrium condition can also be defined in terms of the principles found in physical chemistry, i.e., a **physicochemical equilibrium** (Defay 1966; Monk 2004).

At this point, the author acknowledges that there are multiple paths to approaching a derivation of the Kelvin equation, some of which use visual aids to attempt to reinforce concepts (Ruthven 1984; Gentle and Barnes 2005). However, the author feels that to avoid confusion, a more direct derivation is best and is often how physical chemistry texts present it (Atkins 1990; Rowlinson and Widom 2002; éCernây and Rovnanâikovâa 2002).

The Kelvin equation makes use of a physicochemical equilibrium rooted in the laws of thermodynamics, the second law in particular. The second law of thermodynamics governs the direction in which processes, including chemical interactions, tend to happen when allowed to naturally (or spontaneously) occur. When a process is allowed to play out naturally, the total entropy of the system is increased. As the system's total entropy is increased, ultimately the Gibbs free energy, a thermodynamic quantity, is always tending to be reduced. It is this tendency of the Gibbs free energy to be reduced that allows reactions or interactions to achieve equilibrium. While a comprehensive review and/or derivation of the physicochemical concepts being presented here are beyond the scope of this review, the reader, if so inclined, may consider reviewing the texts being referenced (Atkins and De Paula 2006; Atkins 1990).

The equilibrium of interest results from imposing phase equilibrium on a system of substances. Phase equilibrium is a condition where substances of one phase have either completely stopped interacting with the like substances of other phases or have achieved dynamic equilibrium with the other phases. Meaning, either a substance of a given phase is no longer being spontaneously converted to another phase or the same molar quantity of a substance leaving its current phase for another is simultaneously being replaced. For this condition to exist, both the temperature and pressure of the system are assumed constant and the fundamental equation of chemical thermodynamics (not shown) may be simplified and defined as follows in equation 2.58 (Atkins 1990).

$$dG = \sum dG_i^x \Rightarrow \sum \mu_i^x dn_i^x \quad \text{Equation 2.58}$$

where

- dG : Total infinitesimal change to the Gibbs free energy [*Force* \times *Length*]
- dG_i^x : Partial contribution to the total infinitesimal change to the Gibbs free energy; made by the i^{th} substance of a phase x [*Force* \times *Length*]
- μ_i^x : Chemical potential of the i^{th} substance of a phase x [*(Force* \times *Length*)/*mol*]
- dn_i^x : Infinitesimal change in the molar quantity of the i^{th} substance of a phase x [*mol*]

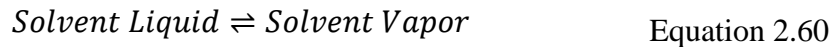
Since it is assumed that the only relevant interactions taking place are between the liquid water solvent and water vapor molecules in the gaseous mixture, equation 2.59 is assumed to be the relevant form of equation 2.58. The assumptions made, regarding the relevant interactions, are based on the assumption that all the other substances in the system are either nonvolatile or chemically inert and therefore are not contributing to the change of the Gibbs free energy of the system.

$$dG = \mu_{solv}^v dn_{solv}^v + \mu_{solv}^L dn_{solv}^L \quad \text{Equation 2.59}$$

where

- μ_{solv}^v : Chemical potential of the solvent vapor $[(Force \times Length)/mol]$
- μ_{solv}^L : Chemical potential of the solvent liquid $[(Force \times Length)/mol]$
- dn_{solv}^v : Infinitesimal change in the molar quantity of the solvent vapor $[mol]$
- dn_{solv}^L : Infinitesimal change in the molar quantity of the solvent liquid $[mol]$

Schematically, the phase equilibrium looks something like:



As an infinitesimal amount of mass starts to spontaneously leave one phase for another, one side of the equilibrium is losing (Gibbs) free energy, while the other is gaining it. So then, in this context where the mass exchange is one-to-one, the infinitesimal molar quantities may each be rewritten generically as infinitesimal masses (dn). But since they are on opposing sides of the equilibrium, their signs are opposing. Meaning, when one side is gaining an infinitesimal amount of mass (dn), the other side is losing the same amount of mass ($-dn$). Determining which side is gaining mass and which side is losing mass is not necessary; to show this, equation 2.59 can be rewritten in either way below (see equations 2.61 and 2.62).

$$\frac{dG}{dn} = (\mu_{solv}^v - \mu_{solv}^L) \quad \text{Equation 2.61}$$

$$\frac{dG}{dn} = (\mu_{solv}^L - \mu_{solv}^v) \quad \text{Equation 2.62}$$

At equilibrium, the system has reached its minimum Gibbs free energy and mass exchange has either stopped or has reached a net zero exchange (i.e. dynamic equilibrium) and consequently the Gibbs free energy change goes to zero. Substituting zero into the left hand side of either equation 2.61 or 2.62 gives the same physicochemical equilibrium statement fundamental to deriving the Kelvin equation.

That is, when a substance in a vapor phase is in equilibrium with its condensed phase, the chemical potentials of either phase are equal, as shown in equation 2.63 (Gentle and Barnes 2005; Atkins and De Paula 2006).

$$\mu_{solv}^L = \mu_{solv}^v \quad \text{Equation 2.63}$$

Equation 2.58 from above came from the fundamental equation of chemical thermodynamics (not shown), for the conditions of constant temperature and constant volume with molar mass allowed to vary. At this point it is also necessary to consider the case where the pressure is allowed to vary and the temperature and molar quantity are constant (Atkins 1990).

$$dG = \sum dG_i^x \Rightarrow \sum V_i^x dp_i^x \quad \text{Equation 2.64}$$

where

- V_i^x : Volume of the i^{th} substance of a phase x [$Length^3$]
 dp_i^x : Infinitesimal change in the partial pressure of the i^{th} substance of a phase x [$Force/Area^2$]

However, the chemical potential of a pure substance is just its Gibbs energy per mol and the volume of the substance is its partial molar volume times its molar quantity, as shown in equations 2.65 and 2.66, respectively (Atkins 1990; Poling, Prausnitz, and O'Connell 2001).

$$\mu_i^x = \frac{G_i^x}{n_i^x} \quad \text{Equation 2.65}$$

$$V_i^x = \hat{V}_i^x n_i^x \quad \text{Equation 2.66}$$

By substitution of equations 2.65 and 2.66; equation 2.64 can be re-written in terms of the change in chemical potential as shown in equation 2.67 (Atkins 1990; Poling, Prausnitz, and O'Connell 2001).

$$d\mu = \sum d\mu_i^x \Rightarrow \sum \hat{V}_i^x dp_i^x \quad \text{Equation 2.67}$$

where

- $d\mu$: Total infinitesimal change to the chemical potential [$(Force \times Length)/mol$]
 $d\mu_i^x$: Partial contribution to the total infinitesimal change to the chemical potential made by the i^{th} substance of a phase x [$(Force \times Length)/mol$]
 \hat{V}_i^x : Partial molar volume of the i^{th} substance of a phase x [$Length^3/mol$]

dp_i^x : Infinitesimal change in the pressure of the i^{th} substance of a phase x
 $[Force/Area^2]$

The two partial contributions to the change in the total chemical potential energy of the system are:

$$d\mu_{solv}^v = \hat{V}_{solv}^v dp_{solv}^v \quad \text{Equation 2.68}$$

$$d\mu_{solv}^L = \hat{V}_{solv}^L dp_{solv}^L \quad \text{Equation 2.69}$$

Starting with a system that has achieved equilibrium, by equation 2.69, if a pressure change is directly applied to only the surface of the liquid solvent, the chemical potential of the liquid solvent is altered. As stated previously (when defining equilibrium vapor pressure), mass transfer that occurs merely from being squeezed out of phase shall be assumed trivial and not considered in this derivation. However, a certain amount of mass driven by the chemical potential imbalance will shift phases to restore equilibrium. Once equilibrium has been restored, equation 2.63 will again be valid, and subsequently so too will equation 2.70.

$$d\mu_{solv}^v = d\mu_{solv}^L \quad \text{Equation 2.70}$$

If the chemical potential of both phases at equilibrium are equal to each other prior to and after the application of the pressure change, then the difference or change in chemical potential is also equal. Therefore, from equation 2.70, equation 2.71 follows.

$$\hat{V}_{solv}^v dp_{solv}^v = \hat{V}_{solv}^L dp_{solv}^L \quad \text{Equation 2.71}$$

Next, one applies the ideal gas law to the solvent vapor, as shown by equation 2.72. Then, solving equation 2.72 explicitly for the solvent vapor's partial molar volume (\hat{V}_{solv}^v), as shown by equation 2.73, it is substituted back into the left hand side of equation 2.71, thus allowing for the elimination of the partial molar volume term belonging to the vapor phase as shown in equation 2.74.

$$p_{solv}^v V_{solv}^v = p_{solv}^v \hat{V}_{solv}^v n_{solv}^v = n_{solv}^v R_u T \quad \text{Equation 2.72}$$

$$\hat{V}_{solv}^v = \frac{R_u T}{p_{solv}^v} \quad \text{Equation 2.73}$$

$$\frac{R_u T}{p_{solv}^v} dp_{solv}^v = \hat{V}_{solv}^L dp_{solv}^L \quad \text{Equation 2.74}$$

where

p_{solv}^v : Pressure of the solvent vapor [Force/Area²]

This is helpful because it cannot be assumed that the partial molar volume term belonging to the vapor phase is constant, as vapor is generally very compressible. Conversely, since the liquid is assumed approximately incompressible, the partial molar volume belonging to it (\hat{V}_{solv}^L) can be used as a constant. It should be explained though, that while the partial molar volume of the liquid solvent is treated as a constant, it is only constant in the context of moderate pressure changes. Partial molar volumes are essentially molecular packing values, which are subject to variation with changes in temperature, solution composition and concentration. The partial molar volume value used for example calculations in this section of the investigation ($\hat{V}_{solv}^L = 18 \text{ cm}^3/\text{mol}$) is that of pure water without solute at 25°C (298.15 K) (Atkins 1990).

The next step is to integrate each side of equation 2.74 from the initial pressure equilibrium condition to the final pressure equilibrium condition. Initially, each of the solvent's phases (vapor and liquid) is in pressure equilibrium with the other ($P_{eq_i} = p_{v_i}$). Therefore, the initial pressure conditions on both sides start there. The final equilibrium vapor pressure condition of the liquid, on the right hand side of the equation, is just the initial equilibrium vapor pressure of the liquid, plus the directly applied change in pressure ($P_{eq_f} = P_{eq_i} + \Delta P \Rightarrow p_{v_i} + \Delta P$). On the left hand side, the final vapor pressure condition is expressed as just the unknown final vapor pressure (p_{v_f}) that results from the solvent's vapor phase achieving equilibrium with its liquid phase. Applying these limits of integration to equation 2.74, we get the expression shown in equation 2.75.

$$R_u T \int_{p_{v_i}}^{p_{v_f}} \frac{1}{p_{solv}^v} dp_{solv}^v = \hat{V}_{solv}^L \int_{p_{v_i}}^{p_{v_i} + \Delta P} dp_{solv}^L \quad \text{Equation 2.75}$$

where

p_{v_f} : Final vapor pressure [Force/Area²]

p_{v_i} : Initial vapor pressure [Force/Area²]

After the integration on both sides has been carried out, a form of the Kelvin equation is revealed.

$$R_u T \ln \left(\frac{p_{v_f}}{p_{v_i}} \right) = \hat{V}_{solv}^L \Delta P \quad \text{Equation 2.76}$$

It is easiest to envision the pressure change term as a positive one (ΔP), where a load is applied mechanically by a piston having a semipermeable head through which vapor alone may pass. In principle, the applied pressure change could also be negative ($-\Delta P$). Since the negative pressure change is in keeping with this investigation's needs, to make the Kelvin equation applicable, one only needs to apply the correct sign, a negative one

(Atkins and De Paula 2006; Atkins 1990). The Laplace equation has already defined a pressure change across the meniscus ($\Delta P = P_2 - P_1$) in terms of constant radii of curvature; equation 2.24 (or 2.57) can be substituted into equation 2.76, with the appropriate sign, to obtain the general form of the Kelvin equation.

$$R_u T \ln \left(\frac{p_{v_f}}{p_{v_i}} \right) = -\hat{V}_{solv}^L \gamma \left(\frac{1}{R_1} + \frac{1}{R_2} \right) \quad \text{Equation 2.77}$$

The change in pressure load is now a function of meniscus curvature. Therefore, the initial vapor pressure at equilibrium (p_{v_i}) can be thought of as the equilibrium vapor pressure of a solvent (or solution) when the effects of curvature are not considered. Conversely, the final vapor pressure at equilibrium (p_{v_f}) can be thought of as the equilibrium vapor pressure when the effects of curvature are considered.

Since the Laplace equation can be expressed in many ways, consequently so too can the Kelvin equation. In the case where one is interested in expressing the Kelvin equation as a function of general pore radii, equation 2.78 may be used.

$$R_u T \ln \left(\frac{p_{v_f}}{p_{v_i}} \right) = -\hat{V}_{solv}^L \gamma \left(\frac{\cos \theta_{c1}}{r_1} + \frac{\cos \theta_{c2}}{r_2} \right) \quad \text{Equation 2.78}$$

In the case of a circular pore, equation 2.78 may be re-written as follows in equation 2.79, and so on.

$$R_u T \ln \left(\frac{p_{v_f}}{p_{v_i}} \right) = -\hat{V}_{solv}^L 2\gamma \left(\frac{\cos \theta_c}{r} \right) \quad \text{Equation 2.79}$$

At this point one can explore the magnitude of the mean tube (or pore) radius needed to create a significant change in the equilibrium vapor pressure. To do this, one first solves equation 2.79 for the ratio of pressures (p_{v_f}/p_{v_i}), as shown in equation 2.80.

$$p_{v_f}/p_{v_i} = e \left[-\frac{\hat{V}_{solv}^L 2\gamma (\cos \theta_c)}{R_u T r} \right] \quad \text{Equation 2.80}$$

As explained by the Laplace equation, as the radius of the tube (or pore) gets smaller, the pressure difference across the interface gets larger. Conversely, the larger the radius becomes, the smaller the pressure difference is. As the radius becomes infinitely large, the pressure change becomes infinitely small. When this occurs the unknown final vapor pressure (p_v) is equal to the known initial vapor pressure (p_{v_i}), and the ratio goes to unity. By using equation 2.80, and plotting the ratio of pressures (p_{v_f}/p_{v_i}) versus the mean radius (r), one can quantify the magnitude of the radius required to create a

significant deviation from unity. Therefore, assuming that pure water (not in a solution) at 25°C (298.15 K) is an acceptable example liquid; one may use the values given in Table 1 to plot equation 2.80, shown by figure 11.

Variable	Value	Units
\hat{V}_{solv}^L	1.8×10^{-5}	$[m^3 / mol]$
T	298.15	$[K]$
γ	0.0720	$[N / m]$
R_u	8.31451	$[(N \cdot m)/(K \cdot mol)]$
θ_c	0.0	$[rad]$

Table 1: Values used to plot the Kelvin equation of Figure 11

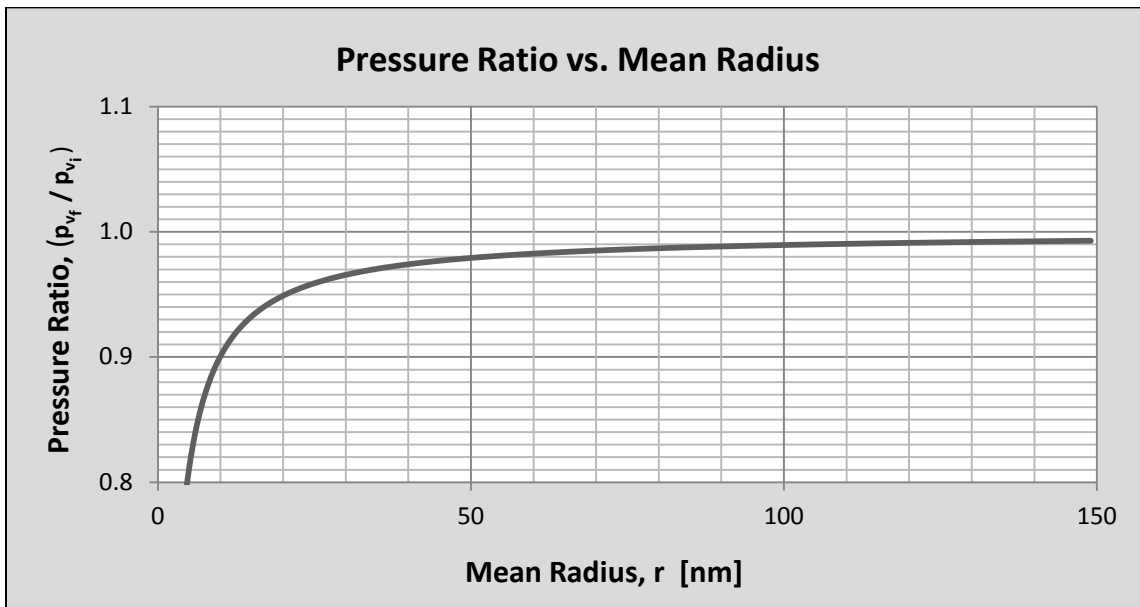


Figure 11: Plot of the Kelvin equation using the values of Table 1

It can be shown by the plot of figure 11 that measureable changes in pressure start somewhere between 50 to 100 nanometers in mean radius, a result that has been concluded by others (Grasley et al. 2006, 51-57). This result serves to validate a key assumption made in deriving the Laplace and subsequently the Kelvin equations; the assumption being that the capillary (or pore) size is sufficiently small so that a constant meniscus curvature can be assumed. However, another large simplifying assumption made here was that the liquid completely wet the capillary (or pore) walls, leading to a contact angle of zero ($\theta_c = 0$). Since it would seem that other values could easily lead to significant variations in the plot of figure 11, the author addresses this next.

Plotting the Kelvin equation using the values from table 1 again, but this time for multiple contact angle values ($\theta_c = 0, 20, 40$ and $60 [deg.]$) as shown by figure 12, one

can see the effects of the various contact angles on the deviation from unity. As can be seen by figure 12, along with some select values from that plot shown in table 2, moderate deviations of the contact angle away from zero have almost no effect on the deviation from unity for the larger radius values. Therefore, the maximum capillary (or pore) size estimate of 50 to 100 nanometers in mean radius still holds. However, as the mean radius gets smaller, the effects of contact angle do become more pronounced; an observation that shall be discussed further, when this investigation explores the topic of moisture sorption isotherms. It should be noted that table 2 starts with the selected value of 3 [nm] in radius. This is because smaller radii may start to become governed by the adhesive forces of the concrete surface. These forces are not accounted for by the Kelvin equation.

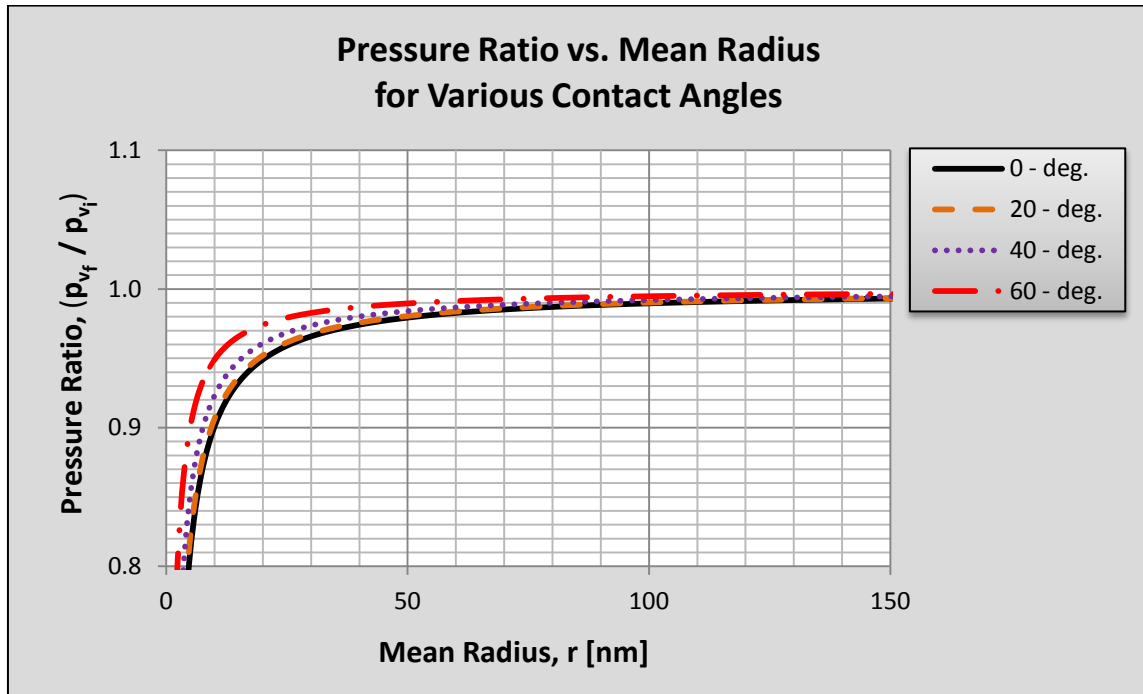


Figure 12: Plot of the Kelvin equation using the values of Table 1, along with various other contact angles.

As it turns out, the single most important take-away from this literature review is that there exists a maximum capillary (or pore) size (of approximately 50 to 100 nanometers in mean radius) above which no significant measurable changes to the equilibrium vapor pressure attributable to meniscus curvature can be made, as shown in figure 13. That is to say, in theory, any amount of meniscus curvature will cause a reduction in the chemical potential at the meniscus interface, causing some amount of change to the equilibrium vapor pressure. Consequently, the relative humidity (a term formally defined later in section 2.2.4.2) would also experience change. However, the changes to the equilibrium vapor pressure (and subsequently the relative humidity) associated by solution progressively filling pores above approximately 50 to 100 nanometers are so small that systems like the one used in this investigation cannot measure them.

Mean Radius, r [nm]	Contact Angle, θ_c [deg.]			
	0	20	40	60
3	0.706	0.721	0.766	0.840
4	0.770	0.782	0.819	0.877
5	0.811	0.822	0.852	0.901
10	0.901	0.906	0.923	0.949
20	0.949	0.952	0.961	0.974
30	0.966	0.968	0.974	0.983
40	0.974	0.976	0.980	0.987
50	0.979	0.981	0.984	0.990
100	0.990	0.990	0.992	0.995
150	0.993	0.993	0.995	0.997

Table 2: Selected pressure ratio values from figure 12

As the reader may recall from previous sections of this review, for conditions (A) and approximately (B) of figure 13, where curvature has virtually no effect, the equilibrium vapor pressure is only dependent upon the liquid's composition/concentration at a temperature. If the container were filled only with pure solution, then the equilibrium vapor pressure would be equal to the saturation vapor pressure of that liquid. If the liquid were a solution (nonvolatile solutes in solvent), then the equilibrium vapor pressure would generally tend to be lower than the saturation vapor pressure. Any deviations predicted by the Kelvin equation, shown as (C) of figure 13, are actually curvature-based deviations with respect to the equilibrium vapor pressure for the liquid of interest, which may or may not be equal to the saturation vapor pressure of the solvent, depending on whether the liquid is only solvent or a solution, respectively. Therefore, the initial vapor pressure at equilibrium (p_{v_i}) cannot be assumed equal to the saturation vapor pressure (p_{sat}), unless the liquid in the capillary (or pore) is only solvent.

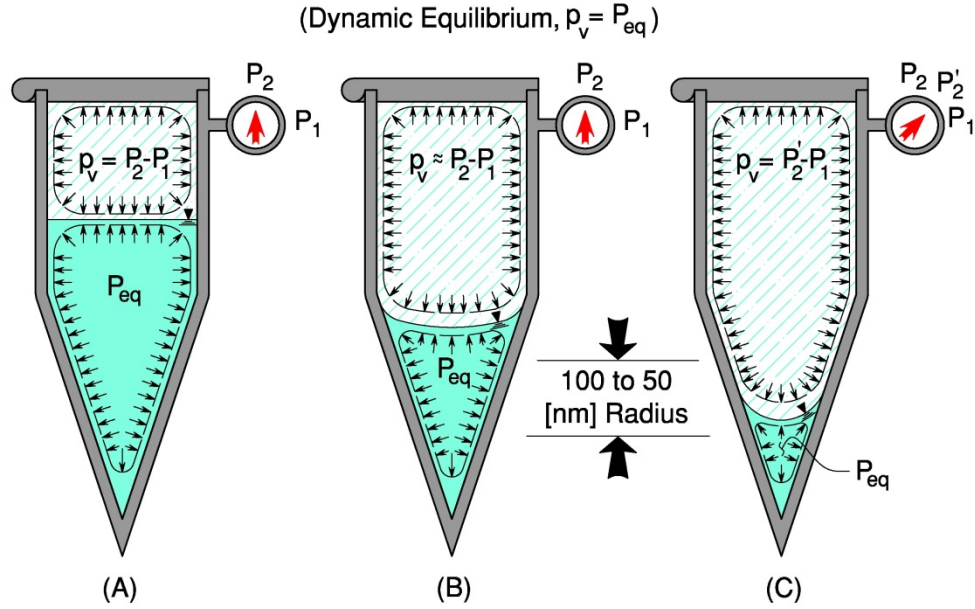


Figure 13: Representation of the vapor pressure at equilibrium of a solvent (or solution) in a sealed, tapered cylindrical container, filled to levels at which the radius is (A) much greater than, (B) slightly greater than or (C) within the maximum mean radial range of 100 to 50 nanometers. Not drawn to scale.

2.2.4 Percentage of Saturation and Relative Humidity Defined

2.2.4.1 Percentage of saturation

Now, having a better understanding of the terms used to define the psychrometry metrics stated at the outset of this literature review, the author can begin the formulation of percentage of saturation (S) and relative humidity (RH). Beginning with the percentage of saturation, one starts with **absolute humidity** (H_{abs}), also known as the mixing ratio. The absolute humidity is defined, shown by equation 2.81, as the amount of water vapor mass (m_v) being held per unit mass of dry gas (m_{dry}), at a temperature (Perry and Green 2008; Wyer 1906).

$$H_{abs} = \frac{m_v}{m_{dry}} \quad \text{Equation 2.81}$$

where

- H_{abs} : Absolute humidity, at a temperature [$mass/mass$]
- m_v : Mass of water vapor being held [$mass$]
- m_{dry} : Mass of the dry gas holding the water vapor [$mass$]

When the mass of water vapor being held equals the maximum storage capacity of the dry gas ($m_v = m_{sat}$), the gas is said to have reached **saturation humidity** (H_{sat}), show by equation 2.82.

$$H_{sat} = \frac{m_{sat}}{m_{dry}} \quad \text{Equation 2.82}$$

where

H_{sat} : Saturation humidity, at a temperature [mass/mass]
 m_{sat} : Saturation mass of water vapor being held [mass]

Using the above definitions, one defines the **percentage of saturation** (or percentage of absolute humidity) (S) as the ratio of absolute humidity to saturation humidity, expressed as a percentage (Perry and Green 2008).

$$S = \frac{H_{abs}}{H_{sat}} \times 100\% \Rightarrow \frac{m_v}{m_{sat}} \times 100\% \quad \text{Equation 2.83}$$

where

S : Percentage of saturation (or percentage of maximum absolute humidity) [%]

Though it shall not be derived here, one could use gas law principles to derive percentage of saturation completely in terms of partial (and total) pressures, at a given temperature, as given by equation 2.84.

$$S = \frac{p_v}{p_{sat}} \left(\frac{P_{total} - p_{sat}}{P_{total} - p_v} \right) \times 100\% \quad \text{Equation 2.84}$$

2.2.4.2 Relative humidity

Like percentage of saturation, relative humidity (RH) is a psychrometry metric used to quantify the degree of humidity held in a gaseous mixture. However, unlike percent of saturation, relative humidity is not derived from partial masses. Instead, relative humidity is defined in terms of partial pressures. Recall, that for a given gaseous mixture, at a given temperature, there exists a maximum or saturation (water) vapor pressure (p_{sat}). Relative humidity is simply the fraction of the saturation vapor pressure (p_v) present, expressed as a percent (see equation 2.85).

$$RH = \frac{p_v}{p_{sat}} \times 100\% \quad \text{Equation 2.85}$$

where

RH : Relative humidity [%]

Comparing equations 2.83 and 2.85, it is clear that the two metrics are analogous quantities. However, a quick inspection of equations 2.84 and 2.85, show that percentage of saturation and relative humidity, though both being measures of humidity content, are not exactly identical quantities. Of the two metrics, relative humidity is the more widely used (Perry and Green 2008) and shall be the preferred metric for this investigation. This is because relative humidity is easier to measure nondestructively. For this reason, the author shall now introduce the Kelvin equation developed previously in terms of relative humidity.

Setting the unknown partial vapor pressure of equation 2.85 equal to the unknown final partial vapor pressure of equation 2.78 ($p_v = p_{vf}$), equation 2.78 may be rewritten in terms of relative humidity (see equations 2.86 and 2.87).

$$\ln\left(\frac{RH}{100\%} \cdot \frac{p_{sat}}{p_{vi}}\right) = \frac{-\hat{V}_{solv}^L \gamma}{R_u T} \left(\frac{\cos \theta_{c1}}{r_1} + \frac{\cos \theta_{c2}}{r_2} \right) \quad \text{Equation 2.86}$$

or

$$\ln\left(\frac{RH}{100\%}\right) - \ln\left(\frac{p_{vi}}{p_{sat}}\right) = \frac{-\hat{V}_{solv}^L \gamma}{R_u T} \left(\frac{\cos \theta_{c1}}{r_1} + \frac{\cos \theta_{c2}}{r_2} \right) \quad \text{Equation 2.87}$$

At this point the reader may recall a section of this review entitled “*Effect of nonvolatile solutes on the equilibrium vapor pressure of a solvent*”, section 2.2.3.3. In that section, the concept of activity was introduced and equation 2.18 was developed. Setting the vapor pressure term of equation 2.18 equal to the known initial vapor pressure ($p_v = p_{vi}$) term, equation 2.87 can be rewritten in terms of the solvent’s activity, as shown by equations 2.90 and 2.91.

$$\ln\left(\frac{RH}{100\%}\right) - \ln(a_s) = \frac{-\hat{V}_{solv}^L \gamma}{R_u T} \left(\frac{\cos \theta_{c1}}{r_1} + \frac{\cos \theta_{c2}}{r_2} \right) \quad \text{Equation 2.90}$$

or

$$\ln\left(\frac{RH}{100\%}\right) - \ln(\psi_s X_s) = \frac{-\hat{V}_{solv}^L \gamma}{R_u T} \left(\frac{\cos \theta_{c1}}{r_1} + \frac{\cos \theta_{c2}}{r_2} \right) \quad \text{Equation 2.91}$$

If the pore liquid were assumed to be pure solvent, then the initial vapor pressure term would be equal to the saturation vapor pressure ($p_{v_i} = p_{sat}$), yielding an activity term equal to unity ($a_s = 1$), subsequently offering the simplified equation 2.92. In this case, one can see that as the principle radii become infinitely large, the relative humidity goes to 100%.

$$\ln\left(\frac{RH}{100\%}\right) = \frac{-\hat{V}_{solv}^L \gamma}{R_u T} \left(\frac{\cos \theta_{c1}}{r_1} + \frac{\cos \theta_{c2}}{r_2} \right) \quad \text{Equation 2.92}$$

If the pore liquid were a nonvolatile, non-electrolyte solution, then Raoult's law may be applicable. Therefore, the activity coefficient would be set equal to a constant value of one ($\psi_s = 1$), resulting in equation 2.93. From this equation, one can see as the principle radii become infinitely large, the relative humidity goes to some value less than 100%.

$$\ln\left(\frac{RH}{100\%}\right) - \ln(X_s) = \frac{-\hat{V}_{solv}^L \gamma}{R_u T} \left(\frac{\cos \theta_{c1}}{r_1} + \frac{\cos \theta_{c2}}{r_2} \right) \quad \text{Equation 2.93}$$

Since pore solution in concrete is generally an electrolyte solution, theoretically the activity coefficient must remain in the equation and therefore equation 2.90 or 2.91 should be used. However, as was pointed out in section 2.2.3.3, based on the findings of a study by Grasley, equation 2.93 may offer satisfactory values for solutions having low concentrations of electrolytes (Grasley and Leung 2011). Due the highly empirical nature of determining activity coefficients, any further exploration of this topic shall be deemed beyond the scope of this investigation. Moving forward, the general expanded form of the Kelvin equation, as shown by equation 2.90, shall be the form used as the author proceeds to discuss relative humidity inside hardened concrete later in this review.

2.3 MOISTURE CONTENT AND RELATIVE HUMIDITY IN CONCRETE

2.3.1 Porosity of Concrete

2.3.1.1 Brief overview of the total porosity volume

At the time a fresh batch of normal concrete (with air entrainment) is placed, it contains some initial amount of mix water content. Then, as the fresh concrete cures, a substantial portion of the initial mix water becomes bound, chemically combined with or adsorbed to hydration products, some is lost to evaporation, and the rest remains unused within the concrete. Once curing has progressed to a point where the concrete has become hardened, though seemingly solid, the concrete contains spaces within devoid of hydration product, and is therefore said to be **porous**. However, just because a material is porous doesn't necessarily mean that it is **permeable**, which indicates the material will allow passage of a fluid (liquids or gases) through it (Mehta and Monteiro 2006; Richardson 2002).

Porosity is a popular term used to describe a void volume of a porous material. Hardened concrete contains a network of pores and other void spaces approximately 0.5 nanometers to 3 millimeters in mean diameter. The range of pore sizes offered to the reader herein were obtained from multiple, reputable, literature sources (Neville 2011; Mehta and Monteiro 2006; Richardson 2002; Kosmatka, Kerkhoff, and Panarese 2002). But it should be noted here that while minor value inconsistencies do seem to exist between the sources, there do not seem to be conflicts with the general orders of magnitude cited. Neglecting any contribution by coarse or fine aggregates, the porosity of concrete is generally subdivided into four groupings: gel pores, capillary pores, entrained air and entrapped air voids. Each of these groups shall be discussed briefly in order of ascending mean diameter (Richardson 2002; Mehta and Monteiro 2006).

2.3.1.2 Gel pores

The **gel pores** are the smallest of the void spaces, with inter-particle spacing ranging in size from 0.5 to 8 nanometers, and most being less than 3 nanometers (Neville 2011; Richardson 2002). Gel pores are the pore solution-filled spaces between hydrated cement gel particles, as represented in figure 14(B), which include the interstitial spaces between the calcium silicate hydrate (**CSH**), calcium trisulfoaluminate hydrate (**ettringite**), calcium hydroxide (**portlandite**), and other hydration products. Interestingly, though hydration products like CSH, ettringite and portlandite are collectively called a gel, they are not gelatinous. Under the lens of a scanning electron microscope, images of crystalline structures with varying geometry can be observed. For a given volume of gel, the gel pores within it make up about 28 to 30 percent of the total volume (Richardson 2002; Mehta and Monteiro 2006; Neville 2011; Neville 2006).

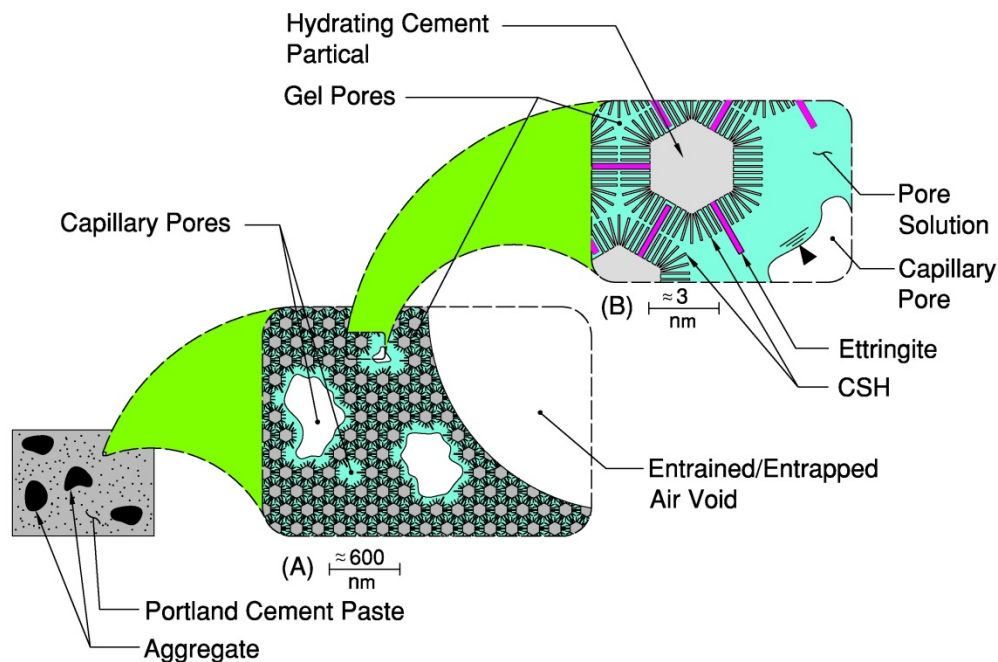


Figure 14: Representation of capillary and gel pores of concrete. The approximate scales given indicate the general magnitude of the (A) capillary pores and (B) Gel pore inter-

particle spacing. Hydrating cement particles are not to scale, and the Portlandite and “other hydration products” are not shown.

2.3.1.3 Capillary pores

Theoretical calculations based solely upon the stoichiometric relationship between anhydrous cement grains and fully hydrated cementitious product (not shown) reveal that an absolute minimum water/cement (w/c) ratio of approximately 0.22 by mass is required (Neville 2006). However, since nearly 30 percent of the total gel volume is made up of gel pores, to ensure full hydration, this space needs to be filled with moisture. Consequently, the w/c ratio corresponding to this moisture condition ranges from 0.32 to 0.38 by mass (Mehta and Monteiro 2006; Popovics 1998; Neville 2011; Richardson 2002). In practice though, due to the tendency of cement particles to cluster together (or flocculate) the mix water does not get uniformly distributed, causing the minimum w/c ratio required for full hydration to be approximately 0.42. Ultimately though, the actual amount of mix water used may vary with the types of admixtures used and any imposed workability requirements. It has been suggested that practical w/c ratios range from 0.40 to 0.50 by mass (Richardson 2002; Popovics 1998; Neville 2006).

Since the practical w/c ratio (0.4 to 0.5 by mass) is larger than the minimum theoretical w/c ratio required to ensure full hydration (0.32 to 0.38 by mass), it is inevitable that there will be reservoirs of extra water in the system existing in places where hydration products have not formed; these are called **capillary pores**, represented by figure 14(A). As a general rule, the larger the w/c ratio becomes, the more unused water that remains in the system, thereby increasing the number and size of the capillary pores. Capillary pores generally range in size from about 10 to 1000 nanometers in mean diameter for well hydrated concrete with low w/c ratios. However, concrete of poor quality can attain capillary pore sizes of up to 50 times larger (Neville 2011; Neville 2006; Richardson 2002). It should be stated that while most hydration occurs early in the life cycle of concrete (the first several days) and proceeds at a slow and declining rate thereafter, the process of hydration may continue for a very long time. As hydration continues over time, the existing capillary voids continue to fill in with hydration products, causing the average capillary pore size of the system to decrease with time (Mehta and Monteiro 2006).

Capillary pores either interconnect with other capillary pores or become disconnected by gel particles/pores, as is discussed further in section 2.3.2.1, creating capillary pores that terminate into dead ends. Figure 15 provides a representation of four possible capillary pore geometric configurations found throughout literature (Meyers 1991; Lamond and Pielert 2006; Diamond 2000; Ishida, Maekawa, and Kishi 2007; Espinosa and Franke 2006, 1954-1968). The simplified, “small” and “large” pores, as labeled in figure 15, are used to represent in a relative way, how pore sizes may transition.

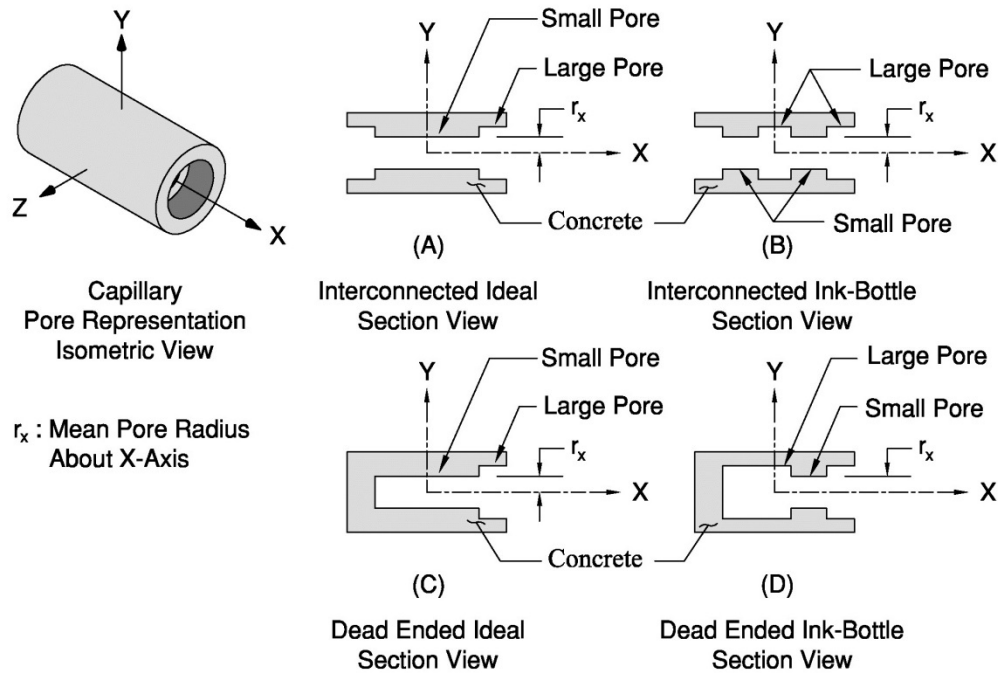


Figure 15: Representation of four possible capillary pore geometries including (A) interconnected ideal, (B) interconnected ink-bottle, (C) dead ended ideal and (D) dead ended ink-bottle.

In experimental work by Winslow and Liu, as referenced in chapter 6 of Neville's book entitled "*Properties of Concrete*" (Winslow and Liu 1990; Neville 2011), they examined the capillary pore structure of concrete paste, that is to say, the paste formed in a system in which aggregate is present. The method of their study included the use of **mercury intrusion porosimetry** (MIP) on various pastes (aggregate free paste, mortar paste and concrete paste) having multiple w/c ratios, temperatures and degrees of hydration maturity. The pore size distributions generated in this study seem to indicate that the capillary pore volume comprised of pores with sizes greater than 100 nanometers in mean radius may be relatively significant. For example, the study showed that a concrete at 20 days of curing at 20 °C with an initial w/c ratio of 0.45 had approximately 25 percent of its capillary pore volume made up by pores having mean radii greater than 100 nanometers. It should be noted that these values represent the capillary pore volume alone. Every effort was made to eliminate or account for entrapped air voids, and having added no air entrainment, causing the approximation above (25 percent) to be conservative. Additionally, Winslow and Liu observed that the pore size distribution of a pure cement paste as opposed to a paste cured in the presence of aggregate are different. The pore size distribution of pure cement paste, after hydration, is such that most of its porosity volume is comprised of pores with mean diameters of less than 100 nanometers. It is hypothesized that this phenomenon is attributable to the increased porosity within the **interfacial transition zone** (ITZ), a layer of hydration products formed at the interface between the bulk of the concrete's paste and aggregate (Mehta and Monteiro 2006; Neville 2011).

While an explanation of the science behind MIP may be found in literature (Popovics 1998), and is closely related to the Kelvin Equation, it is beyond the scope of this investigation. However, having just presented information regarding pore size distributions based on MIP results, the author feels obligated to acknowledge that there are those who have strong feelings regarding the accuracy of pore size distributions obtained using this method. Diamond maintains in a published article, entitled “*Mercury porosimetry: An inappropriate method for the measurement of pore size distributions in cement-based materials*”, that in spite of the historical wide spread application of this method to determine pore size distributions of concrete, that fundamental assumptions render the results ultimately incorrect (Diamond 2000; Lamond and Pielert 2006). In his article, Diamond concludes that the pore size distributions obtained by MIP both overestimate the porosity volumes of smaller capillary pores, and underestimate the porosity volumes of larger capillary pores. In fact, this article sparked a series of responses and counter responses within the materials science community (Wild 2001; Diamond 2001b; Chatterji 2001; Diamond 2001a). Therefore, it is highly probable that the percentage of capillary porosity in concrete attributed to capillary pores of radii greater than 100 nanometers exceeds the percentages extracted from the experimental works of Winslow and Liu.

2.3.1.4 Entrained and entrapped air voids

The largest of the void spaces are entrained and entrapped air voids, also represented by figure 14(A). Entrained air voids (or bubbles) are spherical voids purposely placed or entrained into concrete, primarily through the use of (surfactant) admixtures. Entrained air voids provide volume within the concrete to accommodate the approximate 9 percent expansion of pore solution during periods of freezing and thawing. Entrained air is engineered to be uniformly dispersed throughout the concrete paste without becoming interconnected, with most voids ranging in size from 10,000 to 100,000 nanometers in diameter (Neville 2011; Kosmatka, Kerkhoff, and Panarese 2002; Mehta and Monteiro 2006). Entrapped air voids are generally an order of magnitude greater than that of entrained air voids and range in diameter from 1 to 3 millimeters (1,000,000 to 3,000,000 nanometers). Unlike entrained air, entrapped air voids are not purposefully placed, and are just a consequence of the typical batching, mixing and placement processes.

2.3.2 Moisture Content and Transport Processes in Concrete

2.3.2.1 Interlayer moisture

The mix water remaining in the concrete system as pore solution after the formation of hydration products is found in a variety of places. Assuming that enough initial mix water is used to form gel products, the gel pores that make up nearly one third of the gel's total volume remain completely filled with pore solution. The pore solution that fills these spaces is generally termed **interlayer solution**. In this state of existence, the inter-particle/interstitial spaces are so small that they are assumed to be filled by a single (or monomolecular) layer of solution (Neville 2011; Mehta and Monteiro 2006). As represented by figure 16, a furthering of figure 14(B), the gel pores provide formidable resistance to both moisture loss and transport.

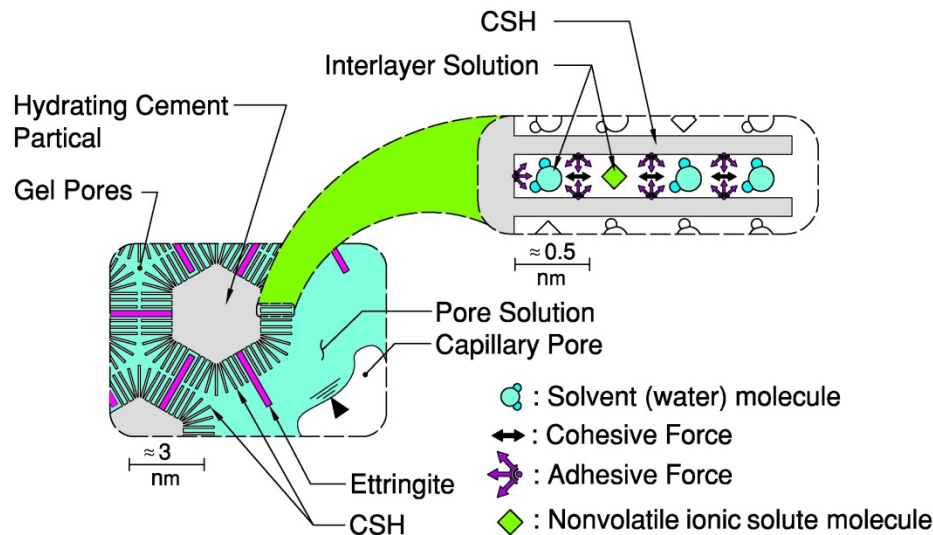


Figure 16: Representation of gel pores and interlayer solution of concrete. The approximate scales indicate the general magnitude of the inter-particle and interlayer spacing of the hydration products. Hydrating cement particles are not to scale, and the Portlandite and “other hydration products” are not shown.

This high resistance to moisture transport is due to both the adhesive forces that cause the solution to become physically adsorbed to interfacing hydration product surfaces, and the cohesive hydrogen bonding forces existing between the solution molecules, effectively capturing the molecules within the gel pores. The resistance to moisture transport through gel pores is so high in fact, that they are assumed to be “water tight”, and provide an effective disconnect between the capillary pores within the system. Of course, the fewer and smaller the capillary pores, the more effective the gel pores are at serving in this function (Richardson 2002; Mehta and Monteiro 2006).

2.3.2.2 Capillary moisture

Moisture also exists as pore solution in the capillary pores. As the reader may recall, these are the spaces created by having more mix water than theoretically required to complete hydration. Pore solution in the capillary pores of concrete exists as either physically **adsorbed solution**, or as **free solution**, as represented in figure 17, also a furthering of figure 14(B). As was discussed earlier, the phenomenon of capillary rise is initiated by adhesive forces at the liquid/solid interface that are more dominant than the cohesive forces between the solution molecules. Similarly, the walls of the capillary pores made up of hydration products, exert a strong adhesive force on the solution molecules at the solution/gel interface and cause an initial layer of solution to adhere to the capillary walls. However, this force of adhesion actually remains a participating force for some extended distance away from the actual interface, estimated to be 1.5 nanometers, and creating up to 5 additional layers of adsorbed solution molecules (Mehta and Monteiro 2006). The solution existing further than 1.5 nanometers away from the capillary walls is said to be free solution, in that its molecules are not affected by the adhesion forces.

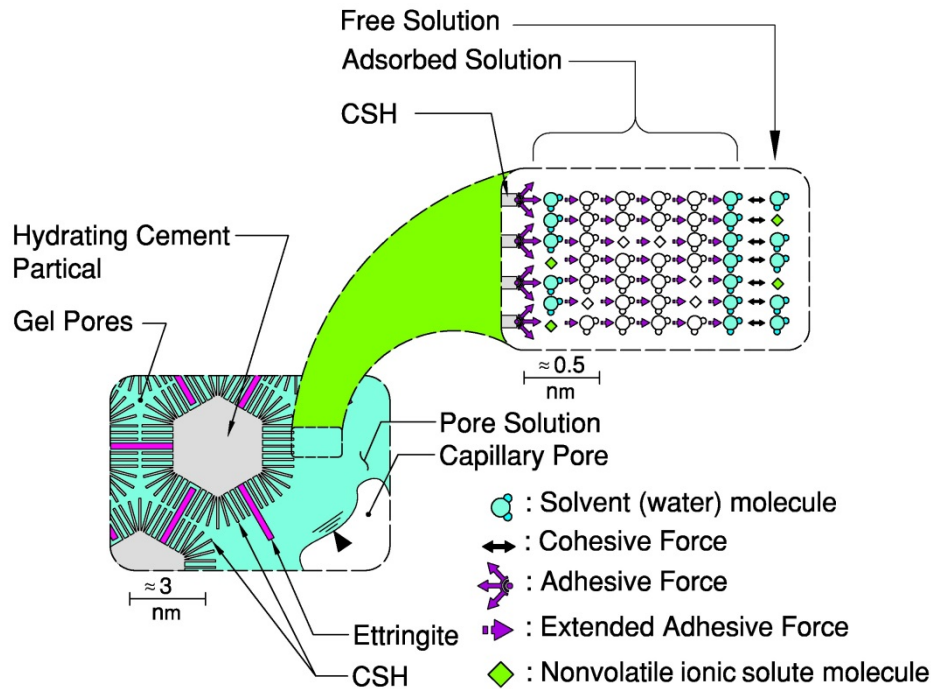


Figure 17: Representation of gel pores and adsorbed solution of concrete. The approximate scales indicate the general magnitude of the hydration product inter-particle spacing and the thickness of the adsorbed layers. Hydrating cement particles are not to scale, and the Portlandite and “other hydration products” are not shown.

Initially, hardened concrete is likely to contain pore solution left over from the unused mix water. In time though, moisture contained in the capillary pores may or may not be transported away from the concrete, a process called **desorption**, by evaporation (Reinhardt and RILEM Technical Committee 146-TCF 1997). Conversely, moisture from external sources may be transported inward, into the concrete's capillary pore system, a process called **sorption**, by the combined transport processes of **absorption** and [water] **vapor diffusion** leading to **adsorption** of both adsorbed and free [**capillary condensed**] moisture (Lamond and Pielert 2006; Richardson 2002; Newman and Choo 2003; Meyers 1991; Mehta and Monteiro 2006; Lyklema 2001). The process of absorption makes use of capillary rise to draw bulk liquid moisture into the system when in direct contact with a liquid source at the concrete's surface and may be thought of as a process of moisture penetration.

Diffusion is the transport or passage of substances spontaneously through a fluid (liquid or gaseous), driven by differences in its concentration, that is to say concentration gradients seeking concentration equilibrium. Therefore, in the context of this investigation, vapor diffusion is the spontaneous transport of water vapor through gases existing in the capillary pore network and other void spaces and is driven by differences in water vapor concentration (a.k.a. vapor pressure gradients) seeking concentration equilibrium (Newman and Choo 2003; Neville 2011).

At this point the author finds it necessary to make the following distinction. Like diffusion, **permeation** is also a transport process; however, it is defined as a process

driven by pressure differences (or pressure gradients) seeking pressure equilibrium. An example of a permeation-based transport process would be absorption, as capillary rise works by pressure gradients. Based on this definition, it is conceivable that the reader may have assumed that permeation would be the mechanism by which water vapor is also transported. However, vapor pressure is just the partial pressure of the (solvent) water vapor within the gaseous mixture and, therefore, should be thought of as a measure of vapor concentration. This line of reasoning can be reinforced by reviewing equations 2.3 to 2.5, as seen earlier in section 2.2.2 of this review (Newman and Choo 2003; Neville 2011).

Adsorption is not a penetration process; rather, it may be understood as a joining process. That is to say, at the capillary surface, moisture (the adsorbate) is removed from the diffused vapor by the inherent adhesive forces of the capillary surface (the adsorbent) and they become joined. The adsorbed layers formed are represented in figure 17. The adhesive forces are sufficiently large everywhere that the adsorbed layers are assumed to be formed first throughout the pore system, without regard for pore size (Lamond and Pielert 2006; Meyers 1991). This adsorbed layering phenomenon, while having only been introduced conceptually, is generally modeled with a classical equation developed by Brunauer, Emmett and Teller (BET), called the **BET equation** (Brunauer, Emmett, and Teller 1938). The BET equation is commented on more fully in section 2.3.3.1 of this review.

As the process of diffusion continues to transport moisture inward, causing the vapor pressure to increase, moisture formation beyond the adsorbed layer forms the free water (or solution) represented in figure 17, which is often called capillary condensation. Capillary condensation is the liquefaction of diffused vapor molecules in response to the vapor pressure inside the capillary pore network exceeding the equilibrium vapor pressure of the liquid solution [initially of adsorbed moisture and then subsequently of prior condensed free moisture] that would have been formed by this point (Gentle and Barnes 2005). However, this condensing free water tends to initiate in the smaller pores first. This is because [in keeping with the Kelvin equation], the pores having the smallest mean radii, as labeled by r_x in figure 15, lower the equilibrium vapor pressure of the solution in these areas the most. Consequently, these smaller pores are able to retain colliding moisture molecules both more efficiently, and at relatively lower vapor pressures, than the larger pores can. As the vapor pressure within the pore network continues to increase, the condensation will progressively fill the larger capillary pores. Interestingly, in materials like concrete it is likely that adsorption and capillary condensation will occur virtually simultaneously (Meyers 1991).

As the vapor pressure in the capillary network begins to decrease, the condensed moisture will progressively evaporate beginning with the larger capillary pores, menisci of which have the least curvature. Should the vapor pressure fall sufficiently low, the adsorbed layers would also start to vaporize. However, [also in keeping with the Kelvin equation] the presence of ink-bottles in the capillary pore network serve to complicate this ideal behavior by causing the larger pores behind them to fill and empty at relatively lower

vapor pressures (Lamond and Pielert 2006; éCernây and Rovnanâikovâa 2002; Meyers 1991).

As covered in the last section of this review (section 2.3.2.1), the gel pores are generally pretty effective at disconnecting the capillary networks, if not completely, then sufficiently that there is an extremely high resistance to moisture transport processes, including absorption and to a somewhat lesser extent vapor diffusion. Consequently, even after prolonged submersion in liquid moisture sources, studies have shown that the depth of moisture penetration by absorption is often relatively shallow (Newman and Choo 2003; Neville 2011). The concrete systems represented by the scope of this investigation are not generally exposed to prolonged submersion; rather, exposure is limited to precipitation events, followed by periods of drying. Therefore, while a small amount of water may be absorbed during a wetting event, an eventual period of drying is likely to evaporate all but a very small fraction of that moisture. The moisture that does remain may eventually diffuse inward (Andrade, Sarriá, and Alonso 1999). As the scope of this investigation includes cover depths of no less than 1 inch, it is assumed that, albeit still a very slow process, vapor diffusion is the primary process for moisture transport. It has also been assumed by the author that, while aged, the subject pore system does not contain sufficiently numerous large crack propagations from the surface to depths such that the assumed dominant moisture transport process would become effected (Reinhardt and RILEM Technical Committee 146-TCF 1997; Neville 2011; Newman and Choo 2003).

Based on multiple literature sources, an ideal representation of how moisture would fill or empty the capillary pore geometries of figure 15 is presented here, by figures 18 and 19 (Lyklema 2001; Lamond and Pielert 2006; Ishida, Maekawa, and Kishi 2007; Gentle and Barnes 2005; Meyers 1991). While the trapped air voids created by the ink-bottles in both figures 18 and 19 are shown to vacate the pores, this may not completely occur. The extent to which trapped air occupies void spaces inside the capillary pore network depends on many things, including the solution surface tension and actual pore geometry (Reinhardt and RILEM Technical Committee 146-TCF 1997).

adsorbed layer, and subsequently any prior condensed solution. The loss of moisture occurs by a reversal of this two-step process, in response to a relative lowering of the vapor pressure in the capillary pores with respect to the equilibrium vapor pressures at various levels of solution content. In this section of the review, focus shall be on the adsorbed multilayer and more specifically understanding the relationship between its thickness and relative humidity.

As was alluded to in an earlier section (section 2.3.2.2), there exists a widely accepted relationship used to model this adsorbed layering phenomena, called the BET equation. However, the BET equation contains a few empirical terms that require estimated or experimentally obtained values. It is for this reason that the author feels it is best not to begin by looking at a form of the BET equation that explicitly expresses the ultimate relationship of interest in this investigation. Rather, it is best to start with the form presented by Meyers, in his book entitled “*Surfaces, Interfaces and Colloids: Principles and Applications*” where he offers (without derivation) a form of the BET equation claimed to be its most common, final form; it is presented below by equations 2.94 and 2.95 (Meyers 1991). The reason why this form is preferred by many shall be apparent shortly.

$$\frac{p_v}{V_A(p_{sat} - p_v)} = \frac{1}{V_M C} + \frac{(C - 1)}{V_M C} \cdot \left(\frac{p_v}{p_{sat}} \right) \quad \text{Equation 2.94}$$

$$C \approx e^{\left[\frac{\Delta H_A - \Delta H_v}{R_u T} \right]} \quad \text{Equation 2.95}$$

where

- V_A : Volume of all the adsorbed moisture layers, at standard temperature and pressure (STP) [defined as 273 K (0° Celsius) and 1 atm] [*Length*³]
- V_M : Volume of the first adsorbed moisture layer, or monolayer at STP [*Length*³]
- ΔH_A : Heat of adsorption [*Energy/mol*]
- ΔH_v : Heat of vaporization [*Energy/mol*]

The BET equation has historically been used as a method of determining the areas of hard to measure surfaces (Meyers 1991). Conceptually, if one had knowledge of the total number of molecules that completely covered a surface of unknown area, that layer being without any molecular [vertical] stacking (i.e. being a monomolecular layer or “monolayer”), then when accompanied by the knowledge of that particular molecule composition and certain [geometric and packing] properties, an area could be calculated (Gentle and Barnes 2005). This monolayer, having a known finite thickness may also be expressed as a volume, a monolayer volume V_M . In practice, determining the monolayer volume is not trivial. To further complicate the task, what if the adsorbed layer contains [vertical] stacking, resulting in a multilayer adsorbed volume V_A ? How would one parse out the molecules belonging to just the monolayer volume? As it turns out, the BET equation shown above by equations 2.94 and 2.95 most easily facilitates the

determination of the [approximate] monolayer volume V_M amidst a multilayer volume V_A , subsequently, allowing the surface area of interest to be calculated.

Prior to explaining how the equation facilitates volume estimation, and thus why the BET equation expressed in the form above is so popular, a little more background should be brought to the reader's attention. Certain adsorbent/adsorbate combinations have very different, very distinct adsorption behaviors, largely depending on the affinity between the adsorbent/adsorbate and the interactions between the adsorbate molecules (Gentle and Barnes 2005; Ruthven 1984). These distinct adsorption differences are most easily seen when one plots the pressure ratio (p_v/p_{sat}) or relative pressure belonging to the adsorbate of interest versus the adsorption ratio (V_A/V_M) or relative adsorption, at a given temperature. Such a plot belongs to a family of plots that relate moisture content to relative pressure (or a similar quantity, like relative humidity), are collectively termed **moisture sorption isotherms**. When the plot expresses relative pressure (or relative humidity) as its magnitude is ascending, it is called a **moisture adsorption isotherm**, or just adsorption isotherm. In the case where the plot represents the relative pressure (or relative humidity) as its magnitude is descending, the plot is called a **moisture desorption isotherm**, or just desorption isotherm (Newman and Choo 2003; ASTM Standard C1498 2004a (2010) e1). Later in section 2.3.3.3, the reader shall realize the need for such a distinction.

It has been determined by Brunauer, Emmett and Teller, the developers of the BET equation, that there are 5 classifications, or types, of adsorption isotherms. Idealized representations of all 5 adsorption isotherm types (not to scale) are presented by figure 20. With a quick inspection of figure 20, one can see that types II and IV tend to have higher affinities between the adsorbent and adsorbate than do the types III and V. More detailed information regarding the BET adsorption isotherm classifications, including discussions on what the various curve shapes indicate about the adsorbent/adsorbate interactions, may be found in the referenced literature (Brunauer, Emmett, and Teller 1938; Gentle and Barnes 2005; Ruthven 1984; Meyers 1991).

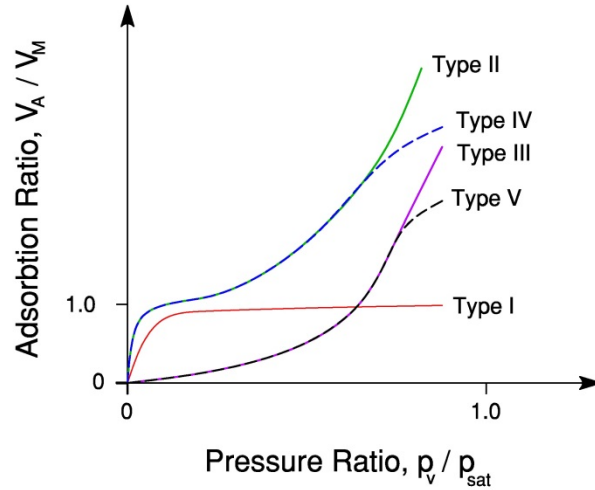


Figure 20: Representation of all 5 adsorption isotherm classifications, as proposed by the BET model.

In the case where the adsorbed layer only extends to a single layer ($V_A/V_M = 1$), the resulting isotherm is that of a type I. The type I isotherm is also called the **Langmuir isotherm**, as it may be modeled using a monolayer adsorption model originally developed in 1918 by Langmuir (not shown) which preceded the BET equation (Langmuir 1918). The BET equation was actually developed by extending the Langmuir model and resulted from the need to model adsorption in the case where the adsorbed layer extended beyond the monolayer ($V_A/V_M > 1$), as indicated by types II through V. With this newer BET model, one is now able to extract the adsorbed monolayer volume V_M from the multilayer volume V_A . Though the BET equation was developed specifically to handle the multilayer cases (types II through V), it can still handle the monolayer case (type I).

The reason that the form presented by equations 2.94 and 2.95 is so popular is because it is the linear form of the BET equation. That is to say, when the pressure ratio (p_v/p_{sat}) on the right hand side of equation 2.94 is plotted against the left hand side of the same equation, one can expect a linear plot, which is typically limited to the pressure ratio range of 0.05 to 0.30 (or 0.50 or depending on the literature source) (Gentle and Barnes 2005; Meyers 1991; Ruthven 1984; Xi, Bažant, and Jennings 1994). Coincidentally, the adsorbed layers in concrete generally range from about 11 % RH at the low end to a range of 30 % to 45 % RH at the high end, or to express equivalently in terms of pressure ratios (by equation 2.85), 0.11, 0.30 and 0.45 respectively. Below about 11% RH, loss of gel pore moisture starts occurring (Mehta and Monteiro 2006; Neville 2011; Lamond and Pielert 2006). The plot, being linear, allows for the determination of both the monolayer volume, V_M , and C term, where the C term, as shown by equation 2.95, contains two empirical parameters. The first parameter is the heat (or enthalpy) of adsorption ΔH_A , which is the energy per unit mole required to separate the adsorbate [monolayer] molecules from the adsorbent surface. The second is the heat (or enthalpy) of vaporization ΔH_v ; defined earlier (see section 2.2.1) as the energy required to vaporize 1

mole of a liquid at 1 atm (Atkins and De Paula 2006; Gentle and Barnes 2005; Ruthven 1984). In general ΔH_v is a well-documented parameter for water.

Interestingly, in the derivation of the BET equation (not shown) the ΔH_A term is applied only to the first layer of adsorbed molecules, while the same ΔH_v term is applied to every other subsequent layer as though they were free water. This assumption plays a pivotal role in producing the [limited] linear region, described earlier, within which useful results may be obtained (Meyers 1991). An example of how the V_M and C (and subsequently ΔH_A) terms may be determined from this linear relationship can be investigated by the reader with an examination of example 29.3 (pg. 888) in Atkins text entitled “Physical Chemistry” (Atkins and De Paula 2006).

Now that the reader has a general understanding of the terms within the BET equation, including both a sense of how they may be arrived at, along with an understanding of the limited range to which they are applicable, the author shall proceed. Rearranging the terms of equation 2.94, the author arrives at a form of the BET equation that is closer to expressing the relationship of interest in this investigation.

$$\frac{V_A}{V_M} = \frac{C p_v}{(p_{sat} - p_v) \left(1 + (C - 1) \cdot \frac{p_v}{p_{sat}} \right)} \quad \text{Equation 2.95}$$

Notice equation 2.95 above places the adsorption ratio (V_A/V_M), or relative adsorption, on the left hand side while keeping the pressure ratio (p_v/p_{sat}) or relative pressure belonging to the adsorbate on the right. Next, after some minor algebraic manipulation, the author obtains the expression shown by equation 2.96

$$\frac{V_A}{V_M} = \frac{p_v}{p_{sat}} \cdot \frac{C}{\left(1 - \frac{p_v}{p_{sat}} \right) \left(1 + (C - 1) \cdot \frac{p_v}{p_{sat}} \right)} \quad \text{Equation 2.96}$$

The author then substitutes equation 2.85 (section 2.2.4.2) into equation 2.96 to obtain an expression (equation 2.97) in terms of relative humidity. The result is the form that the author feels is most useful for the purposes of relating relative humidity RH to the thickness of the adsorbed multilayer thickness.

$$\frac{V_A}{V_M} = \frac{RH}{100\%} \cdot \frac{C}{\left(1 - \frac{RH}{100\%} \right) \left(1 + (C - 1) \cdot \frac{RH}{100\%} \right)} \quad \text{Equation 2.97}$$

Though the left hand side of the equation is the adsorption ratio (V_A/V_M), or relative adsorption, and not really a thickness, the reader can easily make this conversion. The reader may recall each adsorbed [water] layer is approximately 0.25 nanometers thick

(referring to section 2.3.2.2); therefore, when the adsorbed ratio is equal to a whole number, say 6 ($(V_A/V_M) = 6$), then the thickness calculated would be 1.5 nanometers ($t_L = 0.25 \frac{nm}{layer} \times 6 \text{ layers} = 1.5 \text{ nm}$).

Presented above is an extremely basic overview of a historically popular adsorption model that is still relevant today. What was not presented was an actual derivation of the BET equation. Brunauer, Emmett and Teller, in their paper referenced previously, developed the equation using a kinetic derivation and imposing dynamic equilibrium; this sort of derivation can also be seen in texts on the subject (Brunauer, Emmett, and Teller 1938; Gentle and Barnes 2005). In addition to kinetic derivations, others have shown that the BET equation can be derived from other approaches. Lyklema in the second volume of his text titled “Fundamentals of interface and colloid science: solid-liquid interfaces” offers a statistical derivation (Lyklema 2001).

However, due to certain limitations arising from basic assumptions during its derivation, subsequent models have been needed to satisfy various user-specific requirements. In a paper by Bažant entitled “*Moisture diffusion in cementitious materials*”, a partial listing of attempts by others to modify the BET equation is presented (Xi, Bažant, and Jennings 1994). One of the major limitations of the BET equation is that it does not consider the existence of multiple (or mixed) adsorbate molecules, but assumes that the adsorbate is of a single species and does not account for the effects of solutes (i.e., activity). Also, it was derived in the context of a planar (adsorbent) surface and consequently does not account for curvature. Finally, in the section to follow (section 2.3.3.2), the author applies the Kelvin equation to capillary condensed free solution and therein indicating that at some point the BET equation becomes invalid. Using one equation or the other in this way does not fully capture the interaction between the adsorbed and free solution. With exception to the points just addressed, the author leaves any additional commentary on the limits and shortcomings of the BET equation to the literature sources of this review (Meyers 1991; Gentle and Barnes 2005; Xi, Bažant, and Jennings 1994; Hillerborg 1985; Lyklema 2001; Ruthven 1984).

2.3.3.2 Capillary condensed moisture: Kelvin equation

As covered in the previous section of this review (section 2.3.3.1), the BET equation is used with some success to correlate relative humidity with the multilayer volume (or thickness) of moisture that becomes adsorbed to the concrete’s pore surfaces. The free capillary condensed moisture that forms beyond the influence of the adhesive forces of the capillary surface is not adsorbed moisture; therefore, one cannot use the BET equation to make correlations between the condensing volume and relative humidity (Gentle and Barnes 2005). Rather, one would need to employ the Kelvin equation, as expressed in section 2.2.4.2 by equation 2.90 or 2.91; the author has chosen to work with equation 2.90. However, a quick examination of the adsorption/desorption cycle of the “interconnected ideal” pore of figure 18 (section 2.3.2.2) may cause the reader to question how the Kelvin equation would be applied. This configuration does not seemingly contain a meniscus, at least as it was presented in the derivation of the Kelvin

equation, until step III. The moisture configuration shown by step II contains condensed solution lining the capillary pore walls, but not connecting through the middle of the capillary pore, a tube-shaped meniscus. In this case the two orthogonal planes upon which the curvatures of interest lay are taken, as a matter of convenience, to be the planes formed by the YZ and YX axes of figure 15 (section 2.3.1.3). As an aid, based on figure 15, the author has provided figure 21. Using the planes selected, figure 21 contains a cut-away view of the capillary pore; with the moisture and pore geometry scenario as described above.

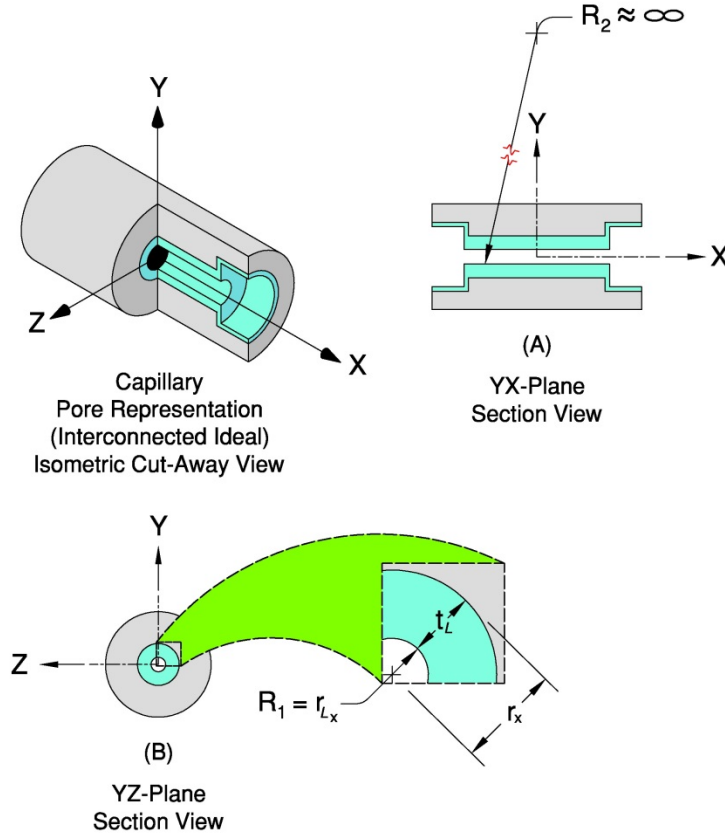


Figure 21: Representation of a capillary pore, having an interconnected ideal geometry and tube-shaped solution formation; including section views along the (A) YX-plane and the (B) YZ-plane.

When the orthogonal YZ (see figure 21(B)) and YX (see figure 21(A)) planes are selected, for this moisture configuration, the Kelvin equation needs to be expressed directly in terms of the constant radii of curvature, as equation 2.90 was really derived to handle the moisture scenario to follow this one. Therefore, substituting an older relationship (examining equations 2.77 and 2.78) into equation 2.90; equation 2.98 becomes the modified form needed.

$$\ln\left(\frac{RH}{100\%}\right) - \ln(a_s) = \frac{-\hat{V}_{solv}^L \gamma}{R_u T} \left(\frac{1}{R_1} + \frac{1}{R_2} \right) \quad \text{Equation 2.98}$$

Since the condensed solution coats the walls of a pore represented to be circular in cross-section, the radius of curvature used to calculate the first curvature term in equation 2.98 is equal to the mean pore radius about the X axis r_x , minus the solution layer thickness t_L (which includes adsorbed and condensed layers). This calculated moisture layer radius (equation 2.99) about the X axis, r_{L_x} , is shown in figure 21(B) and is substituted for the R_1 term. Since the solution layer thickness varies as the condensed volume changes, so too does the R_1 term.

$$r_{L_x} = r_x - t_L \Rightarrow R_1 \quad \text{Equation 2.99}$$

where

- r_{L_x} : Mean radius of a moisture layer in the capillary pore about the x-axis [*Length*]
- r_x : Mean radius of the capillary pore about the x-axis [*Length*]
- t_L : Thickness of the Liquid Layer [*Length*]

With the capillary pore and subsequently the moisture layer represented as being tubular and concentric about the X-axis, the curvature of interest along the YX-plane is assumed to be approximately zero. Therefore, as shown by figure 21(A) the corresponding radius of curvature is taken as approximately infinite (see equation 2.100)

$$R_2 \approx \infty \quad \text{Equation 2.100}$$

Substituting the values obtained/assumed for the orthogonal radii of curvature (R_1 and R_2), as expressed by equations 2.99 and 2.100, into equation 2.98, leaves a form of the Kelvin equation which may be directly applied to this scenario (see equation 2.101).

$$\ln\left(\frac{RH}{100\%}\right) - \ln(a_s) = \frac{-\hat{V}_{solv}^L \gamma}{R_u T} \left(\frac{1}{r_{L_x}}\right) \quad \text{Equation 2.101}$$

Once the condensed volume is sufficient, such that the solution does meet at the center, as shown to occur at step III of figure 18 (“interconnected ideal”), a more familiar looking meniscus emerges. It is this class of moisture scenario that may directly apply the form of the Kelvin equation expressed by equation 2.90. Here, the orthogonal planes, along which the curvatures are most conveniently defined, are the XY and XZ planes of figure 15 (section 2.3.1.3). As an aid, based on figure 15, the author has provided figure 22. Using the planes selected for this scenario, figure 22 contains a cut-away view of the capillary pore; with the moisture and pore geometry as just described.

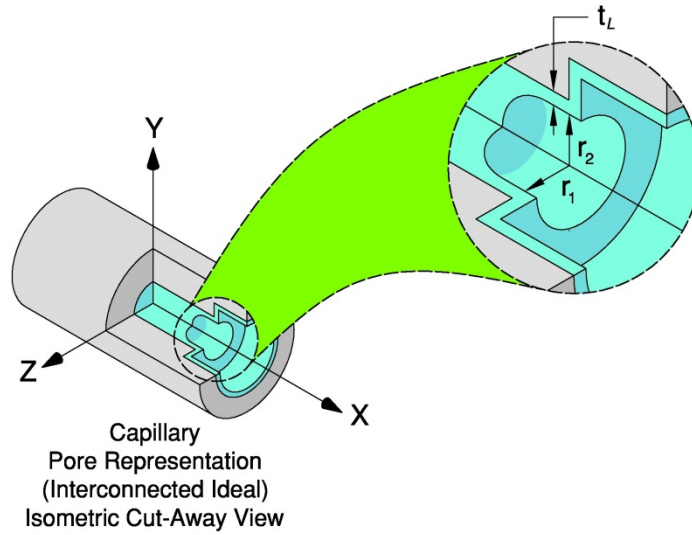


Figure 22: Representation of a capillary pore, having an interconnected ideal geometry and hemispherical shaped solution formation.

The pore radii (r_1 and r_2) used in the calculation of these two curvatures [along the XY and XZ planes] are measured by the perpendicular distances from the X axis in the directions along the Y and Z axes respectively, to the inner surface of the moisture that lines the pore wall at the location where the meniscus terminates into it. However, since the assumption is that of a circular capillary pore cross-section, a spherical meniscus surface is presumed. Therefore, the two distances measured along the Y and Z axes are equal to each other and shall be expressed as the radius of the moisture layer in the capillary pore about the x-axis r_{Lx} , as shown by equation 2.102 (similar to equation 2.99).

$$r_1 = r_2 = (r_x - t_L) \Rightarrow r_{Lx} \quad \text{Equation 2.102}$$

Additionally, one can presume that the orthogonal angles of contact (θ_{c1} and θ_{c2}), at the meniscus/moisture layer interface (not shown in figure 22) are also equal. However, since perfect wetting is historically assumed when using the Kelvin equation, the contact angle is set to zero, as shown by equations 2.103 and 2.104, respectively, resulting in the hemispherical shape of the pore being represented in figure 22.

$$\theta_{c1} = \theta_{c2} \Rightarrow \theta_c \quad \text{Equation 2.103}$$

where

$$\theta_c = 0 \quad \text{Equation 2.104}$$

Substituting equations 2.102, 2.103 and 2.104 into equation 2.90, a formulation of the Kelvin equation useful for the current scenario is determined (see equation 2.105).

$$\ln\left(\frac{RH}{100\%}\right) - \ln(a_s) = \frac{-2\hat{V}_{sol}^L \gamma}{R_u T} \left(\frac{1}{r_{Lx}}\right) \quad \text{Equation 2.105}$$

At the outset of this section, the author called the reader's attention to the “interconnected ideal” pore of figure 18, referencing various steps labeled within. It should be noted that the two ways in which the Kelvin equation was expressed here, by equations 2.101 and 2.105, are equally applicable to all four pore configurations found in figures 18 and 19. In general, equation 2.101 applies to menisci having a tube-shaped surface, while equation 2.105 is applied to menisci having a hemispherical surface.

At this point, the author finds it necessary to make two comments on the use of equation 2.105, the first having to do with the contact angle θ_c . Aside from the fact that capillary pores are not generally [perfectly] circular in cross-section, the contact angle may not be zero as has historically been the assumption, and in the derivation of this equation. In fact, later [in section 2.3.3.3] the author will show how a non-zero contact angle may complicate the relationship between relative humidity and moisture content.

The second point the author would like to make is that there does exist a layer of adsorbed moisture that coats the inside of the capillary pore, causing the curvature of the meniscus to become increased. However, historically many have assumed that the thickness of the adsorbed layer is sufficiently trivial, and may be neglected altogether ($t_L \approx 0$). This simplification reduces the radial term to a constant pore radius r_x (see equation 2.102). However, within literature there are those who would strongly question the use of this simplifying assumption (Meyers 1991). In truth, given the scope of this investigation, where the author is primarily interested in large pore sizes of approximately 100 nanometers in radius (or larger), the assumption that the moisture layer is trivial has merit. A quick review of figure 11 (section 2.2.3.4), reveals that it is unlikely that a variation of a few nanometers will cause any significant change to the relative humidity. Conversely, such a variation may cause a large difference in the smallest of the capillary pores (outside the scope of this investigation). In the derivation of equation 2.105, the author did not assume to neglect the moisture layer primarily to acknowledge the fact that it does exist. However, should the reader wish to explore the effects of these two variables (θ_c and t_L), the author next provides a more general form of equation 2.105, as shown by equation 2.106

$$\ln\left(\frac{RH}{100\%}\right) - \ln(a_s) = \frac{-2\hat{V}_{sol}^L \gamma}{R_u T} \left(\frac{\cos \theta_c}{(r_x - t_L)}\right) \quad \text{Equation 2.106}$$

Notice that this form allows for a non-zero contact angle and includes an explicit variable for moisture layer thickness, t_L , which the reader may set to zero. The equation still assumes a circular cross-section of the capillary pore and a spherical meniscus.

2.3.3.3 Sorption isotherms: relative humidity – based

As was described in section 2.3.3.1, correlated relationships exist between the gained or lost moisture content of materials, like concrete, as a function of a relevant metric, at a given temperature. This kind of relationship is collectively termed a moisture sorption isotherm and may (or may not) be comprised of both moisture adsorption and desorption isotherms. Additionally, the moisture sorption isotherm may contain transitional scanning isotherms, which are explained further, later in this section. The moisture adsorption isotherm is the relationship that occurs as the material takes in moisture during a wetting phase. Conversely, the moisture desorption isotherm is the relationship that occurs as the material sheds moisture during a drying phase. It is assumed that such correlation relationships are developed under, and are applied to, equilibrium conditions (Newman and Choo 2003; ASTM Standard C1498 2004a (2010) e1).

The contained moisture, and the relevant metrics it is correlated to, may be expressed in different ways, as to fit a particular context. In section 2.3.3.1, the contained moisture was expressed as relative adsorption (V_A/V_M) and was correlated to be a function of the relative pressure (p_v/p_{sat}). In the context of explaining the BET equation, this form of expression fit. However, in the larger context of this investigation, the adsorption (and desorption) is not limited to just the adsorbed multilayer; consequently, the author intends to express the contained moisture in at least two ways. One way the reader shall see this relationship expressed, is by a **percentage of [liquid] saturation** S_L [%], as a function of relative humidity RH [%]; shown in figure 23. The percentage of saturation S_L expresses the amount of solution physically held (not chemically combined) within a material, with respect to the total storage capacity of that material. The reader is cautioned not to confuse the percentage of [liquid] saturation S_L with the percentage of [humidity] saturation S ; a psychrometry metric introduced in section 2.2.1. The other way the reader shall see this relationship expressed, is as a **moisture content** MC [%], that is to say the mass of the contained solution, as before, by mass of the dry specimen. The moisture content would also be a function of relative humidity, at a given temperature (not shown in a figure here).

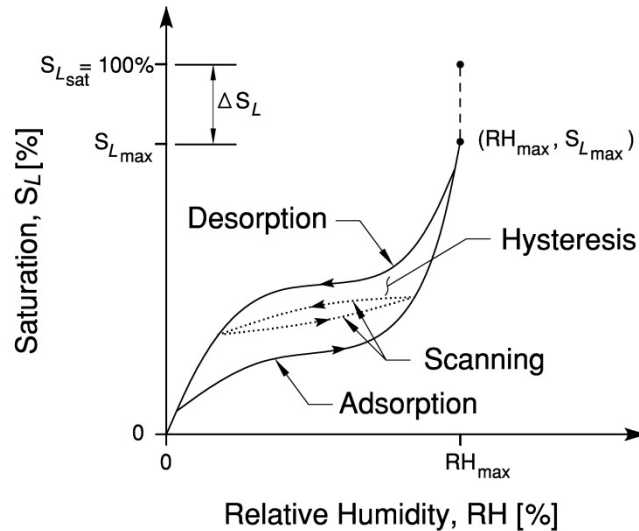


Figure 23: Representation of a moisture sorption isotherm

When plotted, these two relationships, the adsorption and desorption isotherms, may or may not align with each other. If they do not, when plotted a very noticeable **hysteresis** loop is revealed. As shown by figure 23, the adsorption and desorption isotherms are connected by **scanning isotherms**. Interestingly, these isotherms also tend to have a hysteresis loop. Like the adsorption and desorption isotherms, they are developed through experimental correlation. However, research efforts have been undertaken by others to develop ways to predict these particular isotherms (Espinosa and Franke 2006). Porous, cementitious materials like concrete are notorious for having an adsorption/desorption hysteresis. The explanation for this phenomenon is generally attributed to a superposition of a variety of sources, but ultimately it is the unknowable nuances of the material [physical and chemical] makeup that are to blame. The fact that a hysteresis is a part of the constitutive relationship between contained moisture and RH is important. This means that just knowing the RH (and temperature) at a given time is not enough information to determine contained moisture (i.e., moisture content or degree of saturation); additionally, one would need to also track the [wetting and drying] history of the material leading up to the RH (and temperature) of interest.

The most generally accepted sources for this hysteresis phenomenon include the general way a capillary pore fills and empties as it cycles through adsorption and desorption. A quick review of figure 18 (section 2.3.2.2), reveals that the “interconnected ideal” pore follows one path when wetting (steps I to IV), and another path when drying (steps IV to VII). Additionally, the existence of ink-bottle pores, of different sizes and capacities, tend to lower the relative humidity at which a pore may fill or empty, serving to further encourage the varying paths of the adsorption and desorption isotherms, as shown in both figures 18 and 19. It would seem that the only pore geometry unaffected by the adsorption/desorption cycles should be the “dead end ideal” pore of figure 19. However, as was alluded to in section 2.3.3.2, the assumption that the meniscus contact angle is

zero is incorrect. In fact, the contact angle of the meniscus of condensing moisture as it proceeds to fill the capillary pore during a wetting phase is different than the contact angle as the meniscus is receding, during a drying phase. This “*contact angle hysteresis*” is largely attributed to surface roughness of the material being wetted, which causes variations in the surface energy. As a liquid wets a surface, its leading edge gets hung-up in areas low surface energy; consequently, the proceeding contact angle is generally greater than the receding contact angle (Shaw 1998; Meyers 1991). By the Kelvin equation, these differences in the proceeding versus the receding contact angles are a direct source of hysteresis and generally affect all the pore geometry scenarios of figures 18 and 19 (Defay 1966; Meyers 1991; Lyklema 2001; Adamson and Gast 1997).

Before the author proceeds to the next section of this review, a few things should be noted. First, the name of such a relationship, “isotherm”, would imply that any given correlation relationship would apply only at a single temperature, thus requiring many isotherms to be developed to facilitate interpolation between them. In many cases, the effects of temperature variation on the isotherm are fairly negligible. Therefore, Newman and Choo observed that it is generally acceptable to view the moisture sorption isotherm as temperature invariant unless the temperature departure is extremely large or the results required are to be unusually exact (Newman and Choo 2003). Being in agreement with this rationale, the author of this investigation shall employ this simplification and produce only a single moisture isotherm. Second, as the reader may recall from section 2.2.3.3, the dissolved solutes in a solution will tend to reduce the equilibrium vapor pressure of the solvent. In turn, the maximum observable relative humidity at equilibrium is reduced. It is for this reason that the author has decided to use the more general RH_{max} term, instead of assuming total [water] vapor saturation ($RH = 100\%$); as this would imply that the pore moisture is [treated as] pure water. Lastly, based on insights gleaned from the previous sections of this review, the author has provided in figure 23 a change in the percentage of [liquid] saturation term ΔS_L ; not generally seen in a representation of a moisture sorption isotherm. The ΔS_L term expresses moisture saturation beyond the maximum percentage of saturation S_{Lmax} which is generally associated with the maximum relative humidity RH_{max} for a given pore solution. By this the author implies that there must be a [significant] volume of pore solution existing in the largest of the capillary pores and other void spaces which remains undetectable to a relative humidity – based moisture sorption isotherm.

2.4 METHODS OF RELATIVE HUMIDITY CALIBRATION AND MEASUREMENT

2.4.1 General

When selecting a method to measure relative humidity [in concrete] there are many considerations to explore. Additionally, it is often necessary to calibrate the method(s) ultimately used. The purpose here is to give the reader an abbreviated introduction to some existing technologies available for both measurement and calibration. The author has decided that organizationally it makes the most sense to present methods of

calibration prior to the methods of measurement, based on the dual functionality of certain calibration methods to also be used for measurement. The technologies and the abbreviated explanations presented, are based primarily on a more comprehensive text by Wiederhold, entitled “*Water vapor measurement: methods and instrumentation*” (Wiederhold 1997). At this point it should be reinforced that the purpose of this section is not to present a comprehensive overview of all the available technologies, nor provide an overly technical description of the technologies presented. The unveiling of the technologies employed in this investigation along with the rationale for their selection shall be discussed later in section 6.

2.4.2 Methods of Relative Humidity Calibration

2.4.2.1 Overview of calibration classifications and types

Methods of calibration are generally termed **calibration standards**, and are classified as being **primary standards**, **transfer standards** or **secondary devices**; each containing multiple system or device options and being based on a variety of scientific principles. The classification of a calibration standard is determined by whether or not the device or system operates by fundamental psychrometric (or hygrometric) principles, and if so, whether or not the base units of measure, corresponding to those principles, are used directly. In addition to classification, calibration methods are divided into two general types. The first type determines a measured value for the [relative] humidity of a given [sample] atmosphere. In principle, any calibration method of this first type could also serve as a method of measurement. However, for practical and economic reasons many are generally reserved for calibration use only. The second type of calibration standard produces an atmosphere of known [relative] humidity. These second types of standards are used for calibration purposes and in situations where an environment of known [relative] humidity needs to be produced/controlled for experimental purposes.

2.4.2.2 Primary standards

The most accurate of calibration standards are classified as primary standards. Primary standards directly use both fundamental principles and their corresponding base units of measure. The most accurate primary standard, being of the first type, is the **gravimetric hygrometer**. The gravimetric hygrometer separates and weighs the contained moisture from a sample of a gaseous mixture, obtaining a vapor mass m_v . Next, the gravimetric hygrometer accurately determines the volume of the remaining dry sample, facilitating a direct calculation of its dry mass m_{dry} . By equation 2.81 (of section 2.2.4.1), these two base values are used to calculate the absolute humidity (or mixing ratio), a fundamental parameter. Subsequently, the absolute humidity can be transformed into other parameters, including relative humidity. Gravimetric hygrometers, while of the highest accuracy, are complex, expensive, and generally only used by various national standards laboratories throughout the world to calibrate lesser [transfer] standards.

While not quite as accurate as the gravimetric hygrometer, there do exist less expensive and commercially available primary standards. Two of the most common are the **two-pressure** and **two-temperature** precision humidity generators. As the name suggests,

these standards are of the second type, generating an atmosphere of known relative humidity. The two-pressure generator works by saturating a gaseous mixture at a given pressure for fixed temperature. Once saturation has occurred, using gas law relationships, the pressure is reduced, thereby lowering the relative humidity to a desired level. Similarly, the two-temperature generator works by saturating a gaseous mixture, but at a fixed pressure for a given temperature. Once saturation has occurred, using gas law relationships, the temperature is increased, again reducing the relative humidity to a desired level.

2.4.2.3 Transfer standards

The next tier of calibration standards are classified as being transfer standards. The difference between transfer and primary standards involves the use of related units of measure, as opposed to relying directly upon the base units of measure; however, they still operate by fundamental principles. Additionally, transfer standards require occasional calibration by, and should be traceable to, a primary standard. The three most well-known are the **chilled mirror hygrometer**, the **dry/wet bulb psychrometer** and **saturated salt solutions**. The first two (chilled mirror and psychrometer) are of the first type, and may be used to determine relative humidity. The chilled mirror hygrometer works by lowering the temperature of a mirror in the vicinity of a gaseous sample. Provided that the sample contains humidity, at some point condensation will begin to form on the mirror. Condensation forms because the molecules of the gaseous mixture contract in the vicinity of the cooling mirror to such an extent that vapor saturation occurs ($p_v = p_{sat}$). The temperature at the onset of condensation is called the **dew-point temperature**. When combined with other known/measured parameters like the ambient pressure and the initial temperature (or dry-bulb temperature) of the gaseous mixture, then by fundamental relationships, the relative humidity may be determined. While the chilled mirror offers the greatest accuracy of all the transfer standards, it is still relatively expensive to purchase and operate, as it requires skilled operators, constant maintenance and periodic recalibration.

The dry/wet bulb psychrometer is a device that uses two temperature “bulbs”: one being covered by a wetted material, a wet-bulb, and the other left uncovered, a dry-bulb. The wet-bulb will generally produce a lower temperature than the dry-bulb. This is because as the moisture surrounding the wet-bulb evaporates, it takes heat with it. The efficiency of evaporation and thus the amount of heat removed is a function of the ambient relative humidity. If the atmosphere were completely saturated ($RH = 100\%$), then no evaporation would occur and the two bulbs would record the same temperature. The relationship between the wet and dry-bulb temperatures relies on the heat of vaporization, a fundamental relationship. Knowing both the dry and wet-bulb temperatures, combined with the measured ambient pressure parameter, the relative humidity may be determined by fundamental relationships. The fundamental relationships, which allow one to convert between properties like the dew-point temperature or the wet/dry-bulb temperatures and relative humidity, may be calculated; however, psychrometric charts, graphs and tables have been conveniently developed for this purpose.

The final transfer method described in this section is saturated salt solutions. Saturated salt solutions are of the second type, since they are used to generate environments of known relative humidity. This method involves choosing a salt (the solute) to dilute pure water (the solvent) to the point of saturation, at a given temperature. Salt added to the solvent beyond what is required for saturation will remain un-dissolved in the solution and does not affect the environment being generated. In fact, the application of more salt than is required for saturation is expected, to ensure that the solvent remains saturated at all times. Depending on the temperature and salt used, after a sufficient time has passed, different environments of known relative humidity can be generated in a sealed enclosure. Saturated salt solutions are listed among the transfer standards as the values generated by them rely on the fundamental principles governing the colligative properties of solvents, namely the equilibrium vapor pressure. As covered in section 2.2.3.3, by equation 2.18, a reduction to a solvent's saturation vapor pressure is proportional to its activity coefficient in solution, a_s . However, as was also covered in the same section, determining the activity coefficient for an ionic solution is not trivial and generally empirical in nature, especially if the ion concentration is high. In response to this need, a paper was written by Greenspan entitled "*humidity fixed points of binary saturated aqueous solutions*" (Greenspan 1977). In his paper Greenspan generates, from a variety of sources, a collection of saturated salt solutions along with the empirically derived relative humidity environments they will [always] generate, at specific temperatures. This paper eventually became the basis for the ASTM standard E104-02 entitled "standard practice for maintaining constant relative humidity by means of aqueous solutions" (ASTM Standard E104 2002 (2007)). This allows for environments generated by certain saturated salts, at certain temperatures, to be traceable back to a nationally recognized standard. This method of calibration is by far the most inexpensive method of generating an environment of known relative humidity. However, it does require that the user take special precautions to ensure the purity of all solution constituents, and that the temperature of the solution remains [relatively] constant through the duration of the procedure.

2.4.2.4 Secondary devices

The final tier of calibration standards are classified as secondary devices. These methods rely neither on fundamental psychrometric (or hygrometric) principles, nor their base units of measure. Rather, these devices rely on other scientific principles which are predictably affected by, and subsequently correlated to, varying levels of relative humidity. All the secondary devices that will be introduced are of the first type, in that they are used to determine relative humidity. While such devices may be used as a calibration tool, they are more likely to be used as a method of measurement in lab and field settings. It is for this reason that the author shall discontinue any further discussion of secondary devices here, and resume their discussion in the next section (section 2.4.3).

2.4.3 Methods of Relative Humidity Measurement

In the previous section (section 2.4.2) there were several primary and transfer calibration devices introduced, with the potential for being used as lab and/or field measurement devices. However, for practical and economic reasons they are generally reserved for the

calibration of lesser, secondary devices. Of the many secondary devices available to determine relative humidity, the author has decided to limit introductions to just three kinds: the **capacitive polymer sensor**, the **resistive polymer sensor** and the **fiber optic sensor**. Such devices operate by variety of other scientific principles. That is to say, for a given level of ambient relative humidity, based upon some non-psychrometric rationale, they produce a predictable, repeatable and unique response. This response is then correlated to that given level of ambient relative humidity. In reality, such devices are expected to operate over a range of ambient relative humidity, and so [single or multivariable] calibration functions are produced that best fit a range of corresponding responses.

The resistive polymer sensor operates by measuring resistivity levels between an anode and cathode lead, which have been embedded in a resin containing a conductive, polymerized salt. This resin/polymer composite is hygroscopic; that is to say it attracts and adsorbs (or desorbs) moisture from, and in response to, the atmosphere around it. As the atmospheric relative humidity increases, the sensor adsorbs an increasing amount of moisture, leading to increasing levels of conductivity. Consequently, as the conductivity increases between the leads, the resistivity decreases. This inverse relationship that exists between relative humidity and resistivity, for these devices, is then correlated and calibrated by the manufacturer.

Capacitive [thin film] polymer sensors operate by measuring capacitance levels between two conductor plates, separated by a thin film of non-conductive polymer insulation, a **dielectric** material. Dielectric materials, when inserted between capacitor plates, serve to decrease the [voltage] potential between them. By definition, as shown by equation 2.107, when the potential, V , is decreased, the capacitance, C , is increased, assuming the charge, Q , remains constant (Tipler and Mosca 2004).

$$C = \frac{Q}{V} \quad \text{Equation 2.107}$$

The extent to which the polymer can reduce the potential between the capacitor plates is quantified by the **dielectric constant**. The dielectric constant ϵ_c , is the ratio of the potential that would exist between the conductor plates without a dielectric material, V_o , over the potential with the dielectric material, V , as shown by equation 2.108.

$$\epsilon_c = \frac{V_o}{V} \quad \text{Equation 2.108}$$

Substituting equation 2.108 into 2.107 we arrive at an expression that directly indicates the relationship shared by capacitance and the dielectric constant, as all the other values in the expression are assumed constant (see equation 2.109).

$$C = \epsilon_c \frac{Q}{V_o} \quad \text{Equation 2.109}$$

The polymer selected will be hygroscopic and adsorb moisture in amounts that are unique for a given level of ambient relative humidity. As the polymer takes on moisture, the potential between the plates decreases; that is to say, the dielectric constant of the polymer increases along with the capacitance measured. The observed relationship between the capacitance and the ambient relative humidity is then correlated and calibrated for each sensor, by the manufacturer.

The final secondary device the author shall discuss is relatively newer than the other devices covered so far; it is the Fiber optic sensor. An input fiber optic line sends light through a porous, hygroscopic, composite [Fabry–Perot] filter with layers of medium having different initial refraction indexes. A **refraction index**, n_r , is defined as the ratio of the speed of light in a vacuum, c , over the speed with which light passes through a given medium, v , as shown by equation 2.110 (Tipler and Mosca 2004).

$$n_r = \frac{c}{v} \quad \text{Equation 2.110}$$

As the filter adsorbs (or desorbs) moisture from the ambient environment, the speed with which light passes through the various layers changes uniquely; subsequently, by definition, the various refractive indices are changed uniquely. As a consequence, the wavelength properties of the light become shifted. This occurs because the wavelength of light in a medium, λ_m , is related to the refraction index by the ratio of the wavelength of light in a vacuum, λ , over the refraction index, n_r , as shown by equation 2.111.

$$\lambda_m = \frac{\lambda}{n_r} \quad \text{Equation 2.111}$$

The shifted light is reflected back through an output fiber optic line and into a decoder, where the shift is analyzed and correlated to the ambient relative humidity. Again, more detailed information may be found in the book by Wiederhold, and the references contained therein.

While such secondary devices are relatively cheap and easy to operate, there are some drawbacks to their use. Since secondary devices are usually limited in various ways by the technology itself, the user needs to understand the operational limitations. Additionally, frequent recalibration may be required as time and/or changes to the environments in which they are operating may alter the accuracy of any existing calibration, even if they come pre-calibrated by the manufacturer. It is important that any calibration methods used be traceable to a recognized [primary or transfer] standard. Finally, in general, secondary devices are not as accurate over large ranges of relative humidity and other operating conditions (i.e., temperature), as a primary or transfer standard may be. Therefore, if the user requires high accuracy, a calibration may need to be produced over a more specific range of operating conditions. Again, the purpose here is to simply provide a very general introduction to possible kinds of technologies available. For more detailed information, the reader is encouraged to review the text this

information is based upon, and of course any technical [proprietary] information that may be provided by the manufacturer for any specific technology being considered.

2.5 ISSUES AND CONCERNS

Many of the critical equations and concepts either derived and/or presented to this point have been generally accompanied by some further discussion, including issues and concerns pertaining to their limits of applicability and any major assumptions or simplifications made. Therefore, the author does not intend to use this section to restate the things formerly addressed. Rather, the author shall use this section to highlight some of the key issues and concerns associated with using relative humidity-based moisture sorption isotherms to track moisture content levels inside concrete that is exposed to natural weathering. In particular, the author would like to consider the expressed issues and concerns resulting from the experimental efforts of two separate groups of authors.

The first group was led by Dr. Andrade of the Eduardo Torroja Institute of Construction Science, in Madrid, Spain. The details and findings of the experiment of interest were published in a paper entitled “*relative humidity in the interior of concrete exposed to natural and artificial weathering*” (Andrade, Sarria, and Alonso 1999). In this paper, Andrade experimentally tracks the internal relative humidity [and temperature] responses of a set of cylindrical concrete specimens exposed to a variety of natural and artificially produced weathering conditions. While the reader is encouraged to review the entire paper independently, the author would like to call attention to two observations made by Andrade.

First, Andrade observed that, when exposed to [naturally] evolving external temperatures, the specimens experienced constantly evolving internal temperatures. As temperature is a parameter affecting relative humidity, this too was observed to be constantly evolving. The problem is the apparent lag occurring between the evolution of the [measured] internal temperature and the [measured] internal relative humidity. This lag, according to Andrade, would in theory preclude the accurate application of a traditional relative humidity-based moisture sorption isotherm to accurately determine moisture content. This is because moisture sorption isotherms are developed under equilibrium conditions. That is to say, under conditions where the external temperature is fixed, leading to an unchanging internal temperature. Additionally, the external relative humidity is also fixed leading to an unchanging internal relative humidity and a stable internal moisture level; therefore such a lag would not exist.

In addition to the internal relative humidity being unable to stabilize in-step with changing internal temperature variations, it has also been commented on in other literature sources that the apparent observed lag between the evolving internal relative humidity and internal temperature is also in-part the result of a temperature phase difference between the concrete and the sensor. This difference becomes more pronounced with increasing rates of internal temperature change. In a thermally static environment, the temperature of the sensor would equilibrate to the temperature of the concrete. However, in a thermally dynamic environment such is not the case; leading to inaccuracies on the order of approximately $-5\% RH/^{\circ}C$ (Newman and Choo 2003).

Another observation by Andrade was a “sudden increase” to the internal relative humidity of specimens exposed to direct (uncovered) contact with natural rain, which was attributed to a significant diffusion of moisture of both the liquid and vapor phases. Subsequently, after the rain stopped, a drying out occurred and the internal relative humidity of the specimens quickly returned to pre-rain levels. While, it was assumed that all diffused vapor moisture later evacuated the concrete without condensing, the same could not be said of the diffused liquid moisture. Though most of the liquid moisture may have evaporated, Andrade explains that it is inevitable that some fraction of the diffused liquid moisture remains. The implication is that concrete systems exposed to periodic rain/drying events are constantly experiencing changes to their levels of condensed moisture. Since moisture sorption isotherms, as previously stated, are developed under equilibrium conditions, including static moisture levels, dynamically changing moisture levels would also serve to preclude the accurate application of a traditional moisture sorption isotherm. It is for these reasons that Andrade has concluded that traditional relative humidity-based moisture sorption isotherms are incompatible for use with concrete systems exposed to natural weathering. However, Andrade does suggest that if one still wishes to proceed with using a correlated relationship between relative humidity and moisture content, then the errors associated with such a dynamic system would need to be accounted for, perhaps through the use of a numerical model.

Messrs. White and Kunin, both engineers with the Transportation Research & Development Bureau (TR&DB) of the New York State Department of Transportation (NYSDOT), are the second group to be considered. White and Kunin produced a report (No. C06-04) entitled “*Bridge Deck Wearing Surfaces*” (White II and Kunin 2010). The original intent of their investigation was to use relative humidity sensor technology to determine the water-tightness of various highway bridge deck overlay systems. The idea was to embed multiple relative humidity sensors throughout the thickness of the deck and collect internal relative humidity data from which a base line moisture content profile could be generated. Then over time, using the same embedded sensors, the internal relative humidity and corresponding moisture content profile could be tracked and analyzed for changes that may indicate whether or not an overlay system is leaking. It should be noted that the sensors would be placed and sealed in holes drilled into the deck from the underside, to depths of no less than 1 inch from the deck’s top surface.

Though initial laboratory testing indicated that using relative humidity sensors in this way may be viable, actual field implementation yielded unexpected results. All the sensors, once placed in the aged concrete deck, immediately logged internal relative humidity values at or near 100 percent continuously. The sensors, when occasionally pulled and checked, showed significant signs of moisture condensation. Similar field results were again seen in a second bridge. These results led White and Kunin to conclude that determination and tracking of moisture content inside bridge decks of advanced age and weathering (at the depths being measured) by measurement of the internal relative humidity was not a viable option.

The report produced by White and Kunin, provides only abbreviated details pertaining to the experimental method and set-up used. Also they did not include a discussion about how they intended to overcome the issues and concerns raised by Andrade, had their attempt to track internal relative humidity gone as originally intended. Finally, there is almost no [scientific] explanation for the observed internal relative humidity, other than a statement acknowledging the advanced maturity/moisture of the bridge deck of interest, followed by the observation that the closed cavities, produced for the sensor placement, seemed to “attract internal moisture”. However, the take-away concern for the author from this report is the possibility that in [mature] highway bridge decks, at the depths which are most likely to contain reinforcement, moisture levels sufficient to preclude the usefulness of internal relative humidity sensors for determining moisture levels may exist. A primary need for determining relative humidity, and subsequently quantifying moisture, is to better understand moisture related deterioration mechanisms, especially those directly affecting reinforcement.

3. BACKGROUND

Within the context of this investigation, when attempting to generate the moisture profiles of concrete highway bridge decks, conceptually, one would start by obtaining internal relative humidity (and temperature) data from the deck of interest using embedded sensors placed at various vertical depth locations. Subsequently, that data would then pass through a correlation algorithm, to produce discrete moisture content values that can be collectively used to generate a moisture content profile of the vertical cross-section. Perhaps the most critical component to this method of moisture profile determination is the correlation algorithm used. Consequently, central to this investigation is the apparent correlation between relative humidity and moisture content, as described in the literature review; specifically, the relative humidity–based moisture sorption isotherm (or moisture sorption isotherm).

The reason the author has chosen to describe the moisture sorption isotherm correlation as being apparent in the paragraph above is due to the realization that the relative humidity in a concrete system does not actually share a singular and direct relationship to moisture content. Aside from moisture content, there are many other variables contributing to the relative humidity within the concrete system. As the reader may recall, the chemistry (and to some extent temperature) of a pore solution affects its equilibrium vapor pressure, and consequently the maximum relative humidity achievable by the solution in a closed system having zero meniscus curvature, at a given temperature. Increasing moisture content tends to dilute the pore solution, which leads to increased internal relative humidity values; the converse occurs as the moisture content is reduced. Also, an increase of meniscus curvature reduces the solution’s equilibrium vapor pressure, which generally tends to suppress the observed relative humidity. However, in relevant mathematical relationships like the Kelvin and BET equations, the meniscus curvature is generally expressed in terms of cross-sectional radius, thus relating

internal relative humidity to, among other variables, the pore radii. By these equations, it has been shown that, typically, only pores having a mean cross-sectional radius of less than approximately 100 nanometers will effect practical changes to the internal relative humidity.

The reason relative humidity in concrete appears to share a constitutive relationship with contained moisture levels is due primarily to moisture transport and condensation phenomena. Based on fundamental thermodynamic laws, it is generally assumed that diffused [water] vapor condenses in the smallest of the pores first, as these pores would initially contain the lowest chemical potential. Subsequently, the progressively larger pores would then fill, though the existence of ink-bottle pores does affect this ideal process to some extent. As the pores progressively fill, the meniscus curvature becomes progressively reduced, thereby leading to increased internal relative humidity values up to the observable maximum relative humidity achievable by the solution for a given temperature. Likewise, the converse is assumed to occur during periods of moisture content loss. If there were no predictable order to how a capillary system fills or empties, then a uniquely repeatable correlation would not be possible. From this point forward the author shall refrain from describing the moisture sorption isotherm correlation as being apparent, though the reader should keep in mind the true nature of this relationship.

4. PURPOSE

4.1 OBJECTIVE

Per the title, the overarching purpose of this investigation is to “*investigate the viability of using relative humidity-based moisture sorption isotherms to generate moisture content profiles of concrete highway bridge decks*”. However, based on the literature review, there do appear to be at least two potential barriers to its viability: a limited range of detectable moisture content using relative humidity methods and the theoretical incompatibility of moisture sorption isotherms within non-equilibrium systems. The latter is a limitation well understood in literature to exist and is perhaps the most serious potential barrier. From the literature review, it is clear that for many cementitious systems exposed to constantly evolving ambient conditions, the moisture sorption isotherm is unlikely to be a viable correlation option for determining and tracking moisture content. Regardless, as the literature reviewed did not satisfactorily explore systems within the scope of this investigation, it is the objective of the experimental portion of this investigation to test two scope-specific hypotheses posed by the author. Then based on the findings, the author will be able to offer a more conclusive response in regard to whether or not moisture sorption isotherms are viable to generate moisture content profiles in the context of concrete highway bridge decks.

4.2 HYPOTHESES

4.2.1 Hypothesis I: Non-Trivial, Undetectable Moisture Content

It is this author's first hypothesis that *in a concrete highway bridge deck of typical construction, there exists the potential for a non-trivial level of moisture content for which no unique correlation to relative humidity may be made*. This results in a potentially high level of moisture content that would be undetectable by a relative humidity-based moisture sorption isotherm. There exists a maximum percentage of saturation, S_{Lmax} , that is associated with the maximum relative humidity, RH_{max} , for a given pore solution (see figure 23 in section 2.3.3.2). The maximum percentage of saturation is essentially defined by the relative volume of capillary pores having a mean cross-sectional radius no larger than approximately 100 nanometers, though the existence of ink-bottle pores will undoubtedly serve to obscure this definition slightly. The reader may recall that this approximate delineation of pore size may be observed theoretically by plotting the Kelvin equation and has been experimentally validated by others, but has not been determined independently by this author. The potentially undetectable moisture content is expressed by the author as the ΔS_L term of figure 23, wherein moisture exists in capillary pores and other void spaces of mean cross-sectional radius larger than the approximately delineated 100 nanometers. Once the observed internal relative humidity is equal to the maximum relative humidity, RH_{max} , the moisture sorption isotherm is no longer capable of indicating additional moisture content. That is to say, moisture content in excess of S_{Lmax} cannot be uniquely correlated to relative humidity. Consequently, if this excess undetectable potential moisture, ΔS_L , is of a non-trivial magnitude, then the maximum percentage of saturation, S_{Lmax} , should not be assumed to be approximately equal to the saturated moisture content, S_{Lsat} . If this hypothesis is determined to be valid, then this finding would only preclude the moisture sorption isotherm as a viable correlation method for a cross-section of bridges having observed internal relative humidity equal to the maximum observable value, RH_{max} .

4.2.2 Hypothesis II: System Compatibility Assumption

Relative humidity-based moisture sorption isotherms are created by plotting the range of moisture contents of a representative sample versus the corresponding observed [internal] relative humidity values for a given temperature. The sample must reach static thermal and moisture equilibrium with the controlled environment surrounding it for each moisture increment. Because moisture sorption isotherms are created in this way, it is generally understood that they provide inaccurate results when applied to systems of non-equilibrium; that is, systems of evolving moisture content and temperature. According to Dr. Andrade (see section 2.5), to overcome the dynamic limitations of the traditional moisture sorption isotherm, a “numerical” model would be critical to account for all the “different fluxes” (Andrade, Sarria, and Alonso 1999). That being said, though in theory

one should be able to create a model (experimentally or analytically) that would account for dynamic behavior, this author did not uncover such a model during the literature review.

It is this author's second hypothesis that *within a concrete highway bridge deck of typical construction, at depths generally associated with the placement of reinforcement, static thermal and moisture equilibrium may be assumed*. This hypothesis is based on the idea that at a sufficient depth, concrete highway bridge deck systems are both sufficiently large and closed such that dynamically evolving thermal and moisture gradients caused by exposure to natural weathering cycles become substantially attenuated. At this time the author would like to qualify the term "large" to mean that, compared to their thickness, bridge decks are very wide and long. This difference in relative geometry would in theory effectively eliminate, for most internal locations, lateral thermal flux contributions; this would reduce the system to a one-dimensional thermal flux problem. Consequently, while the thermal effusivity is an unchanging property of the material, the observable rates of temperature change would become noticeably attenuated or reduced. Consequently, the system is able to approximately stabilize in-step with evolving conditions, allowing for an approximate compatibility to exist between the moisture sorption isotherm and the exposed system. The validation of such an assumption is critical to this investigation's purpose, as there were at least three different ways identified in the literature review in which errors are introduced as a result of system non-compatibility. If this assumption is not validated, then [traditional] moisture sorption isotherms would not be a viable option in the determination of moisture content profiles for any concrete highway bridge deck system exposed to typical natural weathering conditions.

The first two potential sources of error are associated with evolving internal temperatures. As the temperature inside the system evolves, through conduction, the solution's temperature evolves; in turn, through convection, the temperature inside the cavity formed by the sensor housing is also evolving. Consequently, the observable equilibrium vapor pressure of the system is no longer at equilibrium, and, therefore, the internal relative humidity lags behind the evolving thermal conditions. If the system's temperature does not stop evolving long enough for equilibrium to occur, then any observed relative humidity value will either be too high or too low, depending on the direction of the thermal evolution.

The second potential source of error surfaces when there is thermal non-equilibrium between the sensor and the system being observed by the sensor. As was just stated, through conduction the system thermally evolves; in turn, through convection the temperature in the cavity around the sensor evolves. It is only after the gaseous environment starts to evolve thermally that the temperature of the sensor itself starts to evolve. Given enough time, a thermal equilibrium between the sensor and the system

may be achieved; if not, it is estimated that thermal differences may cause errors on the order of approximately $-5\% RH/^{\circ}C$ (section 2.5).

The third source of error is associated with evolving internal moisture. As a system takes on or loses moisture, solution concentration and meniscus curvature are altered, which lead to changes in the solution's equilibrium vapor pressure and ultimately the internal relative humidity. In turn, the solution tends towards re-establishing equilibrium with the gaseous phase in the cavity created by the sensor housing. If the system is not able to stabilize in-step with evolving moisture conditions, the internal relative humidity will lag behind the evolving system and will be either too high or too low, depending on the direction of moisture evolution.

However, concrete bridge decks are extraordinarily larger than the concrete cylinders or prisms historically used to validate the non-compatibility of moisture sorption isotherms with systems exposed to natural weathering. As noted earlier "larger" is intended to mean that, compared to their thickness, bridge decks are very wide and long. This difference in relative geometry would in theory effectively eliminate, for most internal locations, lateral thermal flux contributions. Consequently, while the thermal effusivity is an unchanging property of the material, the observable rates of temperature change would become noticeably attenuated or reduced. Additionally, for concrete decks fabricated by typical batching and construction methods, at the depths generally associated with the placement of reinforcement, the internal (water) vapor is essentially disconnected from external sources (see section 2.3.2). At such depths, vapor diffusion is the primary transport process, which occurs extremely slowly by comparison to time scales associated with system equilibration. Consequently, it is this author's opinion that this second hypothesis has merit, and should be explored experimentally.

5. SCOPE

As stated previously, the overarching purpose of this investigation is to determine the viability of using moisture sorption isotherms to generate the moisture content profiles of concrete highway bridge decks. The author, having identified likely obstacles to their viability as correlation options, has developed two system-specific hypotheses (see section 4.2), which merit further exploration prior to offering any conclusions. Consequently, the scope of this investigation shall be *limited to the experimental testing of these two hypotheses*. This investigation does not expect to shift the currently understood paradigm in a general sense; the author does hope to uncover system-specific insights, which under the best of outcomes, may allow for system-specific exceptions.

6. METHODOLOGY

6.1 METHODOLOGY – TESTING SYSTEM COMPATIBILITY ASSUMPTION

As was stated in section 4.2.2, the author hypothesized that “*within a concrete highway bridge deck, of typical construction, at depths generally associated with the placement of reinforcement, static thermal and moisture equilibrium may be assumed.*” To test this hypothesis, the author shall employ two methods. The first method attempted will be to generate two moisture content profiles, each belonging to the same steel-reinforced concrete specimen. The first profile shall be generated by moisture sorption isotherms using internal relative humidity and temperature data collected from the specimen while it is exposed to evolving (diurnal) thermal and moisture conditions. A corresponding profile shall be generated gravimetrically. System compatibility may then be determined by direct comparison of the two profiles generated. It should be noted that, based on the literature review, there is a possibility that observed internal relative humidity values may equal the maximum relative humidity, RH_{max} , of the pore solution. Based on the author’s first hypothesis (see section 4.2.1), such an outcome may preclude the production of a relative humidity-based moisture profile for the specimen, and not permit a direct comparison of profiles. Therefore, should this scenario arise, an effort shall be made to reduce the internal moisture content artificially, while still maintaining diurnal thermal conditions. This should be acceptable, as even under induced drying conditions the concrete deck system will still experience moisture evolution and changing thermal cycles.

The second method to test the hypothesis is data interpretation. At depths generally associated with the placement of reinforcement, relative to the time scale needed for system equilibrium to occur, it is reasonable to assume that moisture evolution occurs very slowly. Therefore, it is also reasonable to assume that moisture content would remain fairly constant over the period of a diurnal cycle. Thus, any large variations in the observed internal relative humidity occurring within a diurnal cycle should be attributable to thermal lag effects. That being said, an internal relative humidity data stream that remains fairly unchanged throughout the course of a day is an indication of [approximate] system equilibrium, and thus system compatibility. It should be noted that while large variations would indicate system non-equilibrium, some very slight variation would be expected, as temperature change will theoretically affect the solution’s equilibrium vapor pressure and subsequently the internal relative humidity. Therefore, the author shall examine the collected internal relative humidity data leading up to the creation of the two moisture profiles to assess system equilibrium and thus compatibility in this way.

Before the author goes on to further outline the methodology, a couple of other considerations should be addressed here. First, as the hypothesis is largely system-specific and relies on large relative size (as described in section 4.2.2) and closed system assumptions, it is essential that the specimen used in this experiment be truly representative. Second, it is understood that thermal differences between the specimen and the relative humidity sensor are likely to introduce error. Therefore, an effort to

reduce and quantify any thermal differences shall be made so that, if necessary, corrections can be made.

The *means and methods* section (i.e. section 7) of this investigation shall discuss the specifics of the set-up along with any pertinent rationale. However, here the author shall outline the general sequence of actions to be performed to employ the methodology as described above. The general sequence is as follows:

1. Select appropriate relative humidity and temperature sensors, along with a compatible data acquisition system.
2. Check calibration of sensors over the desired range of operating conditions and, if necessary, recalibrate the sensors.
3. Obtain a representative concrete highway bridge deck specimen.
4. Install the relative humidity and temperature (RH&T and thermocouple) sensor probes in the representative specimen.
5. Monitor and collect sensor probe data over a period of several months.
6. At the conclusion of data monitoring and collection, take several [full] core samples from the representative specimen.
7. Prepare the core samples for moisture sorption isotherm creation. Preparation includes: slicing the cores into disc specimens, drilling holes into the specimens, followed by the placement of RH&T probes inside the holes created. During the process of specimen preparation, accounting for mass change is critical.
8. Create moisture sorption isotherms for each disc specimen.
9. Create gravimetric and moisture sorption isotherm based in-situ moisture content profiles. Internal RH, temperature and mass data collected up to this point shall facilitate these calculations.
10. Create additional profiles for use as tools of analysis. Such profiles would include:
 - a. A profile based on vacuum saturated specimen masses
 - b. A profile based on the masses of specimens at equilibrium with a near saturated RH environment.
 - c. Profiles expressed in terms of degree of saturation, as opposed to being expressed in terms of moisture content.
 - d. A concrete [dry] density profile.
11. Compare and analyze the created profiles.
12. Analyze the collected internal relative humidity and temperature data stream, obtained in step 5 of the sequence, for signs of system thermal lagging, which would be evident by large diurnal variations of the internal relative humidity.

6.2 METHODOLOGY – NON-TRIVIAL, UNDETECTABLE MOISTURE CONTENT

As was stated in section 4.2.1, the author also hypothesized that *“in a concrete highway bridge deck of typical construction, there exists the potential for a non-trivial level of moisture content for which no unique correlation to relative humidity may be made.”*

This hypothesis shall be tested by attempting to experimentally quantify potential moisture capacity in excess of that which may be uniquely identifiable by relative humidity correlation; the following methodology shall be employed. First, the moisture content of representative concrete specimens shall be assessed while at equilibrium with near-saturated ambient conditions. Then, the same specimens shall be placed in a saturation chamber under vacuum pressure to fill any remaining porosity with water. The moisture contents resulting from these two processes shall then be compared. The testing of this hypothesis is to be performed in unison with the creation of the moisture sorption isotherms of the previous test (see section 6.1). The general sequence of this test is as follows:

1. Determine the masses of the disc-shaped concrete samples, while they are at equilibrium with a near-saturated ambient environment. This data shall be obtained during the early phases of step 8, of the previous sections testing sequence (see section 6.1).
2. Prior to drying out the disc-shaped concrete samples, the final step in creating a moisture sorption isotherm, vacuum saturate the specimens with water and determine the masses.
3. Compare the masses obtained in steps 1 and 2 of this section.

7. MATERIALS AND METHODS

7.1 MULTI-SENSOR DATA ACQUISITION SYSTEM

7.1.1 Overview

The first step in the methodology, as outlined in section 6.1, is the selection of an appropriate multi-sensor data acquisition system (DAQ). In general, the multi-sensor DAQ system required for the purposes of this investigation shall be comprised of relative humidity sensors, two kinds of temperature sensors, two kinds of multiplexers and a data-logger. This system would also require primary and back-up power sources; additionally, the system would allow access to sensor programming, data downloads and general operational monitoring. When selecting sensors, it is important that they are functional over the anticipated operational range of environmental conditions and that they meet the constraints imposed by the project's scope. Additionally, the sensors must be compatible with the rest of the DAQ system, that is to say, the multiplexers and data-logger. In turn, the multiplexers and data-logger should also meet the constraints imposed by the

project's scope. Finally, one must also balance the system's overall performance and achievable data quality with economy.

7.1.2 Sensors Selected

Three pieces of data to be collected from the representative bridge deck specimen as part of this investigation are its internal relative humidity (RH_{Int}), internal air temperature (T_{Int}) and internal surface temperature (T_s). The first sensor selected is actually two sensors in one, and will collect both the internal relative humidity and internal *air* temperature data; this sensor, as shown in figure 24, is the SHT75-V4 (V4 refers to version 4 of the SHT75) humidity & temperature (RH & T) sensor, by SENSIRION AG, a Switzerland-based sensor manufacturer. While more comprehensive technical documentation may be found at the SENSIRION AG website (www.sensirion.com), the author shall highlight some of the key features outlined in the version 4.3-May 2010 data sheet (Sensirion 2010). The part of the sensor responsible for detecting relative humidity is capacitive polymer-based. According the manufacturer, the SHT75-V4 comes pre-calibrated, traceable to a NIST standard, with an operating range of 0 to 100% RH; also, the manufacturer claims a maximum RH-accuracy of $\pm 1.8\% RH$ between 10 to 90% RH at 25°C. Above or below this operating range, the accuracy varies linearly up to $\pm 4.0\% RH$; also, the literature indicates a hysteresis of $\pm 1\% RH$. When detecting changes in RH, the time constant ($\mu = 63\%$) is 8 seconds, and therefore requires a total response time of approximately 24 seconds. Additionally, there are some operational and handling warnings provided in the technical literature which shall be highlighted in the discussion of sensor calibration (section 7.2). It should be noted that the calibrated output signal does need to be converted to an RH value by the manufacturers provided formula, which shall also be discussed further in the sensor calibration section, as well as in the DAQ programming section (section 7.1.4).

The part of the sensor responsible for temperature measurement uses bandgap PTAT (Proportional to Absolute Temperature) technology. While the reader should consult with the technical data for a more detailed description of the temperature error, for the operational range of -10 to $60^\circ C$ the manufacturers estimated maximum error is approximately $\pm 0.8^\circ C$, with a minimum error of $\pm 0.3^\circ C$ at $25^\circ C$. It was noted in section 2.5, by Dr. Andrade, that one should be concerned with temperature lag between the sensor and the concrete; consequently the thermal resistance of the sensor should be known. While the manufacturer does not supply a dimensionless Biot Number, they do indicate that, when detecting changes in temperature, the time constant ($\mu = 63\%$) is between 5 and 30 seconds, and therefore would require a total response time of approximately 15 to 90 seconds. In the context of this investigation, this may be considered a relatively instant response time. A key feature of this sensor is that the output data, for relative humidity and temperature, is converted from analog to digital internally, which precludes bias induced by lead resistance. Also, the sensors use a 4-pin system (SCK, VDD, GND and Data), making them pluggable and consequently easily interchangeable.

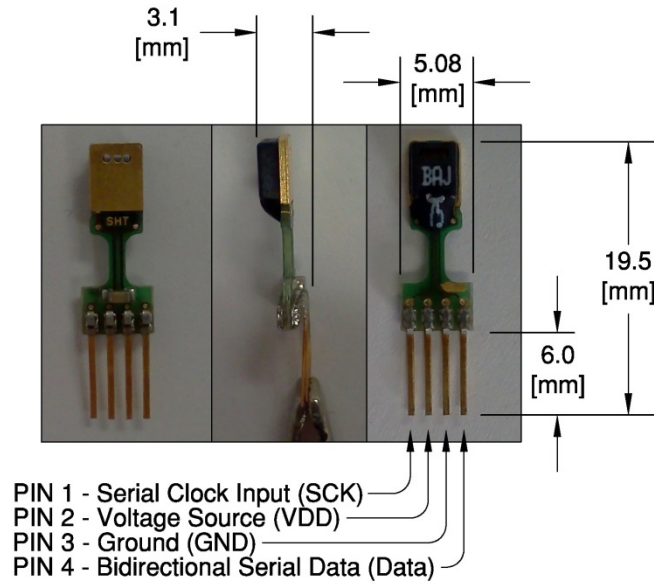


Figure 24: SHT75-V4 relative humidity and temperature sensor with envelope dimensions

To measure the internal *surface* temperature of the concrete, at the approximate location of the SHT75-V4 RH&T sensor, the author shall employ 24-AWG (solid), PFA Polymer insulated, type T (copper-constantan), high performance thermocouple (TC) wire. The particular thermocouple wire selected (Part No. TT-T-24-SLE) was supplied by OMEGA[®] Engineering, Inc., a global company with an office in Stamford, CT. This particular TC wire has special limits of error (SLE) on its accuracy. The special limits of error on this wire include an error range of $\pm 0.5^{\circ}\text{C}$ or 0.4% (whichever is greater) over the temperature range of 0 to 350°C (32 to 662°F); this and other technical data may be found on the company's web site (www.omega.com). It should be noted that prior to shipping the TC wire, the manufacturer tested and labeled it to indicate a deviation of -0.3°F at 212°F .

7.1.3 Multiplexer and Data-Logger Selections

The requirements of the multiplexer and data logger, in addition to sensor compatibility, are their applicability to non-lab environments. They should be durable for long-term exposure to dynamic climatic and physical conditions. In field applications, one could expect a climate envelope to include temperature variations from -20°F to 160°F (-29°C to 71°C), Relative humidity up to 100% with potential for occasional liquid moisture contact (rain, condensation, vehicular splashing, etc.). Dynamic physical conditions would include vibrations and deflection of the structure under vehicular loading and weather phenomena. Looking ahead to future applications, the system should be easily integrated into a broader portfolio of bridge monitoring technologies. Additionally, to allow for practical access to data when placed in remote locations the system and its stored data should be web accessible via a modem/router. Web

accessibility and technology integration are also decisive parameters when determining how scalable the technology is.

As shown in figure 25, the multiplexers selected for this investigation are the AM16/32B Relay Multiplexer and the AM25T Solid State Multiplexer. The AM16/32B is the multiplexer that shall be dedicated to the control of the SHT75-V4 RH&T sensors. The AM16/32B is able to manage up to (16) SHT75-V4 RH&T sensors. Operational temperature ranges from -25°C to 50°C and has an operational relative humidity range of 0 to 95% RH, non-condensing. The AM25T was chosen for two reasons. First, the author wanted to eliminate the complication of using mixed sensor types on a single AM16/32B. Second, the AM25T is a multiplexer designed specifically to control a wide range of thermocouple types. In order to operate a thermocouple sensor, a reference temperature detector (RTD), also known as a thermistor, is required. Unlike the AM16/32B, the AM25T has a built in RTD. The AM25T is capable of controlling up to (25) thermocouple sensors. Its operational temperature range is from -40°C to 85°C with an RTD accuracy of $\pm 0.4^{\circ}\text{C}$ and has an operational relative humidity range of 0 to 95% RH, non-condensing. Both of these multiplexers are products of Campbell Scientific[®], Inc., a measurement and control device company based in Logan, Utah, USA. Additional technical specifications and operation manuals may be obtained online from the company's website (www.campbellsci.com). At the time of this investigation, the revisions of the instruction manual's entitled "*AM16/32B Relay Multiplexer*" and "*AM25T Solid State Multiplexer*" were revisions 1/09 and 1/10 respectively (CSI 2009; CSI 2010a).

The data-logger selected is the CR1000, also a product of Campbell Scientific[®]. Its operational temperature range is from -25°C to 50°C and should be located in non-condensing environment. The function of the data-logger is to execute programming needed to coordinate sensor functions, by way of the multiplexers, then collect and store the resulting sensor data for later retrieval. The CR1000 comes equipped with expandable memory for program and data storage. For direct communication between the CR1000 and a PC, RS-232 and 9-pin CS I/O ports are standard. Additionally, for communication over an IP network (i.e. an internet connection), a single peripheral port is available; however, additional hardware would be required for this functionality. To facilitate the set-up and management of programs and data collection, Campbell Scientific[®], Inc. offers multiple software packages including: PC200W, PC400 and LoggerNet. LoggerNet (Version 4.1) was the software package selected for this investigation. In addition to an internal back-up power source, the CR1000, and by extension the entire DAQ is powered by the PS100, a 12-Vdc 7-Ahr sealed rechargeable battery; the PS100 is itself continuously charged by a wall charger AC power source (#9591). Though not used in this investigation, solar panels could have been used to maintain the charge of the PS100. The PS100 and the wall charger are also products of Campbell Scientific[®]. At the time of this investigation, the revision of the operator's manual available entitled "*CR1000 Measurement and Control System*" was revision 10/10 (CSI 2010b).

To avoid the direct contact of liquid water with the DAQ system, the system shall be housed in a weather-tight enclosure. For this investigation a Campbell Scientific[®], Inc. enclosure, model ENC 12/14 was selected. Additionally, desiccant [bags] should be placed inside the enclosure (though not shown in figure 25) to prevent condensation. As before, additional technical specifications and operation manuals may be obtained online from the company's website (www.campbellsci.com).

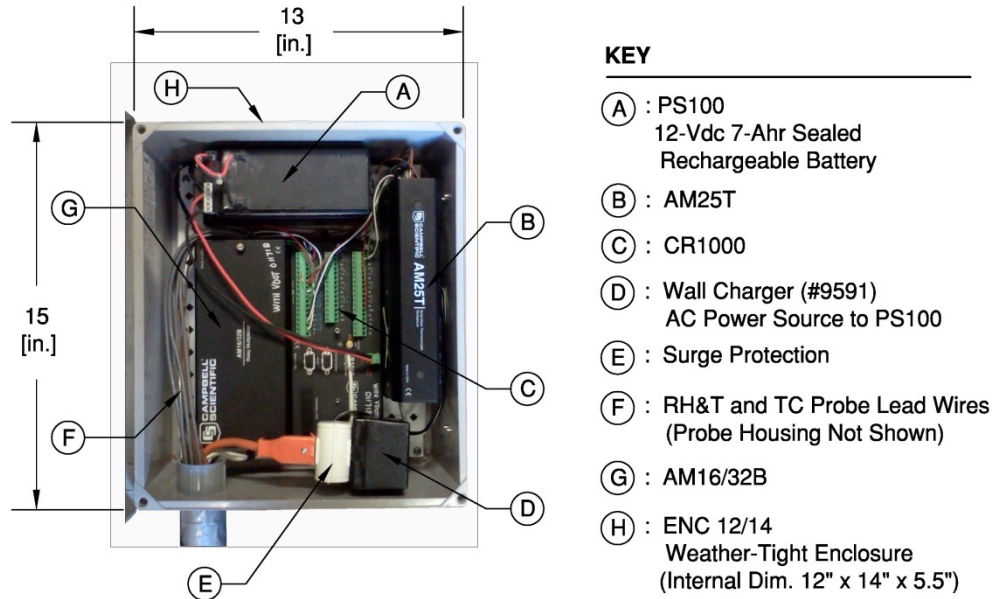


Figure 25: Data acquisition system (DAQ) assembly (complete probes not shown).

7.1.4 DAQ Programming

Custom code was purchased from Campbell Scientific[®] specifically to run the SHT75-V4 RH&T sensor in conjunction with the CR1000 Data-logger and AM16/32B multiplexer; this code was written such that up to two AM16/32B multiplexers could be accommodated (32 RH&T sensors total). It should be noted that the CR1000 uses a programming language called CRBasic, developed by Campbell Scientific[®]. Due to the proprietary nature of this purchased code, it shall not be disseminated in this document. However, a representative of Campbell Scientific[®] can assist anyone looking to purchase this code for their applications. Additionally, as some of the wiring is specific to this proprietary code, the author is shall not to include wiring schematics either. When purchased, within the code's initial commenting, clear wiring instructions are provided.

Pertaining to the signal output conversion formulas used in the code, a couple of things should be highlighted. First, the program creators compensate for temperature increases caused by invoking the sensor's onboard heating element. Second, the manufacturer of the RH&T sensor provides two signal output conversion formulas for relative humidity: one of the formulas compensates for significant temperature departures from 25°C, while the other does not. The purchased code makes use of the formula that offers no temperature compensation; however, this may be modified by the user in the program.

For the purposes of this investigation, the author has decided not to modify the formula directly. Any required calibration or compensation shall be handled with a sensor-specific calibration function developed and applied separately (see section 7.2).

Though the CR1000 is capable of storing multiple programs, it may only run one program at a time. Consequently, a master program that encapsulates the sub-programs necessary to operate all needed sensor types was required. Therefore, starting with the purchased code, used to operate the RH&T sensors, additional code needed to run the type-T thermocouple sensors was created and included. A sub-program of the LoggerNet (Version 4.1) package, called Short Cut, is capable of building basic programs, including a program for a CR1000 and AM25T. Once generated, the code was merged with the purchased code. Alternatively, one may simply purchase the code in this final form from Campbell Scientific[®] and avoid the need to manually combine the programs altogether; for this investigation the author manually combined the codes.

7.1.5 Sensor Probes

Two kinds of sensor probes, or probes, have been designed and fabricated for this investigation; the first design (Probe 1), as shown in figure 26, is intended for placement in the representative bridge deck. The probe housing is cylindrical, allowing for its placement in holes created by conventional means (i.e. drilling or cast). The RH&T sensor is located in the front end of the probe's housing, capped with an optional venting material. The intent of the venting material is to protect the RH&T sensor from particulate matter and stray vacuum grease used in the probe packing process (covered in section 7.3). Additionally, the venting membrane offers protection from direct contact with [non-condensing] liquid moisture, should the probes be used in fresh concrete applications. It should be noted that if the probe is to be used in such an application, the vent is no longer optional.

At the front end of the probe's housing (where the RH&T sensor is located) an exposed thermocouple wire is looped around the exterior. The function the thermocouple sensor serves is to offer a comparison of the concrete's surface temperature at the RH&T sensor level and the temperature being measured by the sensor. This is the method the author has selected to quantify the thermal differences between the sensor and the specimen so that, if necessary, corrections can be made (see section 6.1). Beneath the loop of the thermocouple wire is closed cell rubber weather stripping. The rubber weather stripping serves three functions. First, it serves as a backer material to stop vacuum grease from entering the control volume of interest during the probe packing process. Second, it provides a uniform outward radial spring force, ensuring complete and constant contact between the thermocouple and the concrete. Third, the complete and constant contact of the thermocouple wire created by the radial spring force provides a frictional resistance, helpful in preventing probe movement in the hole. The design specifics and fabrication techniques, for this probe and the one to be discussed next, may be found in Appendix A of this investigation.

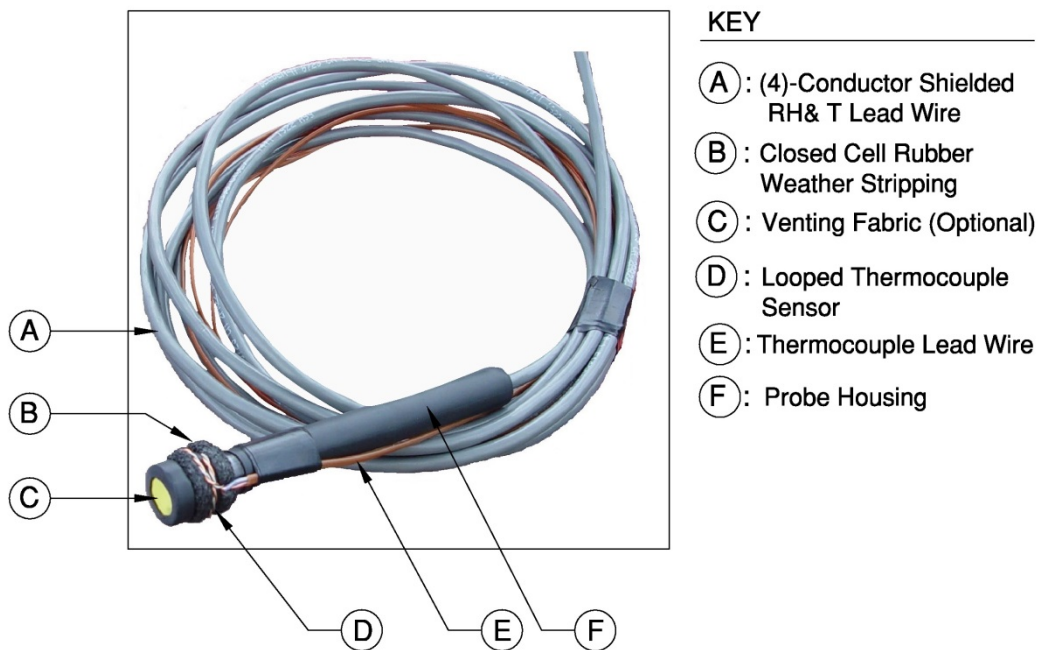


Figure 26: Assembled probe 1 for placement in the full-size representative concrete bridge deck specimen

The second probe (Probe 2) was designed for moisture isotherm creation. This design is similar to the first in many ways, but has a few design differences specific for its intended application. The first noticeable difference is the use of a (4)-conductor connector instead of a continuous lead. As will be discussed at a later time (in section 7.4) the method used to create moisture sorption isotherms requires that specimen samples undergo certain procedures; these procedures would be difficult to accomplish while a probe with a continuous lead is placed inside. Additionally, it is impractical to remove the probe from the specimen samples each time such procedures are performed. This design feature will allow for the practical continuous placement of the probe throughout these procedures, until the probes are no longer required. Second, this design does not require the use of thermocouple sensors, as a moisture sorption isotherm is created under equilibrium conditions, precluding the need to quantify temperature differences between the sample material and the RH & T sensor. The final design differences include: a rubber stopper plug, no optional venting material and no closed-cell weather stripping; the rationale for these design differences will become apparent later in section 7.4.

It must be noted that the probe design used in this investigation is based on a more economical version developed at the University of Illinois at Urbana-Champaign in Urbana, IL (Rodden, Lange, and Grasley 2005). However, revision was necessary to reduce the volume of the cavity created by the probe housing (housing the SHT75-V4 sensor); this should reduce the time necessary for the temperature and internal relative

humidity in the cavity to equilibrate. Also not found in the other design is the incorporation of a thermocouple sensor into the probe housing.

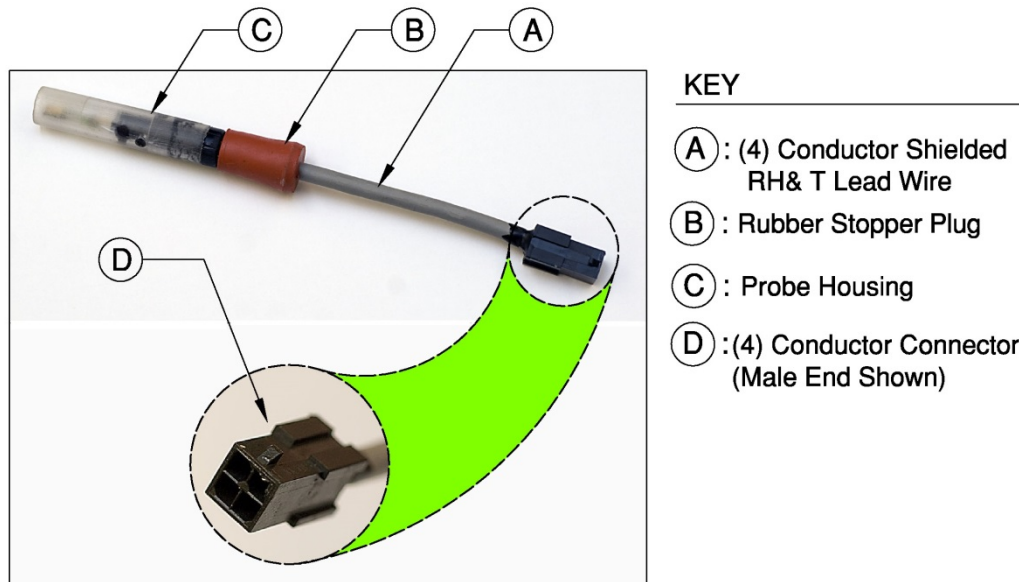


Figure 27: Assembled probe 2 for placement in concrete specimens being used in the creation of moisture sorption isotherms (mating 4-conductor lead wire not shown)

7.2 SENSOR CALIBRATION

7.2.1 Relative Humidity Sensor Calibration Method

It was noted earlier (see section 7.1.2) that the SHT75-V4 (or RH&T) sensor is supplied in a calibrated condition by the manufacturer, traceable to a NIST standard. The operational conditions ranging between 10% to 90% RH are claimed to have an accuracy of $\pm 1.8\%$ RH and an accuracy of up to $\pm 4\%$ RH for operational conditions above that. For the purposes of this investigation, should the actual conditions be higher than 90% RH, accuracies above $\pm 1.8\%$ RH will not be acceptable. Also, as was also noted earlier (see section 7.1.4) the code purchased from Campbell Scientific[®] uses a conversion formula that does not account for significant deviations from 25°C ; however, the representative concrete deck specimen is likely to experience internal temperatures significantly different than 25°C . Finally, if the RH&T sensors were mishandled at some point, this also may be a source of shifting from a calibrated value. For all these reasons, the author shall create sensor-specific RH calibration functions.

The RH calibration method employed is as follows. First, the RH&T sensors were exposed to a stable environment of known relative humidity at specified temperature. The RH environment was generated in general accordance with ASTM E104, entitled “Standard Practice for Maintaining Constant Relative Humidity by Means of Aqueous

Solutions” (ASTM Standard E104 2002 (2007)). This standard provides guidance for generating, within a sealed container, an environment of known relative humidity using various saturated salt solutions at defined temperatures. In general, a salt specified by the standard is mixed into solution with pure water (an aqueous solution), such that the salt saturates the water. Then the solution is sealed inside an approved container at a fixed temperature defined by the standard. Once the solution has achieved dynamic equilibrium (see section 2.2.3.1) a known relative humidity within the container will theoretically exist. It is this environment to which the [functioning] sensors were exposed and calibrated.

As shown by equation 7.1, an **RH theoretical residual** value is defined (by the author) as the difference between a sensor’s measured RH values, prior to the application of a user determined calibration, and the theoretical value of the environment being measured. The second step of the calibration method is to determine several theoretical residual values at discrete [RH and temperature] points, distributed throughout the user-determined operational conditions.

$$Residual_{Theo.} = RH_{Meas.} - RH_{Theo.} \quad \text{Equation 7.1}$$

where

- $Residual_{Theo.}$: RH theoretical residual, based directly on a standard [%]
- $RH_{Meas.}$: Relative humidity as determined by the sensor prior to user calibration [%]
- $RH_{Theo.}$: Theoretical relative humidity produced by a standard [%]

Discrete theoretical environmental [RH and temperature] fixed points applicable to this investigation may be found in table 3; this table was created from a more comprehensive table of values found within ASTM E104, which covers a much wider range of theoretical RH and temperature fixed point values. Also, another theoretical RH value applicable to this investigation, not shown in table 3, is the saturated ($RH = 100\%$) environment produced by pure water in its liquid phase, over all applicable temperature values. When generating an RH calibration function it may not be practical to consider every available theoretical value within scope of operating conditions. However, several thoughtfully distributed fixed point values would be selected. RH calibration functions, applied to sensors placed in the representative specimen, needed to be valid over the operational conditions of approximately 70% to 100% RH and 5°C to 50°C . In the case where the sensors were used in the creation of moisture sorption isotherms, the same operational RH conditions were needed, but specifically at 25°C.

Temp. [°C]	Standard Salt , <i>RH</i> [%](<i>Error</i> [%])		
	Sodium Chloride, NaCl	Potassium Chloride, KCl	Potassium Sulfate, K ₂ SO ₄
5	75.7 (± 0.3)	87.7 (± 0.5)	98.5 (± 1.0)
10	75.7 (± 0.3)	86.8 (± 0.4)	98.2 (± 0.8)
15	75.6 (± 0.2)	85.9 (± 0.4)	97.9 (± 0.7)
20	75.5 (± 0.2)	85.1 (± 0.3)	97.6 (± 0.6)
25	75.3 (± 0.2)	84.2 (± 0.3)	97.3 (± 0.5)
30	75.1 (± 0.2)	83.6 (± 0.3)	97.0 (± 0.4)
35	74.9 (± 0.2)	83.0 (± 0.3)	96.7 (± 0.4)
40	74.7 (± 0.2)	82.3 (± 0.3)	96.4 (± 0.4)
45	74.5 (± 0.2)	81.7 (± 0.3)	96.1 (± 0.4)
50	74.5 (± 0.9)	81.2 (± 0.4)	95.8 (± 0.5)
55	74.5 (± 0.9)	80.7 (± 0.4)	-----
60	74.4 (± 0.9)	80.3 (± 0.5)	-----

Table 3: Theoretical relative humidity values for saturated salt solutions of selected standard salts and temperatures at equilibrium (see ASTM E104 table A1.1)

The third step of the calibration method is the creation of the user-developed RH calibration function for each sensor. This calibration function is to be valid over operational conditions defined by the user. Once several discrete theoretical residual values have been determined for a given RH&T sensor, a [surface] model that best-fits these values is created; the author terms this the **RH residual model**. The RH residual model shall be a function of sensor measured RH and temperature values. That is to say that the model's domain values are the RH&T values as determined by the sensor (in conjunction with the purchased code) prior to the application of a user-developed sensor-specific calibration. It should be recalled that the purchased code makes use of the sensor manufacturer's *temperature independent* RH output conversion formula (see section 7.1.4), which is applied to all sensor RH outputs and is used in the determination of the RH domain values. Similarly, the temperature domain values must first be converted by the manufacturer's Temperature output conversion formula before they can be used in the RH calibration function.

For each sensor, a specific [*i*th] sensor **RH calibration function**, as shown by equation 7.2, is equal to the measured RH (i.e. the domain RH) minus the RH residual as determined by the sensor specific RH residual model, evaluated at the measured RH and corresponding measured temperature (i.e. the domain RH&T).

$$RH_{cal.}^{Si} = RH_{Meas.}^{Si} - Residual_{Mod.}^{Si}(RH_{Meas.}^{Si}, T_{Meas.}^{Si}) \quad \text{Equation 7.2}$$

where

$RH_{cal.}^{Si}$: User determined RH calibration for a specific *i*th sensor [%]

- $RH_{Meas.}^{Si}$: Relative humidity as measured by a specific i^{th} sensor prior to the application of the user determined RH calibration [%]
 $Residual_{Mod.}^{Si}$: The specific i^{th} sensor RH residual model [%]
 (a function of two variables)
 $T_{Meas.}^{Si}$: Temperature as measured by a specific i^{th} sensor [°C]

The fourth and final step of the RH calibration procedure is to apply it. Application of the user determined RH calibration is as follows. When a specific RH&T sensor is multiplexed by the DAQ to take a measurement, it does so and returns a digital signal containing two raw outputs: one for RH and the other for temperature. The raw output values are then converted by the manufacturer's output conversion formulas. It is at this stage in the code, just prior to the tabling of the converted values, that the calibration functions are to be inserted. Each channel (i.e. RH&T sensor) will have its own assigned RH calibration function. Using this method, each RH&T sensor will receive RH calibration custom developed for that sensor. Generically, this part of the program would behave as shown by the "pseudo-code" below:

For $i = 1$ to n

Get RH (i) "RH: Relative Humidity Value"
 Get T (i) "T: Temperature Value"

$RH(i) = RH(i) \times \text{Output Conversion Formula for RH}$
 $T(i) = T(i) \times \text{Output Conversion Formula for T}$

"----- Sensor Specific RH Calibration Code Starts Here -----"

$RH(1) = RH(1) - Residual_{Mod.}^{S1}(RH(1), T(1))$ "Calibration for # 1 probe sensor"
 $RH(2) = RH(2) - Residual_{Mod.}^{S2}(RH(2), T(2))$ "Calibration for # 2 probe sensor"
 \vdots
 $RH(n) = RH(n) - Residual_{Mod.}^{Sn}(RH(n), T(n))$ "Calibration for # n probe sensor"

"----- Sensor Specific RH Calibration Code Ends Here -----"

Table RH (i)
 Table T (i)

If $i = n$, End

Else $i = i + 1$

7.2.2 Temperature Sensor Calibration Method

As was stated before (section 7.1.2), the part of the RH&T sensor responsible for temperature measurement uses bandgap PTAT technology. Over the specified operational

conditions, the manufacturer certifies that the accuracy is within approximately $\pm 0.75\text{ }^{\circ}\text{C}$ with a minimum error of $\pm 0.3\text{ }^{\circ}\text{C}$ at 25°C . The author has accepted the manufacturer's accuracies as reasonable for the purposes of this investigation. Also, it may be observed by reviewing table 3 that an accuracy of this magnitude would have almost no effect on the sensors' RH calibration. Additionally, in the context of calibration shift, the [separate] technology used to measure temperature within this sensor is by far less sensitive to environmental conditions. For these reasons, the author decided not to devise a method of calibration for the RH&T sensor temperature component. The author did, however, compare the temperature values of multiple RH&T sensors exposed simultaneously to the same temperature conditions, and found no outliers. Similarly, the author accepted as reasonable the accuracies presented by the manufacturer of the thermocouple wire, as was presented in section 7.1.2. This acceptance was reinforced by manufacturer testing prior to product shipping, and provision of clearly labeled acceptable deviation of the sensors.

7.2.3 Relative Humidity Sensor Calibration Method – Apparatus Design

As was cited earlier (section 7.2.1), the method used to generate a continuous environment of known relative humidity was in general accordance with ASTM E104. According to sections 7 and 9 of ASMT E104 the following design, as shown in figure 28, would be an acceptable apparatus. A description of the apparatus design is as follows. A semi-double walled container was created by fitting a 2.8 quart plastic inner container inside a 3.0 quart outer container, with a continuous strip of closed-cell rubber weather stripping wedged between the two containers. It should be noted that the closed-cell weather stripping used is adhesive on one side; the adhesive side was affixed to the inside of the outer container, as close to the top as possible. A double walled apparatus is not required by ASTM E104; however, it does require that temperature stability is maintained. This semi-double wall design is meant to attenuate temperature fluctuations that may occur outside the apparatus with the goal of achieving a higher degree of temperature stability inside the apparatus.

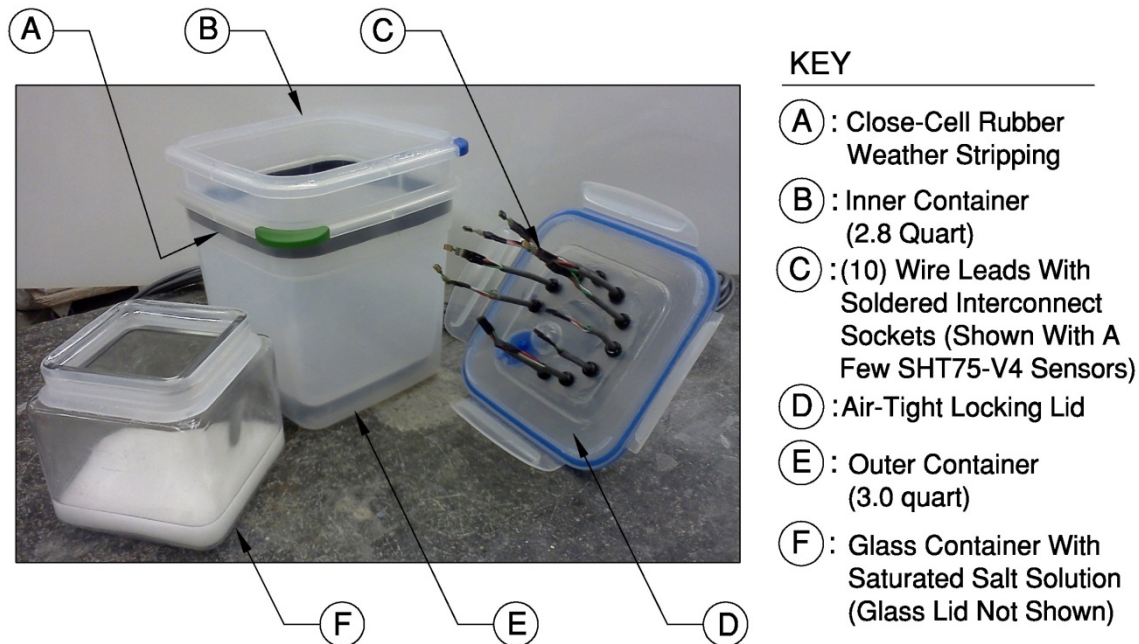


Figure 28: Relative humidity calibration apparatus assembly (deconstructed view)

A glass container, with its lid off, was placed inside the plastic container assembly. It is in this glass container that the saturated salt solution was retained. The use of a glass container in this way serves two functions. First, the specification indicates that if a plastic container, not being an “*appropriate material*” is used to contain the produced RH environment, then a separate container being of an “*appropriate material*” shall be used to actually retain the saturated salt solution; glass was specified as being an “*appropriate material*”. Second, as several saturated salt solutions are generally used, this design approach allows for easy exchange of solutions. When a glass container retaining solution is no longer required it can be removed from the plastic container assembly and stored for future use. Considering the geometry of the plastic container assembly, a glass container was selected to maximize the available surface area at the solution/air interface.

The RH calibration apparatus makes use of a lid that locks down over the plastic container assembly, creating an airtight seal. Passing through the lid are (10)-wire leads with soldered interconnect sockets for plugging in up to (10)-SHT75-V4 sensors. At the location where the wire leads pass through holes in the locking lid, precautions should be taken to secure these joints and ensure airtightness. The author’s solution was to fabricate plastic grommets from the tube plugs used in the RH&T probe fabrication and then use plastic shrink wrap to lock the wire lead around it. Also, non-volatile high vacuum grease at all possible points of air infiltration, including along the locking lid’s rubber seal was used. As note of caution, when determining the length of wire lead needed to pass through the lid, make sure there is sufficient clearance for the SHT75-V4 sensors above the saturated salt solution. If the sensor contacts the solution, irreversible damage to that sensor is likely to occur. Beyond the written description and figures

provided (figures 28 and 29) here, there shall be no further details pertaining to the fabrication of the RH calibration apparatus.



Figure 29: Relative humidity calibration apparatus assembly in an environmental chamber

As shown in figure 29, when the apparatus is assembled and contains the saturated salt solution and a batch of SHT75-V4 (or RH&T) sensors, the entire assembly is placed in an environmental chamber. The chamber is used to control the ambient temperature surrounding the apparatus. By observation, the environmental chamber was able to maintain a set temperature with a stability of approximately $\pm 0.5^{\circ}\text{F}$; however, the stability within the apparatus was much better due to temperature attenuation. The ends of the wire leads coming out of the apparatus are connected to the DAQ system, which runs a program containing a version of the purchased code that does not include, or make use of the user determined RH calibration functions. Additionally, thermocouple wires are not involved.

7.2.4 Example RH Calibration Function Calculation

7.2.4.1 Overview

In this section (section 7.2.4), the author will step through an example RH calibration function calculation for a single RH&T sensor. The example calculations focus specifically on the determination of the initial RH calibration function of the sensor assigned to the number 4 probe; this probe was used in the representative concrete deck specimen. Ultimately a shifting of the output values away from the calibrated state occurred after probe placement, requiring a new calibration function to be developed for the sensor in probe 4 (along with sensors in other probes). This occurrence shall be discussed further in the results section of this investigation. Regardless, the following example is the pattern used for every calibration function developed. The intent of this section is to provide a detailed overview of the steps taken by the author to produce

sensor RH calibrations in a general way, not to document sensor specific calibration nuances for individual sensors calibrations. Consequently, repetition shall be eliminated whenever possible. Sensor specific RH calibrations resulting from the method explored by example calculation have been provided in Appendix – B.

The RH calibration batch selected for this example was the 6th batch, labeled batch 006 (or B006); where, a batch label identifies the unique exposure of a sensor grouping to a single saturated salt-produced environment spanning an entire temperature domain. A given sensor will be exposed to several batches during the RH calibration process. The sensor ultimately selected for use in the number 4 probe was assigned to the sensor 6 position number in the RH calibration apparatus. The reader will notice that a fairly complicated notational system is used; this is necessary to facilitate unique identifications.

7.2.4.2 Step 1 – Data collection from RH calibration apparatus

Groups of up to (10)-RH&T sensors are plugged into the RH calibration apparatus. The apparatus containing a saturated salt solution, selected from table 3, is placed in to the environmental chamber and the locking lid is sealed. The environmental chamber is then set to a temperature, which is also selected from table 3, and the environment inside the RH calibration apparatus is allowed to reach equilibrium. Once equilibrium has been achieved, for the purpose of collecting data used in statistical calculations, additional time is allowed to pass prior to moving forward. Then without opening the RH calibration apparatus, the temperature of the environmental chamber is changed to another temperature, selected from table 3, and the process is repeated until the entire temperature domain required for a given saturated salt solution is covered. A partial plotting of this for a single saturated salt solution may be observed by [the upper portion] of figure 30. In this figure, a group of (10)-RH&T sensors were exposed to an RH environment produced by a sodium chloride (NaCl) saturated salt solution. The temperature domain for this batch (batch 006) of sensors spanned 60°C to 5°C (though not entirely shown in figure 30) with 5°C temperature step changes; the corresponding RH environments produced spanned 74.4 % ($\pm 0.9\%$) to 75.7% ($\pm 0.3\%$), respectively (see table 3).

The progression towards achieving dynamic equilibrium, within the RH calibration apparatus, is monitored by observing the RH&T sensor outputs. Dynamic equilibrium is assumed to occur when the change in RH is sufficiently trivial. In general, as may be observed in [the lower portion of] figure 30, dynamic equilibrium occurs in less than 12 hours. However, to be conservative [at least] 24 hours of exposure time were allowed to pass. Also, for each temperature step, the last 4 hours of the initial 24 hour exposure is used in the [statistical] calibration calculations that follow; this arbitrary data sampling scheme is meant to impose consistency between the calculations.

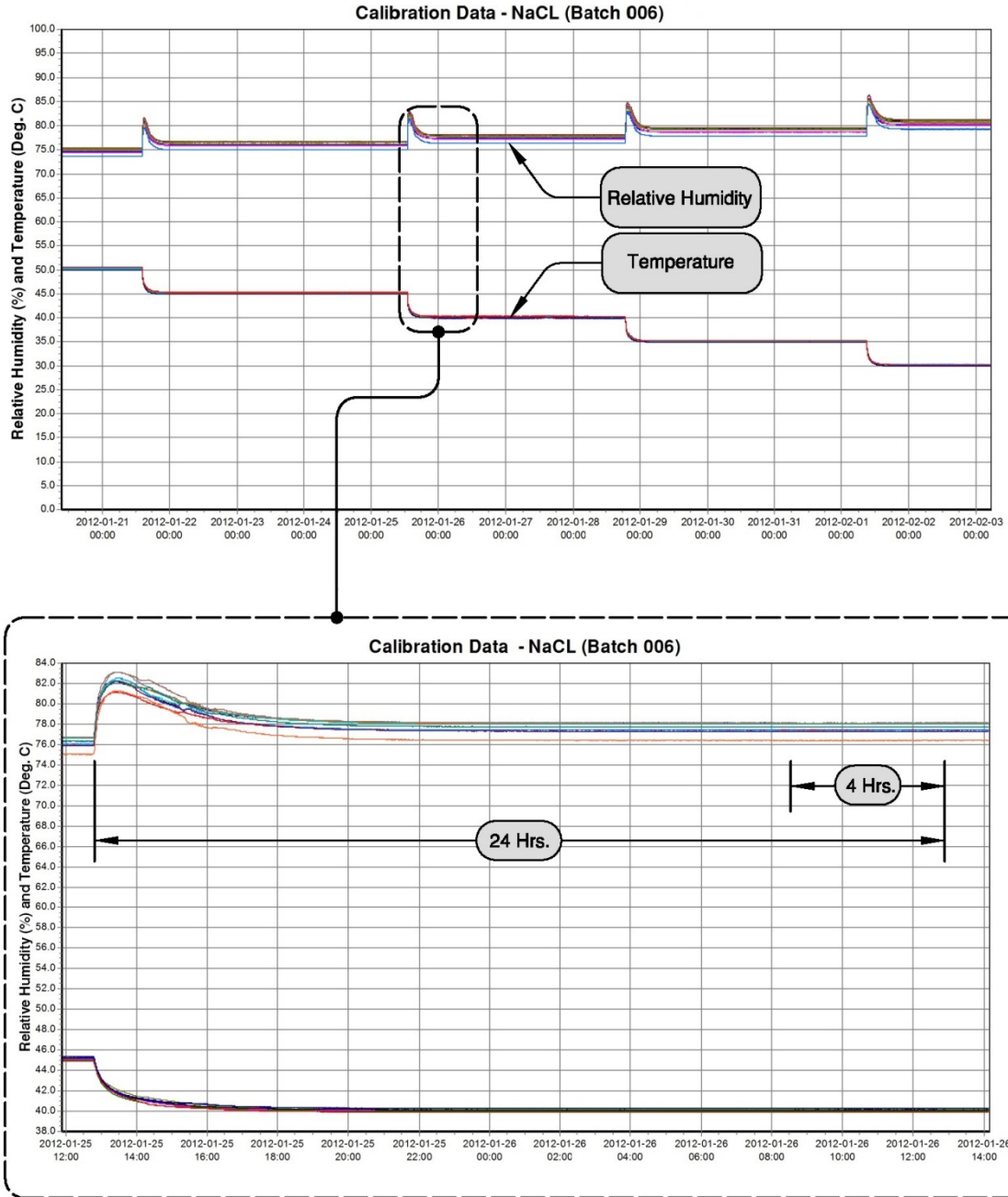


Figure 30: Plotted data for (10)-RH&T sensors inside the RH calibration apparatus containing an NaCl saturated salt solution and highlighting data at the 40°C temperature set point

Once dynamic equilibrium is achieved for a specific saturated salt solution across the desired temperature domain, the process is repeated for all the saturated salt solutions required to span the RH domain. Having collected all the data required for RH&T sensor calibrations from the RH calibration apparatus, the next step is to determine all the theoretical RH residual values used to calculate the RH residual model.

7.2.4.3 Step 2 – Calculation of theoretical RH residual values

For each sensor, theoretical RH residual values need to be calculated spanning the relative humidity and temperature domain of the RH calibration. The first step, of four, in calculating a single sensor specific theoretical RH residual value is to determine the actual temperature within the RH calibration apparatus during dynamic equilibrium for a given temperature. Unfortunately, since the author could not verify that the environmental chamber had been calibrated recently to a NIST traceable standard, the oven set-point temperature could not be assumed correct, requiring another approach. One may recall that the RH&T sensors produce NIST traceable temperature values that are not questioned by the author.

Therefore, the author took the [constant] temperature existing within the RH calibration apparatus at dynamic equilibrium to be equal to the mean of the collective temperatures recorded for all the sensors of a given calibration batch (i.e. batch 006 in this case) over the 4 hour data sampling period as indicated in figure 31(continuing from figure 30), and is mathematically expressed by equation 7.3.

$$T_{Mean,salt}^t = \frac{\sum T_{salt}^{S1,t} + \sum T_{salt}^{S2,t} + \dots + \sum T_{salt}^{Si,t}}{Total\ No.\ of\ Temp.\ Data\ Values} \quad \text{Equation 7.3}$$

(Over a sample period of 4 hours)

where

- $T_{Mean,salt}^t$: Mean temperature presumed to exist inside the RH calibration apparatus, containing a specific saturated salt solution (salt), and of a nominal target temperature (t) [°C]
- $T_{salt}^{S1,t}$: Single measured temperature value by sensor 1 in an environment set to a nominal target temperature ($S1, t$) inside the RH calibration apparatus, containing a specific saturated salt solution (salt) [°C]
- $T_{salt}^{S2,t}$: Single measured temperature value by sensor 2 in an environment set to a nominal target temperature ($S2, t$) inside the RH calibration apparatus, containing a specific saturated salt solution (salt) [°C]
- $T_{salt}^{Si,t}$: Single measured temperature value by the i^{th} sensor in an environment set to a nominal target temperature (Si, t) inside the RH calibration apparatus, containing a specific saturated salt solution (salt) [°C]

It should be noted that sample rates varied between calibration batches, with data collections occurring every 30 to 90 seconds. While different sampling rates occurred

between calibration batches, rates between the sensors of any given batch were consistent. The reason the sampling rates changed between the batches is still unclear; regardless, the number of data points collected in the identified 4-hour sampling period were still sufficiently large. Data quantities ranged from approximately 150 to 500 temperature data values per sensor over a 4-hour sampling period. Continuing to look at the example batch (batch 006), the temperature presumed to exist inside the apparatus, having a nominal set-temperature of 40°C is calculated to be equal to 40.10°C. By a visual inspection of figure 31, the resulting value should look reasonable to the reader.

Having determined an actual temperature for the environment inside the apparatus of the example batch (batch 006) with a nominal set-temperature of 40°C ($T_{Mean,NaCl}^{40} = 40.10^{\circ}\text{C}$), a theoretical relative humidity may now be determined. This is the second step in calculating a theoretical RH residual value. As is seen in table 3, ASTM E104 provides fixed humidity points (FHP's) for various saturated salt solutions at temperatures given in 5°C increments. However, it does not explicitly provide directions for interpolation between these defined fixed points; in truth it does not even indicate that interpolation should be used. To the author, it is clear that interpolation is required here. That is to say, a theoretical relative humidity value corresponding to 40.10°C, existing between the fixed theoretical relative humidity values corresponding to 40°C *and* 45°C needs to be determined. In figure 32 all the fixed points, provided by ASTM E104 for sodium chloride (NaCl), are plotted.

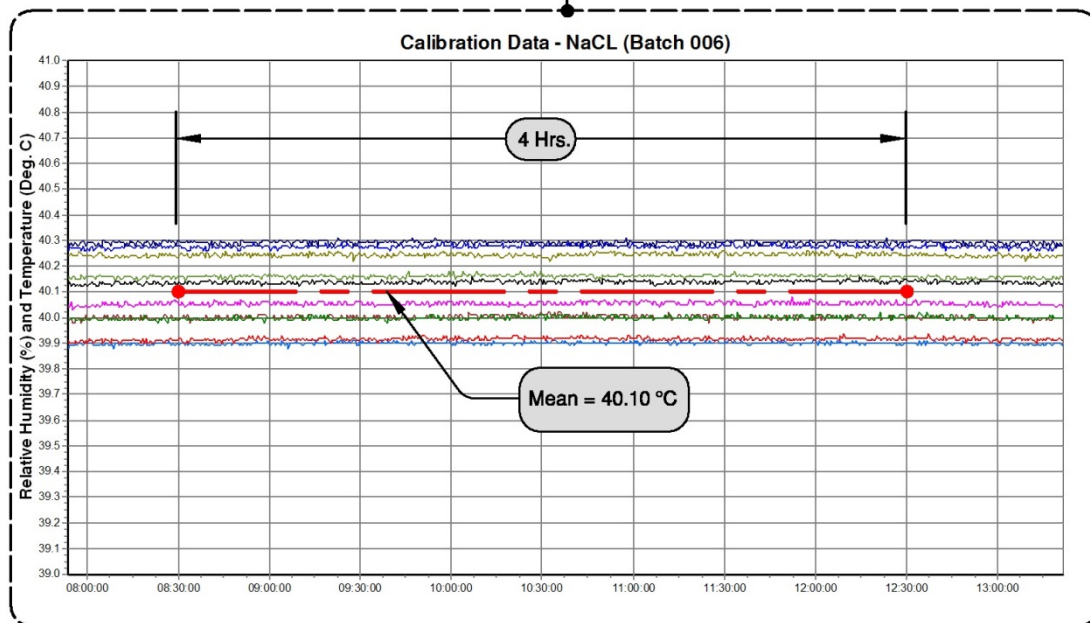
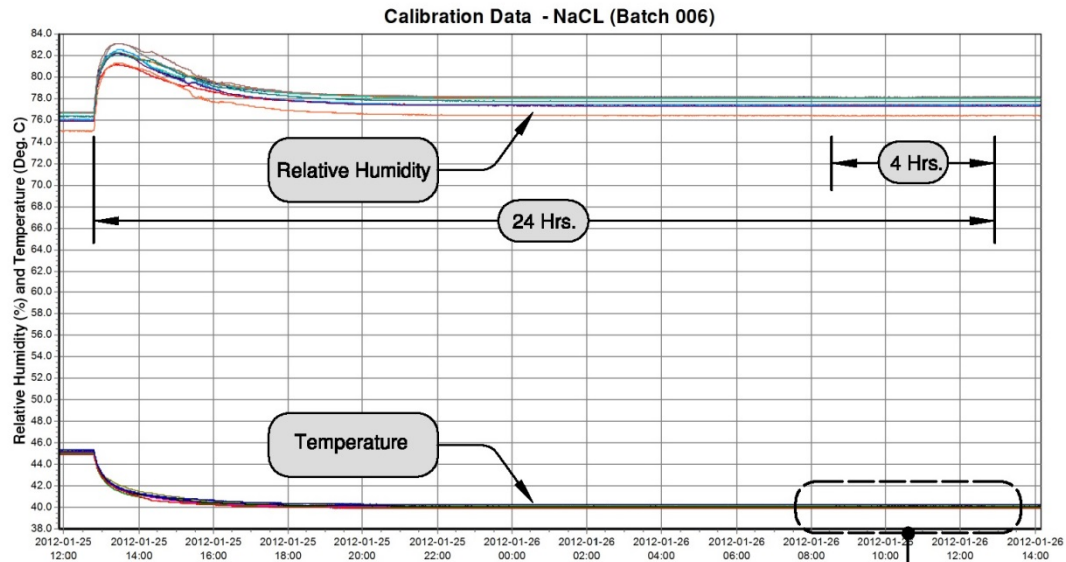


Figure 31: Plotted data for (10)-RH&T sensors inside the RH calibration apparatus containing an NaCl saturated salt solution at the 40°C temperature set point, highlighting the 4-hour sampling period and batch temperature mean.

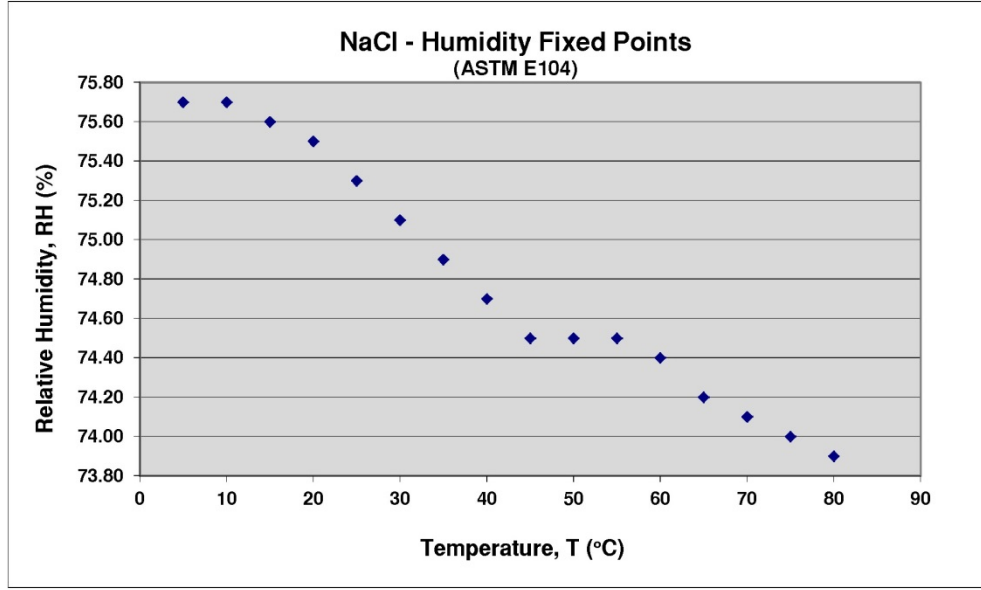


Figure 32: Plotted humidity fixed points for NaCl per ASTM E104

To interpolate between these fixed points, the author chose to employ a quadratic interpolation scheme (or a second order Newton Interpolating Polynomial). This quadratic interpolation takes the form of equation 7.4 (Chapra 2008).

$$RH_{Theo}^{salt,t} = C_1 + C_2(T_{Mean,salt}^t - T_{salt}^{FP1}) + C_3(T_{Mean,salt}^t - T_{salt}^{FP1})(T_{Mean,salt}^t - T_{salt}^{FP2}) \quad \text{Equation 7.4}$$

The coefficients (C_1 , C_2 and C_3) are calculated by equations 7.5, 7.6 and 7.7.

$$C_1 = RH_{salt}^{FP1} \quad \text{Equation 7.5}$$

$$C_2 = \frac{RH_{salt}^{FP2} - C_1}{T_{salt}^{FP2} - T_{salt}^{FP1}} \quad \text{Equation 7.6}$$

$$C_3 = \frac{\left(\frac{RH_{salt}^{FP3} - RH_{salt}^{FP2}}{T_{salt}^{FP3} - T_{salt}^{FP2}} \right) - C_2}{T_{salt}^{FP3} - T_{salt}^{FP1}} \quad \text{Equation 7.7}$$

where

- $RH_{Theo}^{salt,t}$: Theoretical relative humidity within the RH calibration apparatus, at dynamic equilibrium, containing a specific saturated salt and of nominal target temperature ($salt, t$)
- $T_{salt}^{FP1}, T_{salt}^{FP2}$ and T_{salt}^{FP3} : Temperature of the first, second and third known fixed point (FP1, FP2, and FP3 respectively), for a specific saturated salt solution ($salt$), near the interpolation point of interest [°C]
- $RH_{salt}^{FP1}, RH_{salt}^{FP2}$ and RH_{salt}^{FP3} : Relative humidity values corresponding to the first, second and third known fixed point temperature values (FP1, FP2, and FP3 respectively), for a specific saturated salt solution ($salt$), near the interpolation point of interest [%]

The theoretical relative humidity existing inside the example batch at the nominal set point of 40°C, $RH_{Theo}^{NaCl,40}$, was calculated in the following way. Using the fixed points shown in table 4, the coefficients (C_1, C_2 and C_3) are calculated first.

Fixed Point, FP No.	NaCl – Saturated Salt Solution (per ASTM E104)	
	Temperature	Relative Humidity
1	40 °C	74.7 %
2	45 °C	74.5 %
3	50 °C	74.5 %

Table 4: Fixed point values (per ASTM E104) near the interpolation point of interest

$$C_1 = 74.7 \quad \text{Equation 7.8}$$

$$C_2 = \frac{74.5 - 74.7}{45 - 40} = -0.040 \quad \text{Equation 7.9}$$

$$C_3 = \frac{\left(\frac{74.5 - 74.5}{50 - 45}\right) - (-0.04)}{50 - 40} = 0.004 \quad \text{Equation 7.10}$$

Substituting the calculated coefficients (equations 7.8, 7.9 and 7.10) along with other known values into equation 7.4, the following quadratic equation 7.11 is formulated.

$$RH_{Theo}^{NaCl,40} = 74.7 - 0.040(T_{Mean,NaCl}^{40} - 40) + 0.004(T_{Mean,NaCl}^{40} - 40)(T_{Mean,NaCl}^{40} - 45) \quad \text{Equation 7.11}$$

Substituting the temperature of interest ($T_{Mean,NaCl}^{40} = 40.10^\circ\text{C}$) into equation 7.11, the following theoretical relative humidity result has been interpolated (see equations 7.12).

$$RH_{Theo}^{NaCl,40} = 74.69 [\%] \quad \text{Equation 7.12}$$

While the resulting interpolated value does appear to be a trivial departure from its nearest neighboring fixed point (NaCl at 40°C , 75.7%) this will not always be the case; interpolation is necessary.

The third step in calculating a sensor-specific theoretical RH residual value is to determine the mean relative humidity measured by that sensor for this particular environmental condition over the identified 4-hour sampling period. As was stated at the outset, for the purposes of example, the author is interested in the sensor used in probe 4. This particular sensor is in the 6th of 10 positions within the RH calibration apparatus. As shown in figure 33, the mean relative humidity value for sensor 6 over the 4-hour sampling period (of batch 006 at the 40°C nominal temperature set point) is equal to 78.08% (or using the current notation format, $RH_{Mean,NaCl}^{S6,40} = 78.08 [\%]$ over a period of 4 hours). This value was calculated by an equation of the form shown below (see equation 7.13).

$$RH_{Mean,salt}^{Si,t} = \frac{\sum RH_{salt}^{Si,t}}{\text{No. of RH Data Values}} \quad \text{Equation 7.13}$$

(Over a sample period of 4 hours)

where

$RH_{Mean,salt}^{Si,t}$: Mean relative humidity as measured by an i^{th} sensor inside the RH calibration apparatus, containing a specific saturated salt solution (*salt*), and of a nominal target temperature (t) [%]

$RH_{salt}^{Si,t}$: Single relative humidity measurement of an i^{th} sensor inside the RH calibration apparatus, containing a specific saturated salt solution (*salt*), and of a nominal target temperature (t) [%]

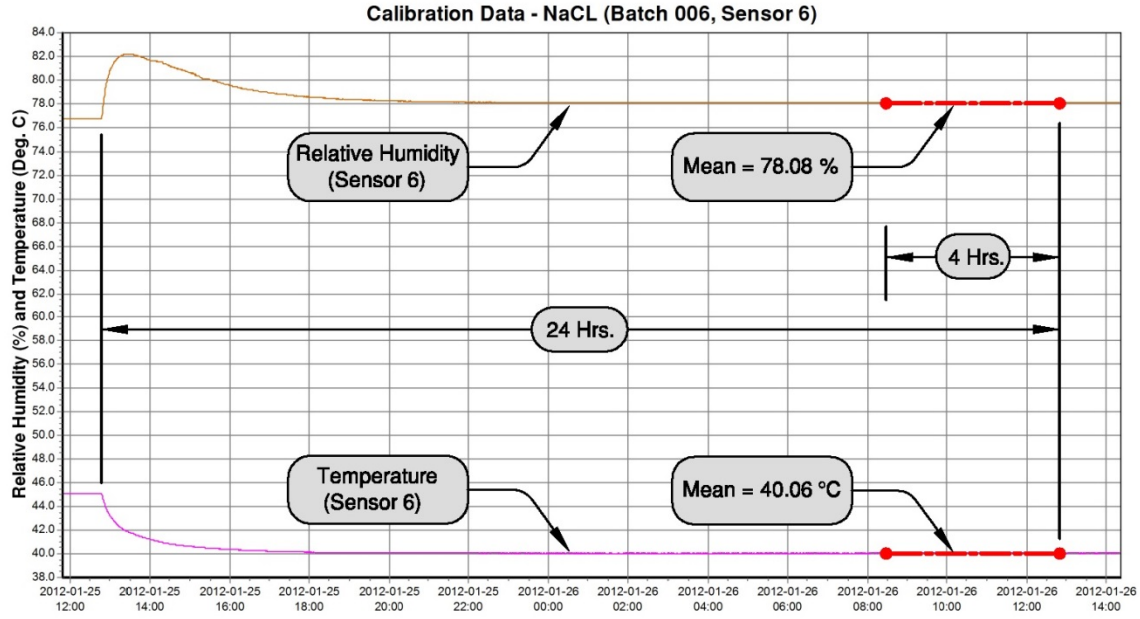


Figure 33: Plotted data for RH&T sensor 6 inside the RH calibration apparatus containing an NaCl saturated salt solution at the 40°C temperature set point, highlighting the 4-hour sampling period with temperature & relative humidity mean values.

Also, shown in figure 33 is the mean temperature value for sensor 6 over the 4-hour sampling period (of batch 006 at the 40°C nominal temperature set point) equal to 40.06°C (or using the current notation format, $T_{Mean,NaCl}^{S6,40} = 40.06^{\circ}\text{C}$ over a period of 4 hours). While the author does not intend to create a temperature calibration, as a group the author is interested in identifying sensors with temperature outliers. It is for this reason that this value is calculated and monitored during RH calibration. This calculation follows a form very similar to equation 7.13, as shown by equation 7.14.

$$T_{Mean,salt}^{Si,t} = \frac{\sum T_{salt}^{Si,t}}{\text{No. of Temp. Data Values}} \quad \text{Equation 7.13}$$

(Over a sample period of 4 hours)

where

$T_{Mean,salt}^{Si,t}$: Mean temperature value as measured by the i^{th} sensor in an environment set to a nominal target temperature (Si , t) inside the RH calibration apparatus, containing a specific saturated salt solution ($salt$) [$^{\circ}\text{C}$]

For the example condition, the fourth and final step in calculating a sensor-specific theoretical RH residual value is to take the difference of the interpolated theoretical RH value, $RH_{Theo}^{NaCl,40}$, and the sensor-specific mean RH value, $RH_{Mean,NaCl}^{S6,40}$. This expressed in general by equation 7.1. However, to satisfy the current notation structure equation 7.1 is now expressed by equation 7.14.

$$Residual_{Theo,salt}^{Si,t} = RH_{Mean,salt}^{Si,t} - RH_{Theo}^{salt,t} \quad \text{Equation 7.14}$$

where

$Residual_{Theo,salt}^{Si,t}$: RH theoretical residual of an i^{th} sensor inside the RH calibration apparatus, containing a specific saturated salt solution (*salt*), and of a nominal target temperature (t) [%]

Specifically, for this example calculation, equation 7.14 becomes equation 7.15.

$$Residual_{Theo,NaCl}^{S6,40} = RH_{Mean,NaCl}^{S6,40} - RH_{Theo}^{NaCl,40} \quad \text{Equation 7.15}$$

Then, after substituting the corresponding values, the following theoretical residual value, for sensor 6, exposed to the example conditions is determined (see equation 7.16).

$$Residual_{Theo,NaCl}^{S6,40} = 78.08\% - 74.69\% \Rightarrow 3.39\% \quad \text{Equation 7.16}$$

So, for this sensor, if the domain values (i.e. the RH&T measured values prior to sensor specific calibration) were equal to 40.06°C and 78.08%, then one would expect an RH departure of 3.39% from the actual RH to exist.

For each temperature set point, the following table (see table 5) of calculations was produced for all the sensors in that batch. Many of the calculations shown in the table have been covered in this example calculation. However, there are a few calculations performed to quantify uncertainties for the measurements taken, not covered in the example. The calculations not discussed include:

- **Departure from total mean temperature** – This value is the difference between the mean temperature of the i^{th} sensor, $T_{Mean,salt}^{Si,t}$ (see equation 7.13) and the total mean temperature, $T_{Mean,salt}^t$ (see equation 7.3); this value is presumed to be equivalent to a temperature residual value.
- **Standard Deviation (STD)** – This value, also called the “*absolute uncertainty*”, is for a single i^{th} sensor temperature (or relative humidity) measurement, determined by the data collected from the i^{th} sensor during the specified 4-hour sampling period. This is an accuracy indicator for a single sensor.
- **Total STD** – This “*absolute uncertainty*” value spans all the sensors in a batch, for a temperature (or relative humidity) measurement, determined by all sensor data collected during the specified 4-hour sampling period. This is used as an accuracy indicator spanning the sensors as a collective.
- **Coefficient of Variation (COV)** – This value, also called the “*relative uncertainty*”, may be thought of as a normalized STD. This is done by dividing the STD by the true temperature (or relative humidity) measurement, which is taken to be equal to the calculated total mean temperature (or the theoretical RH, respectively).

- **Total COV** – This “*relative uncertainty*” may be thought of as the normalized total STD.

Further information pertaining to these uncertainty statistics (STD and COV) may be found in texts on engineering statistics (Navidi 2008). Based on the statistical calculations, like those shown in table 5, the author was able to determine that the RH&T provide sensor results that are very precise; that is to say they provide very repeatable results. When the RH calibration is complete, they will be more accurate as well, where the level of accuracy is relative to the application.

Temperature and Relative Humidity Calculations - Batch 006 (NaCl, 40°C Temp. Set Point)										
Calculations	Temperature									
	Sensor 1 (S1)	Sensor 2 (S2)	Sensor 3 (S3)	Sensor 4 (S4)	Sensor 5 (S5)	Sensor 6 (S6)	Sensor 7 (S7)	Sensor 8 (S8)	Sensor 9 (S9)	Sensor 10 (S10)
Mean Temp.	40.30	39.92	40.01	40.28	40.14	40.06	40.17	40.01	40.25	39.91
Total Mean Temp. (S1 thru S10)	40.10	40.10	40.10	40.10	40.10	40.10	40.10	40.10	40.10	40.10
Departure From Total Mean Temp.	0.20	-0.19	-0.10	0.18	0.04	-0.04	0.06	-0.10	0.14	-0.20
STD	0.0086	0.0078	0.0084	0.0082	0.0086	0.0083	0.0088	0.0096	0.0092	0.0090
Total STD (S1 thru S10)	0.145	0.145	0.145	0.145	0.145	0.145	0.145	0.145	0.145	0.145
COV	0.0214%	0.0195%	0.0209%	0.0203%	0.0214%	0.0208%	0.0218%	0.0241%	0.0230%	0.0227%
Total COV (S1 thru S10)	0.36%	0.36%	0.36%	0.36%	0.36%	0.36%	0.36%	0.36%	0.36%	0.36%
Calculations	Relative Humidity									
	Sensor 1 (S1)	Sensor 2 (S2)	Sensor 3 (S3)	Sensor 4 (S4)	Sensor 5 (S5)	Sensor 6 (S6)	Sensor 7 (S7)	Sensor 8 (S8)	Sensor 9 (S9)	Sensor 10 (S10)
Mean RH	76.41	77.72	78.11	78.13	77.28	78.08	77.38	78.01	78.12	77.41
Theoretical RH	74.69	74.69	74.69	74.69	74.69	74.69	74.69	74.69	74.69	74.69
Residual RH	1.72	3.02	3.42	3.44	2.58	3.39	2.69	3.31	3.43	2.71
STD	0.0158	0.0150	0.0107	0.0152	0.0161	0.0154	0.0145	0.0151	0.0111	0.0113
Total STD (S1 thru S10)	0.557	0.557	0.557	0.557	0.557	0.557	0.557	0.557	0.557	0.557
COV	0.0207%	0.0193%	0.0137%	0.0194%	0.0208%	0.0197%	0.0187%	0.0194%	0.0143%	0.0146%
Total COV (S1 thru S10)	0.75%	0.75%	0.75%	0.75%	0.75%	0.75%	0.75%	0.75%	0.75%	0.75%

Table 5: Tabulated calculation values for all the sensors in the example batch (batch 006) at the example set point temperature (40°C)

7.2.4.3 Step 3 – Calculation of the RH residual and calibration models

In step 2, a theoretical RH residual value was calculated for sensor 6 of batch 006 at a temperature set point of 40°C. This process would be repeated for each sensor in the RH calibration group, until all the theoretical RH residual values chosen to span the relative humidity and temperature domain had been determined. In step 3, the example calculation continues with the calculation of the RH residual model specifically for sensor 6; the reader may recall that this is the sensor assigned to probe 4 in the representative deck specimen. In determining the RH residual values needed, the group of sensors that this specific sensor belonged to was exposed to sodium chloride (NaCl), potassium chloride (KCl) and potassium sulfate (K_2SO_4) saturated salt environments; the corresponding RH calibration batch numbers were 006, 002 and 007 respectively.

Before the author proceeds to calculate a residual model for sensor 6, it may be helpful to look at the following set of plots (figures 34, 35 and 36). For a given saturated salt solution, the theoretical RH residual values, which span the relevant temperature domain, show a high degree of linearity. The author produced similar plots for all the sensors used in this investigation, each having the same level of linearity. This phenomenon has been attributed to the manufacture's calibration of the sensor prior to the author's attempt to attain more precision from the sensors over the user-defined domain. Based on this observation, it was reasonable to assume that the residual model could be produced with a planar function best-fit of the theoretical RH residual values.

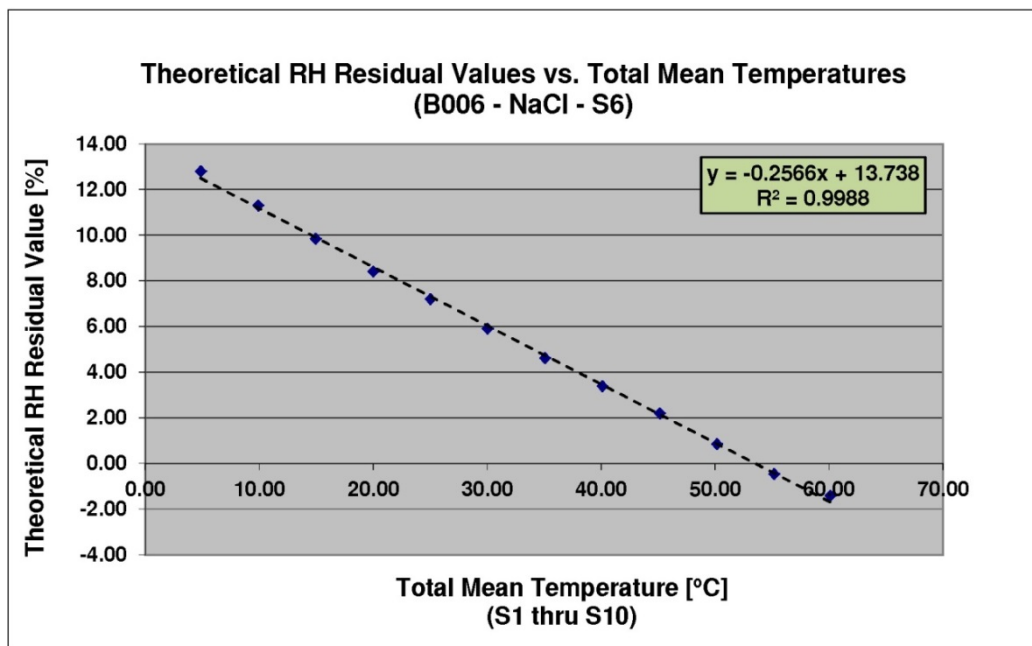


Figure 34: Graph of theoretical RH residual values versus total mean temperatures for sensor 6 of batch 006

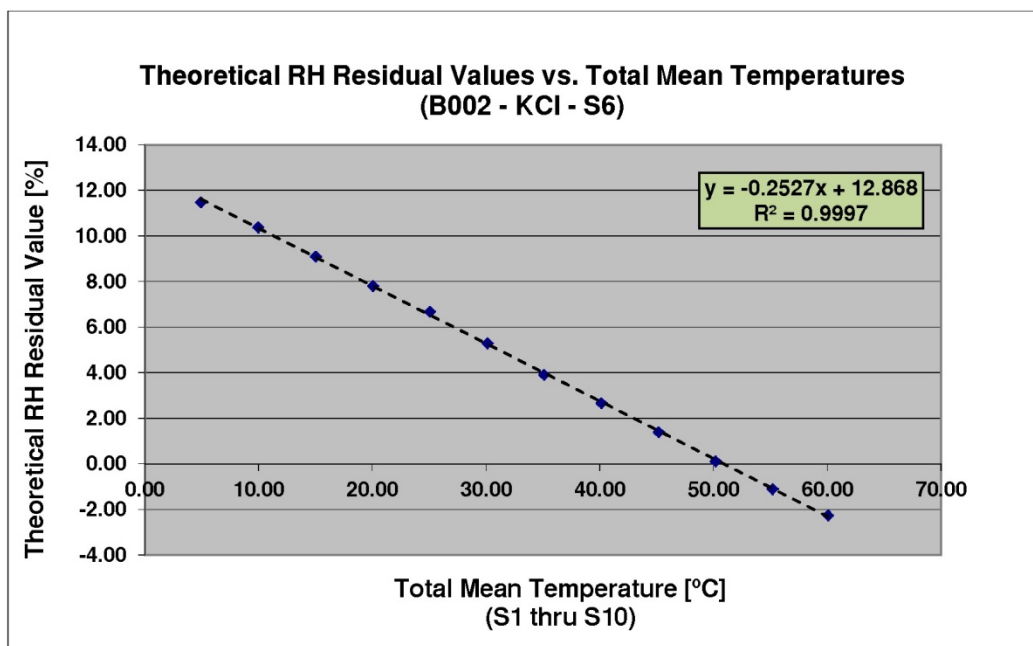


Figure 35: Graph of theoretical RH residual values versus total mean temperatures for sensor 6 of batch 002

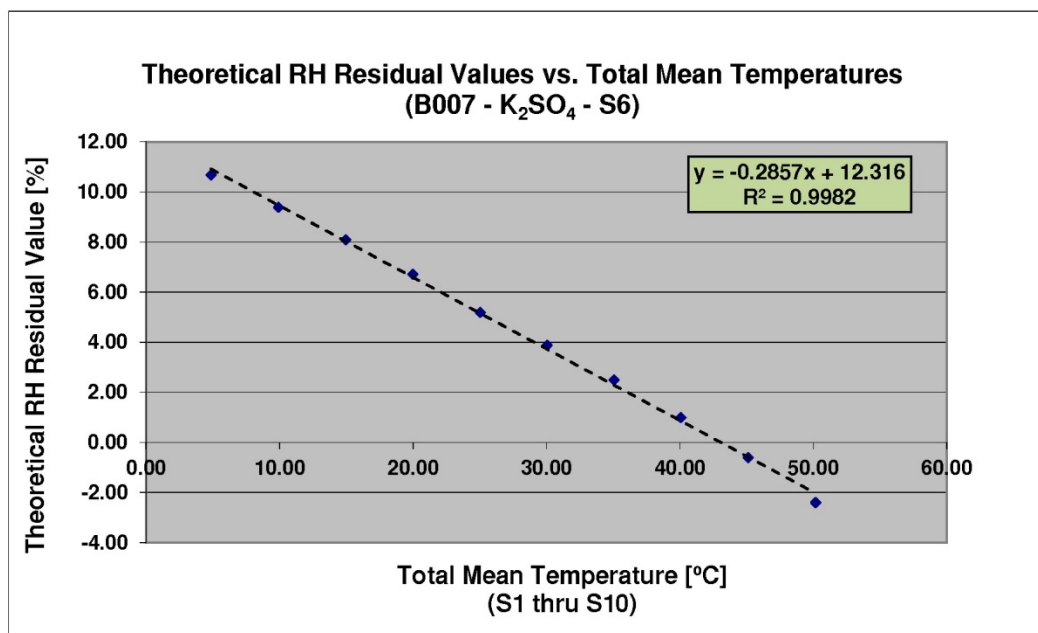


Figure 36: Graph of theoretical RH residual values versus total mean temperatures for sensor 6 of batch 007

After plotting all the theoretical RH residual values for sensor 6 (see table 6), one gets the 3-dimensional plot shown by figure 37. It should be noted that only the data points up to the 50°C nominal set-point temperature were used. Looking at the plotted potassium sulfate (K₂SO₄) data points, next to the data points for the other two salts (as seen in view

b of figure 37), a noticeable non-planar trend is visible. The author does not think that this level of non-planar behavior poses a serious problem for using a best-fit planar function, when the intention is to interpolate RH residual values up to the RH limits of the potassium sulfate (K_2SO_4) saturated salt solution. However, extrapolation beyond the designated limits of this salt solution is not advisable. Since there is a possibility that environments of up to 100% RH may be encountered, this issue should be dealt with. There are at least three solutions to this problem:

1. Use a non-planar RH residual model (a more complex function).
2. Use two different sensors, each having a different best-fit planar function RH residual model. One sensor would be used in the moderate RH environments (below about 95%) and the other sensor be reserved for use in high RH environments. However, the use of a two sensor system would raise issues concerning practical implementation.
3. Use a multi-planar RH residual model (a blending of the first two options). This method would employ the use of two different best-fit planar function RH residual models, with a logic statement governing the models used.

Regardless of the method used, if RH values greater than about 95 to 98% are expected, then additional theoretical RH residual values at 100% should be obtained by exposure to a pure water environment over a temperature domain. A note of caution though: when exposing the sensors to a 100% RH environment, sequence the set-point temperatures in order from low to high, to avoid the formation of condensation on the sensor element.

Sensor – 6 Theoretical RH Residual Coordinate's (B006, 002 and 007, Respectively)			
Data Point No.	Sodium Chloride – NaCl		
	Mean Temperature [°C]	Mean Relative Humidity [%]	Theoretical RH Residual [%]
1	4.93	88.50	12.80
2	9.94	87.00	11.30
3	14.95	85.45	9.85
4	20.00	83.90	8.40
5	25.02	82.49	7.20
6	30.01	81.00	5.90
7	35.03	79.52	4.62
8	40.06	78.08	3.39
9	45.07	76.70	2.20
10	50.10	75.36	0.86
-----	Potassium Chloride - KCl		
1	5.02	99.20	11.49
2	10.04	97.19	10.38
3	15.07	95.00	9.11
4	20.10	92.90	7.81
5	25.09	90.88	6.69
6	30.11	88.89	5.30
7	35.09	86.90	3.92
8	40.11	84.96	2.68
9	45.11	83.10	1.41
10	50.14	81.30	0.12
-----	Potassium Sulfate - K ₂ SO ₄		
1	4.89	109.20	10.69
2	9.94	107.60	9.40
3	14.95	106.00	8.10
4	19.99	104.32	6.72
5	25.02	102.50	5.20
6	30.02	100.89	3.90
7	35.04	99.20	2.50
8	40.05	97.40	1.00
9	45.08	95.50	-0.59
10	50.13	93.40	-2.39

Table 6: All the determined theroretical RH residual values for senor 6 (of batches 006, 002 and 007)

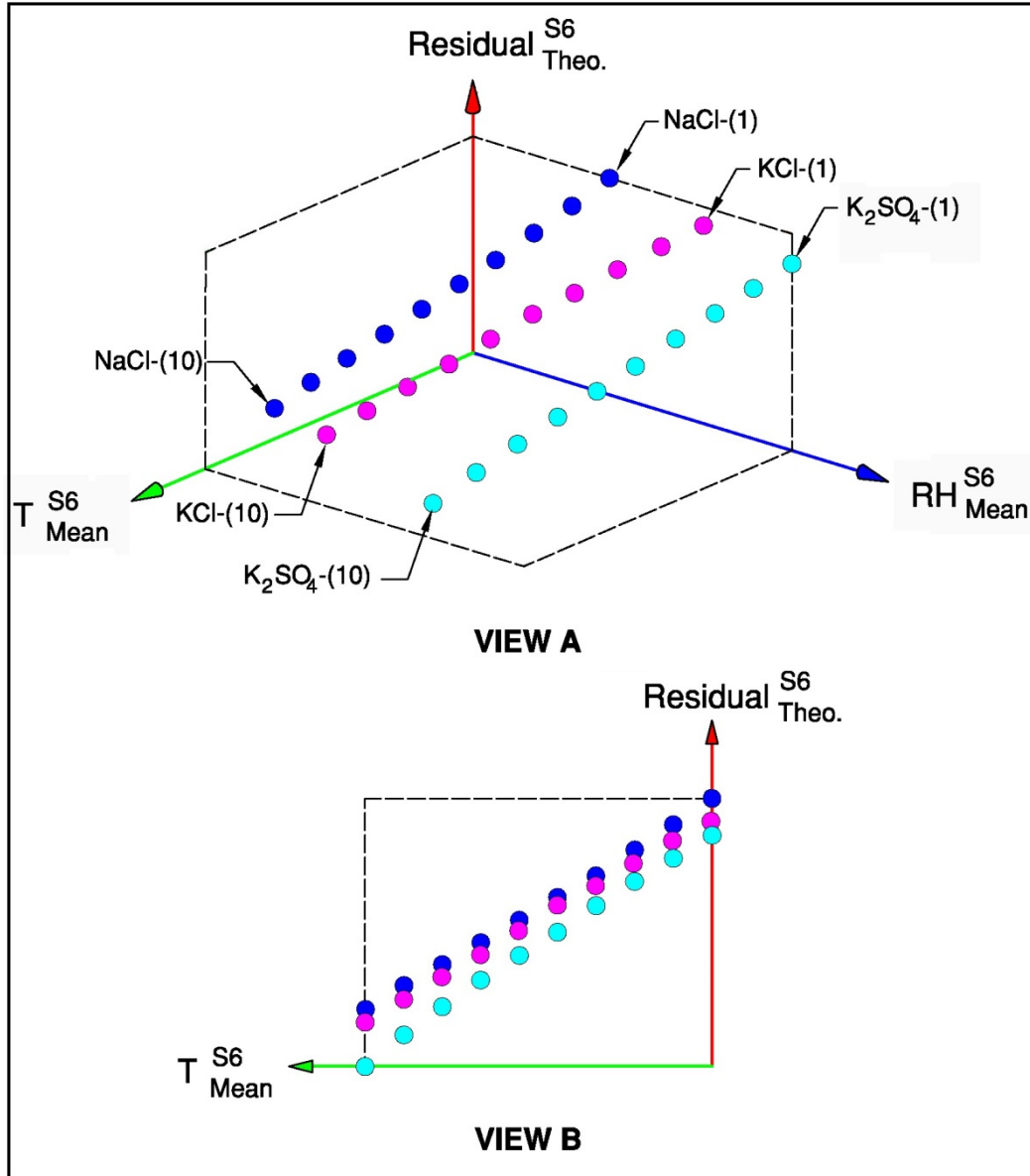


Figure 37: Scatter plot of sensor 6 theoretical RH residual values (batch 006, 002 and 007), with two views.

The author chose to employ the third option when developing the RH residual model. This selection was made for a few reasons. First, a best-fit planar function model, using “least-squares” can be developed with the “LINEST ()” function; this is a function built into the Microsoft® Excel (2007) program. Since the data obtained from the DAQ was exported by the author to this spreadsheet software package for other processing, it was easier to continue to use this package for this purpose as well. Also, the author believes that any added precision gained by using another package or add-on package to obtain a non-linear model would be trivial. Finally, if an operational environment only requires the use of a single-planar function, then the multi-planar model can easily be modified. This modification will be shown later.

In the context of this investigation the equation of the best-fit planar function takes the following form shown by equation 7.17. The Microsoft® Excel (2007) built-in function used to create the planar model, takes in the domain values (RH_{Mean}^{Si} , T_{Mean}^{Si}) and the corresponding theoretical RH residual range values ($Residual_{Theo}^{Si}$). Among the outputs provided are two equation coefficients ($C_{RH,k}^{Si}$, $C_{T,k}^{Si}$), an equation constant ($C_{const.,k}^{Si}$) and the coefficient of determination, R^2 , for assessing the “goodness-of-fit” (Navidi 2008). The two equation coefficients and the equation constant are substituted into equation 7.17.

$$Residual_{Mod.,k}^{Si} = C_{RH,k}^{Si} RH_{Meas.}^{Si} + C_{T,k}^{Si} T_{Meas.}^{Si} + C_{const.,k}^{Si} \quad \text{Equation 7.17}$$

where

- $Residual_{Mod.,k}^{Si}$: The k^{th} RH residual model for a specific i^{th} sensor RH residual model [%] (a function of two variables)
- $C_{RH,k}^{Si}$, $C_{T,k}^{Si}$: The k^{th} relative humidity and temperature coefficients (respectively), for a specific i^{th} sensor
- $C_{const.,k}^{Si}$: The k^{th} constant, for a specific i^{th} sensor

Assuming that a complete RH residual model will only require up to two planar best-fit models, the following logic (or conditional) statement can be calculated. The author starts the calculation with the two planar RH Residual models for a given i^{th} sensor, shown by equation 7.18 and 7.19.

$$Residual_{Mod.,1}^{Si} = C_{RH,1}^{Si} RH_{Meas.}^{Si} + C_{T,1}^{Si} T_{Meas.}^{Si} + C_{const.,1}^{Si} \quad \text{Equation 7.18}$$

$$Residual_{Mod.,2}^{Si} = C_{RH,2}^{Si} RH_{Meas.}^{Si} + C_{T,2}^{Si} T_{Meas.}^{Si} + C_{const.,2}^{Si} \quad \text{Equation 7.19}$$

At the intersection of these two planes equation 7.20 is true.

$$Residual_{Mod.,1}^{Si} = Residual_{Mod.,2}^{Si} \quad \text{Equation 7.20}$$

Since, the logic statement is to exist at this intersecting location, by equation 7.20, equations 7.18 and 7.19 may be set equal to each other. Subsequently, the resulting equality is solved for the RH term, $RH_{Meas.}^{Si}$, as shown by equation 7.21.

$$RH_{Meas.}^{Si} = \frac{(C_{T,2}^{Si} - C_{T,1}^{Si}) T_{Meas.}^{Si} + C_{const.,2}^{Si} - C_{const.,1}^{Si}}{(C_{RH,1}^{Si} - C_{RH,2}^{Si})} \quad \text{Equation 7.21}$$

This equation (equation 7.21) may be used as a delineation function. Serving in this delineation role, the measured RH value is no longer an independent variable; to avoid confusing the notation later on, it is re-labeled here as shown in equation 7.22.

$$RH_{Cond.}^{Si} = \frac{(C_{T,2}^{Si} - C_{T,1}^{Si})T_{Meas.}^{Si} + C_{const.,2}^{Si} - C_{const.,1}^{Si}}{(C_{RH,1}^{Si} - C_{RH,2}^{Si})} \quad \text{Equation 7.22}$$

where

$RH_{Cond.}^{Si}$: Conditional relative humidity for an i^{th} sensor, used in programming logic.
[%]

Now that a delineation function has been developed the complete RH residual model for an i^{th} sensor may be stated (see equation 7.23, 7.24 and 7.25). This is the final form that will be used in the RH calibration function.

$$\begin{aligned} Residual_{Mod.}^{Si} &= Residual_{Mod.,1}^{Si} \\ &\Rightarrow C_{RH,1}^{Si}RH_{Meas.}^{Si} + C_{T,1}^{Si}T_{Meas.}^{Si} + C_{const.,1}^{Si} \end{aligned} \quad \text{Equation 7.23}$$

if

$$RH_{Meas.}^{Si} \leq RH_{Cond.}^{Si} \Rightarrow \frac{(C_{T,2}^{Si} - C_{T,1}^{Si})T_{Meas.}^{Si} + C_{const.,2}^{Si} - C_{const.,1}^{Si}}{(C_{RH,1}^{Si} - C_{RH,2}^{Si})} \quad \text{Equation 7.24}$$

else

$$\begin{aligned} Residual_{Mod.}^{Si} &= Residual_{Mod.,2}^{Si} \\ &\Rightarrow C_{RH,2}^{Si}RH_{Meas.}^{Si} + C_{T,2}^{Si}T_{Meas.}^{Si} + C_{const.,2}^{Si} \end{aligned} \quad \text{Equation 7.25}$$

The author stated earlier that if an operational environment only required the use of a single-planar function, then the multi-planar model can easily be modified. A suggested approach to modifying the multi-planar model is as follows. By equation 7.24 it is obvious that if a single plane is used twice then a division by zero error occurs in the logic statement; the intersection would be infinite. The method that the author used to get around this problem is to introduce a trivial perturbation into the data set, when calculating the second planar best-fit. That is to say, the author chose a single theoretical RH residual value and added a very small value to it (i.e. on the order of 0.0001), prior to calculating the best-fit. This produced two planes which are theoretically different, yet practically speaking the difference is not noticeable in the resulting output.

Based on the inputs of table 6, the Microsoft® Excel (2007) function calculated the following values as shown in table 7, for sensor 6 (of batches 006, 002 and 007). As was

noted, the author at this point felt operational conditions only required the use of a single-planar model; therefore, the perturbation technique was applied.

k th Model No.	$C_{RH,k}^{S6}$	$C_{T,k}^{S6}$	$C_{const.,k}^{Si}$	R ²
1	-0.111468	-0.305696	24.242247	0.995808
2	-0.111469	-0.305696	24.242250	0.995808

Table 7: Planar best-fit values for sensor 6 (of batches 006,002 and 007)

At this point the author has developed an RH residual model for the sensor that will be used in probe 4. The RH calibration model for this sensor is complete when the developed RH residual model is substituted back into equation 7.2. Specifically, for this sensor (sensor 6 of batches 006, 002 and 007) the complete RH calibration function is as follows in equation 7.26.

$$RH_{cal.}^{S6} = RH_{Meas.}^{S6} - Residual_{Mod.}^{S6} \quad \text{Equation 7.26}$$

where

$$Residual_{Mod.}^{S6} = (-0.111468)RH_{Meas.}^{S6} + (-0.305696)T_{Meas.}^{S6} + 24.242247$$

if

$$RH_{Meas.}^{S6} \leq \frac{[(-0.305696) - (-0.305696)]T_{Meas.}^{S6} + (24.242250) - (24.242247)}{[(-0.111468) - (-0.111469)]}$$

else

$$Residual_{Mod.}^{S6} = (-0.111469)RH_{Meas.}^{S6} + (-0.305696)T_{Meas.}^{Si} + 24.242250$$

7.2.4.4 Step 4 – Implementation of the RH calibration model

In section 7.2, the author outlined, in a general way, how a user-defined RH calibration function would be applied to a specific sensor. Using this general form, the RH calibration function developed for sensor 6 (equation 7.26) would be coded to the probe 4 channel on the multiplexer. Each probe has a sensor assigned to it. Consequently, each sensor has a unique calibration developed for it. That code is sequenced in the DAQ code, and depending on the sequence, it is assigned to a corresponding channel on the multiplexer. Therefore, the probe needs to use the channel on the multiplexer that corresponds to the channel assigned to that probe's sensor calibration; otherwise, the wrong RH calibration function will be applied.

7.3 REPRESENTATIVE SPECIMEN AND SENSOR PLACEMENTS

7.3.1 Representative Specimen

The third step of the methodology outlined in section 6.1, was to obtain a representative concrete highway bridge deck specimen; therefore, the author selected an actual section of concrete bridge deck as shown in figure 38. The section of deck selected came from a decommissioned bridge along Route 708 (Red Hill Rd.) in Albemarle County, VA. The precise age of the deck was not determined; however, by observation it is a mature specimen, and was likely in operation for several decades prior to decommissioning and dismantlement. The rationale for selecting this concrete deck specimen is as follows. This investigation is principally interested in looking at the degree to which the scale (i.e. relative size) of a bridge deck may attenuate evolving internal [RH and temperature] conditions in response to continuously evolving external stimuli (i.e., RH, liquid moisture and temperature). In order to focus on this area, at this stage of investigation, the author wanted to be relatively sure that the specimen was fairly inert with respect to many other time dependent factors that had the potential to obscure results and findings. That is to say, the author wanted to be able to assume, with respect to moisture content and movement, the concrete behaved as a non-reactive solid skeleton surrounding a pore network. Consequently, the author needed to be reasonably sure that the structure would have had an opportunity to reach a sufficient level of internal hydration maturity; this precluded the use of a new concrete specimen.

The capillary pores of a new concrete structure, though hardened, are still evolving significantly with time. The author wanted to be sure that the pores would not be evolving in a meaningful way, either through the creation of new cementitious products or shrinkage deformation due to desiccation, during the investigation (Grasley, Lange, and D'Ambrosia 2006; Grasley and Leung 2011). It was assumed that an older specimen would not be susceptible to additional change in pore geometry in the same way a younger specimen would be during the time scale of this investigation. This would include assuming that any ongoing chemical processes effecting pore size (e.g., carbonation), if occurring, would be doing so on a time scale such that they may be neglected (Lamond and Pielert 2006). Additionally, if there were too much remaining mix-water in the large pore cavities, this would likely interfere greatly with RH measurements, by maximizing them, at the depths generally associated with placed reinforcement.

The author would like to note that the reason for targeting depths associated with reinforcement depths (and deeper) was twofold. First, the author wanted to ensure that the RH being determined was being influenced by diffused moisture and not from direct channels originating at the deck's surface (i.e., connected pores or cracks). Second, the author was primarily interested in moisture existing in the bulk of the deck's cross-

section. That is to say, the author was primarily interested in accounting for moisture directly in contact with reinforcement, as its deterioration was of particular interest.



Figure 38: Representative concrete bridge deck specimen (shown with epoxy overlay)

The concrete deck section is approximately square, having longitudinal and transverse dimensions of about 7'-5"; it has a nominal thickness of 8" and weighs approximately 5,500 pounds. The author has decided that a specimen with these dimensions is appropriate, as the hypothesis of section 4.2.2 hinges on the argument that "large" concrete structures, like bridge decks, have internal thermal gradients that are significantly more attenuated than smaller structures (e.g. a 4" x 8" cylinder of concrete).

When delivered, the concrete deck was placed on 5 courses of cement block that was stacked in a U-shaped pattern; for added safety the back side was constructed with an interlocking double course of cement block. Also, the concrete deck was placed with its riding surface facing upward. The final positioning of the deck, as described, was chosen to facilitate a simulation of naturally evolving [diurnal] field conditions and sensor placement technique. The entire structure was built on an existing [level] concrete slab located behind VCTIR's (Virginia Center for Innovation Transportation & Research) laboratory, in Charlottesville, VA. The concrete deck was delivered with an epoxy overlay in place; this was unexpected. Therefore, in order to expose the top of the concrete deck to natural weathering, the epoxy overlay was removed.

7.3.2 Sensor placement and data collection

The fourth step of the methodology outlined in section 6.1, was to install the relative humidity and temperature probes in the representative specimen. As shown in figure 39 the DAQ system (housed in the weather-tight enclosure) is mounted to the cement block wall beneath the concrete bridge deck specimen. Power is supplied to the DAQ system via an [orange] extension cord. The DAQ is grounded by a heavy gauge wire and grounding rod (not visible in figure 39). A cluster of (6)-probes (i.e. probe [type] 1, see

figure 26) were placed in the concrete deck, though only 5 were actually used. The probes were located approximately in the center of the deck, in a rectangular array pattern, spaced apart by approximately 5 inch intervals. The probe leads were run along the bottom of the deck from the location of the sensor array to the DAQ system, held in place by anchored conduit clips.

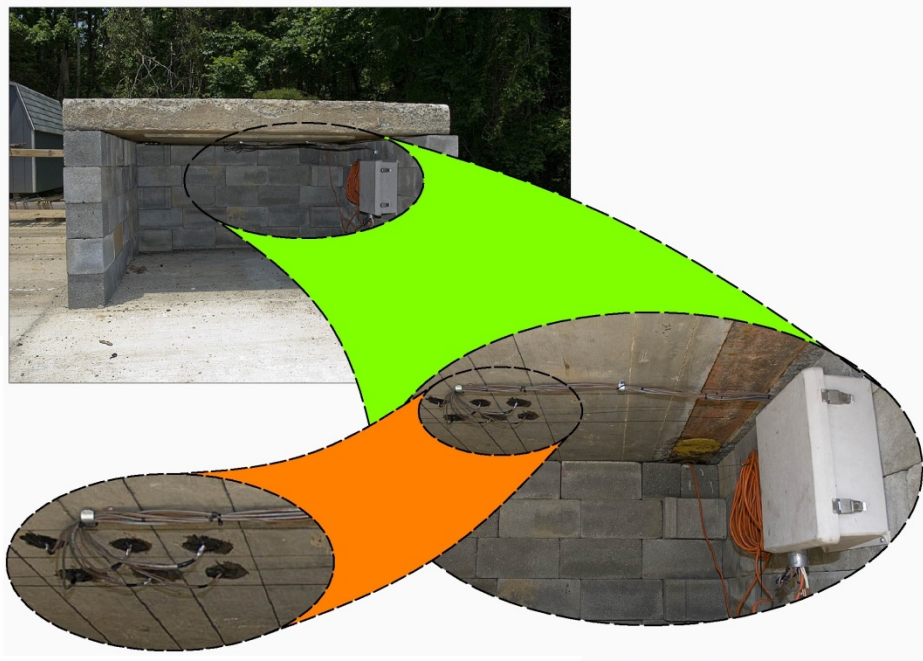


Figure 39: Representative concrete bridge deck with DAQ and probes installed

Each probe was placed in a $\frac{5}{8}$ [in.] diameter drilled hole, with depths that varied for each probe. Table 8 provides the depth assignments for each probe, where the depths are measured from the bottom of the deck. It should be noted that for the purposes of this investigation the author decided to omit the $2\frac{1}{2}$ [in.] depth (i.e. probe No. 2), using only the whole integer depths. Therefore, only 5 of the 6 probes were used in this investigation.

Probe No.	1	2	3	4	5	6
Depth [in.]	2	2.5	3	4	5	6

Table 8: Depth assignments relative to bottom of deck for all probes placed in the representative concrete bridge deck specimen

The probes were placed in the deck in a manner shown by figure 40. That is, a $\frac{5}{8}$ " diameter hole was first drilled into the concrete deck. The hole was then cleaned with a compressed air stream. The probe was inserted into the hole. Some frictional resistance is to be expected due to the thermocouple wire. If there is no resistance, then pull the sensor out, reset the thermocouple wire and re-insert. Fill in the space around the probe

with [non-volatile] high vacuum grease. It should be noted that the vacuum grease (shown in light blue) must be injected into the space, starting from the rubber weather-stripping and working outward. If one applies the grease to the probes exterior and then tries to insert it, the air void in front of the probe will create problems with the control volume of the cavity. The idea here is of two parts: (1) seal off all non-intended contributing concrete surface area and (2) eliminate all unnecessary open cavity volume. A lube-and-insert technique may satisfy the first part, but it will not satisfy the second. The resulting effects from both methods of probe placement are shown in the results section (section 8). To prevent the grease from leaking out of the hole over time, a small amount of silicone (caulking) is applied over the hole, extending radially for about an inch past the edge of the hole. After the silicone sets-up, it will also provide some resistance against probe movement, though the vacuum effect created by proper high vacuum grease injection should preclude such movement. It should be noted that the author is aware of a rubber gasket approach to probe placement, as outlined by ASTM F2170 entitled “*Standard Test Method for Determining Relative Humidity in Concrete Floor Slabs Using in situ Probes*” (ASTM Standard F2170 2011). While in theory this approach seems reasonable, in practice the author is a little skeptical about the quality of the air-tight seal that may be achieved by the [schematically presented] isolation gasket and liner ribs (or fins).

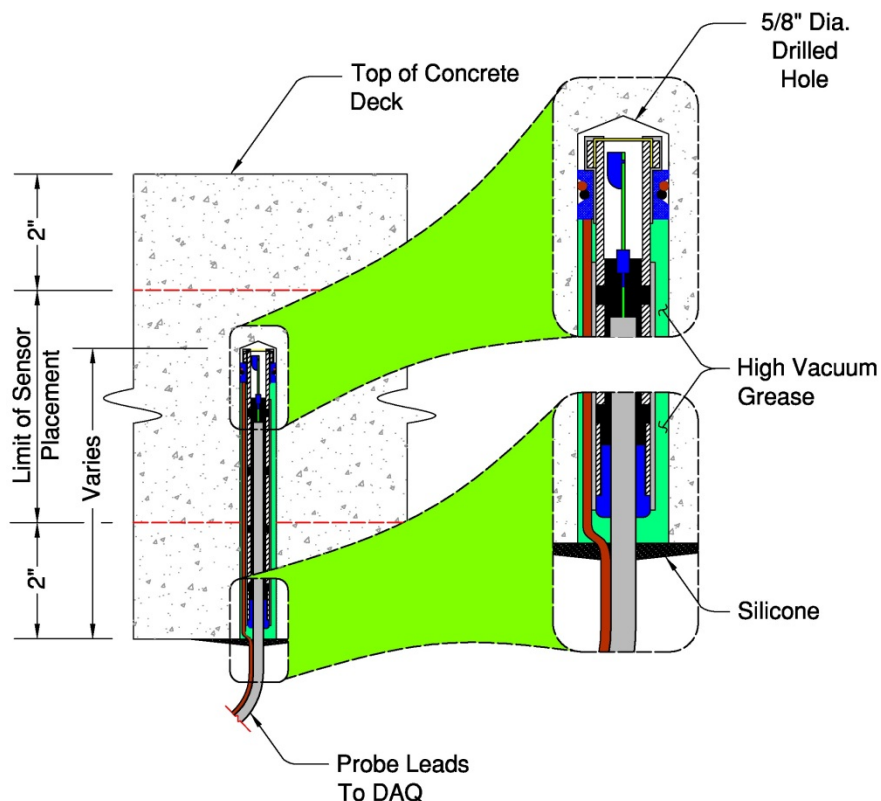


Figure 40: sectional view of a probe properly installed in the representative concrete deck specimen

The fifth step of the methodology outlined in section 6.1 is to collect and monitor the data over a period of several months. This is accomplished by periodic downloading,

processing and examination of the probe data store on the CR1000 data-logger. The data is downloaded via a direct connection over an RS232 serial cable and a laptop PC running the LoggerNet (4.1) software package as described in section 7.1.4. The data is processed and examined after the collected data is exported from LoggerNet (4.1) to a Microsoft® Excel (2007) spreadsheet.

7.4 Moisture SORPTION ISOTHERM CREATION

7.4.1 DAQ and Environmental Apparatus Design

To support the remaining steps of the methodology outlined in section 6.1, it is necessary to have an [acceptable] environment capable of generating multiple stable relative humidity and temperature conditions. This environment will be used in the creation of sorption isotherms. The sorption isotherms used in this investigation are developed, with some modification to, but in general accordance with ASTM C1498, entitled “Standard Test Method for Hygroscopic Sorption Isotherms of Building Materials”, (ASTM Standard C1498 2004a (2010) e1). According to section 5.4.1 of ASTM C1498, an acceptable controlled environment would include one similar to that used by the author to calibrate RH&T sensors (see section 7.2.3). As the reader may recall, this is a two part environmental design. An RH apparatus used to generate and contain relative humidity is placed in a larger programmable environmental chamber capable of producing [relatively] stable temperatures. The stable relative humidity environment in the RH apparatus is generated by saturated salt solutions, per ASTM E104. In this investigation, the author had developed an initial design, which during application proved not to be reliable. Ultimately, the author needed to reject this initial design for a more reliable one. In the interest of scientific disclosure, both designs will be described in this section. The impacts sustained by the initial design were minor and shall be addressed further in a later section (section 7.4.3). The difference between the two designs is limited to the RH apparatus; both designs still use the same temperature-producing environmental chamber and DAQ system.

The first RH apparatus, as shown in figure 41, was large enough to create the sorption isotherms for each of the specimens, to be created in later sections, simultaneously. The plastic box (shown as A) provided the structure for the RH apparatus. An aluminum pan was used to contain the saturated salt solution; the author decided that an aluminum pan would be acceptable, as it would not react with the saturated salt solution. The metal grating would serve as a permeable deck upon which the specimens could be placed. However, specimens contain uncured room temperature vulcanizing (RTV) silicone just after the final processing actions. Consequently, they may not contact the metal grate; the author cut PVC tubing having an outer-diameter (O.D) of 4” into 1” thick rings and attached them to the metal grating. These rings (or offset seats) allow for the seating of the specimen without the RTV having to make contact with a surface.

Once the specimens are placed in the RH apparatus, containing a saturated salt solution, an air-tight bag shaped plastic membrane is [lightly] vacuum sealed around it, containing the environment produced inside. Then this entire assembly is placed inside the

programmable environmental chamber, which is set to some nominal temperature. The flaw in this design has to do with the seal actually provided by the membrane. Two unexpected sources of air infiltration revealed themselves early on in the sorption isotherm creation process. The first source is at the membrane's [double] interlocking, zipper-style, seal. The author is not sure about whether or not a higher than provided level of vacuum is required to optimize the sealing effectiveness of the interlock, but on occasion this seal seemed to become compromised over time. Also, when closely examining the membrane, the author observed punctures. These punctures seemed to be caused by geometric irregularities in the plastic box and/or the environmental chamber's metal rack. Regardless of the source, air-infiltration is not acceptable and the RH apparatus was immediately redesigned.

The second and final RH apparatus, as shown in figure 42, was the solution to the problems caused by the often compromised membrane. This design, like the RH apparatus design used for RH sensor calibration, had a locking air-tight lid. For additional protection against air infiltration, the lid's [red] rubber seal was coated with high vacuum grease. The other major differences include the use of a 9" round glass dish to contain the saturated salt solution, instead of an aluminum dish. The offset seats are as they were in the previous design; however, 1/8" wooden spacers (cut to length) are used to ensure some separation. As this design is a tighter fit for the specimens than the previous one, the spacers are used to ensure that the specimens do not rub against each other. The final major difference is that the RH apparatus may only accommodate up to (4) specimens at a time; therefore, two RH apparatuses were constructed and used simultaneously. Both RH apparatuses were able to fit side-by-side inside the environmental chamber.

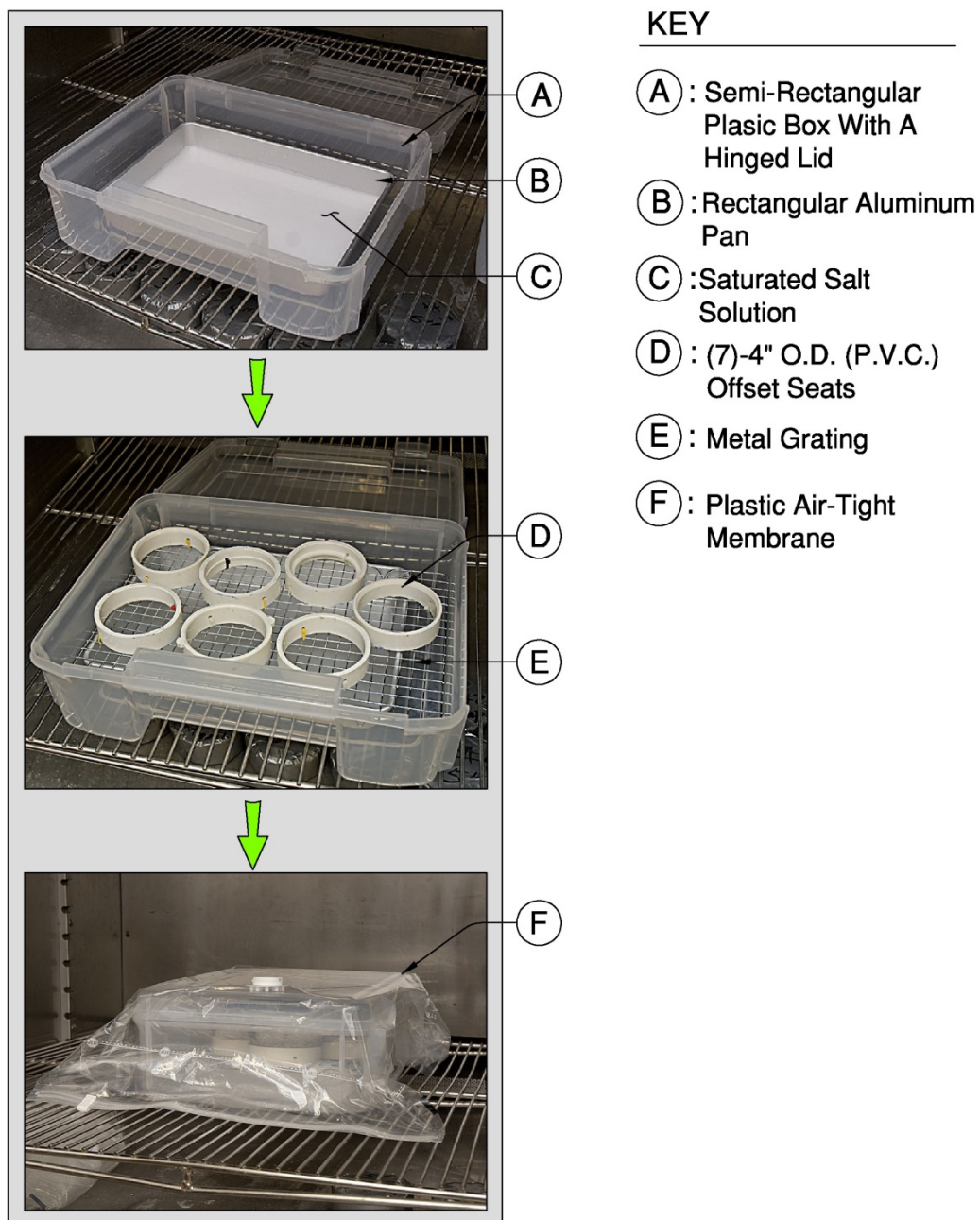


Figure 41: Initial RH apparatus design for sorption isotherm creation (shown inside the environmental chamber)

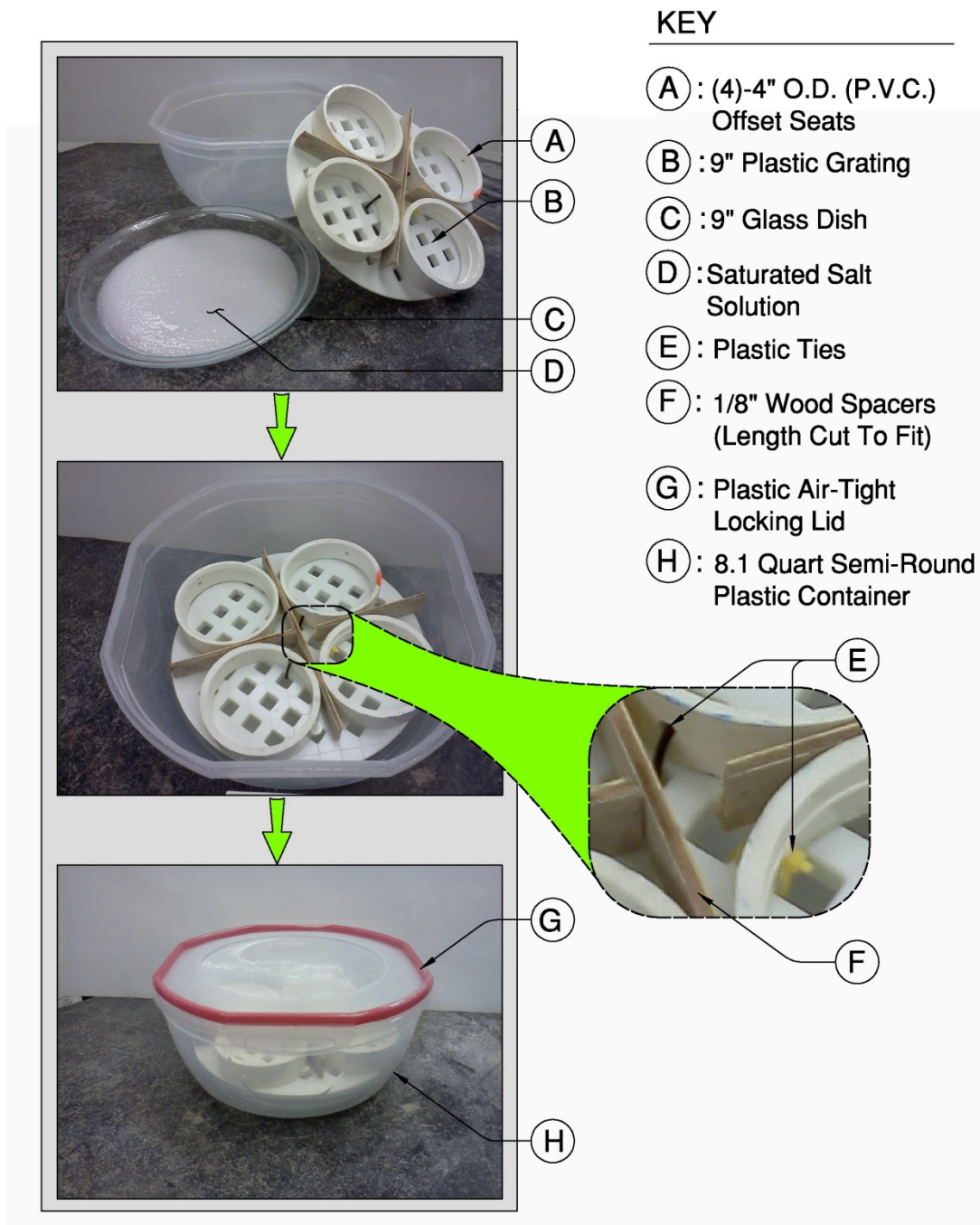


Figure 42: Final RH apparatus design for sorption isotherm creation (not shown inside the environmental chamber)

The data acquisition system (DAQ) used for the purpose of creating sorption isotherms is the same DAQ system used to collect data from the representative concrete bridge deck specimen. Once the cores were taken, as will be discussed in the next section, the DAQ system was powered down and dismantled from the concrete block wall (seen in figure 39) and brought into the lab, to be used in the creation of sorption isotherms. The RH&T

probes (Probe 1) were disconnected from their assigned terminals (on the AM 16/32B and AM 25T) and the new probes (Probe2) were connected; updates to user-defined calibrations were made at this time.

7.4.2 Disc Specimen Design

When sufficient data has been collected, the sixth step of the methodology as outlined in section 6.1 is to take several [full] core samples from the representative concrete deck specimen. The cores taken are nominally 4" in diameter with lengths that span the complete deck thickness of approximately 8". The cores taken are located in the vicinity of the placed probes. Several cores are required; this is due to the required minimum thickness for a given sample specimen used to create the moisture sorption isotherm. Additionally, extra specimens should be collected in the event that initial cores are somehow not acceptable for use. The process to extract the core samples began at approximately 12:00 pm on October 22, 2012. When creating the moisture content profile(s), via moisture sorption isotherms, this is the approximate "time-stamp" that the field data used shall correspond to.

A series of (5) cores were taken using a portable coring drill having a 4" I.D. core barrel. Extracting the sample specimens from the concrete deck involved a wet coring process. That is, water was used in the cutting process to keep the cutting barrel cool, lubricated and to flush out concrete debris. Consequently, once extracted the concrete cylinders were towel dried to remove any added moisture due to the extraction process. It should be noted that in theory wet-coring would cause some net gain of moisture at the surface of the specimen being cored. However, once the core specimen has been towel-dried, compared to the in-situ moisture mass contained below the surface, any residual moisture is considered trivial. Hence, wet-cutting is assumed not to affect the determination of the in-situ moisture mass in a meaningful way. Also, as the author proceeds, there were other various "wet" processes involved (i.e., slicing and drilling); for all of these processes, exposure to cooling water was kept to the minimum necessary to prevent overheating and the same assumption was applied. The cores were then immediately wrapped, to prevent moisture change, until they could be further processed. The wrapping process involved the application of the four following layers. The first layer applied was a plastic wrap, followed by a layer of aluminum foil. The third layer was another layer of plastic wrap applied over the foil. The fourth and final layer was duct tape. The duct tape was applied in such a way that it completely encased all the previous material layers. The core cylinders shall be used to create the moisture sorption isotherms required for this investigation. However, before the cores can be used, per the seventh step of the methodology, they will be processed into multiple smaller [disc-shaped] samples. These smaller disc samples will ultimately facilitate the determination of discrete moisture content values.

In general terms, the collected cores are sliced into discs with an approximate thickness of 1-1/2". The mid-point of a given disc's thickness corresponds to a known depth location within the representative concrete deck. This will facilitate the collection of [relative humidity, temperature and mass] data that is representative of the concrete at that depth in the representative deck specimen. The known depths used shall correspond

to the depth locations of the probes (Probe 1) initially placed in the representative concrete deck. For example, to obtain a disc specimen having the in-situ properties (e.g. density, moisture content, solution composition, and etc.) of the concrete in the vicinity of a probe placed at the 2" depth location, the following steps would be taken. First, one would measure along the core, from the bottom, upwards to a distance of 2". Then, that location along the core would be marked, and a saw cut made $\frac{3}{4}$ " above and below that mark would be made.

Additionally, the disc specimens will have holes drilled into them at the location of the marks. This allows for the placement of the second type of RH&T probe (Probe 2), which was created specifically for this application. This probe will collect RH&T data specific to the disc specimen it is assigned to. The idea is that mass and internal RH&T data may be collected from specimens that are small enough such that any calculations made from the data, including moisture content, may be viewed as "discrete". Additionally, the in-situ "discrete" data collected during the creation of the disc specimens may be used to validate the calculated results at the finale. Presented here is a general, high level, description of a more complicated process. This process is presented in greater detail by the author in appendix C. It should be noted that there were two types of disc specimens prepared. The first type, corresponding to the 2", 3", 4" and 5" depth locations, had RH&T probes installed in them. The second type, corresponding to the 1" and 7" depth locations did not contain probes; they were just plugged with a rubber stopper. However, in every other way these two disc specimen types were prepared identically. A graphical depiction of a finished disc specimen, having a placed RH&T probe, is shown in figure 43.

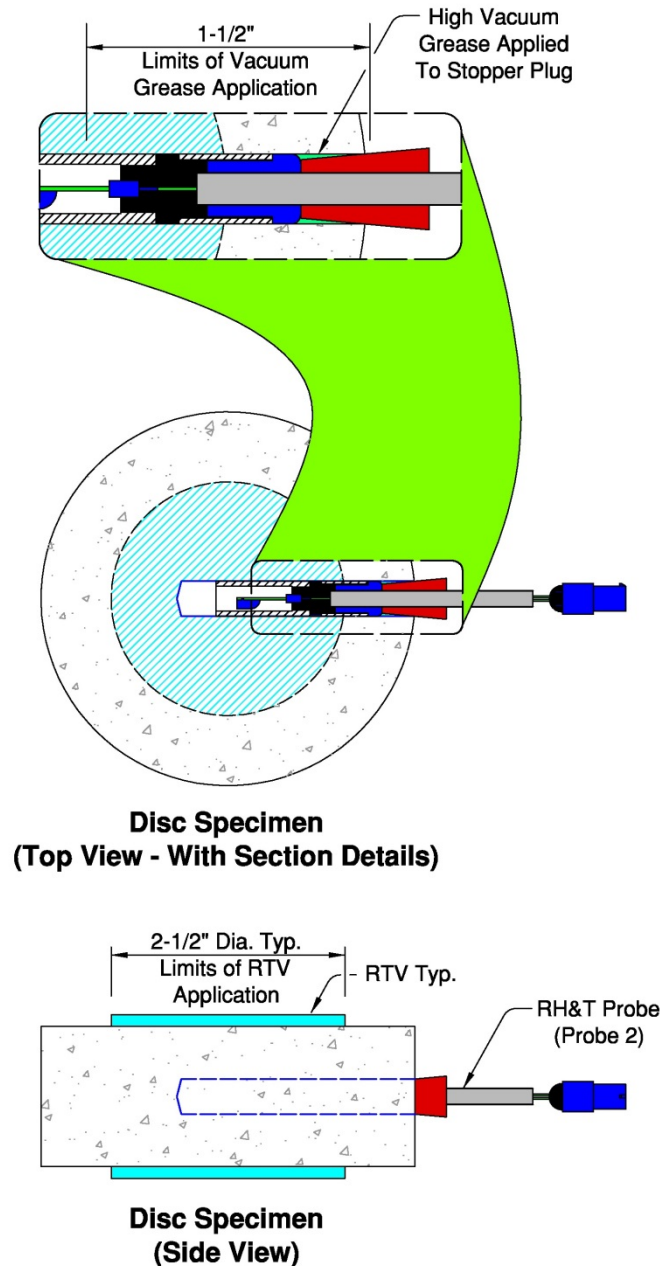


Figure 43: Fully processed concrete disc specimen, shown by side and top views. The top view includes interior probe placement details.

As part of the probe assembly, a rubber stopper was included; the stopper's function is to seal the hole behind the probe. High vacuum grease is applied to the stopper, serving to increase the effectiveness of the seal. Additionally, between the wall of the hole and the exterior wall of the probe housing a thin layer of high vacuum grease is applied. This layer of high vacuum grease extends from the hole entrance inward to a depth of $1\frac{1}{2}$ "; it was placed there for two purposes. First, should the [grease reinforced] rubber stopper fail to seal properly, the vacuum grease would prevent air infiltration along the interface

between the probe housing and the specimen. The second, and more immediate, function it serves is to extend the effective cover distance between the outer generated ambient environment and the inner environment surrounding the sensor. This was done to reduce the chance of a direct pathway between these two. A direct path would undermine the use of probes to measure internal RH.

It should be noted that this method of using internally placed RH&T sensors for sorption isotherm creation is a departure from the ASTM C1498 standard. To determine a hygroscopic material's moisture sorption isotherm, ASTM C1498 uses the observed relationship between the material's contained moisture and the relative humidity generated by the RH apparatus, at equilibrium. However, this would imply that, at equilibrium, the material's internal RH is equal to the externally generated RH. This may be true for the kinds of materials this standard was initially meant to deal with (i.e. insulating materials). However, for the purposes of this investigation, the moisture contained in the material of interest is assumed to be an aqueous electrolyte solution, not water. Consequently, the author did not think it was wise to extend the assumption made by the standard in this area to this application. The author would rather cautiously explore the possibility that at equilibrium the internal RH and external RH values are different. If they are different, then it is the internal RH that is required for this investigation.

As shown in figure 44, to extend the effective cover distance the high vacuum grease works in conjunction with the applied room temperature vulcanizing (RTV) silicone. As shown in both figures (figures 43 and 44), the RTV is applied to the top and bottom of the disc specimen. It should also be noted that the RTV applied to the disc specimen is initially uncured and in a liquid state. However, it is highly viscous and due to the design of the RH apparatus it is not necessary to wait for the RTV to solidify before the moisture sorption isotherm creation process may begin. Also, as neither the high vacuum grease nor the RTV are volatile or hygroscopic, mass change of these materials is assumed not to occur over time.

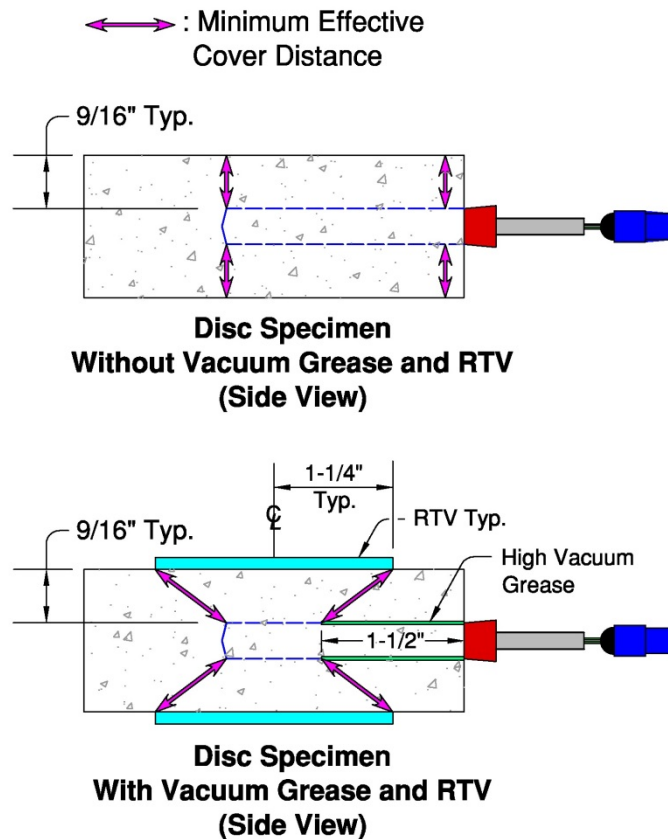


Figure 44: Side views of two versions of a fully processed concrete disc specimen; indicating, qualitatively, the minimum effective cover distance of each version. The first version (on top) is without RTV and the second version (on bottom) is with RTV.

7.4.3 Calculations

7.4.3.1 Introduction

As was described earlier in section 2.3.3, in the context of this investigation, the moisture sorption isotherm is the relationship between a hygroscopic material's contained level of moisture (i.e. moisture content or percentage of saturation) and the relative humidity metric. While external ambient conditions are a driving force, effecting change on the internal conditions of a material, like concrete, the relative humidity of interest is that which is within the material. As stated in the previous section, the author does not assume that, at equilibrium, the internal relative humidity is equal to the external relative humidity generated by the closed saturated salt solution environment.

Procedurally, ASTM C1498 divides the determination of a moisture sorption isotherm into two separate procedures: one for the adsorption isotherm and one for the desorption isotherm. As the reader may recall, the moisture desorption isotherm is the moisture sorption isotherm relationship as just reviewed in the preceding paragraph, but as observed while the material is undergoing moisture loss. Consequently, the moisture

desorption isotherm is created while the externally generated relative humidity is systematically reduced from a maximum to a minimum value, for a given temperature.

It was concluded by the author that, for the purposes of this investigation, only desorption isotherms would be required. This is because the data collected from the representative concrete bridge deck specimen was to span only the relatively warmer [and typically drier] summer months in Charlottesville VA. The cores used to create the disc specimens would be extracted at the end of the summer months. Thus, it seemed reasonable to conclude that by the end of summer, any moisture inside the concrete would be tracking on a path of moisture desorption. This conclusion is reinforced by observations made by Andrade concerning the effects of seasonal cycles on evaporable moisture in concrete (Andrade, Sarria, and Alonso 1999).

7.4.3.2 Desorption data

Once the RH apparatus and disc specimens are assembled, the process to collect desorption data can begin. The author begins by placing the (7) prepared disc specimens into the (2) RH apparatuses, both containing a potassium sulfate (K_2SO_4) saturated salt solution, as shown in figure 45. Then the RH apparatuses, containing the disc specimens and saturated salt solution, are placed in the programmable environmental chamber and the temperature is set to 25°C. One will note, that according to table 3, at 25°C, potassium sulfate will theoretically produce, at equilibrium, an environment of approximately 97.3% relative humidity. According to ASTM C1498, the procedure assumes a temperature of 23°C; however, as the theoretical relative humidity values of table 3, per ASTM E104, are given in 5°C increments, it is convenient to use a temperature of 25°C.

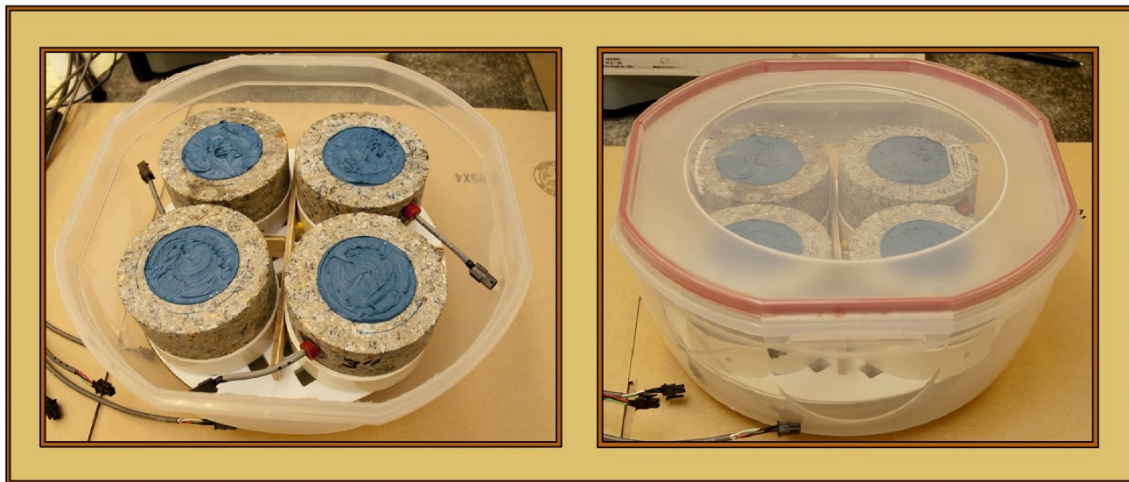


Figure 45: (4)-Concrete disc specimens shown in one of the two RH apparatus (environmental chamber not shown), with the lid off (see left) and lid on (see right)

According to ASTM C1498, the moisture desorption isotherm procedure calls for the specimen to be initially saturated with water. This would be achieved through immersing

the disc specimens in water, over a period of time. The period of time required would depend on whether or not the immersed specimens are simultaneously exposed to a vacuum. The author presumes that this is to ensure that all the data obtained during the procedure lies along the actual path of the moisture desorption isotherm, and not along another possible isotherm curve (i.e. adsorption or scanning). However, for two reasons the author has omitted this part of the procedure. First it was already assumed that the moisture levels in the specimens were tracking along the moisture desorption isotherm, with observed internal relative humidity values being in the general vicinity of 97.3% or higher. Second, and more importantly, by submerging the specimens in water at this point, the author would risk altering the solute content in the concrete. If this were to occur, then the specimens would no longer be representative of the representative bridge deck.

Every three to four days the RH apparatuses were removed from the environmental chamber, one at a time, for data collection. Unlike the probes placed in the representative bridge deck, the probes placed in the disc specimens are not continuously collecting data. The disc specimens are removed from the RH apparatuses and connected to the DAQ system by a (4)-conductor [shielded] wire lead having a female (4)-conductor connector end which mates with the male (4)-conductor connector end belonging to the probe. It is at this time that data collection occurs. Since the probes are sealed inside the disc specimens continuously, internal data can be and is collected immediately. The internal data collected includes relative humidity and temperature values. The reason the probes were not connected to the DAQ for continuous RH and temperature data collection was for two practical reasons. First, the RH and temperature data collected between readings would not have been useful in the actual creation of the moisture sorption isotherm. That is to say, the relevant internal RH and temperature data collected would need to correspond to disc specimen mass values. Second, it was much easier to control the ambient environment being produced without having to make allowances in the design for multiple cords entering the RH apparatus. In hindsight though, it would have been helpful to include a single RH&T sensor to monitor the ambient conditions being produced in the RH apparatus.

Finally, prior to placing the disc specimens back into the RH apparatus, their mass is determined by a calibrated scale; five mass values are taken for each disc specimen and then averaged. This process is repeated until the change in mass, for a given RH environment, has effectively ceased; ASTM C1498 defines a stabilized mass as one that does not change by more than 0.1% of the specimen's mass over 5 readings, each separated by 24 hours. However, as the author wanted to limit the out-of-apparatus time experienced by the specimens, the author chose not open the apparatus every day. Instead, the author monitored the data points, collected every few days, and when several data points, usually spanning more than 5 days, failed to change by more than 0.1% of the specimens mass, a specimen of stable mass was assumed to exist. The author considered this to be a more practical approach, while not violating the general intent of the standard. For a disc specimen of 600 grams, this means that a mass change of less than or equal to 0.6 grams over at least 5 days constitutes a stabilized mass. In truth, the

author waited for the change in mass to become significantly less. In most cases, over a minimum span of 5 days, the mass change was on the order of 0.1 grams or less.

Once mass stabilization occurs, the saturated salt solution is switched to one that will produce a relative humidity in the RH apparatus that is less than the one preceding it. This process is repeated until data spanning the entire required range of internal relative humidity is collected. For the purpose of this investigation, the author decided not to pursue an internal relative humidity of less than approximately 75% when developing the moisture desorption isotherm. Subsequently, the saturated salt solutions used were identical to those found in table 3, at a temperature of 25°C. The desorption data collected for all the specimens shall be presented later. At this time, to reduce clutter and aid the explanation to follow, the author shall present a plot of the desorption data collected for a single disc specimen, shown in figure 46. The disc specimen used in this figure represents the 2" depth location of the representative deck. Figure 46 and all other such plots were created at a nominal temperature of 25°C.

It should be noted that the plotted mass values, of figure 46, are the calculated moisture mass changes of a disc specimen with respect to its original in-situ mass of moisture. That is to say that the in-situ moisture mass serves as the datum from which all mass change is referenced. In general, a moisture mass change calculation takes the form of equation 7.27.

$$m_{\Delta H_2O}^{i-DL} = m_{Avg.Meas.}^{i-DL} - m_{prep}^{i-DL} - m_{In-situ}^{i-DL} \quad \text{Equation 7.27}$$

where

- $m_{\Delta H_2O}^{i-DL}$: Moisture mass change of a disc specimen, representing the i^{th} depth location [mass]
- $m_{Meas.}^{i-DL}$: Mass of a fully prepared disc specimen, representing the i^{th} depth location [mass]
- m_{prep}^{i-DL} : Mass of all non-cementitious materials used in the preparation of the disc specimen, representing the i^{th} depth location [mass]
- $m_{In-situ}^{i-DL}$: The initial in-situ mass of a processed disc specimen, which has not yet been fitted with non-cementitious materials, representing the i^{th} depth location [mass]

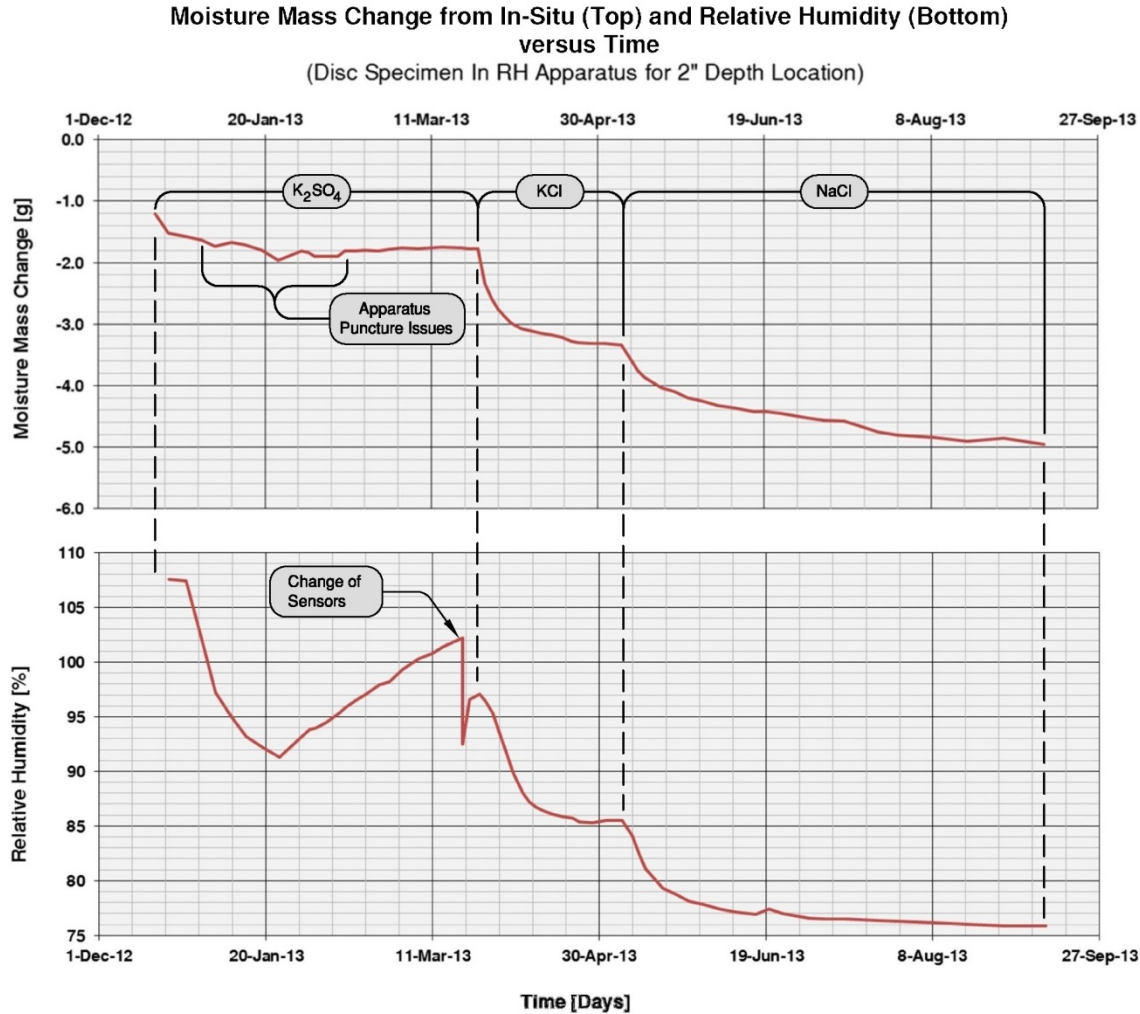


Figure 46: Plotted moisture mass change and relative humidity data versus time for the disc specimen representing the 2" depth location, while exposed to various RH environments produced by saturated salt solutions.

As an example, the author shall proceed to calculate the final moisture mass change value plotted in figure 46. The initial in-situ mass of the disc specimen used to represent the 2" depth location was 740.94 [g]. The determined mass of all the non-cementitious materials used to prepare the specimen (i.e. probe, high vacuum grease and RTV) was 14.87 [g]. The final recorded mass value of the fully prepared disc specimen during exposure to the sodium chloride (NaCl) generated RH environment was 750.85 [g]. Therefore, the moisture mass change at this point in the procedure would be calculated as shown by equation 7.28.

$$m_{\Delta H_2O}^{2"DL} = 750.85 - 14.87 - 740.94 \Rightarrow -4.96 \text{ [g]} \quad \text{Equation 7.28}$$

This result indicates that with respect to its initial in-situ state, at this point in the procedure, the specimen had lost 4.96 grams of moisture (or water). Also, it should be noted that the corresponding internal RH was recorded to be 75.83%. By inspection of figure 46, one can see that over a period of approximately 30 days leading up to this final

value, the change in moisture mass change $\Delta m_{\Delta H_2O}^{i-DL}$ was approximately 0.2 grams. As explained earlier, this conservatively goes far beyond what is required by ASTM C1498, for a sample greater than 700 grams, to conclude a stabilized mass has been reached.

Early in the procedure, during exposure to the potassium sulfate (K_2SO_4) produced RH environment, there were issues with both the apparatus and probe sensors; the effects are observable in figure 46. As described in section 7.4.1, the initial RH apparatus design was unreliable in preventing air infiltration, as the plastic membrane often became punctured. Since data was not collected continuously, it was only at the time of data collection that discovery of this issue occurred. Indication that there was a problem with environmental containment came in the form of erratic mass change behavior, as can be seen in the figure. In spite of efforts to be gentler with the membrane, puncturing the membrane was a constant problem. Immediately after the initial RH apparatus was replaced by the newer design, the “apparatus puncture issues”, as shown on the graph, ceased. Ultimately though, it does not appear that these puncture issues were severe enough to compromise the results of this procedure.

The second issue had to do with the probe sensors, specifically maintaining calibrated RH values. Initially the sensors that were placed in these probes had previously been used in the representative bridge deck. As will be covered in the results section, these sensors had experienced a severe shifting in the RH values they obtained, away from properly calibrated values, due to the undetermined environmental conditions inside the representative bridge deck. It is not clear to the author if the problem was from condensation forming on the sensor, volatile materials inside the concrete or some other problem affecting the hygroscopic material used by the sensor. Consequently though, new calibrations were developed and post-applied to the affected data collected from the representative bridge deck, where applicable. Those particular calibrations were determined immediately once the sensors were removed from the representative deck. However, approximately two months had passed between the time the sensors were removed from the representative bridge deck and the disc specimens were fitted with probes containing these sensors. The author chose not to assume that these calibrations were still valid, so the sensors were calibrated again just prior to placement in the disc specimens. Unfortunately, the same pattern of shifting values occurred again in the disc specimens. Consequently, the author allowed the sensors to continue collecting data in this condition until mass stabilization of the disc specimens occurred. At that time, the sensors were immediately removed and another calibration was quickly determined. The last RH value recorded by these sensors was corrected by this newer calibration.

Then instead of reinstalling the same sensors, the author replaced them with newer sensors, calibrated specifically over the nominal temperature range of 20°C to 30°C. The author did not immediately make any changes to the RH environment. Instead, the author allowed the new sensors to stabilize in the potassium sulfate (K_2SO_4) saturated salt environment. Doing this allowed for a direct comparison between the RH values of the newer sensors and the corrected RH values from the older sensors. The new sensors worked without incident throughout the remainder of this investigation. The calibrations corresponding to the sensors used in the disc specimen probes are located in appendix B.

Figure 47, shows the plotted desorption data collected for all (7) disc specimens. Recall that the specimens representing the 1” and 7” depth locations were not fitted with probes, though they were fitted with all the other materials, including a rubber stopper. Consequently, there were no corresponding RH values to plot for them. Later, the useful parts of this collected data shall be highlighted during the calculation of the moisture desorption isotherms. However, before moving on, the author needs to take a moment and make the following final comments.

As has already been commented on, during the collection of RH data in extreme conditions, the RH values obtained by the user-calibrated sensor may tend to shift away from calibration over time. A solution to this problem, while tedious, is to take the erring sensors after they have “adjusted” to their new extreme environment and obtain new calibrations over the necessary RH and temperature range. The calibrations obtained are then post-applied to applicable affected data. Consequently, from lessons learned during the collection of RH data from the representative bridge deck, the RH values collected during this procedure (i.e. creation of the moisture desorption isotherms) were both the user-calibrated values and non-user (i.e. manufacturer) converted values. This was done by toggling, on and off, the user-created calibrations in the code directly. In hind-sight the code should have been written to table both values simultaneously, without having to manually toggle the code. When needed, having both of these relative humidity values on hand greatly reduces the time required to apply this solution.

As one may observe from looking at figure 30 (in section 7.2.4.2), it takes several hours for the environment inside an RH apparatus to stabilize. Meaning, that if the author were to simply close the RH apparatus after data collection and place the assembly back into the environmental chamber, then several hours may pass during which time the disc specimens are exposed to very different [low] RH conditions. To ensure that the specimens remained on the path of the moisture desorption isotherm, prior to sealing the RH apparatuses, the author would take the assembly into a room having near saturated ambient conditions. It is in this room that after a few moments the RH apparatus would be sealed. This was done to ensure that RH conditions initially inside the apparatus would exceed the lower RH conditions to which the environment would eventually equilibrate.

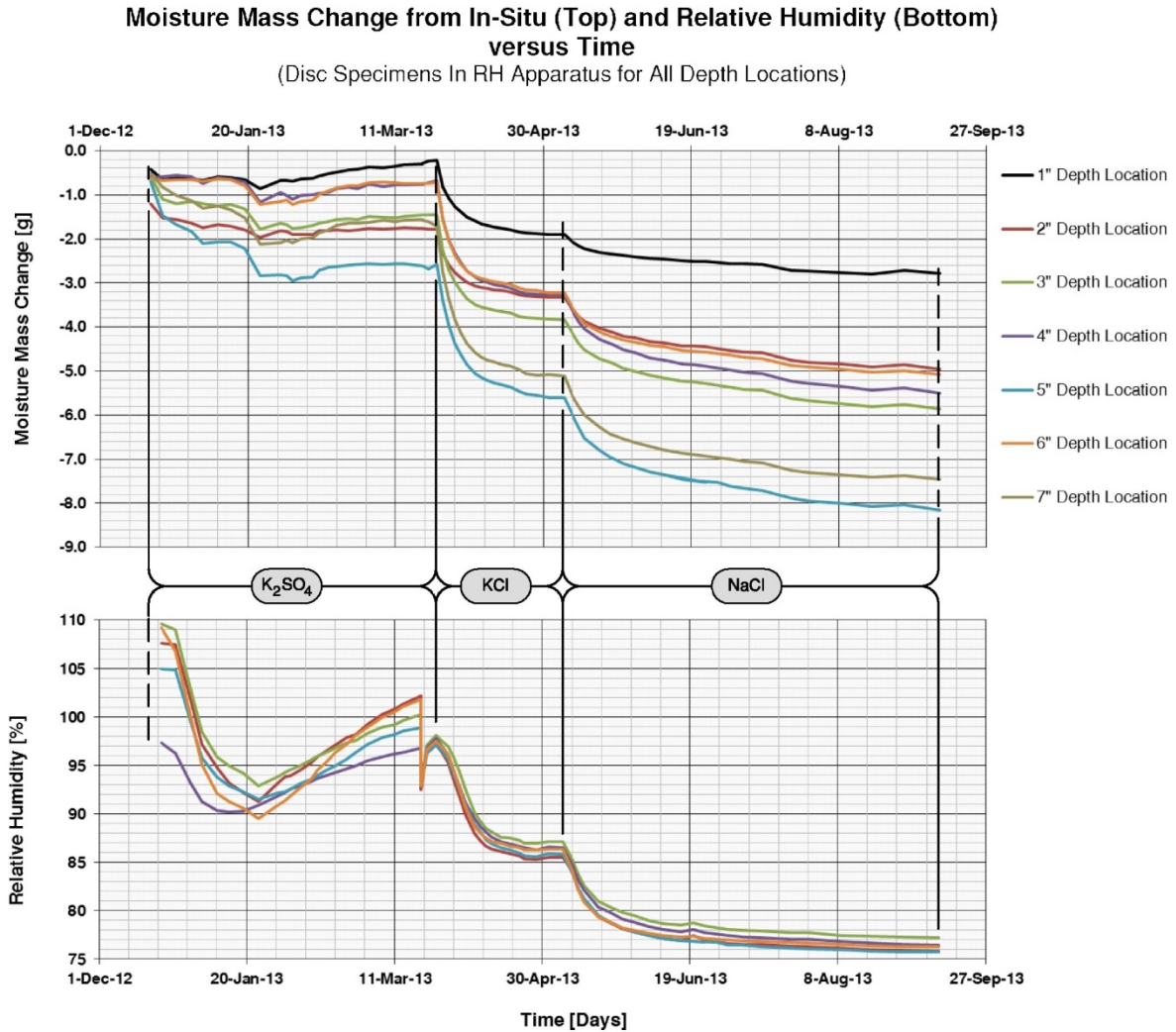


Figure 47: Plotted moisture mass change and relative humidity data versus time for all the disc specimens, while exposed to various RH environments produced by saturated salt solutions.

The author would like to make the following further comments pertaining to the departure of the preceding method from the ASTM C1498 method; in particular the use of internally placed probes. The idea behind using probes, instead of assuming the inner RH is the same as the produced outer RH, was to capture any RH differences that may exist between the internal and external environments for a given mass equilibrium. The author speculated that there might be unidentified influences, stemming from pore geometry or solute concentration, that would affect the chemical potential in such a way that differences might arise. Additionally, the method of sensor placement in the representative slab (i.e., drilling a hole) may have inadvertently altered the observed internal RH from that which would actually exist in the pore system. By placing sensors in the disc specimens, any effects to the representative deck would be replicated in the disc specimen, thereby accounting for any differences between the two systems. However, by inspection of figure 47, it would appear that given [much] more time the

observed internal RH would likely have stabilized to match the ambient produced RH levels. In future attempts to generate moisture sorption isotherms, the environmentally produced RH may be used. Consequently, much smaller concrete samples should be used; this will significantly decrease the time required to reach mass stabilization.

7.4.3.3 Saturated and dry mass determination

Once all the required desorption mass values are collected, as outlined in the previous section (section 7.4.3.2), the next step is to obtain the extreme mass values, in particular, the absolute [moisture] saturated and oven-dried masses for all disc specimens. This process begins by removing all the non-cementitious materials from the specimens. Ultimately though, the author was not successful in removing all the material. Inevitably, some of the RTV and high vacuum grease will remain inside the specimen's pores. However, an accounting of this unremoved material mass was made and used in later calculations to adjust the mass. Depending on the disc specimen, the unremoved material masses spanned from 0.38 to 1.10 grams. These materials were assumed to remain unremoved and unchanged in mass throughout the proceeding processes.

The first extreme mass to be determined was the absolute saturated mass of the disc specimens. ASTM C1498 briefly describes two methods for saturating hygroscopic materials to an “acceptable” level. The first of the methods include submersion of the specimen [in water] for 3-days while under vacuum (below 0.4 atm). The other method was to submerge the specimens for a period of 7 days if a vacuum environment was not to be used. As noted before, this standard was not necessarily written with concrete in mind. Similar to the first method above, the standard ASTM C1202 entitled “*standard test method for electrical indication of concrete's ability to resist chloride ion penetration*” offers a vacuum saturation sub-method written with hardened concrete samples in mind; the samples used in the standard are of similar geometry to those used in this investigation (ASTM Standard C1202 2012). It was in general accordance with the vacuum saturation process that the author proceeded to saturate the disc specimens. That is to say, there are several steps taken by ASTM C1202 to prepare the specimens for that standard's intended application, which are not germane and ignored for this investigation.

A vacuum saturation apparatus, similar to the one in ASTM C1202, is shown by figure 48. The top two panels of figure 48 show that the disc specimens are carefully placed inside the base of the vacuum desiccator. Once inside, the desiccator's lid is sealed over its base and a vacuum is created by the vacuum pump. The disc specimens remain in this environment for one hour. Then filtered water is drawn into the desiccator until the specimens are submerged, as also shown in figure 48 (bottom panel). The vacuum is maintained for an additional 3 hours. Finally, the vacuum is removed and the disc specimens remain submerged for no less than 16 hours longer. The author repeated this process three times to ensure that the specimens had reached a stable saturated mass. The specimens remained submerged between the process repetitions. In the previous section, the author avoided the use of this sort of saturation. This was to cautiously avoid any procedure which would disturb the internal chemistry of the specimen. However, at this

time the collection of internal RH data had concluded and the author no longer needed to be cautious in this respect.

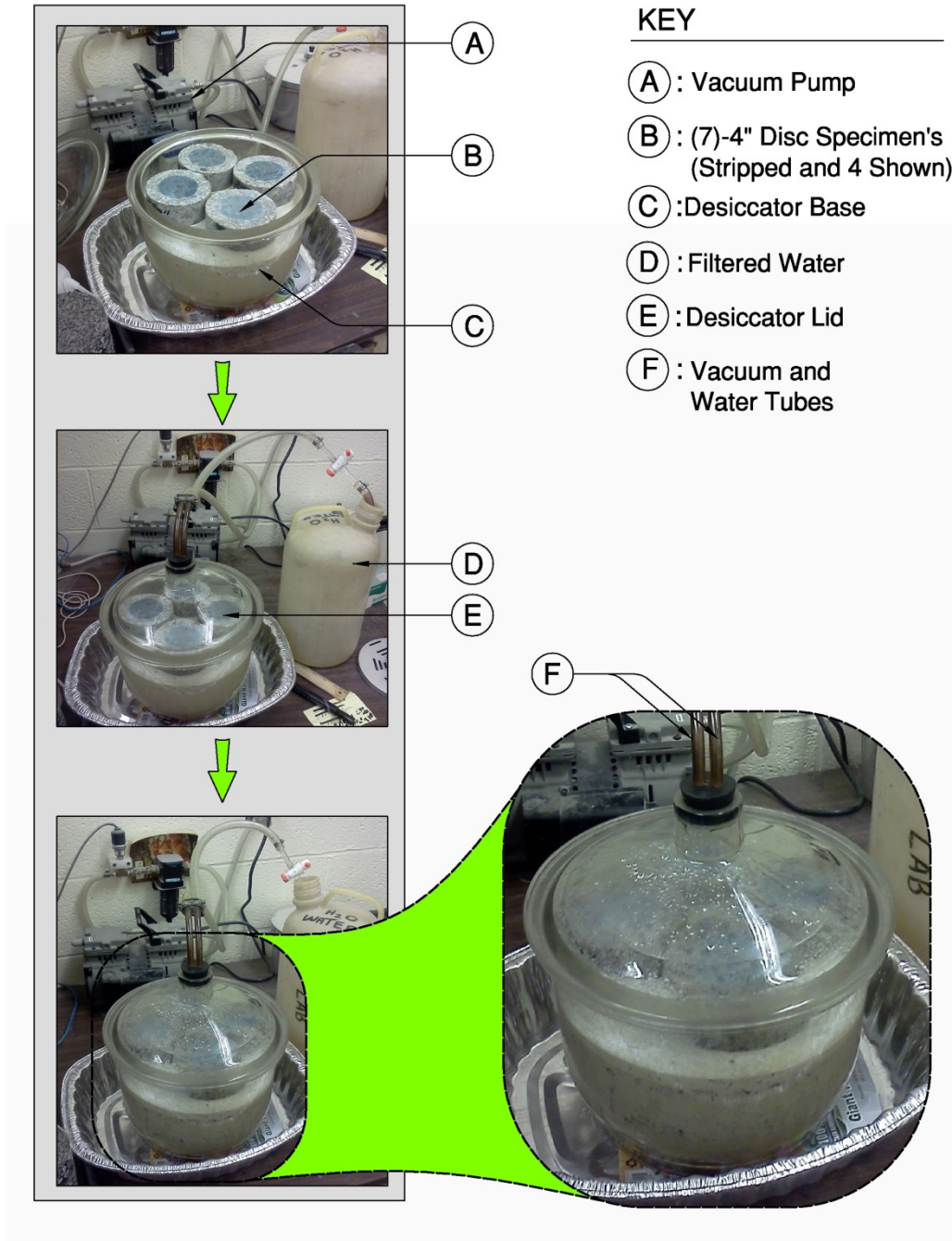


Figure 48: Vacuum saturation apparatus with all disc specimens inside (top), the vacuum is applied (middle) and specimens are submerged (bottom)

The second extreme mass to be determined was the oven dry mass of the disc specimens. As before, ASTM C1498 provides some instruction as to how this might be accomplished, but no clear instructions are specifically provided for hardened concrete. Consequently, the author decided to dry the specimen in general accordance with the standard ASTM C642 entitled “*standard test method for density, absorption, and voids in hardened concrete*” (ASTM Standard C642 2006). A sub-method in ASTM C642 specifically deals with determining the oven-dry mass of hardened concrete. ASTM C642 specifies that samples are placed in an oven at a temperature of 100 to 110°C (212 to 230°F) for periods of time no less than 24 hours. Then allow the specimen to cool down in a desiccator prior to weighing. This is repeated until a stable mass is reached. A stable mass is defined by the lesser mass of two successive values, where the difference in the measured masses is less than 0.5% of the lesser mass.

The author placed the (7) disc specimens in an oven and gradually increased the temperature over several days to approximately 260°F. This was done to ensure that the specimens would not be damaged by heating the specimens too rapidly. The author initially did not wait for the specimens to cool; they were weighted immediately as they were removed from the oven. The author assumed mass values were finally stabilized when mass differences on the order of 0.2 grams were achieved; for a least specimen weight of 600 grams, any change below 3 grams would indicate a stable dry mass. The author took the final mass values when the specimens were at room temperature after the specimens were allowed to cool in a desiccator with a desiccant. The final mass was on average approximately 0.3 grams greater than the previous uncooled values, but not sufficiently different to alter the conclusion of stable dry condition.

From the disc specimen mass values obtained during these two processes, moisture mass change values for each specimen with respect to the in-situ moisture mass were determined. The moisture mass change values were calculated in a manner similar to those calculated in section 7.4.3.2. The only difference is the following substitutions to equation 7.27.

$$m_{Avg.Meas.}^{i-DL} \rightarrow m_{Avg.Strip.}^{i-DL} \quad \text{Equation 7.29}$$

$$m_{prep}^{i-DL} \rightarrow m_{Unremoved}^{i-DL} \quad \text{Equation 7.30}$$

where

- $m_{Unremoved}^{i-DL}$: Mass of all non-cementitious materials which remain unremoved from the disc specimen, representing the i^{th} depth location [mass]
 $m_{Avg.Strip.}^{i-DL}$: Mass of a disc specimen having been stripped of most non-cementitious materials, representing the i^{th} depth location [mass]

As an example, the author shall proceed to calculate both of the extreme moisture mass change values for the disc specimen representing the 2” depth location. As was given in the last example calculation, the initial in-situ mass of the disc specimen used to represent

the 2" depth location was 740.94 [g]. The determined mass of all the non-cementitious materials which remained unremoved was calculated to be 1.10 [g]. The recorded stable mass value for the saturated condition was 748.87 [g] and for the dried condition was 712.27 [g]. Therefore, the extreme moisture mass change values for the saturated and dried conditions are calculated below by equations 7.31 and 7.32 respectively.

for the saturated condition

$$m_{\Delta H_2O}^{2"DL} = 748.87 - 1.10 - 740.94 \Rightarrow 6.83[g] \quad \text{Equation 7.31}$$

for the dried condition

$$m_{\Delta H_2O}^{2"DL} = 712.27 - 1.10 - 740.94 \Rightarrow -29.77 [g] \quad \text{Equation 7.32}$$

These results indicate that with respect to its initial in-situ state, at these points in the procedure, the specimen gained 6.83 grams of moisture (or water) in the saturated condition and lost 29.77 grams in the dried condition. These results along with the other calculated values, specifically for the disc specimen representing the 2" depth location, were plotted and shown in figure 49; this figure continues from figure 46. It should be noted that the difference between these two extreme values indicates that the total approximate mass of moisture this disc specimen is capable of containing is 30.60 grams. Additionally, the author has provided plots of the calculated moisture mass change values for all the disc specimens during this procedure in figure 50; this figure continues from figure 47.

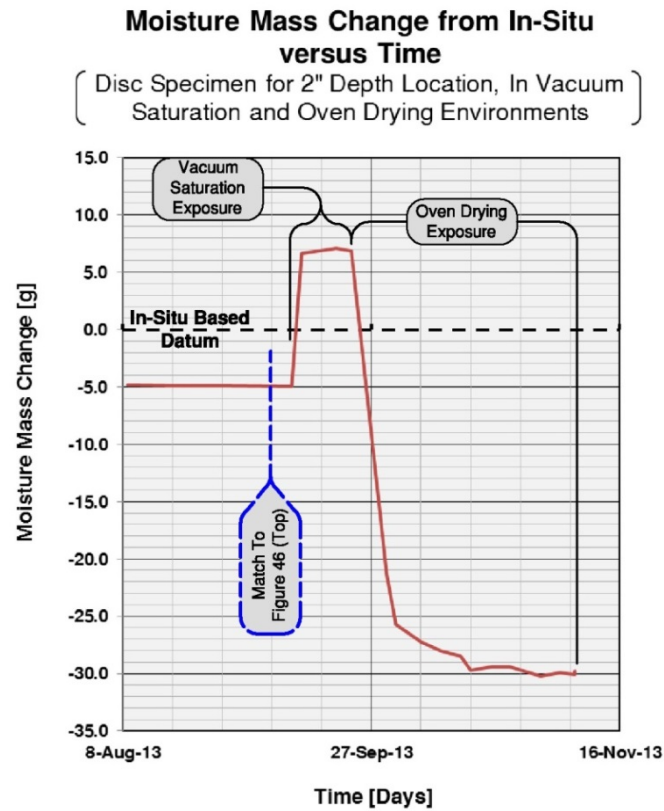


Figure 49: Plotted moisture mass change versus time for the 2" disc specimen, while exposed to vacuum saturation and oven drying conditions

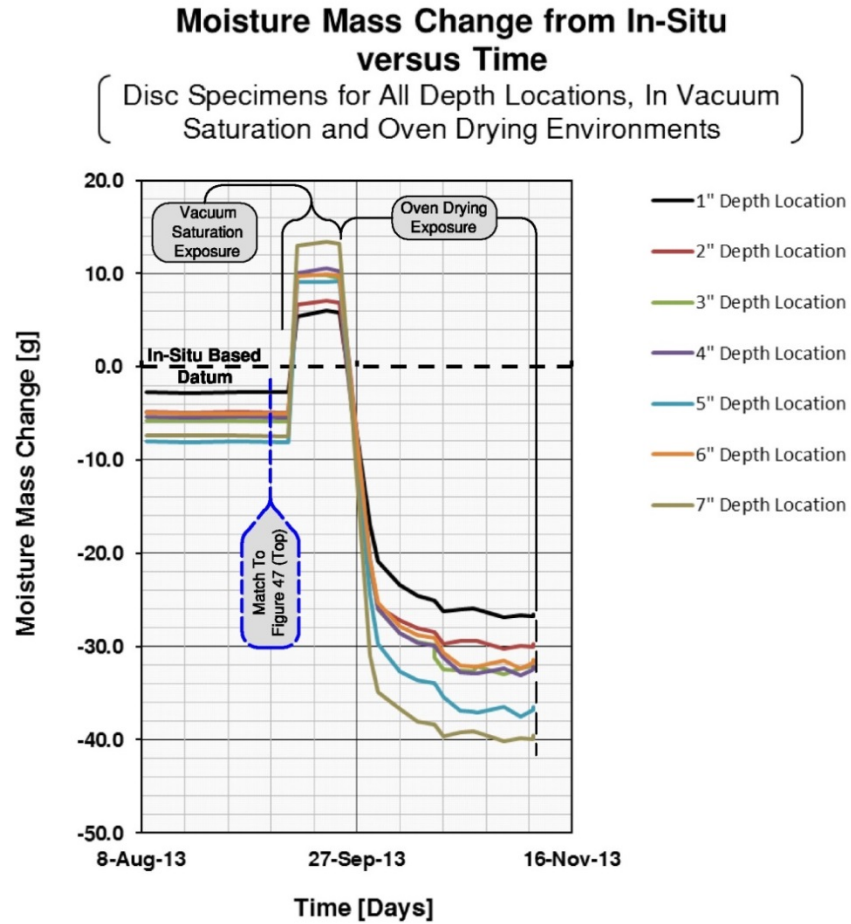


Figure 50: Plotted moisture mass change versus time for the all disc specimens, while exposed to vacuum saturation and oven drying conditions

7.4.3.4 Moisture sorption (desorption) isotherm

At this time the author has all the mass data required to create moisture desorption isotherms for the applicable disc specimens. A summary of stabilized values, necessary for many of the calculations to follow, is provided in table 9.

Depth [in.]	In-Situ Mass [g]	Moisture Mass Change and RH Values							
		Desorption						Extreme	
		K ₂ SO ₄		KCl		NaCl		Sat.	Dry
		Mass [g]	RH [%]	Mass [g]	RH [%]	Mass [g]	RH [%]	Mass [g]	Mass [g]
1	702.82	-0.22	N/A	-1.90	N/A	-2.78	N/A	5.87	-26.55
2	740.94	-1.77	97.10	-3.33	85.50	-4.96	75.83	6.83	-29.77
3	757.50	-1.45	98.10	-3.83	87.10	-5.87	77.20	9.51	-32.06
4	747.12	-0.68	97.80	-3.28	86.50	-5.51	76.47	10.29	-32.13
5	722.56	-2.59	97.10	-5.60	85.80	-8.15	75.71	9.16	-36.47
6	665.09	-0.71	97.50	-3.23	86.40	-5.07	76.29	9.80	-31.39
7	706.99	-1.70	N/A	-5.10	N/A	-7.46	N/A	13.24	-39.54

Table 9: Table of stabilized moisture mass change and RH values for all disc specimens

In section 2.3.3.3 of this investigation the author had indicated that moisture sorption isotherm may be expressed in terms of percentage of [liquid] saturation, S_L , versus relative humidity or as moisture content, MC , versus relative humidity. The percentage of saturation and moisture content calculations are straight forward and are of the general forms shown by equations 7.33 and 7.34, respectively.

$$S_L = \frac{\text{Solution Mass}}{\text{Maximum Solution Mass}} \times 100\% \quad \text{Equation 7.33}$$

$$MC = \frac{\text{Solution Mass}}{\text{Dry Specimen Mass}} \times 100\% \quad \text{Equation 7.34}$$

Where

$$\text{Solution Mass} = \text{Moisture Mass Change} - \text{Dry Moisture Mass Change} \quad \text{Equation 7.35}$$

$$\text{Maximum Solution Mass} = \text{Sat. Moisture Mass Change} - \text{Dry Moisture Mass Change} \quad \text{Equation 7.36}$$

$$\text{Dry Specimen Mass} = \text{In-Situ Mass} + \text{Dry Moisture Mass Change} \quad \text{Equation 7.37}$$

As an example, the author shall calculate the percent of saturation and moisture content values for the disc specimen representing the 2" depth location, having stabilized in the RH environment produced by the potassium sulfate (K₂SO₄) saturated salt solution.

Obtaining the necessary values from table 9, the following required masses are determined first.

$$\text{Solution Mass} = -1.77 - (-29.77) \Rightarrow 28.00 [g] \quad \text{Equation 7.38}$$

$$\text{Maximum Solution Mass} = 6.83 - (-29.77) \Rightarrow 36.60 [g] \quad \text{Equation 7.39}$$

$$\text{Dry Specimen Mass} = 740.94 + (-29.77) \Rightarrow 711.17 [g] \quad \text{Equation 7.40}$$

Now the author substitutes these determined values into equations 7.33 and 7.34 to obtain the following percentage of saturation and moisture content values.

$$S_L = \frac{28.00}{36.60} \times 100\% \Rightarrow 76.50\% \quad \text{Equation 7.41}$$

$$MC = \frac{28.00}{711.17} \times 100\% \Rightarrow 3.94\% \quad \text{Equation 7.42}$$

Following this pattern, all the required values for determining the moisture sorption (desorption) isotherms used herein may be found summarized in table 10. In this table, percentage of saturation and moisture content values for the disc specimens representing the 1" and 7" depth locations are provided. While they do not have corresponding internal relative humidity values, and therefore shall have no moisture desorption isotherms associated with them, these values will be used at a later time.

Depth [in.]	K ₂ SO ₄			KCl			NaCl		
	S _L [%]	MC [%]	RH [%]	S _L [%]	MC [%]	RH [%]	S _L [%]	MC [%]	RH [%]
1	81.21	3.89	N/A	76.03	3.64	N/A	73.32	3.51	N/A
2	76.50	3.94	97.10	72.23	3.72	85.50	67.78	3.49	75.83
3	73.64	4.22	98.10	67.92	3.89	87.10	63.02	3.61	77.20
4	74.14	4.40	97.80	68.02	4.04	86.50	62.76	3.72	76.47
5	74.26	4.94	97.10	67.65	4.50	85.80	62.07	4.13	75.71
6	74.48	4.84	97.50	68.38	4.44	86.40	63.89	4.15	76.29
7	71.70	5.67	N/A	65.25	5.16	N/A	60.78	4.81	N/A

Table 10: Table of stabilized percentage of saturation, moisture content and RH values for all disc specimens

It is at this time that the moisture desorption isotherms for the applicable represented depths (i.e. 2", 3", 4", 5" and 6") may be calculated. This is accomplished by first plotting the three values for percent of saturation to the corresponding internal relative humidity values for each disc specimen. Then a second order polynomial is fit to the three data points and a function is produced which is used to interpolate between the set

points. In a similar manner this is repeated for the three moisture content values. The following (10) figures are the moisture desorption isotherms determined for all the applicable represented depth locations. The first (5) are expressed in terms of percent of saturation and the last (5) in terms of moisture content.

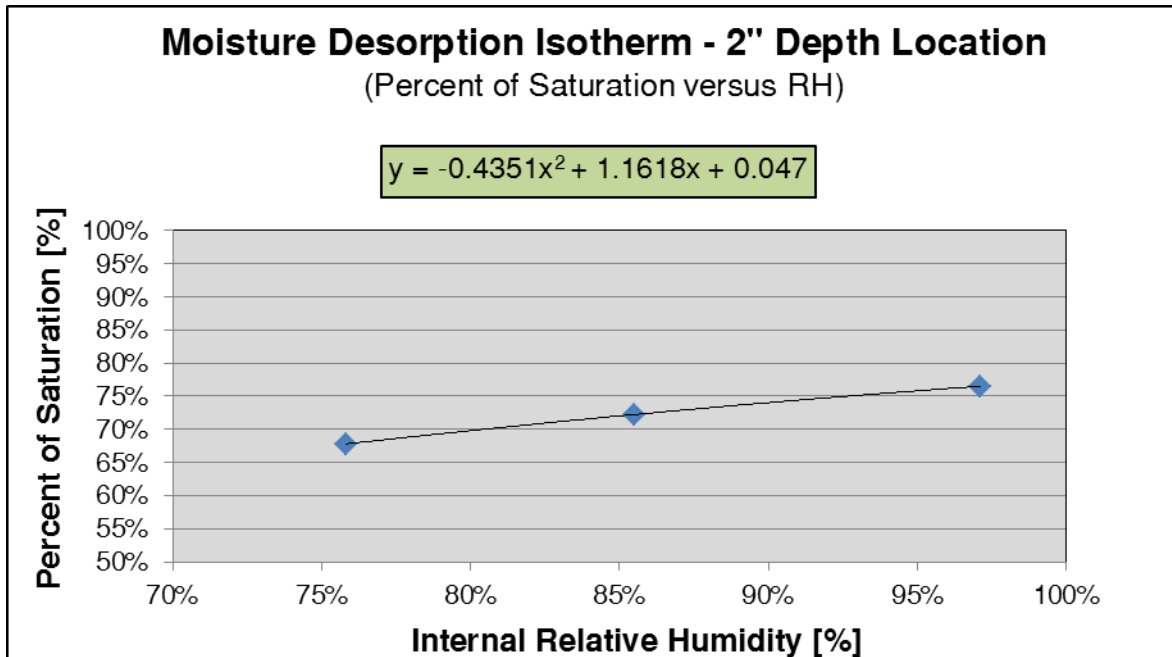


Figure 51: Moisture desorption isotherm representing the 2" depth location expressed in terms of percent of saturation

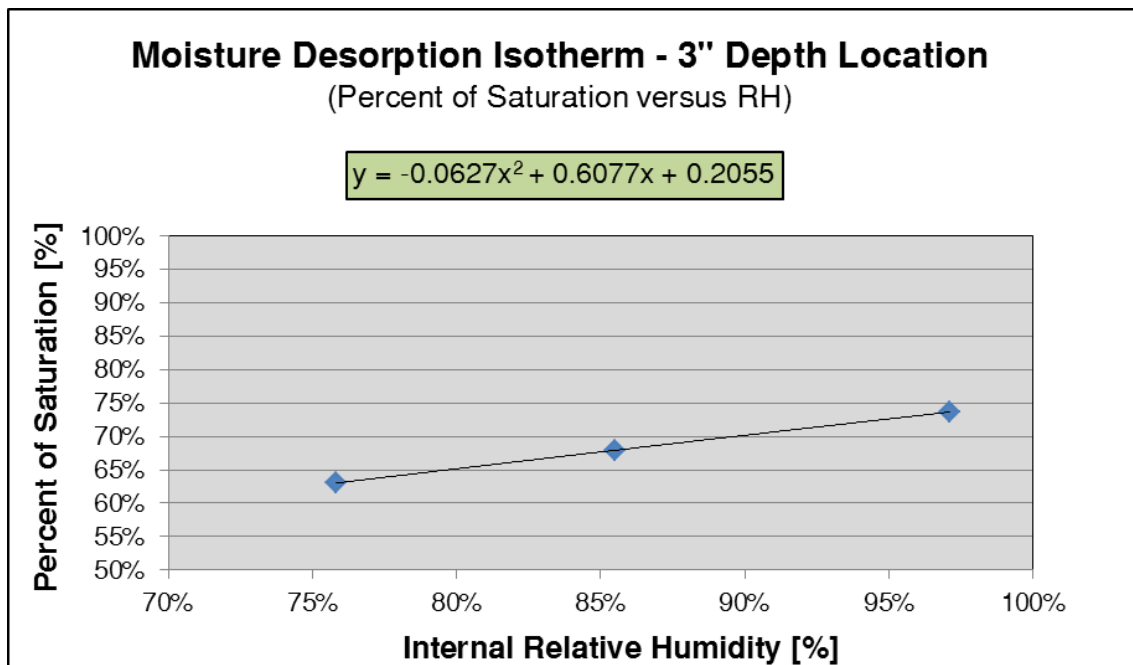


Figure 52: Moisture desorption isotherm representing the 3" depth location expressed in terms of percent of saturation

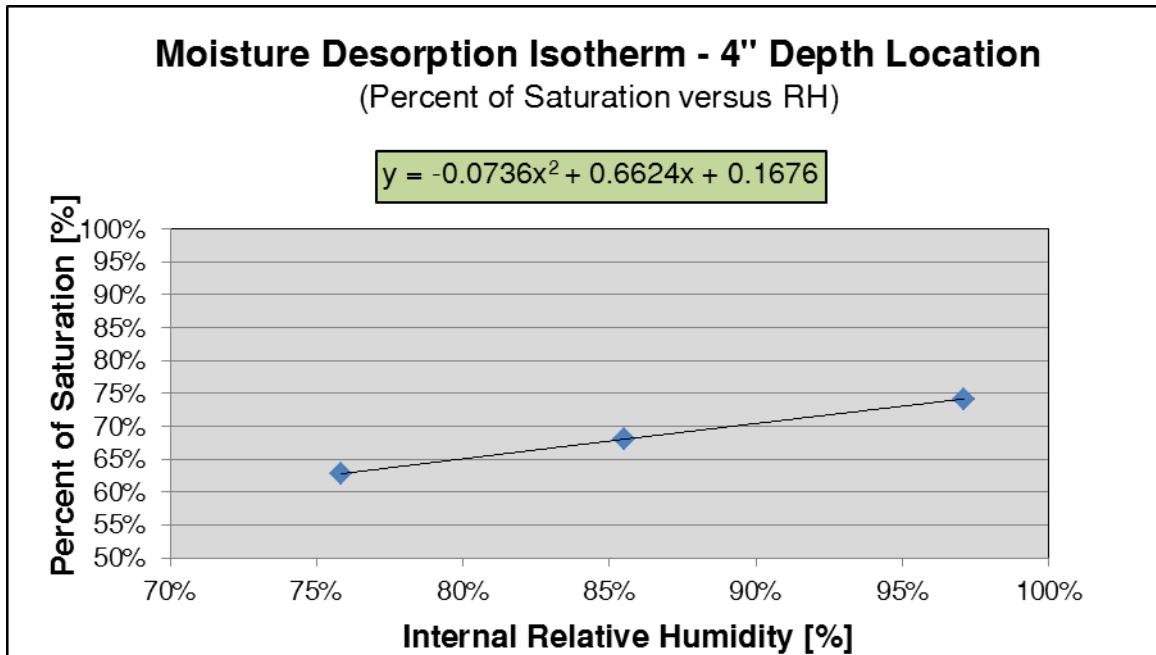


Figure 53: Moisture desorption isotherm representing the 4" depth location expressed in terms of percent of saturation

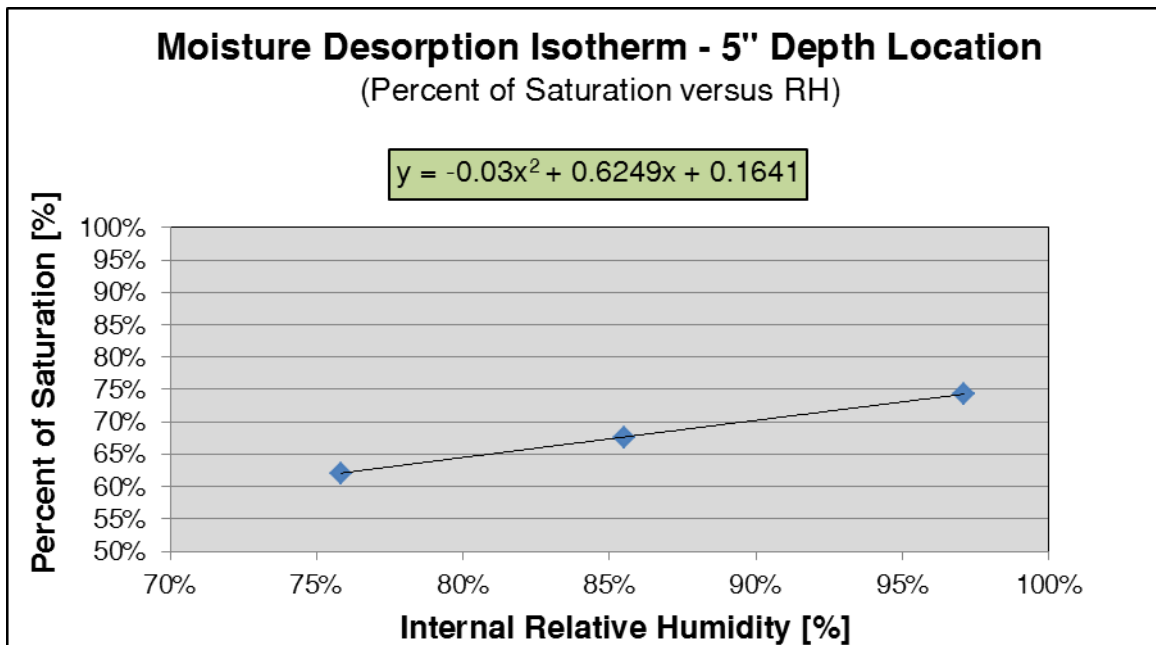


Figure 54: Moisture desorption isotherm representing the 5" depth location expressed in terms of percent of saturation

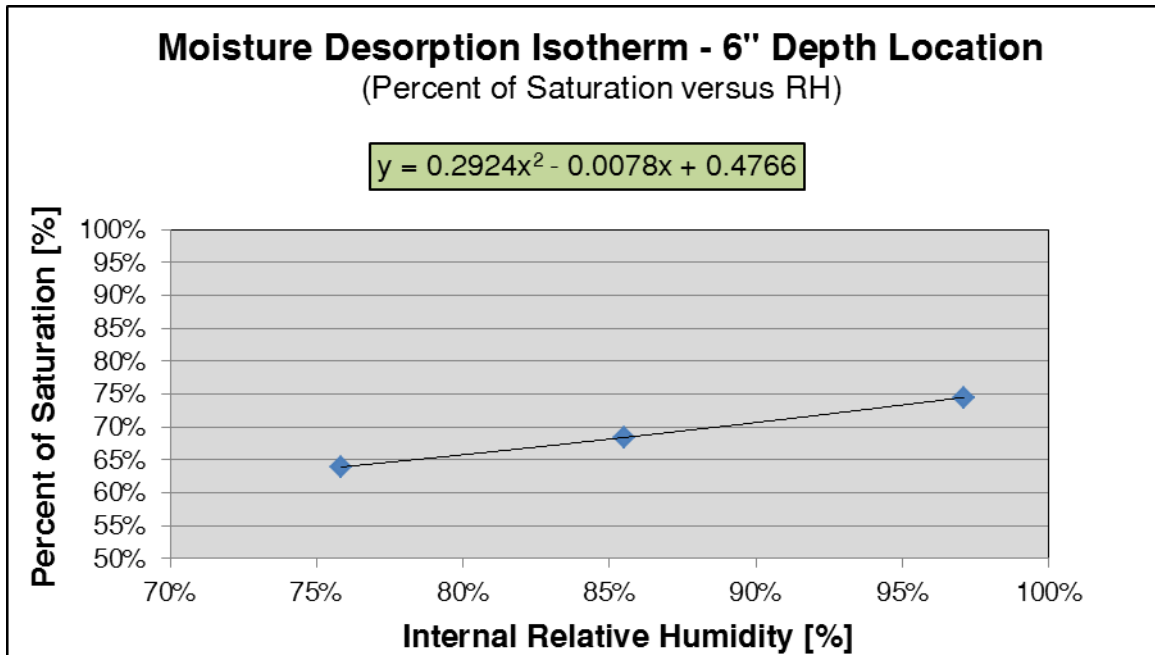


Figure 55: Moisture desorption isotherm representing the 6" depth location expressed in terms of percent of saturation

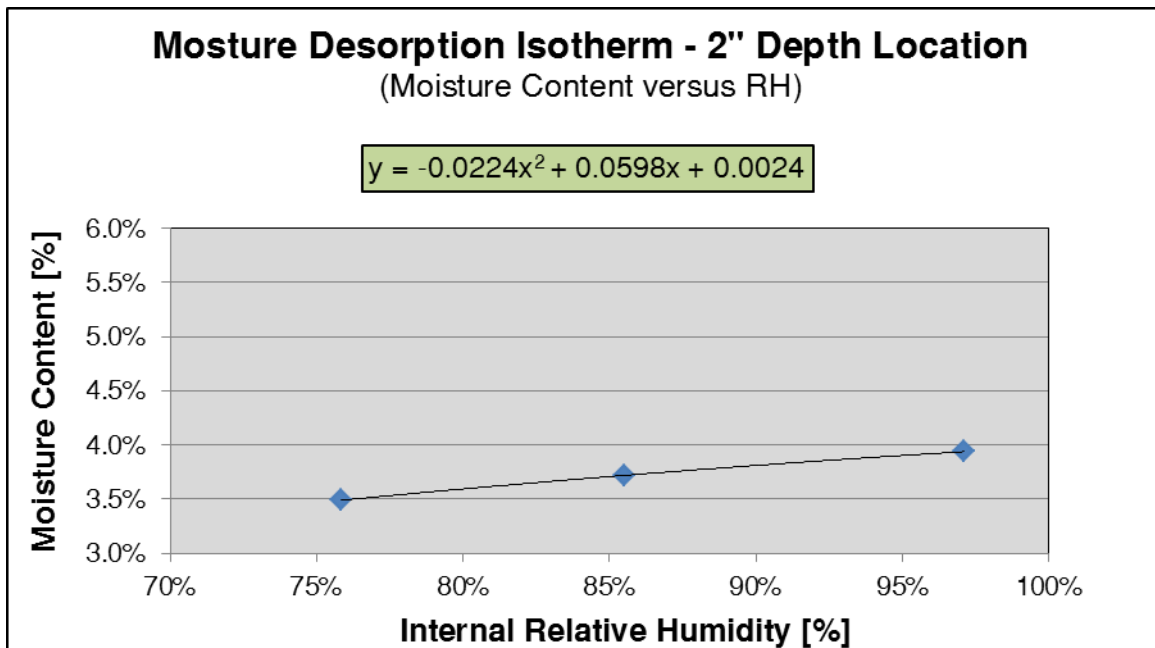


Figure 56: Moisture desorption isotherm representing the 2" depth location expressed in terms of moisture content

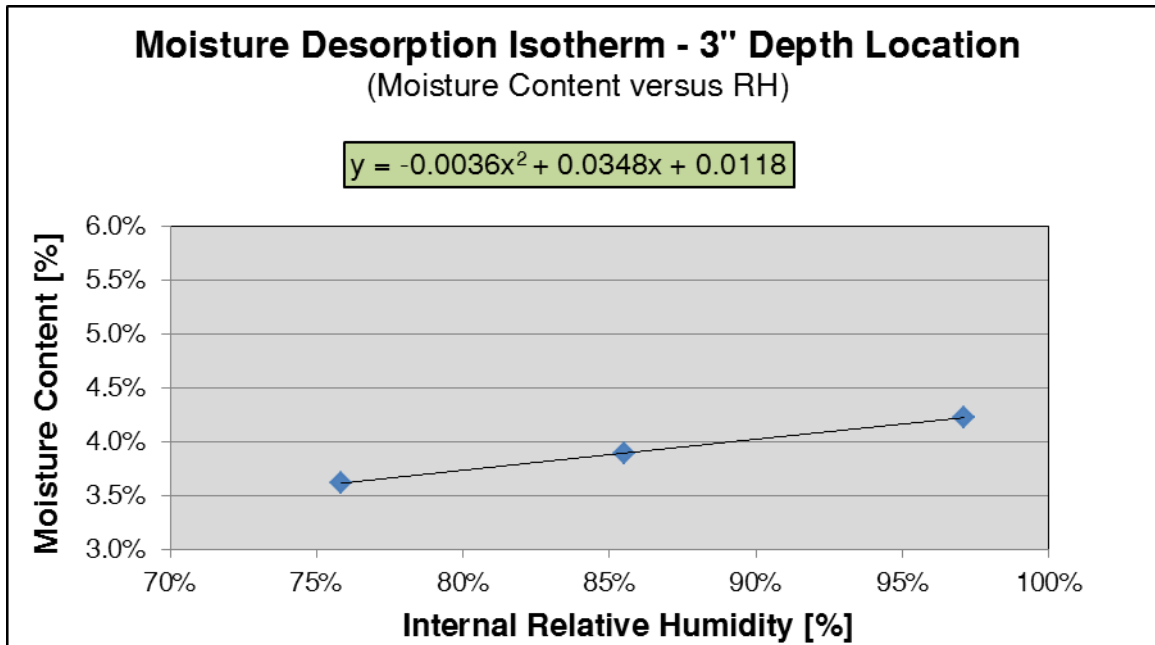


Figure 57: Moisture desorption isotherm representing the 3" depth location expressed in terms of moisture content

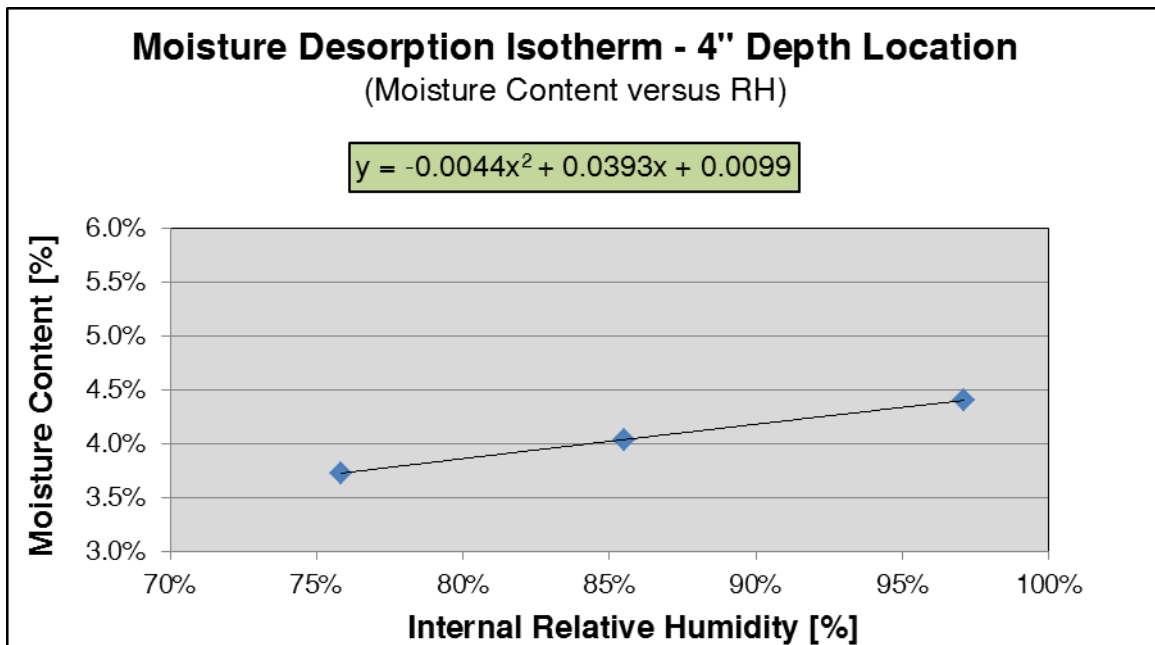


Figure 58: Moisture desorption isotherm representing the 4" depth location expressed in terms of moisture content

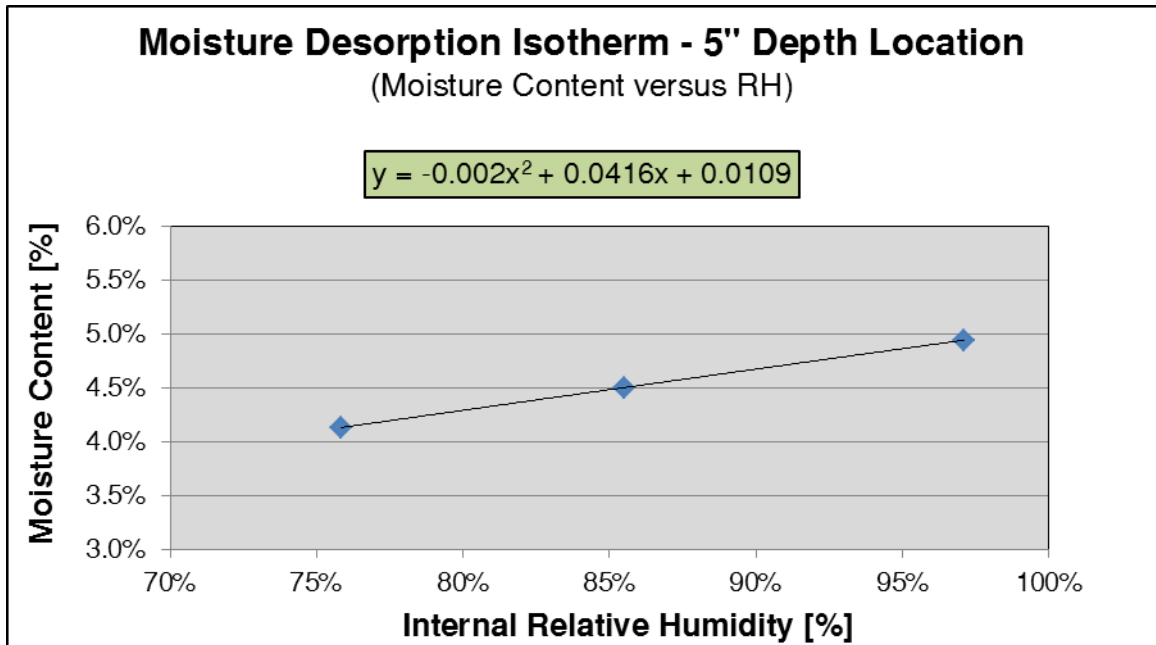


Figure 59: Moisture desorption isotherm representing the 5" depth location expressed in terms of moisture content

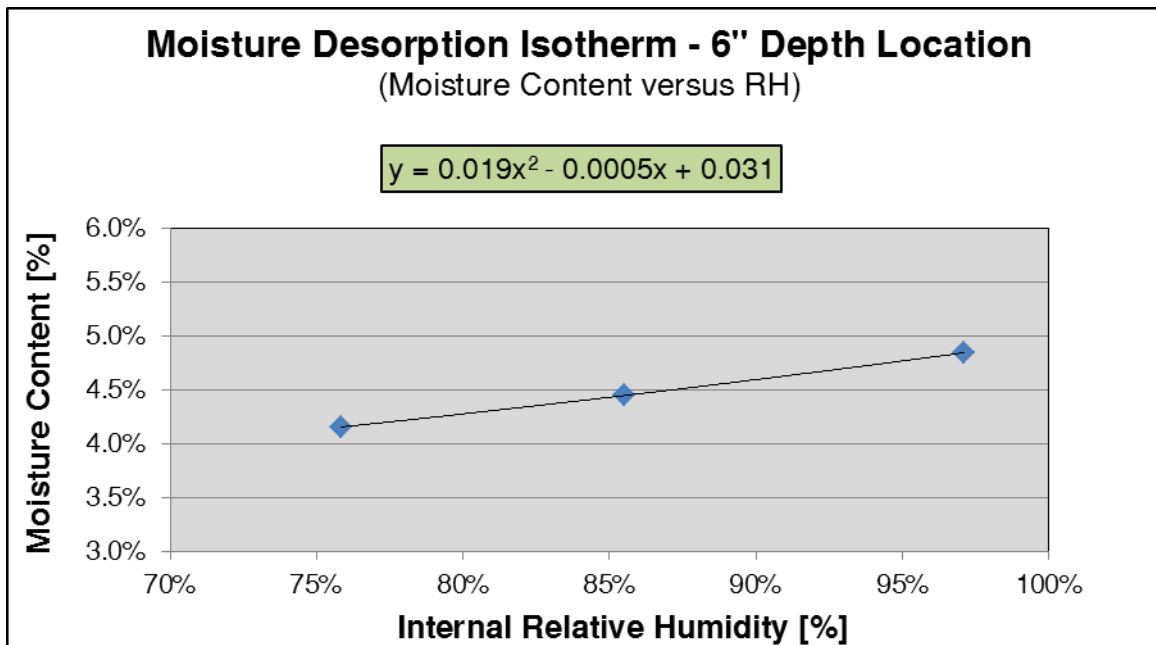


Figure 60: Moisture desorption isotherm representing the 5" depth location expressed in terms of moisture content

8. RESULTS

8.1 COLLECTED DATA FROM REPRESENTATIVE BRIDGE DECK SPECIMEN

The internal relative humidity and temperature data collected are presented in this section. However, as was commented on at various times in section 7.4, the author had several set-backs in obtaining valid internal RH values. Ultimately, the author feels strongly that valid values were achieved. The explanation the author shall now provide is tedious but necessary. It should also be noted that as there were no noticeable setbacks concerning the temperature data obtained from the RH&T sensors or thermocouples, that data shall be displayed with the final adjusted plots. The first plot to be shown, by figure 61, is of all the internal RH data collected spanning June 16, 2012 to October 26, 2012. The time interval for data collection was set to a five minute sample rate, but the plots used were created by using every other data point. Figure 61 is shown in its unadjusted condition; that is to say prior to any post-measurement calibration efforts. This figure may be divided into two separate plots: prior to and after August 15, 2012. The internal relative humidity data prior to this time delineation is shown in figure 62, and shall be discussed at this time.

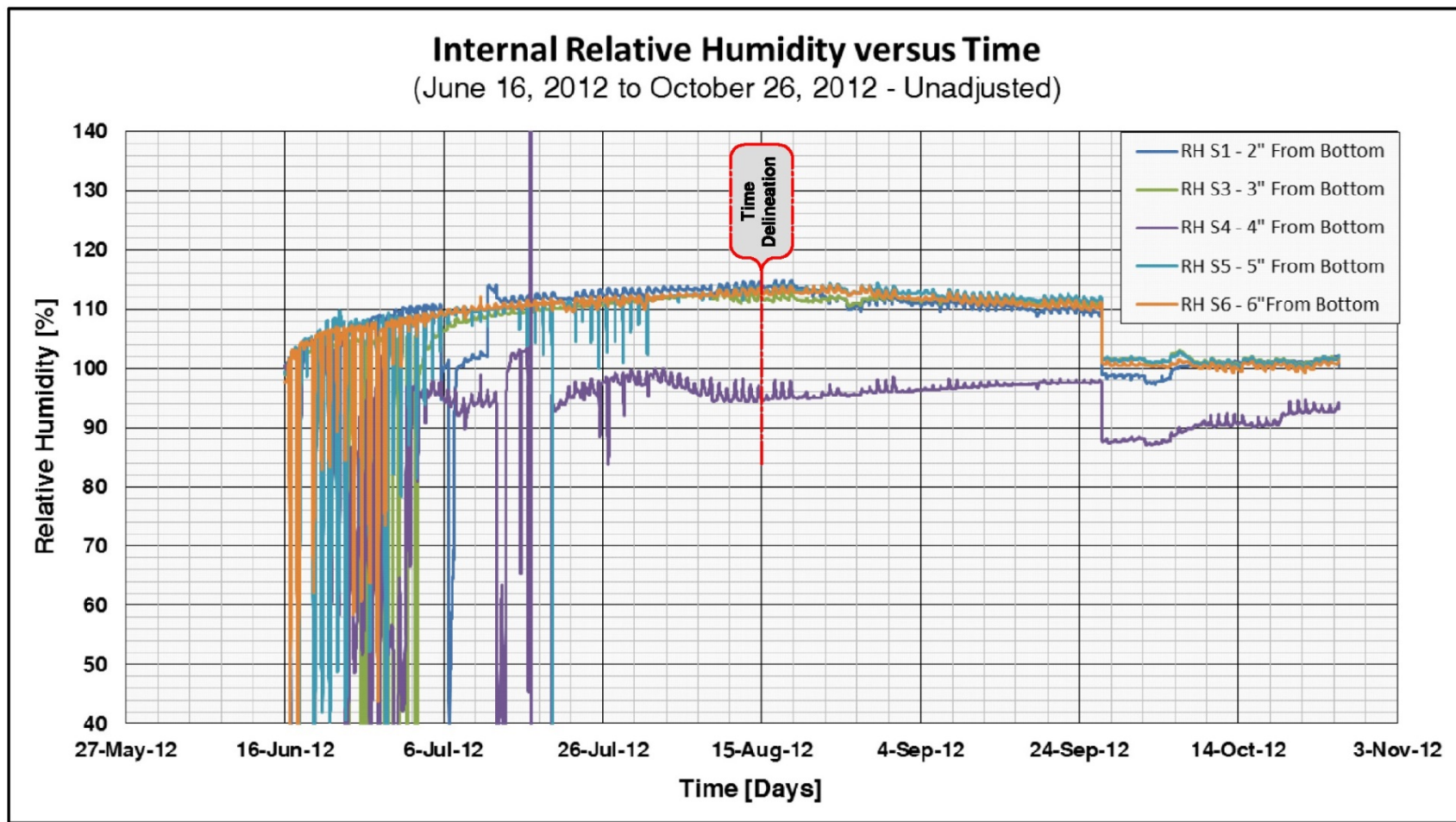


Figure 61: Unadjusted internal relative humidity versus time, from June 16, 2012 to October 26, 2012

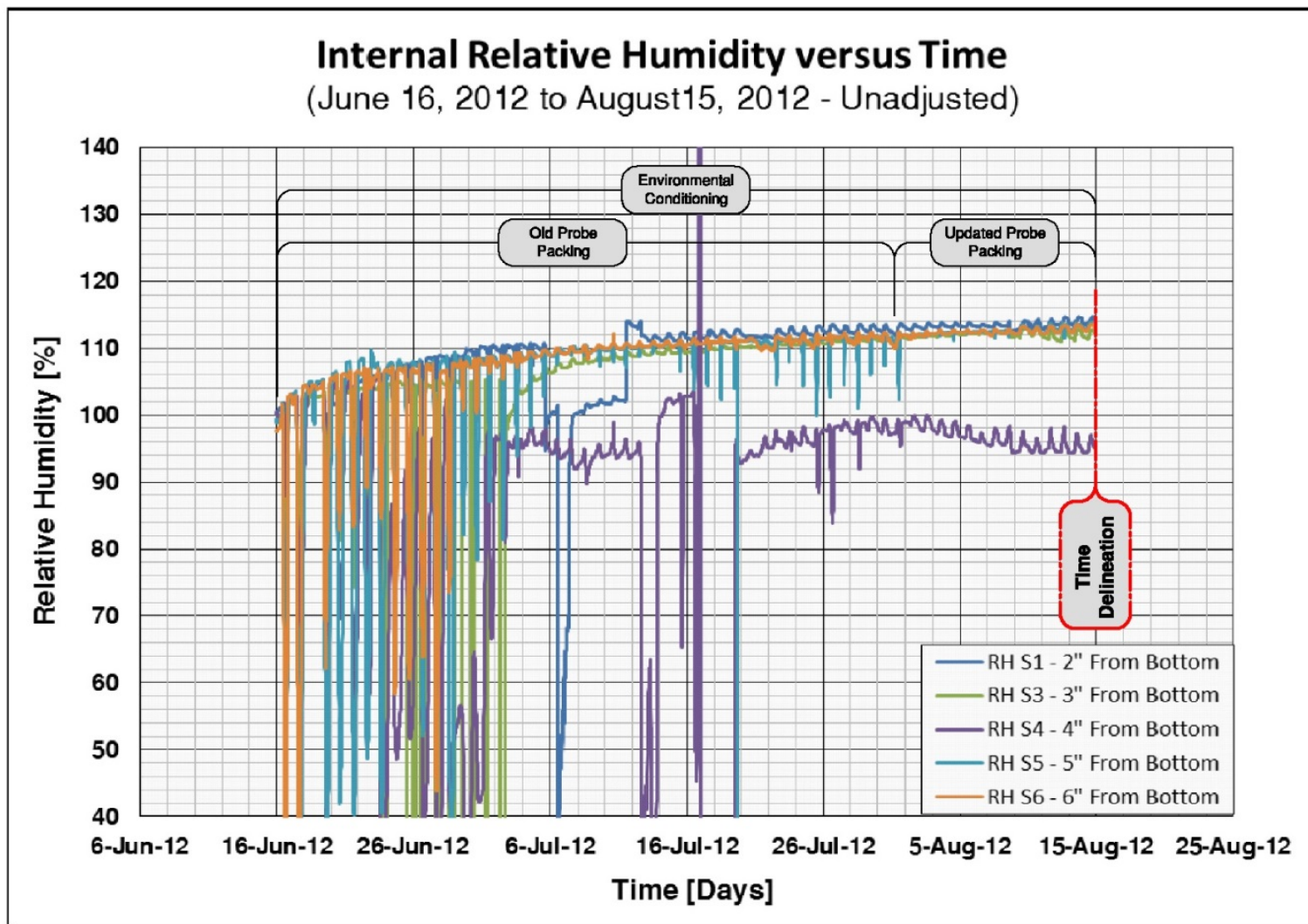


Figure 62: Unadjusted internal relative humidity versus time, from June 16, 2012 to August 15, 2012

When the probes (of the probe 1 kind), as shown in figure 26 (section 7.1.5) were initially placed, the method of placement was as follows. High vacuum grease was generously applied to the probe's exterior, after which the probe was inserted into the hole. The intention was for the placement to be as shown in figure 40 (section 7.3.2). However, the flaw in this approach was that the author had not accounted for the entrapped air void that was created. That is to say, as the probe was being inserted, there was no place for the air ahead of the seal to escape, and consequently the entrapped air pushed back on the vacuum grease. The resulting air void would ultimately be something larger than the desired cavity surrounding the sensor inside the probe. The larger unknown control volume created by this approach consequently caused the relatively large amplitude fluctuations in internal RH values seen in figure 62. As the author realized the flaw in this approach, the author carefully repacked the probes.

The updated probe packing procedure was as follows. First, the probes were carefully removed from the holes, and the holes were cleaned of excess high vacuum grease. This was a rather tedious process, as one needs to be concerned with not getting the vacuum grease into, and sealing off, the areas of interest. Once this was done, the probe, having also been cleaned off, was reinserted into the hole, this time without being initially coated with high vacuum grease. Once the probes were inserted, high vacuum grease was injected into the hole, starting from just behind the weather stripping and working outward. The author noticed that the probe fixity felt [physically] very firm in this new placement. Once all the sensors had been repacked using this updated approach, the fluctuating amplitude of the internal RH values seemed to be greatly reduced. The author attributes the reduction in RH fluctuation amplitude to the smaller control volume achieved (i.e., smaller cavity around the sensor).

Another issue that concerned the author was the ever-increasing internal RH values being collected. Almost immediately upper RH values reported by the sensors were exceeding 100%, with stabilization occurring at approximately 114%. Commonly in the high atmosphere, in the vicinity of extremely small water droplets supersaturated conditions (i.e., RH greater than 100%) do exist (Atkins 1990; Grasley et al. 2006). However, in the context of this investigation RH values above 100% are not meaningful; the author attributes this observed shifting to environmental conditioning of the sensors. That is to say, over a period of time the sensors adapted to unanticipated environmental conditions. The reader may recall that the sensors operate by interrogating a hygroscopic material that is sensitive to environmental conditions. The sensor, during the collection of all RH&T values, used the on-board heating element to [try to] prevent condensation. Consequently, while this does not necessarily exclude the possibility of condensation, it is speculated that there is real possibility that other unknown internal conditions may have affected the hygroscopic material over time (i.e., conditioned it). In a technical paper by Dr. Januarti Jaya Ekaputri, (written as a doctoral student of the University of Tokyo, Department of Civil Engineering), entitled "*Internal Relative Humidity Measurement on Moisture Distribution of Mortar Considering Self-Dessication at Early Ages*," the sensors used were the same as those used in this investigation (Ekaputri et al. 2009). Under certain fresh concrete conditions, specifically when using blast furnace

slag (BFS), the sensors used were behaving in a manner similar to the sensors used in this investigation. It should be noted that Dr. Ekaputri replicated the procedure using ordinary fresh cement, with no such behavior observed. Then when Dr. Ekaputri placed the sensors into hardened cement containing BFS, under lab conditions, the observed values became normal. Based on this, the author speculates that there may be factors influencing the hygroscopic material used in the sensor, when in the presence of high moisture (or high RH), attributable to the concrete's chemical or admixture composition. In any case at some point in time the sensors stabilized, as did the sensors Dr. Ekaputri used in the fresh mix, and discontinuing their RH ascent; the date at which change appeared to stabilize was on approximately August 15, 2012. Any solution used to adjust the RH values obtained would need to be applied to stable values; that is to say, values not obtained while the probes sensors were still undergoing conditioning. For this reason the RH data obtained prior to August 15, 2012 will be disregarded.

Around the time the sensor's RH values were stabilizing, the author was unsure about how to proceed. The original calibrations were not working out and the author thought that perhaps moisture condensation on the sensors might be the problem. Consequently, the author decided to create an enclosure around the representative deck and place a dehumidifier inside, which operated continuously, as shown in figure 63. The idea was that if the internal moisture levels could be reduced, then the sensors may dry out and it would be possible to still investigate the moisture sorption isotherms under dynamically evolving conditions, even if not entirely naturally. Though the moisture levels would be artificially lowered, the system would still be dynamically evolving in both contained moisture and temperature. It was hoped that this would lower the internal moisture levels just enough to enable creation of a moisture profile based on moisture sorption isotherms, which could then be compared against a gravimetrically based isotherm. Initially, this appeared to be working, as a downward trend could be observed in figure 64. However, as will be shown later, the misleading response observed seems to be primarily temperature driven, rather than the result of moisture loss. In truth, the period of exposure spanning from approximately August 15, 2012 to October 9, 2012 did virtually nothing to alter the sensor values. It is possible though that the internal moisture reserve was sufficient to resist the nearly two month exposure to constant drying.



Figure 63: Representative bridge deck in the sealed dehumidification enclosure

Seeking other possible sources of error that could explain the observed values, the author explored the possibility that the user-defined calibrations were using temperature values that had not been converted properly (i.e., from Fahrenheit to Celsius units). The author applied the appropriate temperature conversions to the user-defined calibrations on approximately September 27, 2012. However, the author soon realized that no conversion mistake had been made; the sensors had just become conditioned inside the concrete. The solution would ultimately need to include the re-calibration of the sensors, with the new calibrations being post-applied to the stabilized data. Instead of removing the unit conversion, the author allowed the sensors to continue to collect data in this manner. The author would simply undo the effects of the unit conversion during the post-processing phase.

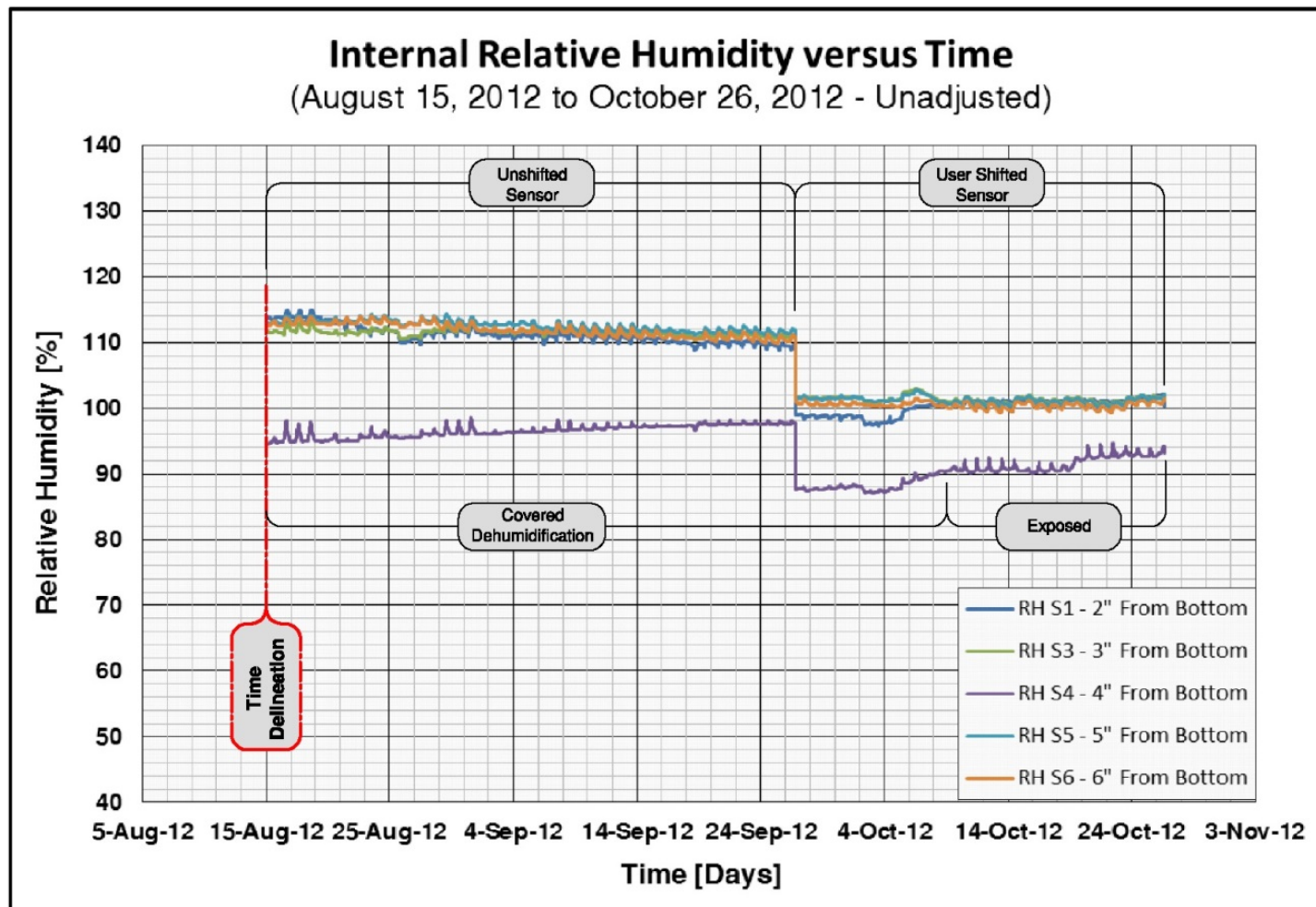


Figure 64: Unadjusted internal relative humidity versus time, from June 16, 2012 to August 15, 2012

On October 26, several days after the cores had been extracted, the author carefully removed each probe and quickly placed each of the sensors into the RH apparatus containing the potassium sulfate (K_2SO_4) saturated salt solution (see table 3 in section 7.2 for theoretical RH values). Once values across the temperature range of 5 to 50 °C were obtained for calibration purposes, the author repeated the process with the potassium chloride (KCl) saturated salt solution. It occurred to the author that the KCl environment was a relatively dry environment for a sensor that had just been conditioned in a relatively humid environment (i.e., inside the representative concrete deck). So to make sure that the author had not inadvertently altered the sensors' conditioned state, they were run again in the K_2SO_4 produced RH environment. As it turns out, the time they spent in the KCl produced RH environment did affect them, by about a 3% RH shift. Consequently, the author determined the extent of the shift for each sensor, by comparison of the two K_2SO_4 values (i.e., before and after exposure to KCl), and corrected the KCl values; this of course, assumed that the calibration was still exhibiting planar behavior. The values, obtained from the sensors in the representative deck, were passed back through the incorrect calibrations to obtain the "raw" RH values. In the case of the values that had received an unnecessary unit conversion, their "raw" values were determined after the effects of the unit conversion were reversed. The raw values, that is to say the values that would be obtained in the absence of a user-determined conversion, were then post-processed by the newly determined calibrations. Since the RH&T sensor temperature values were not questioned, they were used "as is." Again, this sort of post-processing could only be applied to values corresponding to a point in time where the RH&T sensors had reached a stabilized conditioning; hence, the values prior to approximately August 15, 2012 could not be corrected. The corrected values were plotted and shown in figure 65, along with the corresponding temperature values. It should be noted that the sensor in probe number four always stood out as different from the others, as seen in figures 61, 62, 64 and 65. Based on the values obtained after post-processing the RH data, the author has concluded that the sensor in this probe has somehow become corrupted. Consequently, a moisture value at this depth location, based on a moisture sorption isotherm, will not be attempted.

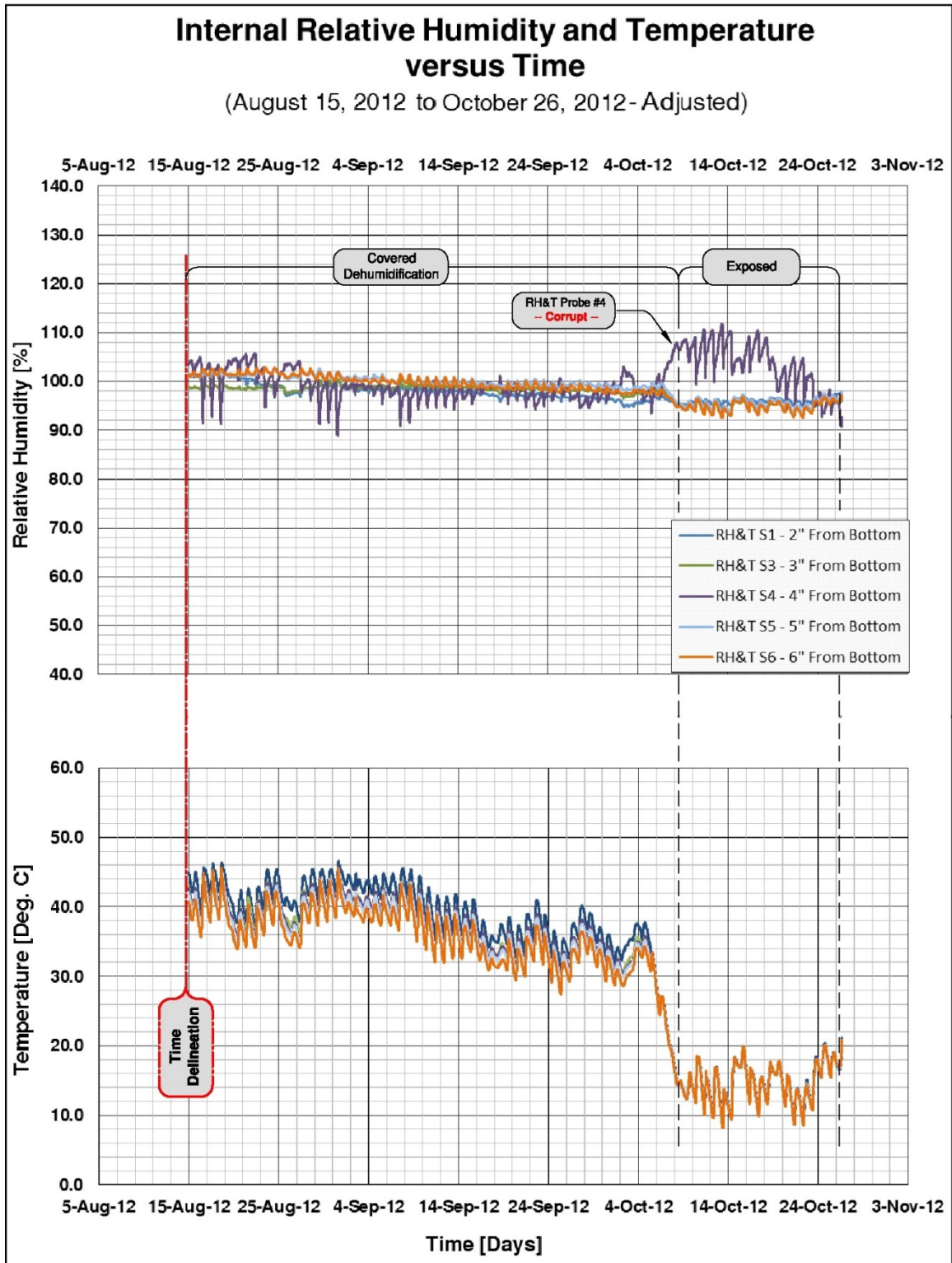


Figure 65: Adjusted internal relative humidity and temperature versus time, from August 15, 2012 to October 26, 2012

Before the author proceeds to calculate moisture profiles, the author needs to present the temperature data obtained by the thermocouple sensors. As the reader may recall, there is concern that thermal lag between the representative concrete deck and the sensor could cause errors of approximately $-5\% RH/^{\circ}C$ (section 2.5). The idea was that the thermocouples would take independent temperature readings of the concrete directly, while the SHT75 sensors are obtaining temperature values at the RH sensor location. The values would be compared to quantify thermal differences between the sensor and the specimen; then, if necessary, corrections can be made. Figure 66 offers a comparison of the temperature values obtained by each sensor, the general similarity of values can be observed. Figures 67 through 71 offer a close-up view of the temperatures around the time when the core extractions occurred, as indicated in figure 66. To aid the reader in a visual comparison of values, the two temperature measurement sources were plotted on the same graph, with each graph containing just a single depth location.

As can be observed (in figures 67 through 71), there does exist a level of recorded temperature difference between the two sources of temperature data on the order of up to $0.5^{\circ}C$ at times. However, this can be attributed to differences in the sensors' manufacturer calibrations. Thermal lag differences between the concrete deck and the RH&T sensors would manifest themselves in the form "temperature phase shifting." This does not appear to be occurring. Consequently, the author has concluded that no adjustments for this type of thermal lag difference are warranted, as the temperature within the cavity appears to be evolving in-step with the concrete's evolving temperature.

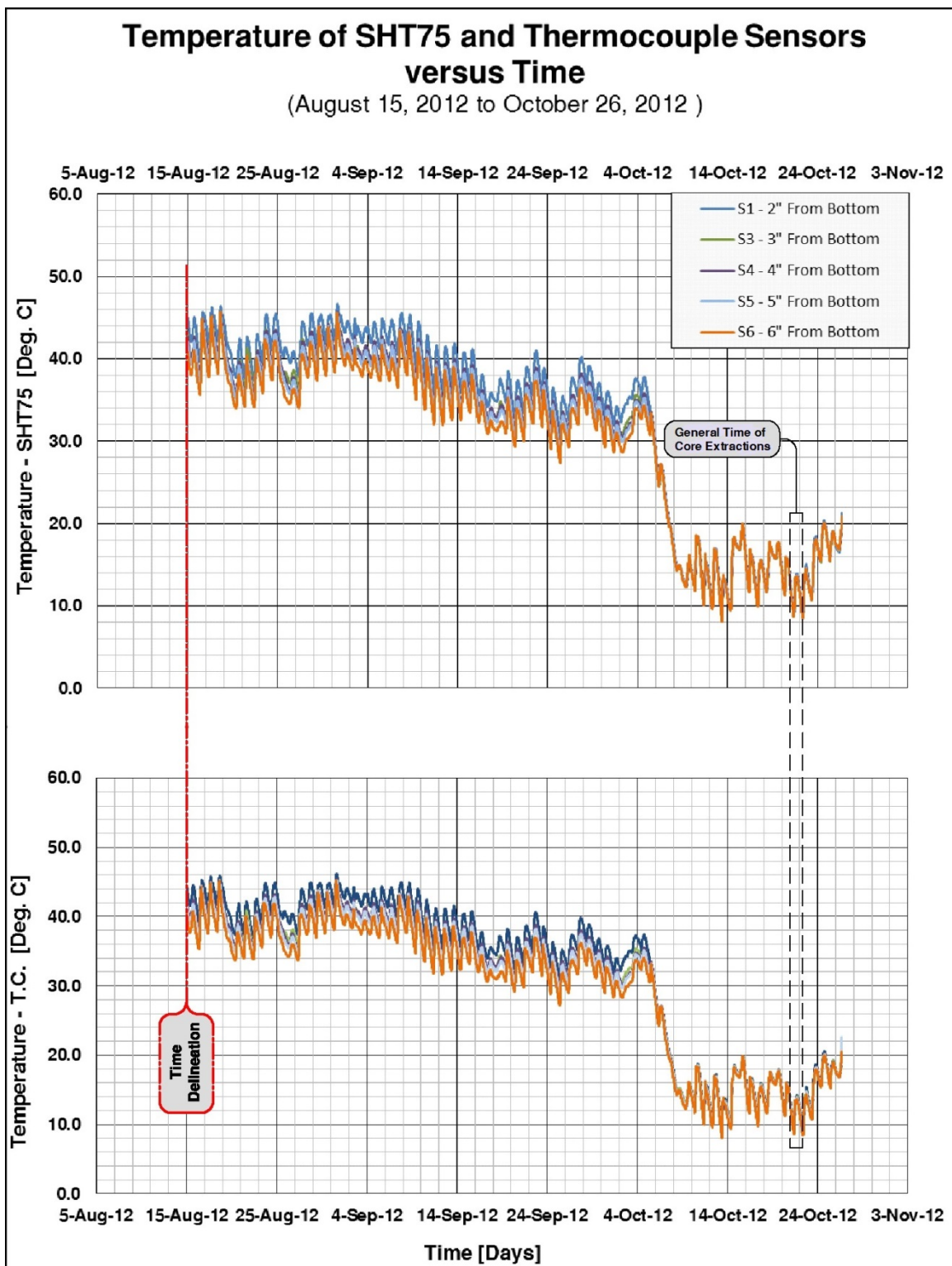


Figure 66: Temperature of SHT75 and thermocouple (T.C.) sensors versus time, from August 15, 2012 to October 26, 2012

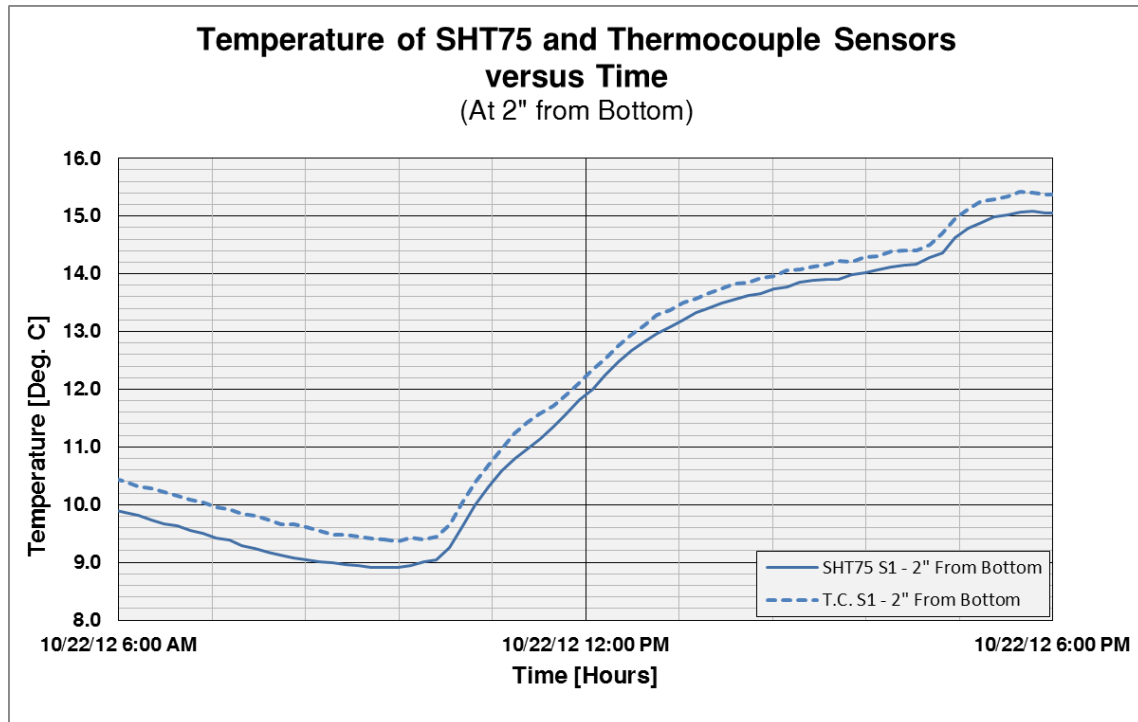


Figure 67: Temperature of SHT75 and thermocouple (T.C.) sensors versus time, on the date of the core extractions at the 2" location as measured from the bottom of the deck

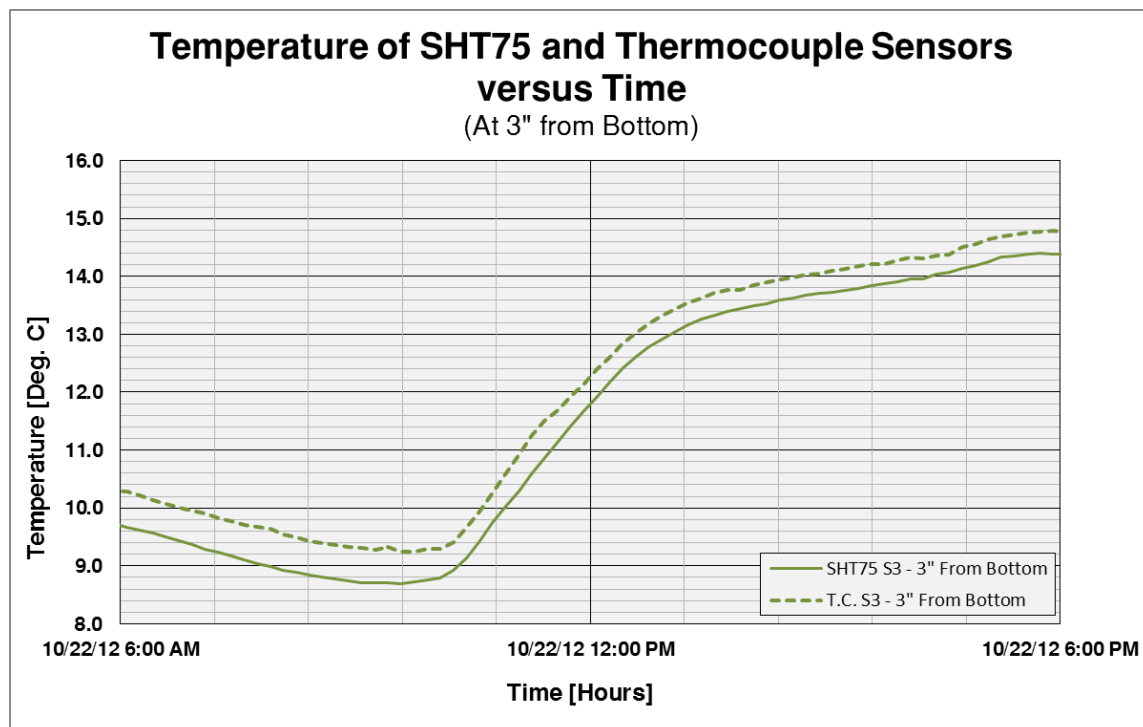


Figure 68: Temperature of SHT75 and thermocouple (T.C.) sensors versus time, on the date of the core extractions at the 3" location as measured from the bottom of the deck

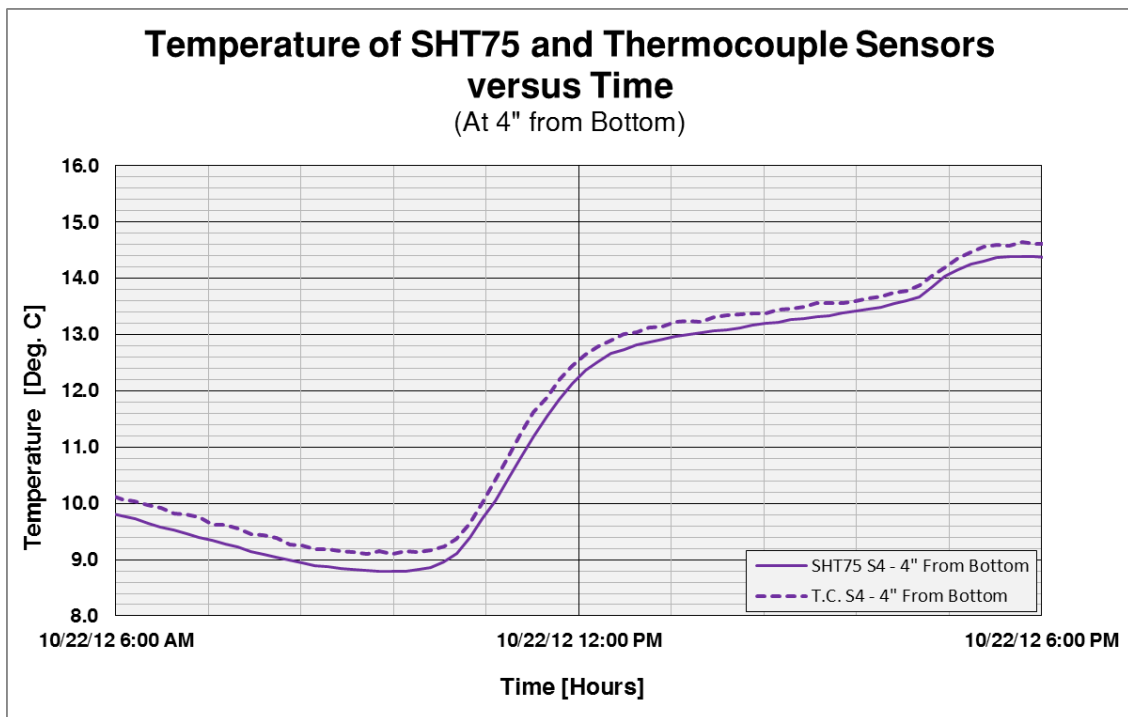


Figure 69: Temperature of SHT75 and thermocouple (T.C.) sensors versus time, on the date of the core extractions at the 4" location as measured from the bottom of the deck

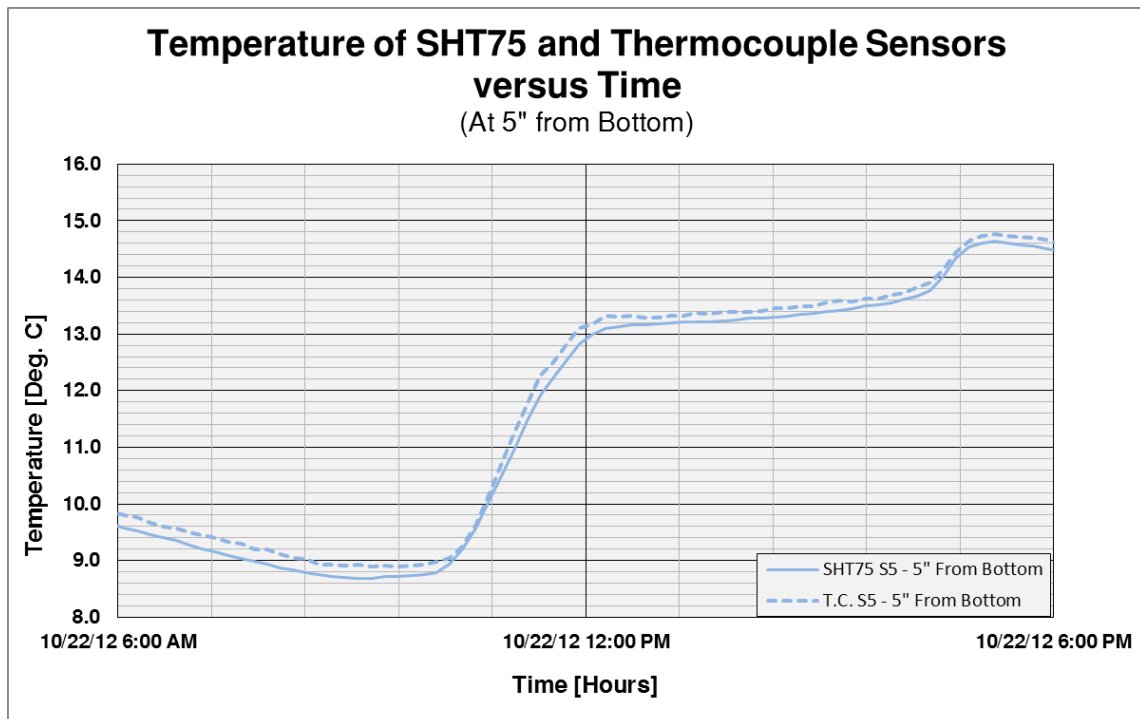


Figure 70: Temperature of SHT75 and thermocouple (T.C.) sensors versus time, on the date of the core extractions at the 5" location as measured from the bottom of the deck

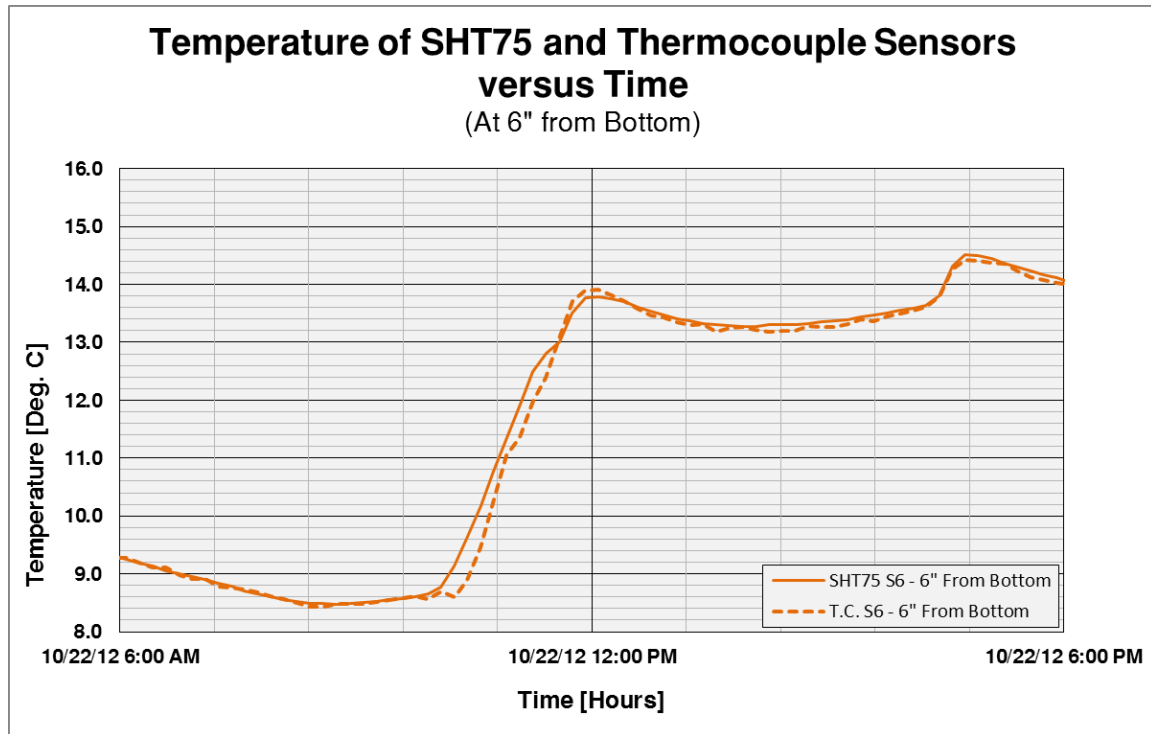


Figure 71: Temperature of SHT75 and thermocouple (T.C.) sensors versus time, on the date of the core extractions at the 6" location as measured from the bottom of the deck

Next the author shall present, in figure 72, the plotted relative humidity and temperature data obtained on the date when the core extractions occurred, followed by a table of values (table 11) containing the RH&T values for each depth location at the time of core extraction; that is to say, at the DAQ time stamp assumed. These values shall be used in the following section to generate moisture sorption (desorption) isotherm—based moisture profiles.

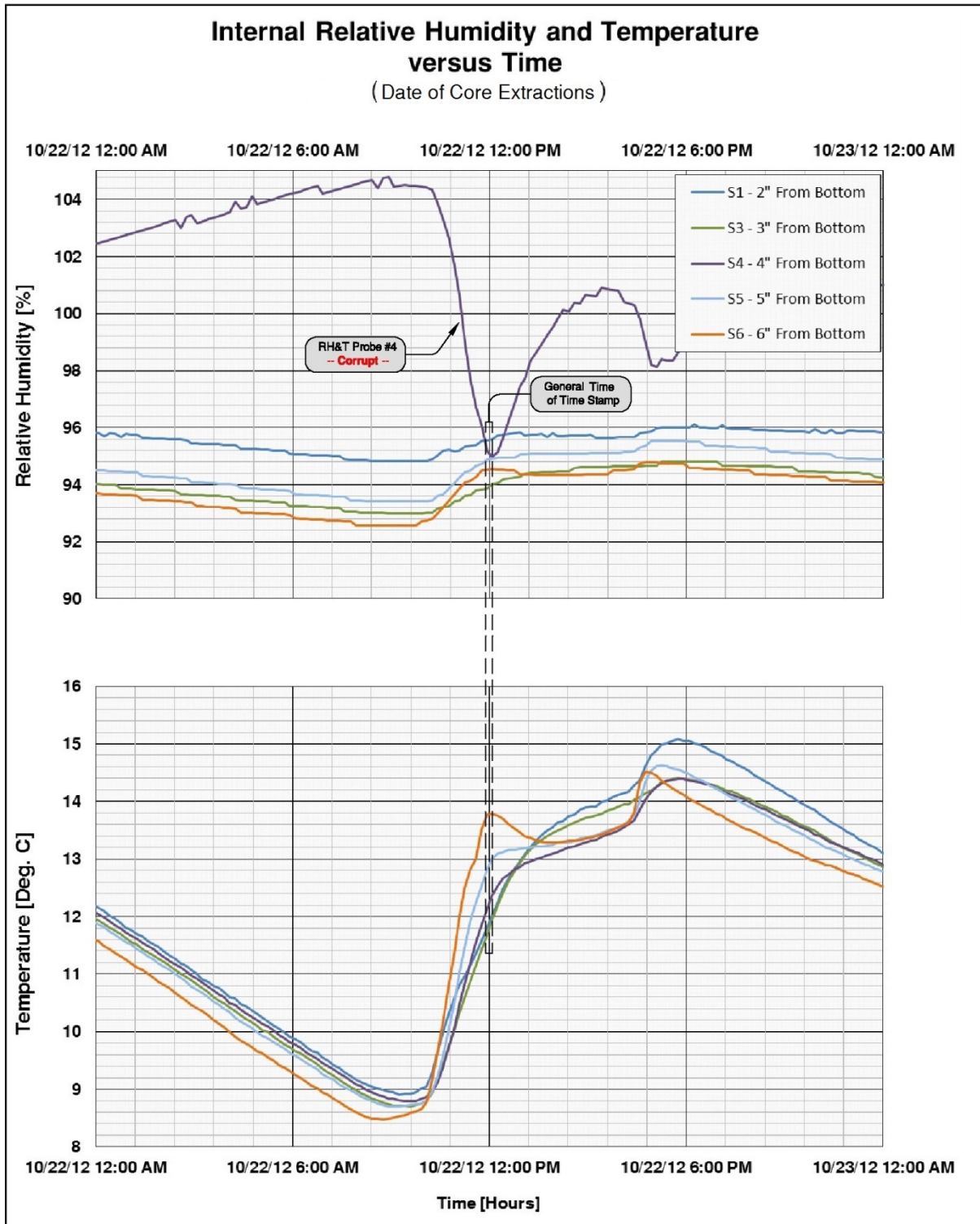


Figure 72: Adjusted internal relative humidity and temperature versus time on the date of the core extractions, with the approximate time stamp location.

Probe Depth from Bottom [in.]	Adjusted Field Data at Time of Core Extraction		
	Date and Time	Temperature [°C]	Internal RH [%]
1	N/A	N/A	N/A
2	10/22/12 12:05 PM	12.0	95.58
3	10/22/12 12:05 PM	11.9	94.02
4	10/22/12 12:05 PM	12.4	-- Corrupt --
5	10/22/12 12:05 PM	13.0	94.92
6	10/22/12 12:05 PM	13.8	94.54
7	N/A	N/A	N/A

Table 11: Adjusted internal relative humidity and temperature data at the time of core extraction

8.2 MOISTURE CONTENT AND PERCENT OF SATURATION PROFILES

Moisture content (MC) and percent of saturation (S_L) profiles based on discrete values will be plotted in this section. However, prior to this, a few remaining calculations remain. First, using the moisture content and percent of saturation, moisture sorption (desorption) isotherms as shown by figures 51 through 60. The author calculated the moisture content and percent of saturation values required for plotting the relative humidity—based moisture profiles. Since the moisture sorption isotherms, though created at 25°C, are assumed for the purposes of this investigation to be temperature independent, the only required input values are the adjusted RH values provided in table 11. The resulting values, along with other calculated values, are found in tables 12 and 13. The following is a brief explanation of these other values.

The in-situ gravimetric profile is considered to be the “true” moisture profile of the representative bridge deck at the time of core extraction (i.e., the actual in-situ moisture profile). The discrete moisture values upon which it is based are determined directly through mass measurements. These discrete gravimetric points are calculated by equations 7.33 and 7.34 (section 7.4.3.3), where the moisture mass change value used by the supporting equation 7.35 is taken to be zero (*Moisture Mass Change = 0 grams*). In addition to the in-situ gravimetric and relative humidity—based, moisture content and percent of saturation profiles, three other general profiles will be helpful during a later discussion of the findings.

Two of these other profiles are also moisture profiles, determined gravimetrically, but are not the in-situ gravimetric profile. The first one is based on the vacuum-saturated moisture mass of the disc specimens, and shall be termed the vacuum-saturated gravimetric profile. Like the in-situ gravimetric profile, it's discrete values are also determined by equations 7.33 and 7.35; however, the moisture mass change values are taken to be equal to those found in the extreme saturated column of table 9 (section 7.4.3.3). This profile will represent the moisture profile that would exist if every void space were saturated by pore solution. The second moisture profile is based on the moisture mass obtained when the disc specimens were brought to equilibrium in the near saturated RH environment containing the potassium sulfate

(K₂SO₄) saturated salt solution. This will be used to represent a moisture profile obtained by the upper limit of the moisture sorption isotherm. In theory, this profile would be, approximately, the maximum moisture profile that a relative humidity—based moisture sorption isotherm could be used to determine. The author shall term this the K₂SO₄ gravimetric profile. Like the profile before it, the discrete moisture values used to determine it makes use of equations 7.33 and 7.35, but in this case, the moisture mass change values are taken to be equal to those found in the K₂SO₄ column of table 9. These values were calculated and are shown in table 10. Each profile to this point (i.e., the relative humidity—based the in-situ gravimetric, the vacuum saturated and the K₂SO₄ gravimetric) shall be expressed in terms of both moisture content and percent of saturation.

Depth [in.]	Moisture Sorption Isotherm Based		Gravimetrically Determined					
			In-Situ		Vacuum Saturated		K ₂ SO ₄	
	S _L [%]	MC [%]	S _L [%]	MC [%]	S _L [%]	MC [%]	S _L [%]	MC [%]
1	N/A	N/A	81.89	3.93	100	4.79	81.21	3.89
2	76.00	3.91	81.34	4.19	100	5.15	76.50	3.94
3	72.14	4.13	77.13	4.42	100	5.73	73.64	4.22
4	-Corrupt -	-Corrupt -	75.75	4.49	100	5.93	74.14	4.40
5	73.02	4.86	79.93	5.32	100	6.65	74.26	4.94
6	73.06	4.75	76.21	4.95	100	6.50	74.48	4.84
7	N/A	N/A	74.92	5.92	100	7.91	71.70	5.67

Table 12: Discrete, moisture sorption isotherm based and gravimetrically determined moisture values, expressed in terms of percent of saturation and moisture content.

To further complement the findings discussion, the author has decided to provide a profile of the concrete's density (ρ_c). As the density of concrete and its level of porosity generally share an inverse relationship, this profile may be used to indicate the general change in porosity through the representative deck thickness. The following general method was used to determine the discrete concrete density values. At the time the final dry mass values for each disc specimen were determined, they were also submerged in water and an immediate mass was obtained (i.e. weighed under water at 25°C.) This submerged mass, along with the dry mass values, were used to directly to calculate the density of the disc specimens. Based loosely on the bulk density equations of a more rigorous ASTM standard, the equation of the form shown by equation 8.1 was used (ASTM Standard C642 2006). For convenience, both the specimens' submerged and dry masses are provided by the author in table 13 along with all the calculated disc specimen densities.

$$\rho_c = \frac{\text{Dry Mass}}{\text{Dry Mass} - \text{Submerged Mass}} \times \rho_w \times 100\% \quad \text{Equation 8.1}$$

where

ρ_w : Density of water = 1 [g/cm³]

Depth [in.]	Dry mass [g]	Submerged mass [g]	Density [g/cm ³]
1	676.27	398.92	2.44
2	711.17	419.00	2.43
3	725.43	422.17	2.39
4	714.99	415.23	2.39
5	686.08	395.68	2.36
6	633.70	366.42	2.37
7	667.44	375.72	2.29

Table 13: Discrete concrete disc specimen densities

The following figure 73 will now show all the profiles, as determined by the discrete points tabulated in tables 12 and 13.

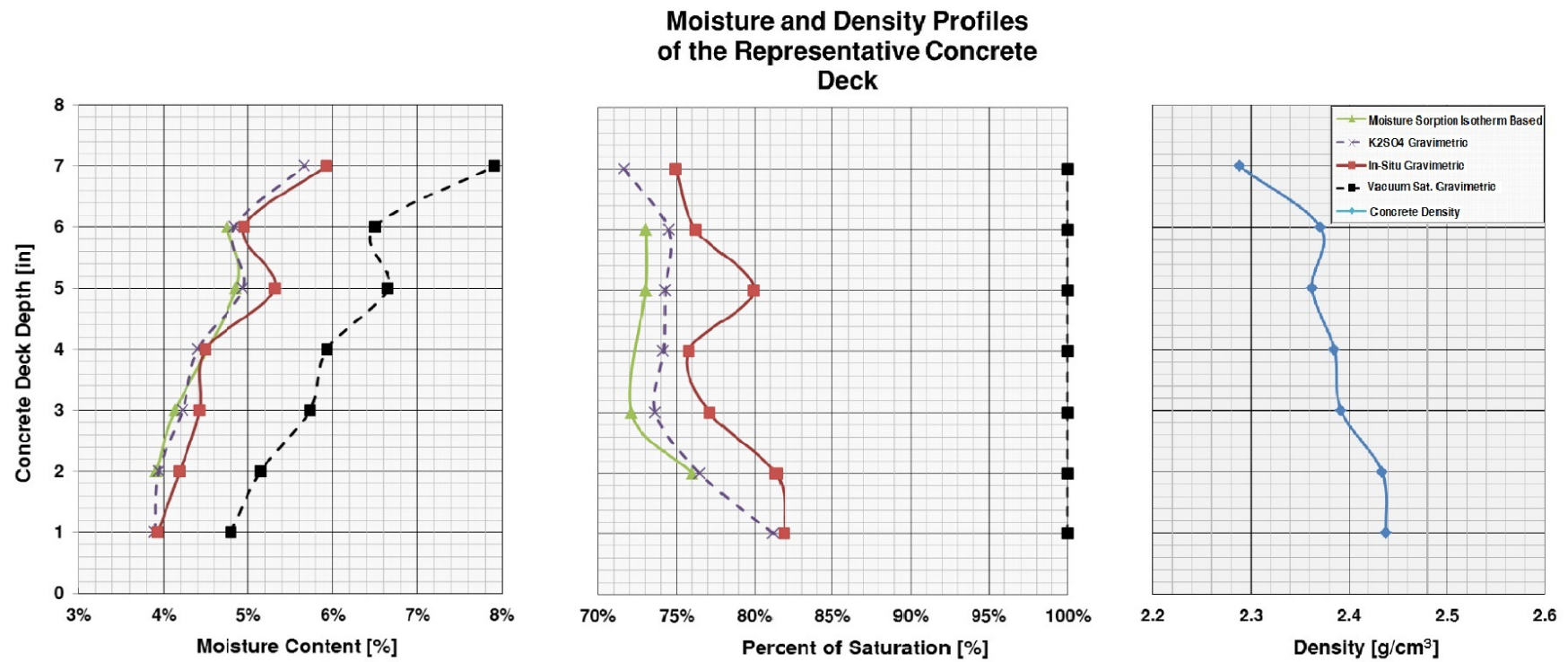


Figure 73: Moisture and density profiles of the representative concrete deck, based on the discrete values found in tables 12 and 13, expressed in terms of both percent of saturation and moisture content.

9. FINDINGS

As was stated in section 4.2.2, the author hypothesized that “*within a concrete highway bridge deck, of typical construction, at depths generally associated with the placement of reinforcement, static thermal and moisture equilibrium may be assumed.*” The methodologies to be employed, as outlined in section 6.1, were divided into two distinct approaches. Then the author would, gravimetrically, determine the moisture profile of the representative bridge deck. This profile would represent the actual in-situ moisture present in the representative bridge deck, and would be the standard for all comparisons. In addition, the author would create a moisture profile using the relative humidity—based moisture sorption isotherms. This profile would be generated by [relative humidity and temperature] data collected from the representative bridge deck at the time the cores were extracted from the deck, which is the time the data used to create the in-situ gravimetric profile was obtained. Provided that the moisture levels contained inside the representative concrete deck were not sufficient to force the obtained internal RH&T values to the extreme [high RH] limits of the moisture sorption isotherm, then a direct comparison could be made. If the assumption of static thermal and moisture equilibrium was valid, in theory, these two particular moisture profiles (i.e., using moisture content and percent of saturation—based moisture metrics) would synchronize. Concerning the comparison of profiles, the following should be noted. The profiles seen in figure 73 were generated by fitting a smooth curve to the discrete values determined earlier. Consequently, when comparing profiles, the reader should be more concerned with the discrete *points* than the smooth line that appears to connect them. This is especially true in the case of the moisture sorption isotherm—based profiles, as they lack a discrete value at the 4” depth.

Ultimately, as is indicated by both of the moisture profiles in figure 73, the in-situ gravimetrically determined profiles (i.e., the solid red profiles) clearly exceeded the practical limits of the determined moisture sorption isotherms. The limits of the isotherm are delineated in figure 73 by moisture profiles created gravimetrically from concrete disc specimens that had been allowed to achieve [moisture] mass equilibrium in the nearly saturated environment produced by the potassium sulfate (K_2SO_4) saturated salt solution (i.e., the dashed purple line). As the reader may recall, the corresponding internal RH values ranged from approximately 97% to 98% in this sealed environment (at 25°C). Though the in-situ gravimetric moisture profile clearly does exceed the limits of the moisture sorption isotherm, the reader may notice that the moisture profiles generated by the moisture sorption isotherms (i.e., the solid green profiles) in most cases do not quite reach the delineated practical limits of the moisture sorption isotherm. Therefore, one would expect at these depth locations to see profile synchronization if the hypothesis were valid. That is to say, if the hypothesis were valid, then one would only expect one of two outcomes. First, in the case where the in-situ moisture levels were to cause the internal RH values to maximize, then the moisture sorption isotherm—based profiles would over-lap or slightly exceed, the K_2SO_4 gravimetric profiles. The second outcome

is the synchronization of the moisture sorption isotherm—based profile with the in-situ gravimetric profile. Any other result would seemingly invalidate the author's hypothesis, as was restated above.

As the moisture sorption isotherm—based profiles do not meet or exceed the K₂SO₄ gravimetric profiles at many locations, nor do they synchronize with the in-situ gravimetric profile at these locations, one might conclude that the hypothesis has been invalidated. At first this seemed to be the case. However, upon further investigation, the author realized that an assumption must be questioned. The assumption being referred to was one based on literature sources; it was assumed that the moisture sorption isotherms were temperature independent for most practical applications containing moderate temperature variations, including this application. The author now realizes that this should not have been assumed. RH values obtained from the representative bridge deck, at the time associated with the core extractions, were associated with internal temperatures spanning 12°C to 14°C, which is 13°C to 11°C below the temperature in which the moisture sorption isotherms were created. If the author had developed two moisture sorption isotherms, each based on a different temperature, then by using the Clausius-Clapeyron equation (section 2.2.3.2) any other relevant moisture sorption isotherm could have been mathematically determined. However, since only a single moisture sorption isotherm was developed, another approach will be needed.

In an attempt to adjust the observed RH value to account for temperature differences, the author started by employing the Kelvin equation. The idea being that by holding certain variables constant, including the pore mean radius, across two different temperatures, an equality expression could be developed and used to estimate a temperature-adjusted RH. Starting with the form of the Kelvin equation given by equation 2.105 (section 2.3.3.2), the author assumes that the solution activity is equal to one ($a_s = 1$), and therefore comes out of the expression (since, $\ln(1) = 0$). This was assumed because the activity of the pore solution was not determined during this investigation, and therefore the following estimation shall assume that the solution is pure water. Consequently, the following equation is written (see equation 9.1).

$$\ln\left(\frac{RH}{100\%}\right) = \frac{-2\hat{V}_{solv}^L \gamma}{R_u T} \left(\frac{1}{r_{Lx}}\right) \quad \text{Equation 9.1}$$

Assuming that pore radius (r_{Lx}) and the molar volume (\hat{V}_{solv}^L) terms are constant for two temperatures of interest, the following equality may be written, as shown by equation 9.2. The subscripting, $i^\circ\text{C}$, denotes values (i.e., temperature (T), RH or surface tension(γ)) existing at the initial (or field) temperature conditions. Likewise, the subscripting, 25°C , denotes values at the final (or moisture isotherm) temperature conditions, assumed to be 25°C.

$$\frac{T_{i^\circ\text{C}}}{\gamma_{i^\circ\text{C}}} \ln\left(\frac{RH_{i^\circ\text{C}}}{100\%}\right) = \frac{T_{25^\circ\text{C}}}{\gamma_{25^\circ\text{C}}} \ln\left(\frac{RH_{25^\circ\text{C}}}{100\%}\right) \quad \text{Equation 9.2}$$

Solving equation 9.2 for the adjusted relative humidity at the temperature of interest, $RH_{25^{\circ}\text{C}}$, equation 9.3 is obtained. It should be recalled that Kelvin units for temperature are to be used.

$$RH_{25^{\circ}\text{C}} = 100\% \left(\frac{RH_{i^{\circ}\text{C}}}{100\%} \right)^{\left(\frac{T_{i^{\circ}\text{C}}}{T_{25^{\circ}\text{C}}} \times \frac{\gamma_{25^{\circ}\text{C}}}{\gamma_{i^{\circ}\text{C}}} \right)} \quad \text{Equation 9.3}$$

Using equation 9.3, table 14 is generated. Table 14 contains all the temperature-adjusted RH values; additionally, it contains all the variable values used. It should be noted that the surface tension values were taken to be those of pure water at the various indicated temperatures and at standard pressure; the surface tension values were linearly interpolated from tables contained in a document by N.B. Vargaftik and others entitled “International tables of the surface tension of water” (Vargaftik, Volkov, and Voljak 1983); this document may be downloaded from the NIST website (www.nist.gov).

Depth	Initial Relative Humidity ($RH_{i^{\circ}\text{C}}$)	Initial Temperature ($T_{i^{\circ}\text{C}}$)		Desired Temperature ($T_{25^{\circ}\text{C}}$)	Surface Tension at Initial Temp. ($\gamma_{i^{\circ}\text{C}}$)	Surface Tension at Desired Temp. ($\gamma_{25^{\circ}\text{C}}$)	Temp.- Adjusted Relative Humidity ($RH_{25^{\circ}\text{C}}$)
[in.]	[%]	[°C]	[K]	[K]	[N/m]	[N/m]	[%]
2	95.58	12.00	285.15	298.15	0.07394	0.07199	95.88
3	94.01	11.93	285.08	298.15	0.07395	0.07199	94.42
4	Corrupt	Corrupt	Corrupt	Corrupt	Corrupt	Corrupt	Corrupt
5	94.92	12.99	286.14	298.15	0.07379	0.07199	95.24
6	94.54	13.79	286.94	298.15	0.07368	0.07199	94.86

Table 14: Kelvin equation—based calculated effective internal relative humidity values at 25°C, along with supporting values

Using the Kelvin equation, as was shown in table 14, the in-situ relative humidity values were adjusted for temperature to permit more accurate calculations of moisture using the moisture sorption isotherms created at 25°C; the resulting temperature-based adjustments were on the order of +0.4% RH. However, there were many assumptions made when formulating equations 9.2 and 9.3, which neglect the effects of temperature change. Specifically, it was assumed that the pore radius remained constant. Increases in temperature will, in theory, cause the volume of many liquids, like water, to expand. The effects from such volumetric change on the RH inside concrete pores are noticeable. A volumetric increase causes the water to expand into pores having larger radii. Consequently, the observed RH becomes increased; this effect is not accounted for by equations 9.2 and 9.3. In a paper written by Dr. Zachary C. Grasley and Dr. David A. Lange, entitled “*Thermal dilatation and internal relative humidity of hardened cement paste*,” this apparent under-estimation by the Kelvin equation is commented on (Grasley and Lange 2007). In their paper, Grasley and Lange point to the research of Fariborz Radjy (and others) performed while at the Technical University of Denmark (DTU). A

model offered by Radjy, shown graphically in the report by Grasley and Lange, indicates that the Kelvin equation will underestimate temperature change effects by approximately half. According to the graph offered in the report by Grasley and Lange, based on the starting observed internal relative humidity values, the adjustment to the RH values in this investigation should be on the order of 0.08% RH / °C. The results of this adjustment, based on the work of Radjy, are shown in table 15. Additionally, the percent of saturation (S_L) and moisture content (MC) values, based on the temperature-adjusted RH values were determined by the moisture sorption isotherms and included in table 15. Subsequently, new plots based on these updated discrete values were created, as shown by figures 74 and 75.

Depth [in.]	Adjusted Internal RH & T Values		Moisture Sorption Isotherm Based - Adjusted	
	RH [%]	Temp. [°C]	S_L [%]	MC [%]
1	N/A	N/A	N/A	N/A
2	96.62	25	76.34	3.93
3	95.06	25	72.65	4.16
4	Corrupt	Corrupt	Corrupt	Corrupt
5	95.88	25	73.57	4.89
6	95.44	25	73.55	4.78
7	N/A	N/A	N/A	N/A

Table 15: Calculated internal relative humidity values adjusted for 25°C, based on the model by Radjy, along with the corresponding adjusted moisture sorption isotherm—based discrete moisture values

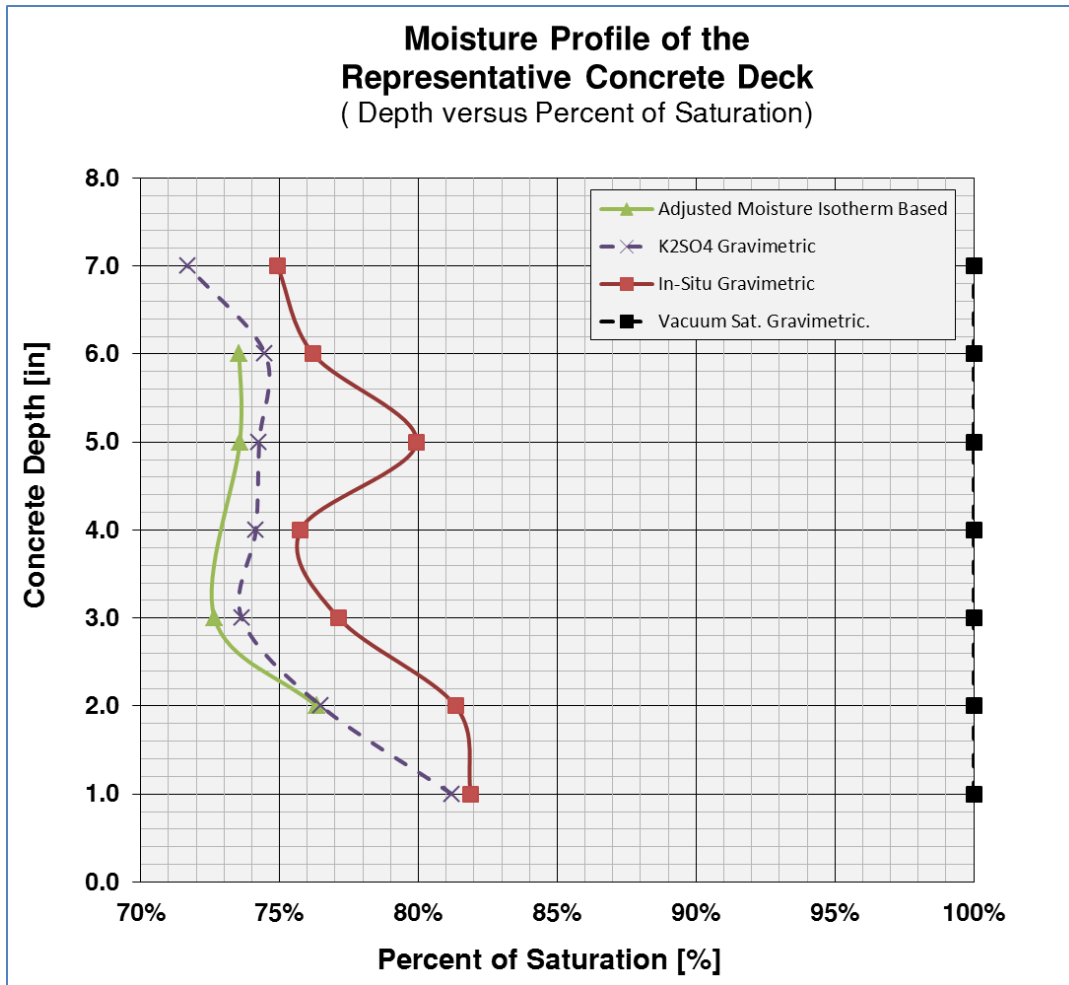


Figure 74: Moisture profiles for the representative concrete deck, expressed as percent of saturation, including the temperature-adjusted moisture sorption isotherm—based profile.

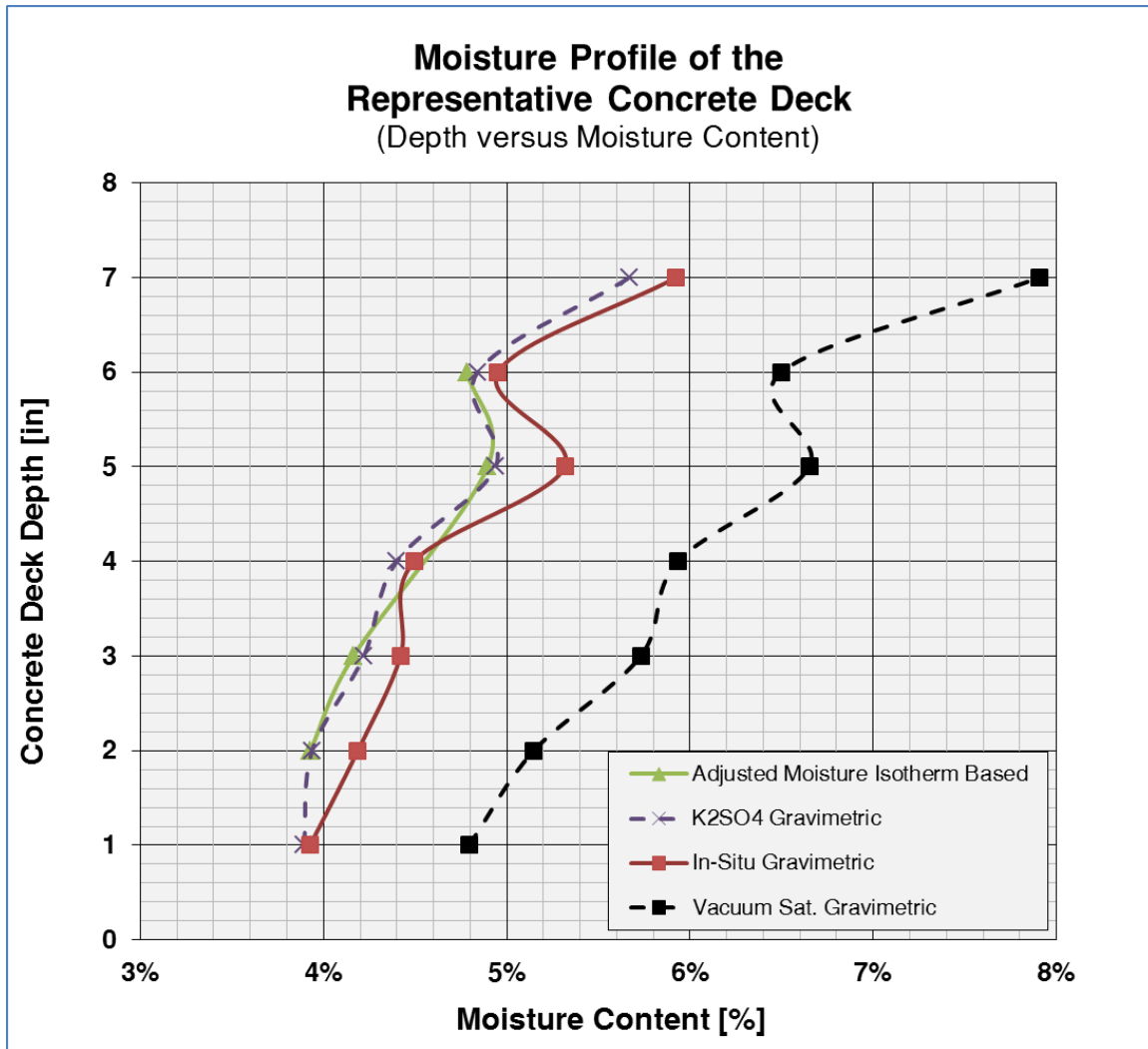


Figure 75: Moisture profiles for the representative concrete deck, expressed as moisture content, including the temperature-adjusted moisture sorption isotherm—based profile.

After the moisture profiles were adjusted to reflect the temperature difference (as shown in figures 74 and 75), the reader will notice that, although the adjusted moisture sorption isotherm—based profiles have moved further to the right, some of the discrete values do not exactly line up on (or surpass) the K₂SO₄-based gravimetric profile. At this time the limitations of the sensor need to be considered. While it would be nice to assume that the values obtained from a “calibrated” sensor are exact, in truth there are several factors that affect a sensor’s accuracy; two are mentioned now. As was noted in section 7.1.2, the manufacturer of the RH&T sensor documented that the sensor itself contained a hysteresis on the order of $\pm 1\%$ RH. Additionally, as is shown in table 3 (section 7.2.1), the theoretical RH values for saturated salt environments used to calibrate the sensors had accuracies on the order of $\pm 0.5\%$ RH in vicinity of the temperature and relative humidity of interest. If one were to assume a perfect calibration was achieved, then the best accuracy achievable would be approximately $\pm 1.5\%$ RH. Practically speaking, all the RH differences between the discrete values used to generate the adjusted moisture

isotherm-based profile, and those used to generate the K₂SO₄-based gravimetric profile are within this range of accuracy, as shown in table 16. Therefore, the author can assume that the RH values obtained were maximized values. That is to say, the effects of meniscus curvature on the suppression of the observed in-situ RH would be too small for the author to measure.

Depth [in.]	Adjusted RH Values (from Table 15) [%]	K ₂ SO ₄ RH Values (from Table 9) [%]	Difference in RH Values [%]
1	N/A	N/A	N/A
2	96.62	97.10	-0.48
3	95.06	98.10	-3.04
4	Corrupt	Corrupt	Corrupt
5	95.88	97.10	-1.22
6	95.44	97.50	-2.06
7	N/A	N/A	N/A

Table 16: Calculated RH differences between the adjusted RH values (from table 15), initially obtained from the representative bridge deck at the time of core extraction, and the RH values (from table 9) obtained inside the disc specimens when at equilibrium in a K₂SO₄-produced environment.

That being said, it is clear that the moisture sorption isotherm-based profile was returning the highest values for moisture that were allowed by the moisture sorption isotherm. Consequently, while a direct comparison of the [adjusted] moisture sorption isotherm-based moisture and in-situ gravimetric profiles may not be able to indicate the validity of the moisture sorption isotherm for use with this dynamically evolving system (or others like it), it does not invalidate it either. As the reader may recall, the author had stated earlier that figure 64 looked a little misleading. It was only a coincidence that their seemed to be a downward trend of the measured internal relative humidity during the exposure to the dehumidified environment. As the preceding exploration shows, the observed change to the internal relative humidity would actually be attributed to temperature variations.

As mentioned at the beginning of this section, the methodologies to be employed, as outlined in section 6.1, were divided into two distinct approaches. The direct comparison approach was just performed and has been shown not to be an option for determining the viability of using relative humidity-based moisture sorption isotherms for determining moisture profiles. The second approach is data interpretation, which is really a qualitative approach. It was assumed by the author that, relative to the time scale needed for system equilibrium to occur, it is reasonable to assume that moisture evolution occurs very slowly. Consequently, it is also reasonable to assume that moisture content would remain fairly constant over the period of a diurnal cycle. Qualitatively speaking then, an internal relative humidity data stream that remains fairly unchanged throughout the course of a day is an indication of [approximate] system equilibrium, and thus system compatibility. As shown, temperature variations, even during the span of a day, will affect the observed internal relative humidity. However, this is not necessarily due to

moisture sorption isotherm compatibility issues. Any contained system of aqueous solution, at dynamic equilibrium, will experience changes to its equilibrium vapor pressure after temperature changes are made to the system. This effect is shown to be true by the Clausius-Clapeyron equation. However, large variations to the observed internal relative humidity, which are out of line with values resulting from [legitimate] temperature changes to the solution, would be an indication that temperature lag effects are invalidating the results obtained by the moisture sorption isotherm.

Figure 72 provides the internal relative humidity and temperature values spanning a day. By observation, every depth location experienced changes to the measured internal relative humidity. However, the changes measured were gradual and on the order of 1% to 2% RH. These internal RH changes are completely in line with temperature changes of a static system and do not seem to indicate the existence of predominant thermal lag effects. The approximate maximum rate of temperature evolution observed in this system was $3^{\circ}\text{C}/\text{Hour}$. Such thermal lag effects are, however, visible in figure 62, prior to the new sensor packing method. This would seem to indicate that there is an inverse relationship involving the control volume (i.e., the size of the created cavity) and the relative size of the structure (as further defined in section 4.2.2). That is to say, as the structure becomes larger, the attenuation of temperature becomes greater. Consequently, the rate of temperature evolution decreases. Inversely, as the control volume decreases, lesser amounts of time are required for the system to achieve dynamic equilibrium. At some point there is effectively time synchronization between these two concepts, resulting in a dynamically evolving system that effectively behaves as a static one. When this occurs, the use of moisture sorption isotherms to create moisture profiles is valid. The author believes that the data supports this, and validates the hypothesis stated in section 4.2.2.

As was stated in section 4.2.1, the author also hypothesized that *“in a concrete highway bridge deck of typical construction, there exists the potential for a non-trivial level of moisture content for which no unique correlation to relative humidity may be made”*. By comparing the vacuum-saturated gravimetrically determined moisture profiles (i.e., the dashed black lines) with the K_2SO_4 gravimetric profiles, it is clear that there is significant change between these two profiles. The reader may recall that the saturated gravimetric profiles indicate the physical [absolute] maximum amount of moisture a concrete system can hold, while the K_2SO_4 gravimetric profiles indicate an approximate delineation of the upper moisture values uniquely detectable by using relative humidity methods. Moisture levels that exist approximately between these two profiles could not be determined using relative humidity methods. That is to say at some point, as approximately defined by the K_2SO_4 gravimetric profile, the relationship between the concrete deck’s moisture levels and correlated internal relative humidity values breaks down. If, however, the difference between these two profiles is sufficiently small, meaning that a specimen at equilibrium in an environment produced by the K_2SO_4 saturated salt solution is approximately saturated in the absolute sense, then the moisture content could be taken as the upper limit indicated by the moisture sorption isotherm. According to the results of this investigation, this is not so. The change in percent of saturation (ΔS_L), as indicated in figure 23 (see section 2.3.3.3), ranges between 18 and 28%. This is certainly a

sufficiently large potential difference. Consequently, if internal RH values are being observed that correspond to the [high] extreme end of the moisture sorption isotherm, then a moisture level should not be accessed using this method. This result validates the author's hypothesis stated in section 4.2.1.

10. DISCUSSION

The author has come to understand that the relationship that appears to exist in hardened concrete between the internal relative humidity and corresponding moisture levels are not direct relations. There is no direct scientific principle that relates a given volume of solution, independent of containment properties, to a definitive level of relative humidity. Rather, solution chemistry, temperature, pore geometry and moisture transport phenomena are really responsible for the [apparent] correlation; a constitutive relationship. This constitutive relationship, termed the relative humidity—based moisture sorption isotherm, is principally governed by the effects of capillary pore size (i.e., the mean radius).

In theory, any amount of [concave] curvature at the meniscus interface will suppress a solution's chemical potential, causing the solution's equilibrium vapor pressure to become lowered, thus reducing the relative humidity generated by the solution in a closed system. That is to say, in theory the constitutive relationship (i.e., the moisture sorption isotherm) holds in the presence of any amount of curvature produced by the capillary pores; However, as shown by the Kelvin equation, it is not until moisture becomes limited to capillary pores of no larger than 50 to 100 nanometers that practical changes to the internal relative humidity are observable by conventional methods of relative humidity measurement. The author realized that as a consequence, once moisture begins to fill capillary pore spaces having radii greater than approximately 50 to 100 nanometers, the only [practical] measurable relative humidity possible is the maximum value for the given solution at a temperature, where meniscus curvature has no effect. Once the observable relative humidity has become effectively maximized, for a given temperature, any additional moisture that fills the progressively larger pore spaces would not continue to be identifiable by a unique relative humidity value.

By comparing the moisture masses of specimens that were allowed to reach equilibrium in nearly saturated ambient conditions to the moisture masses of the same specimens having undergone vacuum saturation, it was clear that the potential for moisture containment beyond what is identifiable by the moisture sorption isotherm is not trivial (e.g., 18% to 28% of total moisture capacity, observed in this investigation). Therefore, once the observed internal RH values are maximized, the moisture sorption isotherm is no longer a valid method for determining moisture levels, nor should the maximum moisture of a moisture sorption isotherm, for a given temperature, be assumed. As was seen during this investigation and similar attempts by others to quantify moisture levels in aged concrete decks (at depths associated with [steel] reinforcement) using relative humidity methods, this sort of maximized RH outcome is typical. However, this outcome does not necessarily preclude the use of relative humidity—based moisture sorption isotherms from being a tool for determining moisture levels in all bridge decks. This

investigation did not include hardened concrete bridge decks spanning multiple levels of maturity or initial internal moisture nor did it attempt to investigate depth locations near the deck's surface. This outcome simply acknowledges a definite possible barrier to successful implementation of the method in certain applications; it does not invalidate the method.

The initial perceived barrier to using relative humidity—based moisture sorption isotherms as a viable moisture determination method was founded on theory and small-scale experimental conclusions. Moisture sorption isotherms are created under environmentally controlled conditions, where a fix ambient environment is produced and representative specimens are given the time to achieve [mass] equilibrium with this fixed environment. Consequently, the correlated relationship (i.e., mass versus relative humidity) is really representative of a static system. The [concrete] structures of interest, however, are in a perpetual state of internal temperature and moisture change, and are never given the opportunity to truly achieve equilibrium with the environment. As a result, it has been long assumed, and validated through small scale testing, that the moisture sorption isotherm could not be applied in its current form to systems exposed to natural weathering conditions.

However, when this method was investigated on a larger scale, the author was able to determine that a [concrete] structure's "larger" relative geometry plays a significant role in whether or not this barrier is valid in a practical sense (as elaborated on in section 4.2.2). That is to say, while this barrier does hold true on a theoretical level, the error associated with using the method in [concrete] structures exposed to natural weathering conditions becomes increasingly trivial with increasing size. At some point, the structure is large enough such that it may be assumed that the observed internal [relative humidity and temperature] conditions are evolving in step with the structure's evolving thermal and moisture state. Consequently, on a practical level, relative humidity—based moisture sorption isotherms may be considered a viable moisture determination method.

11. CONCLUSIONS

In conclusion, it was experimentally shown that the thermal and moisture lag effects which have historically precluded the use of a relative humidity—based moisture sorption isotherms as a correlation tool for determining moisture levels in smaller concrete structures exposed to natural weathering are significantly smaller in larger concrete structures. Consequently, the use of relative humidity—based moisture sorption isotherms to determine the internal moisture levels of concrete bridge decks is a viable method in concept. A more likely barrier to the successful application of this method is the limited range of identifiable moisture content offered by the moisture sorption isotherms. At some point, a level of moisture, short of saturation, is reached that corresponds to a maximized internal RH value for a pore solution at a given temperature. Beyond that level of moisture content, the observed internal RH values remain unchanged (i.e., maximized). Consequently, the moisture sorption isotherm cannot identify these increased levels of moisture. If the moisture level in the system of interest

is providing maximized observable internal RH values, then the method breaks down and is no longer viable.

12. RECOMMENDATIONS

Based on the author's conclusions, the viability of using relative humidity—based moisture sorption isotherms for determining moisture levels in concrete bridge decks must really be determined on a case-by-case basis. That is to say, each structure may, or may not, have existing moisture conditions that preclude the use of this method. Consequently, the author recommends that, prior to the deployment of a full-scale RH&T sensor array, investigators perform an initial reconnaissance and spot-check the structure of interest using a portable RH probe. If internal RH values approaching saturation (i.e., 100% RH) are observed, then further efforts to use this method are unlikely to produce the desired results.

If the reconnaissance produces favorable results, the next recommendation is that every effort be made to ensure that the control volume around the sensor is minimized and remains sealed. A sign that the probes were not properly installed are large amplitude shifts in the observed internal relative humidity levels, which is an indication that, relative to the size of the structure, the cavity is too large and temperature lag effects are present. The final recommendation has to do with the sensors' functioning behavior. If the sensors being used are like the ones used in this investigation (i.e. capacitive-based), then the investigator may need to allow time for the sensors to become conditioned to the environment inside the concrete structure. Once conditioned, a calibration may be determined and applied.

In terms of future research, the author has several recommendations. First, this investigation dealt with many set-backs pertaining to sensor calibration issues. The hygroscopic material used in the capacitive type sensor was unable to maintain its initial calibration once placed in the concrete deck. The author was unable to determine the cause of the shifting, but the values eventually stabilized; it is speculated that condensation or a combination of perpetual high relative humidity and undetermined material (or chemical) factors may be to blame. Regardless, future research efforts should include investigating alternative methods for RH&T determination. Second, the representative concrete deck specimen used during this investigation was aged and ultimately contained excessive levels of moisture that maximized the observable internal RH values. In the future, investigations should include bridge decks with less initial moisture. Younger bridges or those located in more arid environments might provide lower initial moistures, contrary to earlier assumptions made by the author (see section 7.3.1). Third, the relative humidity—based moisture sorption isotherms were developed from cores taken between the openings in the reinforcement grid. Therefore, this developed constitutive relationship would apply to the concrete between the reinforcement. However, it would seem that at the interface, between the concrete and the reinforcement, the existence of an interfacial transition zone (ITZ) would cause the moisture levels to be different than those which would identified by the generated moisture sorption isotherm; an investigation into this may be warranted.

Finally, due to seasonal variations, bridge decks are likely to be exposed to freezing temperatures; this area may warrant investigation, as freeze-thaw is not a trivial deterioration mechanism. When freezing of the pore solution occurs, expansion of the solution volume is on the order of 9%. However, investigation of this would likely be a much more complicated issue. This is because within a pore, solution will generally freeze at temperatures below 0°C (32°F); this is because conditions inside the pore structure reduce the chemical potential of the solution and shift the triple point of the solution further left (see figure 1, section 2.1). This is the result of a couple of factors. First, the pore solution is not pure water. The presence of dissolved salts, among other solutes, alone would serve to suppress the freezing temperature of the solution. Next, the small pore geometry acts to suppress the chemical potential of the solution and would consequently also suppress the freezing temperature of the solution. To complicate this, since the chemical potential is a function of pore size, so too is the freezing temperature. That is to say, the pore solution's freezing temperature is not fixed. Pore solution will progressively freeze starting from the largest pores to the smallest as the temperature is progressively reduced. For most practical purposes, the moisture in the gel pores is assumed to not freeze at all (Neville 2011).

13. ACRONYMS & VARIABLES

A	Area or Point A	$[length^2]$ or $[Unitless]$
A_p	Projected area	$[length^2]$
a	Semi-major axis of an ellipse	$[length]$
a_s	Activity of solvent in a solution	$[mol/mol]$
b	Semi-minor axis of an ellipse	$[length]$
C	Capacitance	
$C_{const.,k}^{Si}$	The k^{th} constant, belonging to the k^{th} RH residual [sub-] model of a specific i^{th} sensor RH residual model	$[\%]$
$C_{RH,k}^{Si}$	The k^{th} relative humidity coefficient, belonging to the k^{th} RH residual [sub-] model of a specific i^{th} sensor RH residual model	
$C_{T,k}^{Si}$	The k^{th} relative temperature coefficient, belonging to the k^{th} RH residual [sub-] model of a specific i^{th} sensor RH residual model	
c	Speed of light in a vacuum	$[length/time]$
dA	Infinitesimal area	$[length^2]$
dA_p	Infinitesimal projected area	$[length^2]$
$dF_{(\Delta p)}$	Infinitesimal force resulting from a pressure imbalance	$[Force]$
$dF_{v(\Delta p)}$	Infinitesimal vertical force component resulting from a pressure imbalance	$[Force]$
$dF_{v(\gamma)_1}$	Infinitesimal surface tension force acting in the vertical direction on the principle section DFB of figure 10	$[Force]$
$dF_{v(\gamma)_2}$	Infinitesimal surface tension force acting in the vertical direction on the principle section AGC of figure 10	$[Force]$
dG	Total infinitesimal change to the Gibbs free energy	$[Force \times Length]$
dG_i^x	Partial contribution to the total infinitesimal change to the Gibbs free energy; made by the i^{th} substance of a phase x	$[Force \times Length]$
dl	Infinitesimal (perimeter) length	$[Length]$
dn	Infinitesimal change in the molar quantity	$[mol]$
dn_i^x	Infinitesimal change in the molar quantity of the i^{th} substance of a phase x	$[mol]$
dn_{solv}^L	Infinitesimal change in the molar quantity of the solvent liquid	$[mol]$

dn_{solv}^v	Infinitesimal change in the molar quantity of the solvent vapor	[mol]
dp_i^x	Infinitesimal change in the pressure of the i^{th} substance of a phase x	[Force/area ²]
$d\theta_z$	Infinitesimal angle of rotation about the vertical z-axis	[Rad.]
$d\mu$	Total infinitesimal change to the chemical potential	[(Force×Length)/mol]
$d\mu_i^x$	Partial contribution to the total infinitesimal change to the chemical potential; made by the i^{th} substance of a phase x	[(Force×Length)/mol]
$d\mu_{solv}^L$	Infinitesimal change to the chemical potential of the solvent liquid	[(Force×Length)/mol]
$d\mu_{solv}^v$	Infinitesimal change to the chemical potential of the solvent vapor	[(Force×Length)/mol]
$F_{(\Delta p)}$	Total pressure imbalance force	[Force]
$F_{v(\Delta p)}$	Total pressure imbalance force acting in the vertical direction	[Force]
$F_{(\gamma)}$	Total surface tension force	[Force]
$F_{v(\gamma)}$	Total surface tension force acting in the vertical direction	[Force]
g	Gravitational acceleration constant	[length/time ²]
G	Gibbs free energy	[Force × Length]
G_i^x	Gibbs free energy of an i^{th} substance of a phase x	[Force × Length]
h	Height distance	[length]
H_{abs}	Absolute humidity, at a temperature	[mass/mass]
H_{sat}	Saturation humidity, at a temperature	[mass/mass]
i	Van't Hoff Factor	[mol/mol]
K	Curvature of an arbitrary normal section	[1/Length]
K_{\perp}	Curvature of an arbitrary normal section, orthogonal to the section containing curvature K	[1/Length]
k	Mean curvature	[1/Length]
k_1	Principle (max or min) meniscus curvature, orthogonal to k_2	[1/Length]
k_2	Principle (min or max) meniscus curvature, orthogonal to k_1	[1/Length]
MC	Moisture content	[%]
m_{dry}	Mass of dry air	[mass]
m_{sat}	Saturation mass of water vapor	[mass]
m_v	Mass of vapor, assumed to be water	[mass]
$m_{Avg.Strip.}^{i-DL}$	Mass of a disc specimen having been	[mass]

	stripped of most non-cementitious materials, representing the i^{th} depth location	
$m_{Meas.}^{i-DL}$	Mass of a fully prepared disc specimen, representing the i^{th} depth location	[mass]
$m_{In-situ}^{i-DL}$	The initial in-situ mass of a processed disc specimen, which has not yet been fitted with non-cementitious materials, representing the i^{th} depth location	[mass]
m_{prep}^{i-DL}	Mass of all non-cementitious materials used in the preparation of the disc specimen, representing the i^{th} depth location	[mass]
$m_{Unremoved}^{i-DL}$	Mass of all non-cementitious materials which remain unremoved from the disc specimen, representing the i^{th} depth location	[mass]
$m_{\Delta H_2O}^{i-DL}$	Moisture mass change of a disc specimen, representing the i^{th} depth location	[mass]
n	Number of moles, or molar quantity	[mol]
n_i^x	Molar quantity of the i^{th} substance of a phase x	[mol]
n_g	Number of gas moles	[mol]
n_r	Refractive index	
n_{sol}	Number of solute moles	[mol]
n_{solv}	Number of solvent moles	[mol]
n_v	Number of vapor moles	[mol]
P	Pressure	[Force/Length ²]
P_{atm}	Atmospheric pressure	[Force/Length ²]
P_{CR}	Critical pressure	[Force/Length ²]
P_{eq}	Equilibrium vapor pressure (or vapor pressure) of a liquid	[Force/Length ²]
$P_{eq(soln)}$	Equilibrium vapor pressure (or vapor pressure) of a liquid solution	[Force/Length ²]
$P_{eq(solv)}$	Equilibrium vapor pressure (or vapor pressure) of a liquid solvent	[Force/Length ²]
$P_{eq,A}$	Equilibrium vapor pressure (or vapor pressure) of a liquid at temperature A	[Force/Length ²]
$P_{eq,B}$	Equilibrium vapor pressure (or vapor pressure) of a liquid at temperature B	[Force/Length ²]
P_{eqf}	Final equilibrium vapor pressure (or vapor pressure) of a liquid	[Force/Length ²]
P_{eqi}	Initial equilibrium vapor pressure (or vapor pressure) of a liquid	[Force/Length ²]
P_{gauge}	Gauge pressure	[Force/Length ²]

P_{total}	Total pressure of the gaseous (gas-vapor) mixture	$[Force/Length^2]$
P_1	Pressure on the concave side of the meniscus	$[Force/Length^2]$
P_2	Pressure on the convex side of the meniscus	$[Force/Length^2]$
p_N	Partial pressure of the N^{th} gas or vapor in the gaseous mixture	$[Force/Length^2]$
p_{sat}	Saturation vapor pressure of a gaseous mixture	$[Force/Length^2]$
p_i^x	Pressure of the i^{th} substance of a phase x	$[Force/Length^2]$
p_{solv}^L	Pressure of the liquid solvent	$[Force/Length^2]$
p_{solv}^v	Pressure of the solvent vapor	$[Force/Length^2]$
p_v	Vapor pressure of a gaseous mixture	$[Force/Length^2]$
p_{vf}	Final vapor pressure of a gaseous mixture	$[Force/Length^2]$
p_{vi}	Initial vapor pressure of a gaseous mixture	$[Force/Length^2]$
Q	Total electric charge	
R	Mean radius of the meniscus	$[length]$
r	Mean radius of a capillary tube (or pore)	$[length]$
r_{L_x}	Mean radius of a moisture layer in a capillary tube (or pore) about an x-axis	$[length]$
r_{L_z}	Mean radius of a moisture layer in a capillary tube (or pore) about an z-axis	$[length]$
r_x	Mean radius of a capillary tube (or pore) about the x-axis	$[length]$
r_z	Mean radius of a capillary tube (or pore) about the z-axis	$[length]$
r_1	Principle (max or min) tube (or pore) radius, orthogonal to r_2	$[length]$
r_2	Principle (min or max) tube (or pore) radius, orthogonal to r_1	$[length]$
$Residual_{Mod.}^{Si}$	RH residual model for a specific i^{th} sensor	$[\%]$
$Residual_{Mod.,k}^{Si}$	The k^{th} RH residual [sub-] model of a specific i^{th} sensor RH residual model	$[\%]$
$Residual_{Theo.}$	RH theoretical residual, based directly on a standard	$[\%]$
$Residual_{Theo,salt}^{Si,t}$	RH theoretical residual of an i^{th} sensor inside the RH calibration apparatus, containing a specific saturated salt solution (salt), at a nominal target temperature (t)	$[\%]$
RH	Relative humidity	$[\%]$
$RH_{cal.}^{Si}$	User determined RH calibration for a specific i^{th} sensor	$[\%]$
$RH_{Cond.}^{Si}$	Conditional relative humidity for an i^{th}	$[\%]$

	sensor, used in programming logic.	
RH_{max}	Maximum relative humidity	[%]
$RH_{Mean,salt}^{Si,t}$	Mean relative humidity as measured by an i^{th} sensor inside the RH calibration apparatus, containing a specific saturated salt solution (salt), at a nominal target temperature (t)	[%]
$RH_{Meas.}$	Relative humidity as determined by the sensor prior to user calibration	[%]
$RH_{Meas.}^{Si}$	Relative humidity as measured by a specific i^{th} sensor prior to the application of the user determined RH calibration	[%]
RH_{salt}^{FPI}	Relative humidity values corresponding to an i^{th} fixed point temperature value, for a specific saturated salt solution (salt), near the interpolation point of interest	[%]
$RH_{salt}^{Si,t}$	Single relative humidity measurement of an i^{th} sensor inside the RH calibration apparatus, containing a specific saturated salt solution (salt), at a nominal target temperature (t)	[%]
$RH_{Theo.}$	Theoretical relative humidity produced by a standard	[%]
$RH_{Theo}^{salt,t}$	Theoretical relative humidity within the RH calibration apparatus, at dynamic equilibrium, containing a specific saturated salt and of nominal target temperature (salt, t)	[%]
R_u	Universal Gas Constant ~ 8.31451	$J/(K \times mol)$
R_1	Principle meniscus radius of curvature, orthogonal to R_2	[Length]
R_1^*	Arbitrary meniscus radius of curvature, orthogonal to R_2^*	[Length]
R_2	Principle meniscus radius of curvature, orthogonal to R_1	[Length]
R_2^*	Arbitrary meniscus radius of curvature, orthogonal to R_1^*	[Length]
S	Percentage of [humidity] saturation (or percentage of absolute humidity)	[%]
S_L	Percentage of [liquid] saturation	[%]
T	Temperature	[° Temp]
T_A	Temperature A	[° Temp]
T_B	Temperature B	[° Temp]
T_{CR}	Critical temperature	[° Temp]
t_L	Liquid layer thickness	[Length]

$T_{Mean,salt}^t$	Mean temperature presumed to exist inside the RH calibration apparatus, containing a specific saturated salt solution (salt), and of a nominal target temperature (t)	[° Temp, °C]
$T_{Mean,salt}^{Si,t}$	Mean temperature value as measured by the i^{th} sensor in an environment set to a nominal target temperature (Si, t) inside the RH calibration apparatus, containing a specific saturated salt solution (salt)	[° Temp, °C]
T_{salt}^{FPI}	Temperature of an i^{th} fixed point, for a specific saturated salt solution (salt), near the interpolation point of interest	[° Temp, °C]
$T_{salt}^{Si,t}$	Single measured temperature value by the i^{th} sensor in an environment set to a nominal target temperature (Si, t) inside the RH calibration apparatus, containing a specific saturated salt solution (salt)	[° Temp, °C]
V	Volume	[Length ³]
\mathbb{V}	Potential	
\mathbb{V}_o	Initial potential	
V_i^x	Volume of the i^{th} substance of a phase x	[Length ³]
\hat{V}	Molar volume	[Length ³ /mol]
\hat{V}_i^x	Partial molar volume of the i^{th} substance of a phase x	[Length ³ /mol]
v	Speed of light through a medium	
w	Moisture Content	[%]
w/c	Water to cement ratio (by volume or mass)	[Length ³ /Length ³] or [mass/mass]
X_s	Mole fraction of solvent molecules in the solution	[mol/mol]
α	Arbitrary angle used to locate a point along the arc length of a circular sector (see figure 10)	[Rad.]
β	Angle between the principle normal section along which the curvature k_1 is defined and the arbitrary normal section along which the arbitrary curvature k is defined	[Rad.]
ΔH_A	Heat of adsorption	[Energy/mol]
ΔH_v	Heat of vaporization	[Energy/mol]
$\Delta m_{\Delta H_2O}^{i-DL}$	Change in the Moisture mass change of a disc specimen, representing the i^{th} depth location	[mass]
ΔP	Change in pressure	[Force/Length ²]
ΔS_L	Change in the percentage of [liquid]	[%]

	saturation	
μ_i^x	Chemical potential of the i^{th} substance of a phase x	$[(\text{Force} \times \text{Length})/\text{mol}]$
μ_{solv}^L	Chemical potential of the solvent liquid	$[(\text{Force} \times \text{Length})/\text{mol}]$
μ_{solv}^v	Chemical potential of the solvent vapor	$[(\text{Force} \times \text{Length})/\text{mol}]$
γ	Surface tension	$[\text{Force}/\text{Length}]$
γ_v	Vertical component of surface tension	$[\text{Force}/\text{Length}]$
ε	Arc length of a sector	$[\text{Length}]$
ϵ_c	Dielectric constant	
θ_c	Angle of contact	$[\text{Rad.}]$
θ_{c1}	Principle (max or min) contact angle, orthogonal to θ_{c2}	$[\text{Rad.}]$
θ_{c2}	Principle (min or max) contact angle, orthogonal to θ_{c1}	$[\text{Rad.}]$
θ_z	Angle of rotation about the vertical z-axis	$[\text{Rad.}]$
θ_1	Small angle of a circular sector of a radius (R_1) and an arclength (ε) on the principle section DFB of figure 10	$[\text{Rad.}]$
θ_2	Small angle of a circular sector of a radius (R_2) and an arclength (ε) on the principle section AGC of figure 10	$[\text{Rad.}]$
ρ	Density	$[\text{mass}/\text{Length}^3]$
ρ_c	Concrete density	$[\text{mass}/\text{Length}^3]$
ρ_w	Water density	$[\text{mass}/\text{Length}^3]$
ρ_{soln}	Solution density	$[\text{mass}/\text{Length}^3]$
ρ_{solv}	Solvent density	$[\text{mass}/\text{Length}^3]$
ψ_s	Activity Coefficient of solvent in a solution	$[\text{Unitless}]$

14. ACKNOWLEDGEMENTS

In matters of programming with CRBasic, the author relied heavily on the experience of Jon Emenheiser. I would also like acknowledge and thank those who served on my graduate committee including: Dr. Michael C. Brown, Dr. Steven B. Chase, Dr. Thomas T. Baber, Dr. Devin K. Harris and Dr. Zachary C. Grasley. I would also like to express gratitude to my wife, Tameka, who has always supported me.

15. BIBLIOGRAPHY

- Adamson, Arthur W. and Alice P. Gast. 1997. *Physical Chemistry of Surfaces*. A Wiley-Interscience Publication. 6th ed. New York: Wiley.
- Andrade, C., J. Sarriá, and C. Alonso. 1999. "Relative Humidity in the Interior of Concrete Exposed to Natural and Artificial Weathering." *Cement and Concrete Research* 29 (8): 1249-1259. doi:10.1016/S0008-8846(99)00123-4.
- ASTM Standard C1202. 2012. *Standard Test Method for Electrical Indication of Concrete's Ability to Resist Chloride Ion Penetration*. West Conshohocken, PA: ASTM International. doi:10.1520/C1202-12. www.astm.org.
- ASTM Standard C1498. 2004a (2010) e1. *Standard Test Method for Hygroscopic Sorption Isotherms of Building Materials*. West Conshohocken, PA: ASTM International. doi:10.1520/C1498-04AR10E01. www.astm.org.
- ASTM Standard C642. 2006. *Standard Test Method for Density, Absorption, and Voids in Hardened Concrete*. West Conshohocken, PA: ASTM International. doi:10.1520/C0642-06. www.astm.org.
- ASTM Standard E104. 2002 (2007). *Standard Practice for Maintaining Constant Relative Humidity by Means of Aqueous Solutions*. West Conshohocken, PA: ASTM International. doi:10.1520/E0104-02R07. www.astm.org.
- ASTM Standard F2170. 2011. *Standard Test Method for Determining Relative Humidity in Concrete Slabs using in Situ Probes*. West Conshohocken, PA: ASTM International. doi:10.1520/F2170-11. www.astm.org.
- Atkins, P. W. 1990. *Physical Chemistry*. 4th ed. New York: Freeman.
- . 2006. *Atkins' Physical Chemistry*. 8th ed. Oxford ; New York: Oxford University Press.
- Brunauer, Stephen, P. H. Emmett, and Edward Teller. 1938. *Adsorption of Gases in Multimolecular Layers*. *Journal of the American Chemical Society*. Vol. 60 American Chemical Society. doi:10.1021/ja01269a023.
- Chapra, Steven C. 2008. *Applied Numerical Methods with MATLAB for Engineers and Scientists*. 2nd ed. Boston: McGraw-Hill Higher Education.
- Chatterji, S. 2001. "A Discussion of the Paper "Mercury Porosimetry—an Inappropriate Method for the Measurement of Pore Size Distributions in Cement-Based Materials"

by S. Diamond." *Cement and Concrete Research* 31 (11): 1657-1658.
doi:10.1016/S0008-8846(01)00618-4.

CSI. 2009. *Instruction Manual: AM16/32B Relay Multiplexer*. 815 West 1800 North, Logan Utah 84321-1784: CAMPBELL SCIENTIFIC, INC. (CSI).

———. . 2010a. *Instruction Manual: AM25T Solid State Multiplexer*. 815 West 1800 North, Logan, Utah 84321-1784: CAMPBELL SCIENTIFIC, INC. (CSI).

———. . 2010b. *Operator's Manual: CR1000 Measurement and Control System*. 815 West 1800 North, Logan Utah 84321-1784: CAMPBELL SCIENTIFIC, INC. (CSI).

Defay, Raymond, I. Prigogine, and A. Bellemans. 1966. *Surface Tension and Adsorption*. London: Longmans.

Diamond, Sidney. 2000. "Mercury Porosimetry: An Inappropriate Method for the Measurement of Pore Size Distributions in Cement-Based Materials." *Cement and Concrete Research* 30 (10): 1517-1525. doi:10.1016/S0008-8846(00)00370-7.

———. 2001a. "Reply to the Discussion by S. Chatterji of the Paper "Mercury Porosimetry—an Inappropriate Method for the Measurement of Pore Size Distributions in Cement-Based Materials". " *Cement and Concrete Research* 31 (11): 1659. doi:10.1016/S0008-8846(01)00619-6.

———. 2001b. "Reply to the Discussion by S. Wild of the Paper "Mercury Porosimetry—an Inappropriate Method for the Measurement of Pore Size Distributions in Cement-Based Materials". " *Cement and Concrete Research* 31 (11): 1655-1656. doi:10.1016/S0008-8846(01)00617-2.

éCernây, Robert and Pavla Rovnanâikovâa. 2002. *Transport Processes in Concrete*. London ; New York: Spon Press.

Ekaputri, Januarti Jaya, Amiltra Bongochgetsakul, Tetsuya Ishida, and Koichi Maekawa. 2009. "Internal Relative Humidity Measurement on Moisture Distribution of Mortar Considering Self-Dessication at Early Ages." *Japan Concrete Institute* 31 (1): 643-648. www.data.jci-net.or.jp/data_pdf/31/031-01-1101.pdf.

Espinosa, Rosa Maria and Lutz Franke. 2006. "Inkbottle Pore-Method: Prediction of Hygroscopic Water Content in Hardened Cement Paste at Variable Climatic Conditions." *Cement and Concrete Research* 36 (10): 1954-1968.
doi:10.1016/j.cemconres.2006.06.011.

Gentle, Ian and Geoff Barnes. 2005. *Interfacial Science: An Introduction*. Oxford ; New York: Oxford University Press.

- Grasley, Zachary C., David A. Lange, Matthew D. D'Ambrosia, and Salvador Villalobos-Chapa. 2006. "Relative Humidity in Concrete: What does it Mean?" *Concrete International* 28 (10): 51-57.
- Grasley, Zachary C. and Chin K. Leung. 2011. "Desiccation Shrinkage of Cementitious Materials as an Aging, Poroviscoelastic Response." *Cement and Concrete Research* 41 (1): 77-89. doi:10.1016/j.cemconres.2010.09.008.
- Grasley, Zachary, David Lange, and Matthew D'Ambrosia. 2006. *Internal Relative Humidity and Drying Stress Gradients in Concrete*. Vol. 39 Springer Netherlands. doi:10.1617/s11527-006-9090-3.
- Grasley, Zachary C and David A Lange. 2007. "Thermal Dilation and Internal Relative Humidity of Hardened Cement Paste." *Materials and Structures* 40 (3): 311. doi:10.1617/s11527-006-9108-x. <http://dx.doi.org/10.1617/s11527-006-9108-x>.
- Greenspan, Lewis. 1977. "Humidity Fixed Points of Binary Saturated Aqueous Solutions." *Journal of Research of the National Bureau of Standards. Section A: Physics and Chemistry* 81A (1): 89-96.
- Hillerborg, Arne. 1985. "A Modified Absorption Theory." *Cement and Concrete Research* 15 (5): 809-816. doi:10.1016/0008-8846(85)90147-4.
- Horvath, A. L. 1985. *Handbook of Aqueous Electrolyte Solutions: Physical Properties, Estimation, and Correlation Methods*. Ellis Horwood Series in Physical Chemistry. Chichester; New York: Ellis Horwood; Halsted Press.
- Ishida, Tetsuya, Koichi Maekawa, and Toshiharu Kishi. 2007. "Enhanced Modeling of Moisture Equilibrium and Transport in Cementitious Materials Under Arbitrary Temperature and Relative Humidity History." *Cement and Concrete Research* 37 (4): 565-578. doi:10.1016/j.cemconres.2006.11.015.
- Kosmatka, Steven H., Beatrix Kerkhoff, and William C. Panarese. 2002. *Design and Control of Concrete Mixtures*. Engineering Bulletin. 14th ed. Skokie, Ill.: Portland Cement Association.
- Kreyszig, Erwin. 1991. *Differential Geometry*. New York: Dover Publications.
- Lamond, Joseph F. and J. H. Pielert. 2006. *Significance of Tests and Properties of Concrete and Concrete-Making Materials*. Stp. Vol. 169D. West Conshohocken, PA: ASTM International.
- Langmuir, Irving. 1918. *The Adsorption of Gases on Plane Surfaces of Glass, Mica and Platinum*. Vol. 40 American Chemical Society. doi:10.1021/ja02242a004.

- Larson, Ron, Robert P. Hostetler, and Bruce H. Edwards. 2002. *Calculus with Analytic Geometry*. 7th ed. Boston: Houghton Mifflin Co.
- Lyklema, J. 2001. *Solid-Liquid Interfaces*. Fundamentals of Interface and Colloid Science. Reprint ed. Vol. 2. London u.a.: Academic Press.
- Masterton, William L. and Cecile N. Hurley. 2004. *Chemistry: Principles and Reactions*. 5th ed. Belmont, CA: Thomson-Brooks/Cole.
- Mehta, P. K. and Paulo J. M. Monteiro. 2006. *Concrete: Microstructure, Properties, and Materials*. 3rd ed. New York: McGraw-Hill.
- Meyers, Drew. 1991. *Surfaces, Interfaces, and Colloids: Principles and Applications*. New York, N.Y.: VCH Publishers.
- Monk, Paul M. S. 2004. *Physical Chemistry: Understanding our Chemical World*. Chichester, West Sussex, England ; Hoboken, NJ: Wiley.
- Navidi, William Cyrus. 2008. *Statistics for Engineers and Scientists*. 2nd ed. Boston: McGraw-Hill Higher Education.
- Neville, Adam M. 2006. *Concrete: Neville's Insights and Issues*. London: Thomas Telford.
- . 2011. *Properties of Concrete*. 5th ed. Harlow, England ; New York: Pearson.
- Newman, John and B. S. Choo. 2003. *Advanced Concrete Technology*. Amsterdam ; Boston: Elsevier/Butterworth-Heinemann.
- Perry, Robert H. and Don W. Green. 2008. *Perry's Chemical Engineers' Handbook*. 8th ed. New York: McGraw-Hill.
- Pitzer, Kenneth S. 1991. *Activity Coefficients in Electrolyte Solutions*. 2nd ed. Boca Raton: CRC Press.
- Poling, Bruce E., J. M. Prausnitz, and John P. O'Connell. 2001. *The Properties of Gases and Liquids*. 5th ed. New York: McGraw-Hill.
- Popovics, Sandor. 1998. *Strength and Related Properties of Concrete: A Quantitative Approach*. New York: Wiley.
- Reinhardt, H. W. and RILEM Technical Committee 146-TCF. 1997. *Penetration and Permeability of Concrete : Barriers to Organic and Contaminating Liquids : State-of-the-Art Report Prepared by Members of the RILEM Technical Committee 146-TCF*. RILEM Report. 1st ed. Vol. 16. London ;New York: E & FN Spon.

- Richardson, Mark G. 2002. *Fundamentals of Durable Reinforced Concrete*. Modern Concrete Technology. Vol. 12. London ;New York: Spon Press.
- Rodden, Robert, David A. Lange, and Zachary C. Grasley. "Development of a PC Independent Internal Relative Humidity-Temperature Measurement and Logging System for Concrete."University of Illinois at Urbana-Champaign (UIUC), Urbana, IL.
- Rowlinson, J. S. and B. Widom. 2002. *Molecular Theory of Capillarity*. Dover ed. Mineola, N.Y.: Dover Publications.
- Ruthven, Douglas M. 1984. *Principles of Adsorption and Adsorption Processes*. New York: Wiley.
- Sensirion. 2010. *Data Sheet SHT7x (SHT71, SHT75) Humidity and Temperature Sensor*. Eggbühlstr. 14, P.O. Box CH-8052 Zurich, Switzerland: Sensirion AG.
- Shaw, Duncan. 1998. *Introduction to Colloid and Surface Chemistry*. 4th ed. 225 Wildwood Avenue, Woburn, MA 01801-2041: Elsevier Butterworth-Heinemann.
- Skjaeveland, Svein M. 1993. *Derivation of the Laplace Equation*. Working Papers from Rogaland University Centre. Vol. 185. Stavanger: Hsr.
- Tipler, Paul Allen and Gene Mosca. 2004. *Physics for Scientists and Engineers*. 5th , extended ed. New York: W.H. Freeman.
- Vargaftik, N. B., B. N. Volkov, and L. D. Voljak. 1983. "International Tables of the Surface Tension of Water." *Reprint no. 231 from Journal of Physical and Chemical Reference Data* 12 (3): 817-820. <http://www.nist.gov/srd/reprints.cfm>.
- Washington, Allyn J. 1999. *Basic Technical Mathematics*. 7th ed. Reading, Mass.: Addison Wesley.
- White II, Harry L. and Jon D. Kunin. 2010. *Bridge Deck Wearing Surfaces*. 50 Wolf Road, Albany NY 12232: Transportation Research & Development Bureau (TR&DB) of the New York State Department of Transportation (NYSDOT).
- Wiederhold, P. R. 1997. *Water Vapor Measurement, Methods, and Instrumentation*. New York: Marcel Dekker.
- Wild, Stan. 2001. "A Discussion of the Paper “Mercury Porosimetry—an Inappropriate Method for the Measurement of Pore Size Distributions in Cement-Based Materials” by S. Diamond." *Cement and Concrete Research* 31 (11): 1653-1654. doi:10.1016/S0008-8846(01)00616-0.

- Winslow, Douglas and Ding Liu. 1990. "The Pore Structure of Paste in Concrete." *Cement and Concrete Research* 20 (2): 227-235. doi:10.1016/0008-8846(90)90075-9.
- Wyer, Samuel S. 1906. *A Treatise on Producer-Gas and Gas-Producers*. New York etc.: Engineering and mining journal.
- Xi, Yunping, Zdeněk P. Bažant, and Hamlin M. Jennings. 1994. "Moisture Diffusion in Cementitious Materials Adsorption Isotherms." *Advanced Cement Based Materials* 1 (6): 248-257. doi:10.1016/1065-7355(94)90033-7.
- Zumdahl, Steven S. and Susan A. Zumdahl. 2003. *Chemistry*. 6th ed. Boston: Houghton Mifflin.

16. Appendices

16.1 APPENDIX – A: SENSOR PROBE DESIGN AND FABRICATION TECHNIQUES

16.1.1 Probe 1

Disclaimer: *Pertaining to the design of the sensor probe, excluding the SHT75 sensor component, the author does not specifically endorse any particular material or vendor used in the design of the sensor lead. Any product and/or vendor called out in the design, is merely a factual accounting of that which was used as part of this investigation. Equivalent materials and/or other vendors may be substituted.*

As was mentioned in section 7.1.5, there are two basic probe designs; the first design (Probe 1) is intended for placement in the representative bridge deck. The fabrication and assembly of Probe1 shall be described first. In the next section (section 16.1.2) the fabrication and assembly of the second design (Probe 2) will be addressed.

Step 1: Solder a (4)-lead interconnect socket to a length of shielded (4)-conductor, 20 gauge (AWG) wire. The length of wire used should be at least 8 to 12 inches longer than the required total lead length. An acceptable 4-pin interconnect was purchased from MILL-MAX[®] (Product No.P851-93-004-10-001000). Technical documentation and specifications may be obtained from their website (www.mill-max.com). An insulating shrink wrap was applied to the exposed pins and wires at the soldered connection, to prevent the contact of neighboring wires. The shrink wrap was applied prior to soldering, and shrunk-fit after the soldering. Care should be taken to avoid premature shrinkage of the insulating wrap during the soldering process. An example of the finished product can be seen in figure A1.

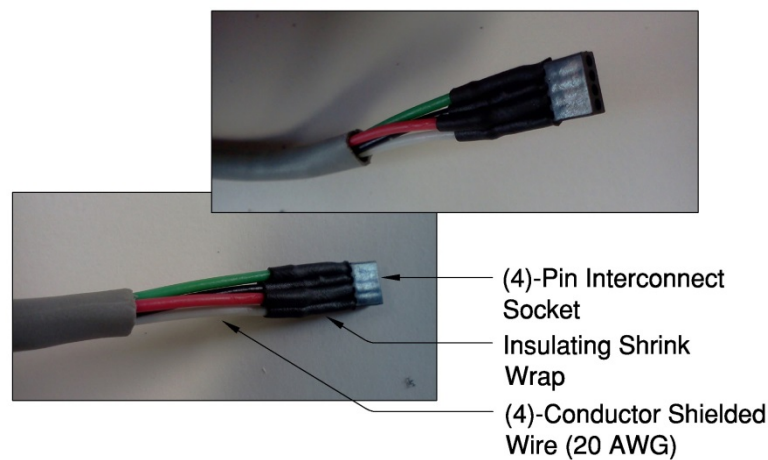
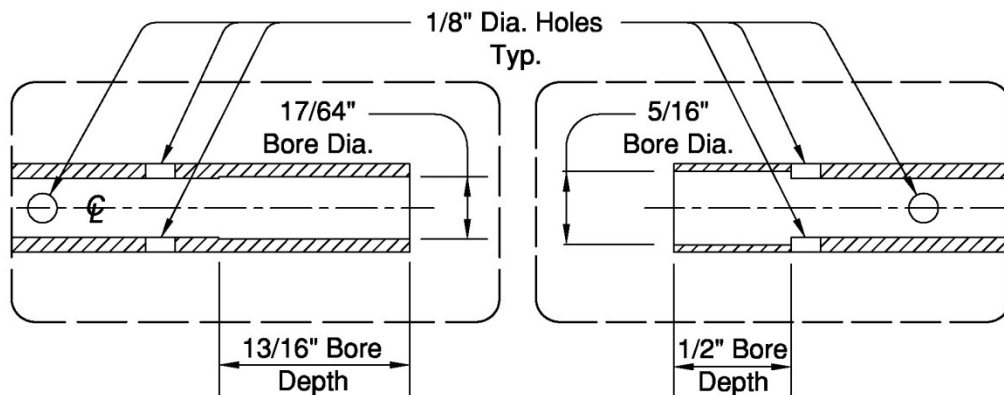
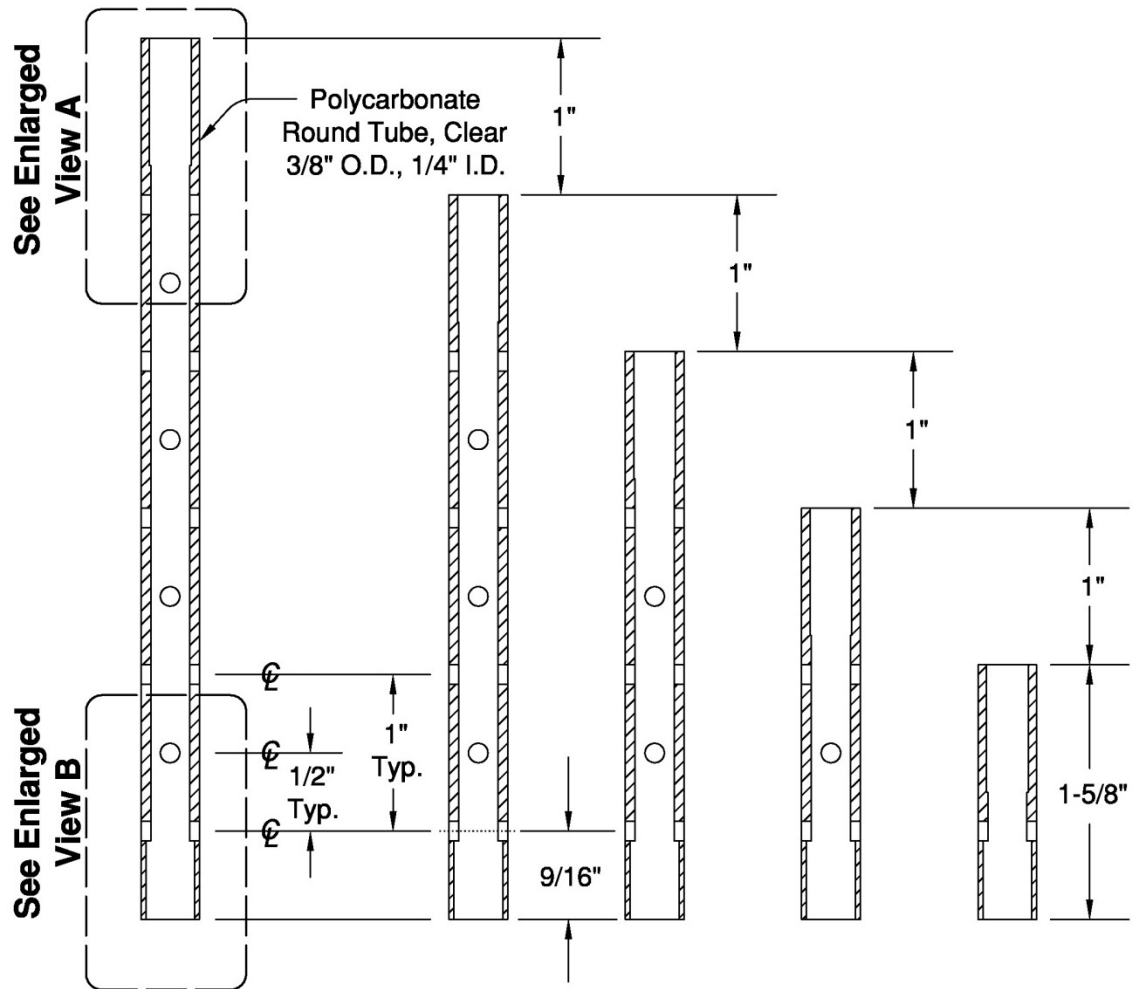


Figure A1: Interconnect socket soldered to a lead wire, with insulating shrink-wrap

Step 2: Cut to length and machine clear round stock impact-resistant polycarbonate tubing ($3/8"$ O.D., $1/4"$ I.D.) according to figure A2. The stock polycarbonate tubing was purchased from McMaster-Carr[®] (product No. 8585K11); purchases may be made online from their website (www.mcmaster.com). Starting from the right and moving to the left (of figure A2), the lengths increase in increments of one inch. The two details which show bore depths and sizes (see Enlarged View A and B) are applicable to all lengths indicated. The $1/8"$ diameter holes shown are created by drilling through the round stock (creating a set of holes). The first set of holes is centered at $9/16"$ from the bottom, as shown. Subsequently, at $1/2"$ increments from the first set of holes, additional holes are centered and created in an alternating, 90° , pattern about the tube's longitudinal axis. The total number of holes for a given length is indicated by inspection of figure A2. The lengths shown, from right to left, are intended for placement in the specimen at depths ranging from 2 to 6 inches (whole integer depths), respectively. In the case where placement is at a fractional depth (say $2.5"$), then the housing length may be modified accordingly; alternatively, the closest shorter length may be used. It should be noted that the $1/8"$ diameter holes serves a few functions. The holes allow for easier silicone injection, a task explained later during the assembly procedure; they will also facilitate quicker, uniform and a more complete curing of the injected silicone. Then, once the injected silicone cures, the filled holes will offer a mechanical interlock preventing the sensor from moving inside the housing.

Step 3: In order to assemble all the sensor leads with consistent quality and sensor cavity volume (i.e., a consistent control volume), a fixture was created; the fixture serves a few functions. First, it locates the (4)-pin interconnect socket in the probe housing. Second, it maintains the cavity that the sensor will need to eventually occupy. Third it supports the entire assembly, during a silicone injection process (step 5) until the support is no longer required. The design of the fixture is shown in figure A3; this design is capable of supporting up to 5 sensor assemblies at a time.

Step 4: The next component required is a tube plug that will cover the back end of the housing assembly, but allow for the shielded (4)-conductor wire to pass through it. Prior to fabrication, stock tube plugs were ordered from International Equipment Components, Inc., based in Signal Hill, CA. The tube plugs selected for this application were round polyethylene tube plugs to accommodate a $3/8"$ tubing O.D. (product No. IL24D – CAP – RD). Technical specifications may be downloaded from the company's website (www.iec-corp.com). Some modification to this component is necessary, as the stock tube plug does not initially accommodate the passage of the shielded (4)-conductor wire. Therefore, a hole is to be drilled through it. In general, the hole should allow passage of the fully insulated lead wire, threaded by the end of the lead wire without the soldered (4)-pin interconnect socket, while providing a snug fit. While the actual size of the drilled hole may vary, the author used a $11/64"$ diameter drill bit to clear a passage. The next couple of steps are the actual assembly of the probe. Prior to the application of the silicone filler material (step 5), the assembly should look as shown in figure A4 (shown on the fixture), though, probe housing lengths will vary.



Enlarged View A

Enlarged View B

Figure A2: Sensor probe housing fabrication drawing with machining details

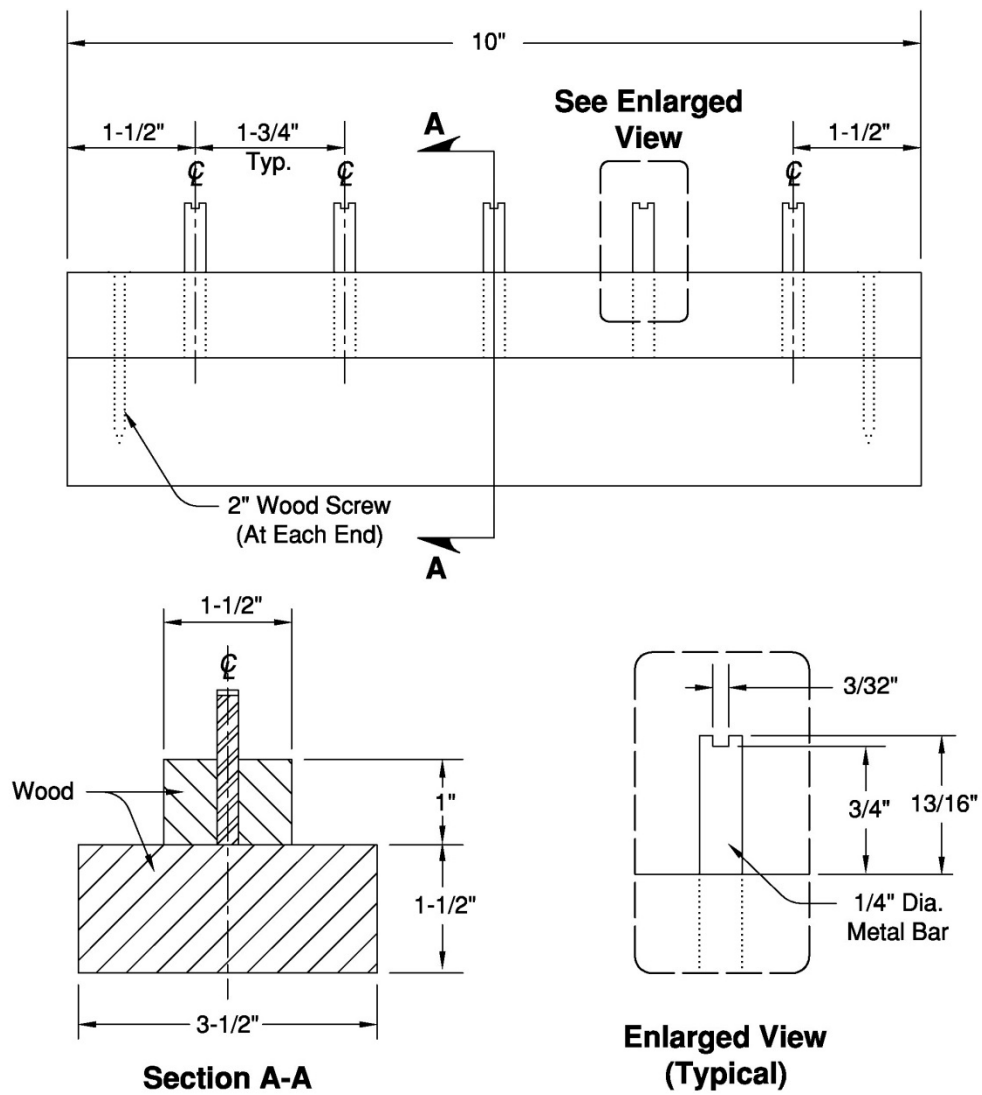


Figure A3: Sensor assembly fixture

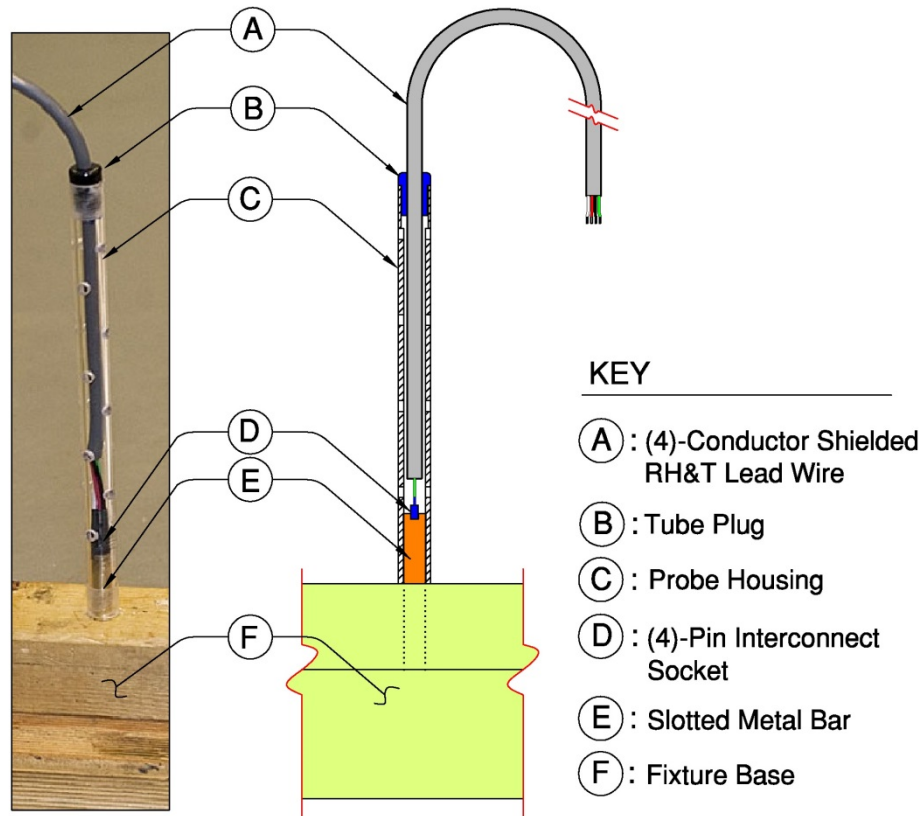


Figure A4: Example probe assembly prior to application of silicone (shown on the fixture)

Step 5: This step involves the application of silicone filler. The silicone filler material used (i.e., black silicone window and door caulking) was purchased from Lowe's[®] (product No. 219088, model No. LW5030); product details may be viewed on the Lowe's[®] company's website (www.lowes.com). Application of the silicone material begins by slipping the tube plug off the probe housing, allowing access to the housing's inside, while the rest of the assembly remains in place on the fixture. Then the silicone is injected into the probe housing through the 1/8" diameter holes and the exposed top, as shown in figure A5 (left). Once filled, the tube plug is placed back onto the sensor housing (figure A5 (middle)) and any excess silicone overflow is wiped off. This process is done for all the assemblies on the fixture (figure A5 (right)). They are then left undisturbed for approximately one week prior to being taken off the fixture. It should be noted that while a period of one week was allowed by the author for curing, the actual time required was not determined. Once taken off fixture, the [user calibrated] SHT75 sensors would be plugged into the (4)-pin interconnect socket. That is to say the (4)-pins of the SHT75 plug into the 4 exposed holes of the (4)-pin interconnect socket. The receiving holes should be free of silicone filler and able to receive the sensor. If some of the silicone filler ends up clogging any of the holes of the (4)-pin interconnect socket, then a small needle may be used to clear the obstructed holes.

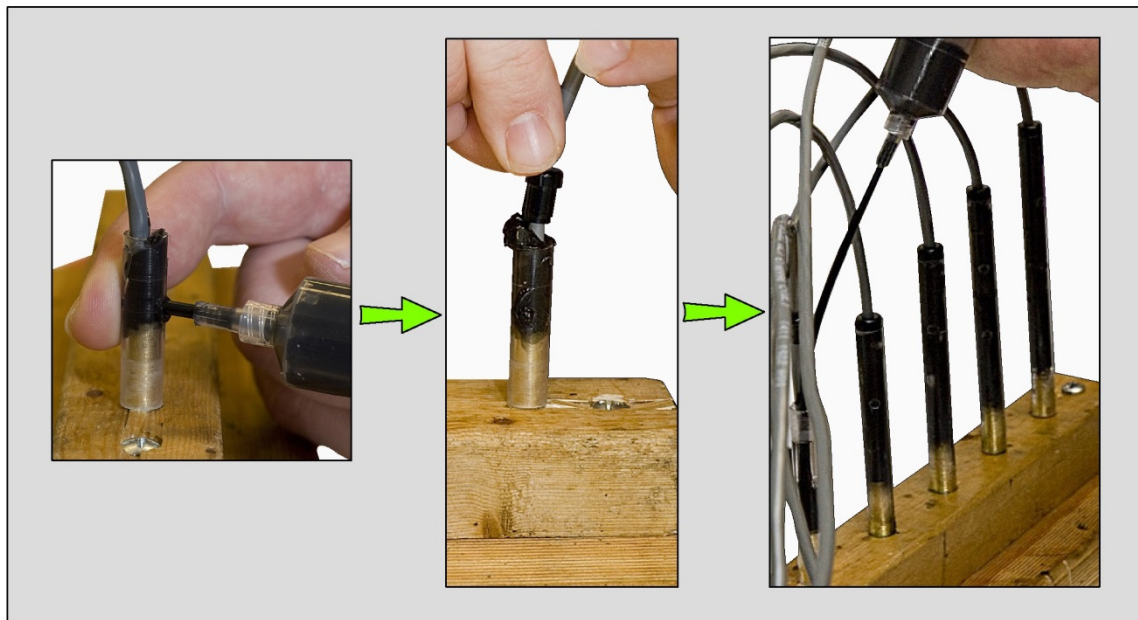


Figure A5: Example injection process, of black silicone into probe assembly

Step 6: In order to have a probe assembly that looks like the one shown in figure 26 (section 7.1.5), the reader would need to include all the steps shown in figure A6 (steps 6A through 6E). Step 6A (see figure A6) shows the application of a protective venting material. There are several materials in the market place, similar to GORE[®] Protective Vents (www.gore.com); these products prevent liquid and particulates from passing through them but allow airflow. For this investigation the author decided to use a protective venting material developed by General Electric[®] (GE[®]) (www.ge-energy.com), and supplied by Label Technologies Inc., Atlanta (LTI Atlanta), a converting and die-cutting company based in Suwanee, GA. The particular product used was called “LTI Yellow 76”; at the time this vent material was obtained (July 2011), it was claimed to offer the highest unit airflow properties in the industry. However, this claim was not confirmed by the author. Requests for technical specifications may be directed to the LTI Atlanta company website (www.ltiatlanta.com).

The vent used has a side with an adhesive material which is centered over, and pressed onto, the top of the probe housing. Any excess venting material that hangs over the top of the probe housing would be folded over the housing sides, as shown. Additionally, the author used a plastic heat shrink material to cover the body of the probe housing. This was done to protect the housing from normal wear-and-tear. A small amount of high vacuum grease was applied between the heat-shrink material and the housing to prevent this from becoming a path of air infiltration. Step 6B shows the application of a spring collar component around the [folded] excess vent material. This serves to prevent the vent material from becoming separated from the probe housing. The spring collar used was constructed by the author. Fabrication of the spring collar began by obtaining a piece of stock polycarbonate round tube, having an O.D. of 1/2" and an initial I.D.

of 3/8". Sections of tube, 3/16" long, were sliced off; however, just prior to that, a drill bit was used to bore the I.D. to 13/32". The final step was to cut a break in the ring; this break allows the ring to expand radially. It should be noted that if the reader feels that the use of a spring collar is warranted for their application, many other collar types may be considered including a purchased spring collar (i.e., manufactured by someone else), elastic banding or an O-ring. Step 6C shows the application of a plastic heat shrink material over the spring collar. This was used to ensure that the spring collar was sufficiently captured and would not move during placement or removal of the probe from the concrete bridge deck specimen.

Step 6D shows the application of a closed-cell rubber weather stripping around the exterior of the probe housing, just behind the spring collar. It should be noted that the thickness of the weather stripping is governed by the clearance between the probe housing and the drilled hole created for the placement of the sensor; consequently, the weather stripping thickness will need to be modified (i.e., cut) to fit. Recall that the drilled hole is 5/8" in diameter and the O.D. of the probe is 3/8". By this rationale a thickness of approximately 3/16" was used by the author. The width of the weather stripping used was 3/8". Additionally, the weather stripping used had an adhesive side, which was used to create a bond between it and the probe housing. Though the weather stripping is bonded to the probe housing by the adhesive side, the author still used a centrally located rubber O-ring. The O-ring was purchased from Lowe's® (product No. 198968, model No. 96724); the dimensions of the specific O-ring product are 3/8" x 1/2" x 1/16". Additional product details may be viewed on the company's website (www.lowes.com). The O-ring not only reinforced the bond between the weather stripping and the probe housing, but also provided a groove in which the thermocouple sensor's looping may be placed, as shown in step 6E. Finally, though not shown in figure A6, one would attach the thermocouple sensor lead wire to the probe's housing. As shown in figure 26, this was accomplished by simply taping the lead, with electrical tape, to the sensor housing.

It should be noted that the use of a venting material was intended to protect the sensor from debris and any moisture that would condense in the concrete cavity and subsequently drip onto the sensor. However, it would seem that unless the probes are to be placed in fresh concrete, there may be very little value to using a protective vent material; that is to say the reader may wish to omit some of the fabrication steps, in particular steps 6A through 6C. The only steps that were not optional for the purpose of this investigation were those that included the attachment of the closed-cell rubber weather stripping and thermocouple sensor components (step 6D and 6E).

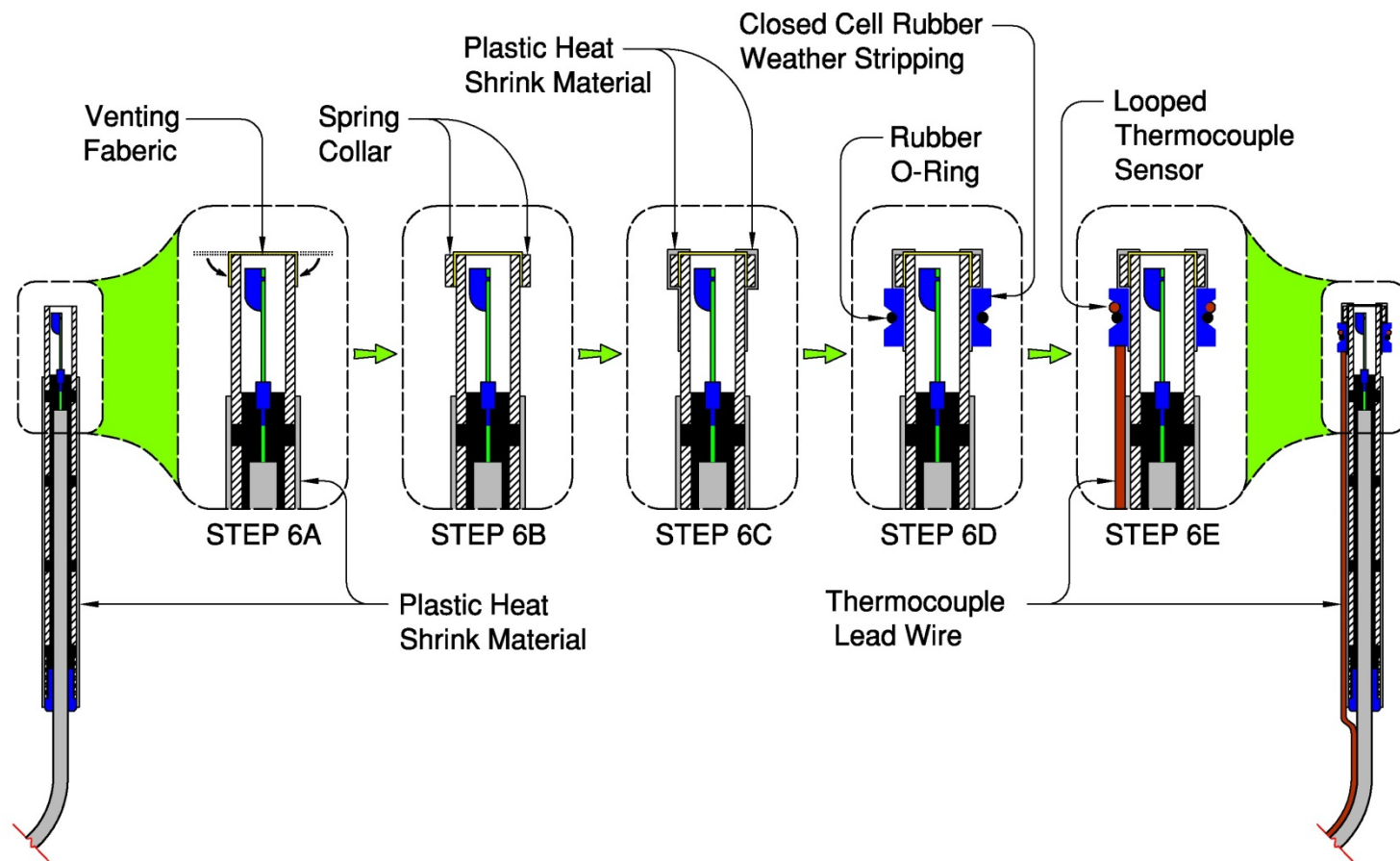


Figure A6: Final steps of the probe 1 assembly used by the author

16.1.2 Probe 2

In this section, the fabrication and assembly of the second design (Probe 2), as shown in figure 27 (section 7.1.5) will be addressed. Probe 2 was designed for placement in the disc specimens that were used to create the moisture sorption isotherms. Consequently, there were a few design differences. However, such differences did not significantly impact the initial stages of sensor fabrication and assembly. Therefore, the first 5 fabrication and assembly steps used to create the first probe (Probe 1) were also used to create the second probe (Probe 2). The only difference is that the probe 1 design spans several probe housing lengths, while the probe 2 design is of a single probe housing length, specifically the 1 - 5/8" length as shown in figure A2. Since the steps to follow occur after the first 5 steps of the last section (section 16.1.1) have been accomplished, the sequence in this section begins with step 6.

Steps 1 through 5: See steps 1 through 5, of section 16.1.1

Steps 6: Once the nominally 2" probe assemblies are removed from the fixture, the lead wire (i.e., the 4-conductor shielded RH&T lead wire) is cut such that only a few inches of lead wire are still extending from the rear of the probe assembly. A rubber stopper plug, with a hole drilled through it such that the lead wire just passes through it, is added to the assembly as can be seen in figure 27. The rubber stopper used was 5/16" diameter at the small end and 7/16" diameter at the large end, and had a length of 11/16".

Step 7: At this time a male 4-conductor connector is attached to the lead wire extending from the probe assembly. The mating female 4-conductor connector is attached to length of lead wire not still attached to the probe assembly. The lead wire with the female connector end is wired directly to the DAQ. Molex[®] Micro-Fit 3.0[™] connectors were used in this application; they were purchased from Mouser[®] electronics. Technical and ordering information for the male and female connector ends used (Catalog No. 538-43020-0401 and Catalog No. 538-43025-0400, respectively) along with the corresponding male pins and female sockets (Catalog No. 538-43031-0008 and Catalog No. 538-43030-0008, respectively) may be found on the Mouser[®] company website (www.mouser.com). It should be noted that, once joined, at the location where the connector and the lead wire meet, a small amount of [black] liquid electrical tape was applied to cover and protect the connection.

Step 8: After the connectors are attached, the exterior of the probe housing is sanded, as shown in figure A7, until it just fits into the holes that were created in the disc specimens. It should be noted that the housing was plugged with a sponge material to prevent particulate matter, resulting from the sanding process, from getting into the sensor cavity. Testing the fit of the probe assembly required that the wrapping around the hole in the disc specimen be breached. The author made a small incision in the vicinity of the disc specimen hole, exposing the hole, then covered the exposed area with a piece of duct tape. When it was time to test the fit, the duct tape was momentarily peeled back, the

probe assembly was wiped clean and the fit was tested; after the fit was tested, the breach was covered back over. This is an iterative process. It should also be noted that once all the probe assemblies were fitted, step 9 was immediately performed.

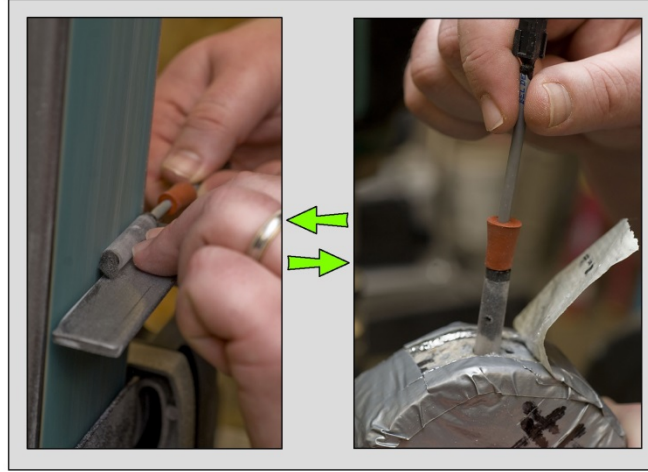


Figure A7: Fitting the probe assembly into the disc specimen; an iterative process of sanding (left) and test fitting (right).

Step 9: At this point, the probe assembly is nearly complete. Just before the disc specimens are prepared to be used in creation of the moisture sorption isotherms, as outlined in section 7.4.2, the probe assembly is fitted with the SHT75 sensor. The finished probe is then placed into the disc specimen, in the manner also described in section 7.4.2.

16.2 APPENDIX – B: RH & T SENSOR CALIBRATIONS

The following RH calibration function (equations 16.1, 16.2, 16.3 and 16.4) is programmed into the DAQ code, and is used to handle the user-defined sensor-specific calibrations. Most of the calibration function, shown below, was brought forward from the example calculation performed in section 7.2.4 (equations 7.2, 7.23, 7.24 and 7.25, respectively). The general programming form was shown in section 7.2.1 through the use of pseudo-code.

$$RH_{cal.}^{Si} = RH_{Meas.}^{Si} - Residual_{Mod.}^{Si} \quad \text{Equation 16.1}$$

Where

$$\begin{aligned} Residual_{Mod.}^{Si} &= Residual_{Mod.,1}^{Si} \\ &\Rightarrow C_{RH,1}^{Si} RH_{Meas.}^{Si} + C_{T,1}^{Si} T_{Meas.}^{Si} + C_{const.,1}^{Si} \end{aligned} \quad \text{Equation 16.2}$$

if

$$RH_{Meas.}^{Si} \leq RH_{Cond.}^{Si} \Rightarrow \frac{(C_{T,2}^{Si} - C_{T,1}^{Si})T_{Meas.}^{Si} + C_{const.,2}^{Si} - C_{const.,1}^{Si}}{(C_{RH,1}^{Si} - C_{RH,2}^{Si})} \quad \text{Equation 16.3}$$

else

$$\begin{aligned} Residual_{Mod.}^{Si} &= Residual_{Mod.,2}^{Si} \\ &\Rightarrow C_{RH,2}^{Si}RH_{Meas.}^{Si} + C_{T,2}^{Si}T_{Meas.}^{Si} + C_{const.,2}^{Si} \end{aligned} \quad \text{Equation 16.4}$$

The following tables provide the equation coefficients ($C_{RH,k}^{Si}, C_{T,k}^{Si}$), equation constants ($C_{const.,k}^{Si}$) and the coefficients of determination (R^2) for each sensor used in the representative bridge deck (table B1) and in the disc specimens (table B2), along with their corresponding probe assignments. In most cases, a probe's assigned sensor required recalibration, and at times replacement. Therefore, all calibration values shall be presented in sequence of oldest to newest (top to bottom, respectively) for a given sensor in an assigned probe. Also, since the sensor number merely indicates the sensor's position inside the RH calibration apparatus, the author uses subscripting (A# through E#) to help the reader track the sensors used in a given probe, and be able to identify a sensor recalibration versus sensor replacement. When the subscript does not change for a given sensor number, this would indicate only recalibration was performed, with the physical sensor remaining unchanged; when the subscript increments to another value (ex. A1→A2), this would indicate that the sensor was replaced. Finally, the author has provided table B3, which indicates the saturated [salt] solution environment being used with the given batch number.

Probe No.	Sensor No.	Batch Numbers Used	k th Model No.	$C_{RH,k}^{Si}$	$C_{T,k}^{Si}$	$C_{const,k}^{Si}$	R ²	Notes
1	5 _(A1)	006,002, 007	1	-0.125591	-0.311680	24.653680	0.9957	4
			2	-0.125591	-0.311679	24.653674	0.9957	1,4
1	1 _(A1)	014,015	1	-0.218691	-0.326850	48.134206	0.9740	2,5
			2	-0.218691	-0.326851	48.134209	0.9740	1,2,5
3	7 _(B1)	006,002, 007	1	-0.071136	-0.280649	19.151872	0.9919	4
			2	-0.071136	-0.280649	19.151868	0.9919	1,4
3	2 _(B1)	014,015	1	-0.239988	-0.315860	52.235409	0.9695	2,5
			2	-0.239988	-0.315860	52.235414	0.9695	1,2,5
4	6 _(C1)	006,002, 007	1	-0.111468	-0.305696	24.242247	0.9958	3,4
			2	-0.111469	-0.305696	24.242250	0.9958	1,3,4
4	3 _(C1)	014,015	1	4.654637	1.475026	-514.5667	0.9914	2,3,5
			2	4.654637	1.4750267	-514.5667	0.9914	1,2,3,5
5	8 _(D1)	006,002, 007	1	-0.122858	-0.304174	25.078564	0.9953	4
			2	-0.122858	-0.304173	25.078556	0.9953	1,4
5	4 _(D1)	014,015	1	-0.322267	-0.360673	61.664175	0.9737	2,5
			2	-0.322267	-0.360673	61.664180	0.9737	1,2,5
6	9 _(E1)	006,002, 007	1	-0.100424	-0.297608	23.223201	0.9965	4
			2	-0.100424	-0.297608	23.223194	0.9965	1,4
6	5 _(E1)	014,015	1	-0.320875	-0.367707	62.290393	0.9788	2,5
			2	-0.320875	-0.367707	62.290399	0.9788	1,2,5

Table B1: Planar best-fit values for each the sensors used in the representative bridge deck

Probe No.	Sensor No.	Batch Numbers Used	k th Model No.	$C_{RH,k}^{Si}$	$C_{T,k}^{Si}$	$C_{const,k}^{Si}$	R ²	Notes
1	1 _(A1)	014,015	1	-0.218691	-0.326850	48.134206	0.9740	2,5
			2	-0.218691	-0.326851	48.134209	0.9740	1,2,5
1	1 _(A1)	024,025	1	-0.708656	-0.445098	102.266980	0.9999	1,6
			2	-0.708657	-0.445098	102.267061	0.9999	6
1	1 _(A2)	020,021, 022,023	1	-0.176763	-0.326420	25.417146	0.9946	
			2	-0.598143	-0.435347	69.179773	0.9951	
2	2 _(B1)	014,015	1	-0.239988	-0.315860	52.235409	0.9695	2,5
			2	-0.239988	-0.315860	52.235414	0.9695	1,2,5
2	2 _(B1)	024,025	1	-0.992841	-0.483971	137.523770	0.9981	1,6
			2	-0.992842	-0.483971	137.523866	0.9981	6
2	2 _(B2)	020,021, 022,023	1	-0.280766	-0.359901	37.106516	0.9882	
			2	-0.532217	-0.410173	63.042031	0.9870	
3	3 _(C1)	014,015	1	4.654637	1.475026	-514.5667	0.9914	2,3,5
			2	4.654637	1.4750267	-514.5667	0.9914	1,2,3,5
3	3 _(C1)	024,025	1	0.285368	-0.225436	-15.806382	0.9992	1,3,6
			2	0.285368	-0.225436	-15.806348	0.9992	3,6
3	3 _(C2)	020,021, 022,023	1	-0.342206	-0.373804	47.595831	0.9936	
			2	-0.592946	-0.430296	74.364464	0.9863	
4	4 _(D2)	018, 019	1	-1.464903	-0.560098	191.931334	0.9998	
			2	-1.464902	-0.560098	191.931329	0.9998	1
4	4 _(D2)	024,025	1	-0.167052	-0.292995	39.748670	0.9966	1,6
			2	-0.167053	-0.292995	39.748728	0.9966	6
4	4 _(D3)	020,021, 022,023	1	-0.352841	-0.384713	49.074041	0.9931	
			2	-0.687052	-0.457671	84.716112	0.9864	
6	5 _(E1)	014,015	1	-0.320875	-0.367707	62.290393	0.9788	2,5
			2	-0.320875	-0.367707	62.290399	0.9788	1,2,5
5	5 _(E1)	024,025	1	-0.930639	-0.517372	131.113101	0.9999	1,6
			2	-0.930631	-0.517372	131.113193	0.9999	6
5	5 _(E2)	020,021, 022,023	1	-0.350213	-0.372257	48.373111	0.9934	
			2	-0.656020	-0.444238	81.091233	0.9810	

Table B2: Planar best-fit values for each the sensors used in the disc specimens

Notes to accompany tables B1 and B2:

1. Single RH residual model assumed, perturbation technique was applied
2. It was determined that a + 3% RH shift should be applied to values obtained from Batch No. 015
3. This sensor was declared “corrupt” by the author
4. Calibration function initially used in the representative bridge deck.
5. Calibration function used to post process the data and account for the sensor conditioning.
6. Calibration function used to post process the first data point obtained from the disc specimens

Batch Number	Saturated Solution Environment
002	Potassium Chloride (KCl)
006	Sodium Chloride (NaCl)
007	Potassium Sulfate (K_2SO_4)
014	Potassium Sulfate (K_2SO_4)
015	Potassium Chloride (KCl)
018	Potassium Sulfate (K_2SO_4)
019	Pure Water (H_2O)
020	Sodium Chloride (NaCl)
021	Potassium Chloride (KCl)
022	Potassium Sulfate (K_2SO_4)
023	Pure Water (H_2O)
024	Pure Water (H_2O)
025	Potassium Sulfate (K_2SO_4)

Table B3: Batch numbers and corresponding saturated solution environments

16.3 APPENDIX – C: PREPARATION OF CONCRETE DISC SPECIMENS

This section expounds upon a brief description, provided earlier in section 7.4.2, of the process used by the author to prepare the disc specimens that were used in the creation of the moisture sorption isotherms. Disc specimen preparation began by marking specific depth locations along at least two of the cylindrical cores extracted from the representative bridge deck specimen. The marked depths corresponded to the depths at which the sensor probes (Probe 1), used in the representative deck specimen, were placed (i.e. at the 2”, 3”, 4”, 5” and 6” depth locations) and were assigned to specific cores. Additionally, markings at the 1” and 7” depths were also created. Though RH&T information was not collected at these depths in the representative specimen, nor would it be collected in the disc specimens during the creation of the moisture sorption isotherms, gravimetrically determined moisture mass values were assessed. These assessed values were used to provide more complete gravimetric-based moisture profiles.

As was noted earlier in section 7.4.2, the reason several cores are required, in addition to possible core unacceptability, is the [author’s] required nominal thickness for a given disc specimen. Since probe depth locations are at 1” depth increments and the thickness of a disc specimen is nominally 1-1/2”, it is not possible for a single core to supply all the disc specimens required. Figure C1 provides an idealized way in which all the depths may be assigned across two given acceptable cores. As shown in figure C1, the thicknesses of the disc specimens symmetrically straddle the various marked depth locations. Also, as the depths for sensor probe (Probe 1) placement in the representative concrete deck specimen were measured from the bottom of the slab, so too the markings should be made with respect the end of the cylinder corresponding to the bottom of the representative deck specimen. The point here is to show why no less than two cores are needed. In the case of this investigation, such an idealized assignment scheme was not

possible. Due to core fracturing, delaminations and steel reinforcement inclusions, this author needed (3) core specimens to generate all the required discs specimens.

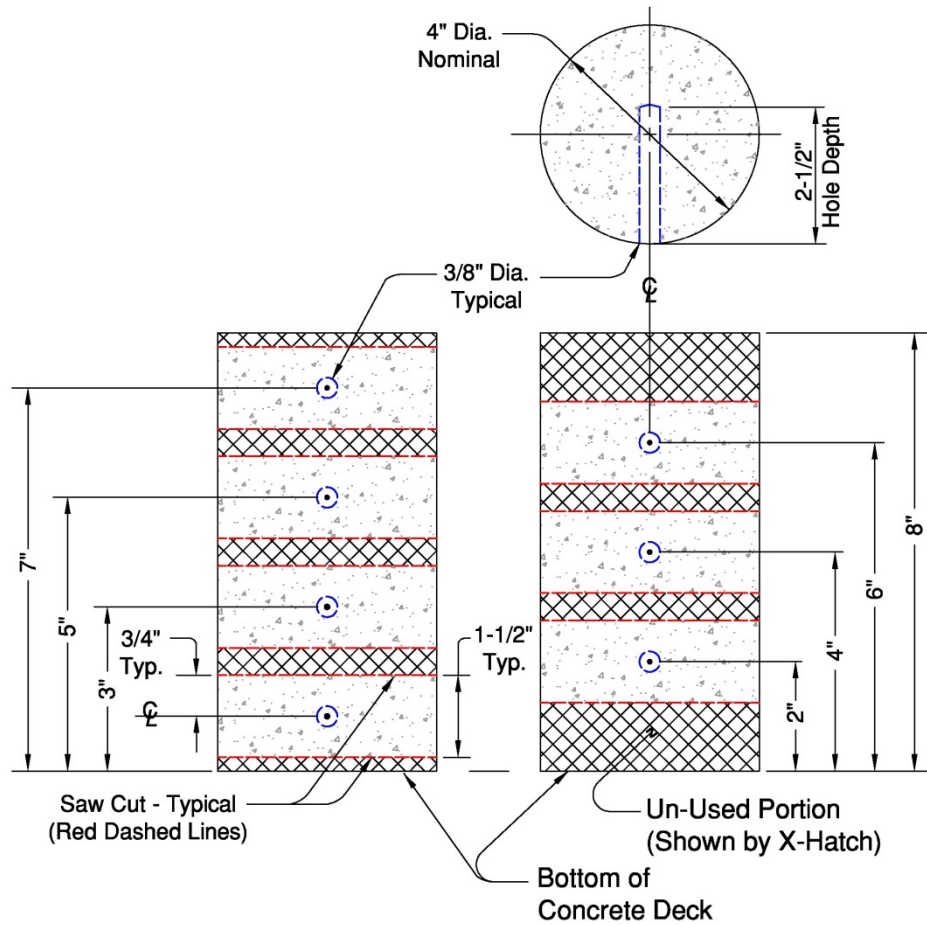


Figure C1: Views of (2)-core specimens taken from the representative concrete bridge deck, showing a suggested pattern for the creation of (7)-disc specimens.

At this point, it should be noted that only one core is unwrapped and processed at a time. This was done to prevent unnecessary exposure to ambient conditions during this preparation process. Also, as was noted in section 7.4.2, there are several “wet” processes that are necessary to prepare a disc specimen. These wet processes include the extraction of the core specimens from the representative bridge deck, drilling holes into the disc specimens for sensor probe (Probe 2) placement, and saw-cutting. As was also noted in section 7.4.2, in theory, wet-coring would cause some net gain of moisture at the surface of the specimens. However, once the specimens have been towel-dried, compared to the in-situ moisture mass contained below the surface, any residual moisture is considered trivial. Hence, wet processes are assumed not to affect the determination of the in-situ moisture mass, or other gravimetrically obtained masses, in a meaningful way.

Next, at the marked locations, 3/8" diameter holes (2-1/2" deep) are [wet] drilled into the specimen to facilitate the [later] placement of probes (Probe 2) specifically designed for the creation of the moisture sorption isotherms. This includes creating holes at the 1" and 7" depth locations. As noted previously, at these last two locations (i.e. at the 1" and 7" locations), probes were not actually placed. Rather, the holes were created for the purpose of ensuring uniform processing of specimens across all the depths. In the interest of constructability, all the holes assigned to a given core cylinder should be created prior to the next step. Once all the holes in a given core cylinder have been created, saw-cuts are made as indicated in figure C1; as noted, this is a wet process. Once these processes are completed for a given core specimen, the resulting disc specimens are towel-dried and weighed. It should be noted that just before and after each processing step from this point in time and onward, no matter how small the step, a mass value was taken; this allowed the author to account for mass changes not attributed to moisture loss or gain. Once weighed, the disc specimens were individually wrapped using the same multi-layer process used to initially wrap the core specimens after they were extracted from the representative bridge deck (see section 7.4.2). They remained wrapped until the sensor probes (Probe 2) were ready for placement. When processing of the core cylinders was complete, there were 7 disc specimens in total.